2018

Chemical Approaches to Dynein Inhibition

Jonathan Baruch Steinman

CHEMICAL APPROACHES TO DYNEIN INHIBITION

A Thesis Presented to the Faculty of

The Rockefeller University

in Partial Fulfillment of the Requirements for

the degree of Doctor of Philosophy

by

Jonathan Baruch Steinman

June 2018

CHEMICAL APPROACHES TO DYNEIN INHIBITION

Jonathan Baruch Steinman, Ph.D.

The Rockefeller University 2018

Cells utilize energy to maintain order within the cytoplasm. Motor proteins are the enzymes that convert the chemical energy contained in adenosine triphosphate (ATP) into directed movement along polarized filaments of actin and tubulin within cells. Dyneins are the primary enzymes that drive motion toward the stable "minus ends" of tubulin-containing filaments known as microtubules. This protein family is divided into two sub-families. Axonemal dyneins drive flagellar beating while cytoplasmic dyneins (hereafter, dyneins) are required a wide array of cellular processes including moving RNAs, proteins, and whole organelles and for the formation, maintenance, and positioning of the mitotic spindle, the protein apparatus that ensures proper cell division. Dyneins move their cargos at velocities > 1μm/sec in cells and contribute to processes that occur on timescales of minutes and seconds. Perturbations that act on a comparable timescale to dynein are best suited to study this dynamic motor protein. Small molecules (molecular weight <1000 Daltons) can generally engage their target within minutes. However the first cell-permeable small molecule antagonists of dynein, the ciliobrevins, have only recently been identified. As these compounds have suboptimal chemical properties and low potency, their use as probes for studying dynein has been limited. The work presented here describes a chemistry-based approach to develop new antagonists of dyneins and the resulting identification of three new classes of dynein inhibitors.

The first chapter "Chemical probes for dynein" motivates the need for cell-permeable dynein antagonists. It summarizes the available antagonists for dynein and describes their discovery and utility. Where possible, the features of these dynein inhibitors are considered in light of the concepts of selectivity and principles of protein-ligand binding. In the outlook, prospects for future development of dynein inhibitors are presented in the context of recent advances in design and development of potent and selective inhibitors for other members of the ATPases Associated with diverse cellular Activities (AAA+) protein family, to which dynein belongs.

In the second chapter, "Chemical structure-guided design of dynapyrazoles, cell-permeable dynein inhibitors with a unique mode of action," I present a rational approach to the development of derivatives of ciliobrevins that have improved potency and several improved chemical properties relative to the ciliobrevins. Structural analysis of the ciliobrevins suggested the hypothesis that replacing the isomerizable core of these compounds with a rigid tricyclic heterocycle and synthesis of such compounds led to the identification of two compounds that had 6-8 fold improved potency compared to ciliobrevin D (named the dynapyrazoles). An analysis of the mechanism of inhibition of dynein 1 by dynapyrazole A revealed that it inhibited the microtubule-stimulated ATPase activity of dynein, but did not potently inhibit the basal ATPase activity. This finding and further biochemical analyses revealed that dynapyrazole A likely inhibits the ATPase activity of dynein 1 that arises at just one of its four ATP-binding sites, AAA1. Taken together, these findings suggest that dynapyrazole A is likely to be a useful probe for studying dynein.

Subsequent chapters extend this chemical structure-guided approach to the identification and characterization of two other compound scaffolds that inhibit dynein—pyrazolopyrimidinone-based derivatives of dynapyrazoles and structurally-unrelated diaminoquinazolines. The mechanisms and sites of inhibition of these compound classes were analyzed using biochemical and structural techniques.

Finally, I present an outlook chapter in which I discuss the trends emerging from the dynein inhibitors I discovered during the course of my PhD. Most dynein inhibitors do not act in a substrate-competitive mechanism and I posit that this may be a consequence of the complex chemomechanical cycle of dynein, which involves allosteric communication between distinct ATPase sites. All compounds with identified sites of inhibition act at the AAA1 ATPase site. I propose that this may be due to the low apparent affinity of this site for ATP. In conclusion, I suggest experiments that are likely to be valuable to more clearly understand the dynein inhibitors presently available and to develop improved dynein inhibitors in the future.

Dedication

Where there is a will, there is a way…

In loving memory of Shoshana Gavrielov.

כן זה ביוטכנולוגיה…

Acknowledgements

I extend deep gratitude to the many people who contributed to my studies.

Alone we are weak, together we are strong.

To Susan-Thank you for keeping me focused. Thank you even more for distracting me.

To my parents-Thank you for starting me out along this path in life and for supporting me every step of the way.

To my colleagues and many collaborators-Your energy, commitment, and curiosity made this work possible and made this time fun.

To the MD/PhD program: Ruthie, Renee, Olaf-Thank you for giving me the opportunity to be here and providing an ongoing sense of family and support.

To my committee members: Dr. Andersen, Dr. Brady, Dr. Cantley, and Dr. Funabiki-Thank you for your energy, attention, and feedback over the years.

To Dr. Bhabha-Thank you for agreeing to be my external examiner and for the insights your work provided in understanding the complexities of dynein.

To Tarun-Thank you for teaching me to be guided and bounded only by what can be measured. Thank you for helping me set reasonable goals and for pushing me to reach them.

Table of Contents

List of Figures

List of Tables

List of Appendices

Chapter 1: Chemical probes for dynein

1.1 Introduction

Eukaryotic cells must perform multiple complex processes within a confined space to live and divide. To accomplish this, cells utilize energy to maintain spatial order(1). Cytoskeletal filaments, such as microtubules and actin fibers, are polarized polymeric arrays of proteins on which directional motion over micron-scale distances is possible. Motor proteins provide the force necessary for directed intracellular motion along these cytoskeletal filaments by converting the chemical energy in adenosine triphosphate (ATP) into kinetic energy. Repeated cycles of ATP hydrolysis by motor proteins power the motion of cargos ranging in size from single proteins to whole organelles(2). Several microtubule-based motor proteins have evolved to play specialized roles within eukaryotic cells(1).

Dynein, the first microtubule-based motor protein discovered, is responsible for most of the microtubule minus-end directed transport in eukaryotic cells. It is now clear that dynein dependent transport is important for a wide range of cellular processes, including organelle positioning, mRNA transport, and cell division(2). Dynein is a fast motor, driving cargo transport at speeds of 1-10 μm/sec(3). Therefore, properly dissecting the function of this motor protein requires controlled perturbations of its activity on timescales of seconds to minutes. Such acute inhibition of protein function is possible with cell permeable chemical inhibitors.

A

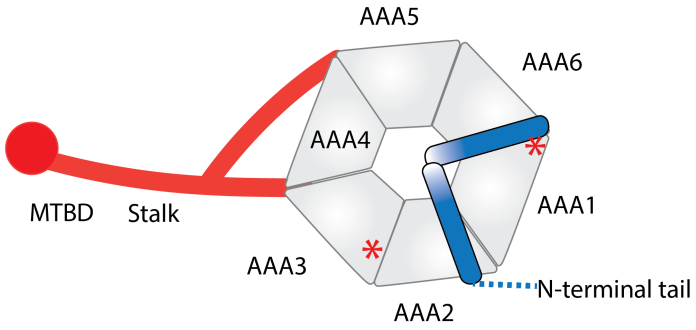

B

	Walker A	Walker B	Arg finger	N loop
cytoplasmic dynein 1 (AAA1)	**GP**a**G**t**GKT**e	wgc**FDE**fNrL	atVs**R**c**G**mV	qdkLvqtpl
cytoplasmic dynein 2 (AAA1)	**GP**a**G**t**GKT**e	wgc**FDE**fNrL	atIs**R**m**G**mI	askLvytpl
p97 (D2)	**GP**p**G**c**GKT**l	vlf**FDE**lDsI	paIl**R**p**G**rL	wedIggled
NSF (D1)	**GP**p**G**c**GKT**l	iii**FDE**iDaI	eaLl**R**p**G**rL	kmgIggldk

C

	Walker A	Walker B	Arg finger	N loop
cytoplasmic dynein 1 (AAA1)	**GPAGTGKTE**	**WGCFDEFNRL**	**ATVSR**c**GMV**	qdK**LV**q**TPL**
cytoplasmic dynein 2 (AAA1)	**GPAGTGKTE**	**WGCFDEFNRL**	**ATISR**m**GMI**	asK**LV**y**TPL**
axonemal dynein 5 (AAA1)	**GPAGTGKTE**	**WGCFDEFNRL**	**ATVSR**n**GMV**	tdR**LV**i**TPL**

D

	Walker A	Walker B	Arg finger	N loop
cytoplasmic dynein 1 (AAA3)	**G**pp**G**sg**K**tm	vLFcdE**INLP**	**AL**fnr**C**vLn	pdvV**V**ptl**D**
cytoplasmic dynein 2 (AAA3)	**G**pp**G**cg**K**gm	vLYlkD**INLP**	**AL**hkk**C**qVl	tlpV**I**qtp**D**
axonemal dynein 5 (AAA3)	**G**eq**G**ta**K**tv	tVFidD**VNMP**	**AL**isg**C**tId	gsiL**V**pnv**D**

FIGURE 1.1 Dynein, a motor protein in the AAA+ superfamily. (A) Schematic of dynein heavy chain structure. ATP hydrolyzing domains are indicated with an asterisk. Grey: AAA domains. Blue: linker. Red: stalk and microtubule binding domain (MTBD). (B) Alignment nucleotide binding motifs in dynein 1 (AAA1), dynein 2 (AAA1), p97 (D2) and NSF (D1). Alignment of ATP-binding motifs for AAA1 (C) or AAA3 (D) in dynein 1, dynein 2, and axonemal dynein 5. In (B-D) Identical residues across a given comparison are shown with bold capitals, similar residues are capitals, variable residues are lowercase. Key residues defining a motif are red. Uniprot accession numbers: human cytoplasmic dynein 1 (Q14204), human cytoplasmic dynein 2 (Q8NCM8), human axonemal dynein 5 (Q8TE73), human p97 (P55072), human N-ethylmaleimide sensitive factor (P46459).

Dyneins can be divided into nine families comprised of seven axonemal dyneins and two classes of cytoplasmic dyneins(4). Axonemal dyneins are localized to axoneme-containing organelles and drive ciliary and flagellar beating. Cytoplasmic dynein 2 is restricted to cilia and flagella, including the primary cilium, a signaling organelle required for Hedgehog pathway activity, but this dynein isoform does not participate in ciliary beating. Rather it drives motion of cargos along the axoneme toward the base of the cilium, a process termed retrograde intraflagellar transport. By contrast, cytoplasmic dynein 1 is located in the cytoplasm and participates in transport of many types of cargo. In this chapter 'dynein' refers to cytoplasmic dynein, unless indicated otherwise.

The ATP-hydrolyzing heavy chains of dynein belong to the of the AAA+ protein family (ATPases associated with diverse cellular activities), which is characterized by the AAA domain, a common structural motif for ATP binding(5). These proteins typically function as oligomers (often hexamers), with ATP bound at the interface of two AAA domains. AAA+ enzymes couple nucleotide hydrolysis with conformational changes that lead to substrate remodeling or motion. In the case of dynein, all six AAA domains are in one single large polypeptide and ATP hydrolysis leads to successive steps of the motor protein along microtubule tracks.

The heavy chain of cytoplasmic dynein is a 500 kDa polypeptide that in cells functions as a homodimer bound to multiple accessory proteins. In order to move processively, the dynein complex (mass ~1.5 MDa) must bind dynactin, another megadalton-size multiprotein complex(6, 7). At the N-terminus of the dynein heavy chain is a ~50-60 nm long 'tail' that mediates dimerization and interacts with adaptors necessary for cargo binding(8). The C-terminus features the six AAA domains and the microtubule

binding domain (MTBD), which caps a ~15 nm coiled-coil stalk that extends from AAA4. A coiled-coil "buttress" emerging from AAA5 supports the stalk. In the dynein complex, ATP hydrolysis occurs mainly at two sites, AAA1 and AAA3, although AAA3 is active only in a subset of cytoplasmic dyneins(8) (ATP-binding sites are numbered such that AAA1 refers to the site between AAA+ domains 1 and 2). Of these sites, AAA1 is the major ATPase, whose activity is controlled by other AAA sites and accessory proteins(8).

In this chapter, we review the recent advances in developing chemical inhibitors to probe dynein function. We highlight the ciliobrevins, the first selective cell-permeable small molecule inhibitors of dynein. We discuss the discovery of these compounds, their use and how these chemical probes may be improved. We also discuss other strategies that have been developed to probe dynein function with fast temporal control.

1.2 General approach to inhibiting dynein

One simple approach to inhibiting dynein is to block its enzymatic activity using inhibitors that target its ATP-binding sites. The challenge of inhibiting the ATP-binding site is one of *selectivity*—how can a small molecule bind this site in dynein but not inhibit other nucleotide-binding enzymes? The structures of several AAA+ proteins have been solved and it is clear that their ATP binding sites are remarkably similar. Root mean squared deviations between Cα atoms are in the range of 1.5 to 2.5 Å for residues that constitute the nucleotide-binding core(5). ATP binds in a pocket containing a series of loops emanating from the top of several parallel β-sheets(5). Polar residues such as the Walker A lysine coordinate negatively charged phosphate groups. The Walker B glutamate and aspartate orient the hydrolytic water molecule, while the "arginine finger",

which extends from the adjacent AAA domain, stabilizes the terminal phosphate for nucleophilic attack by water. The adenine base forms hydrogen bonds with the peptide backbone of the "N-loop", and hydrophobic side chains of this motif contribute to the binding of adenine(9).

Although this general mode of interaction with ATP is conserved across AAA+ proteins, at the level of primary sequence these proteins have diverged to a greater degree. Variability in residue composition is tolerated adjacent to invariant residues, such as the Walker A lysine, the Walker B aspartate/glutamate, and the arginine finger (see Figure 1.1). Comparison of the ATP binding pockets between dynein and other AAA+ enzymes or among human dynein isoforms (Figure 1.1B, 1.1C-D) shows a high degree of similarity among residues that contact phosphate groups in ATP. By contrast, the residues positioned near the two hydrogen bonds that anchor the adenine base to the peptide backbone are more variable (N loop, Figure 1.1B-D). These comparisons suggest that it may be possible to identify small molecules that selectively target the ATP-binding site of one dynein isoform. In principle, inhibitor's potency can be established via contacts with conserved residues and specificity can be achieved through interactions with non-conserved residues in dynein's ATP-binding pocket.

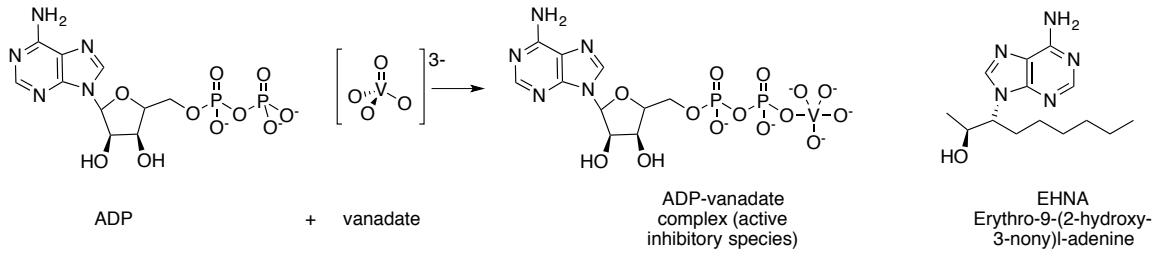

FIGURE 1.2 Nucleotide mimetic inhibitors of dynein. (A) Structure of the vanadate ion and its reaction with ADP to form the inhibitory species ADP-vanadate. (B) Structure of EHNA.

1.3 Nucleotide-mimetic inhibitors of dynein

Compounds that mimic ATP and the other nucleic acids are well-established enzyme inhibitors(10). In the case of nucleotide ATPase mimetics, these compounds bind to enzymes in a manner similar to the endogenous nucleotide substrate but either lack a hydrolyzable phosphate moiety or have a slowly-hydrolyzable phosphate-like group.

Vanadate

Less than a decade after the discovery of dynein, researchers identified a "trace nucleotide contaminant" present in some batches of commercial ATP as an inhibitor of purified dynein(11, 12). Careful analysis of the batch composition of ATP led to the identification of this inhibitory contaminant as vanadate, an inorganic anion sometimes present in the animal muscle from which ATP was purified(13).

In general, vanadate exists as a tetra-coordinate $(VO_4)^{3-}$ anion but can also form a pentacoordinate complex. The relevant species for its inhibitory activity is ADP-vanadate, in which a terminal oxygen atom of ADP is bound to vanadium. This molecule has a trigonal-bipyramidal geometry at vanadium, which mimics the transition state formed during nucleophilic attack by water on the gamma phosphate of ATP(14). The stable substrate-vanadate complex is bound more tightly than the substrate or product, leading to potent inhibition of enzymatic activity by vanadate(15). Because this transition state is common to many enzymatic phosphate hydrolysis reactions, ADP-vanadate binds many ATP-binding enzymes and is generally accepted as a promiscuous antagonist of enzymatic phosphate-ester hydrolysis (including ATP) and phosphate transfer reactions(16).

The principles of inhibition by vanadate hold true in the case of dynein: the ion-ADP adduct potently (IC_{50}s usually 1-10μM) inhibits many isoforms of dynein from different species in a nucleotide-dependent fashion. X-ray crystallography confirmed that dynein binds ADP-vanadate using the same Walker-A and B residues that ordinarily interact with the gamma phosphate of ATP(17).

Interestingly, although dynein has multiple sites capable of binding ATP, the ADP-vanadate complex is bound only in AAA1 in a crystal structure(17). This may reflect a selective binding of ADP-vanadate to AAA1 or simply the fact that ATP turnover—and thus ADP-vanadate binding—occurs most rapidly at site 1. Though it stands to reason that vanadate could inhibit any enzyme that hydrolyzes ATP, it does not bind to *all* nucleotide hydrolyzing proteins. Indeed, vanadate exhibits selective inhibition of dynein relative to other cytoskeletal motors such as myosin and kinesin, a property that made it a useful early probe for dynein(11, 18). A serendipitous discovery that irradiation of dynein-ADP-vanadate complexes with UV light leads to specific photocleavage in one site within the enzyme enabled annotation of dynein's structure and the commonalities between different dynein isoforms before this could be done by other approaches now commonly used(19). The fact that dynein is cleaved at only one site, later identified as AAA1, helped establish this site as the primary site of ATP hydrolysis in this large and complex enzyme(20). Vanadate's hydrophilicity restricts its membrane permeability, which has limited its use in cellular settings.

Erythro-9-[3-(2-hydroxynonyl)]Adenine (EHNA)

EHNA was identified as a dynein inhibitor by researchers studying sperm motility(21). It had previously been shown to inhibit protein carboxymethlyase activity under certain conditions, which was thought to account for the observation that EHNA blocks sperm motility. However, even under conditions where carboxymethylase activity was only minimally inhibited, EHNA rapidly inhibited sperm motility. Further, it blocked motion of demembranated spermatozoa, and this inhibition could be reversed by addition of excess ATP, suggesting a direct effect on axonemal dynein, the ATPase that generated flagellar beating. Experiments on purified axonemal dynein confirmed direct inhibition of its ATPase activity(21).

EHNA is composed of an adenine base linked via N-9 (the site of linkage to ribose in adenosine/ATP) to an aliphatic alcohol. This compound is more hydrophobic than other nucleotide mimetics and is likely cell permeable, as it inhibits the motility of intact sperm.

The IC_{50} for EHNA inhibition of dynein varies from ~200μM for dynein from sea urchin sperm to ~1mM for dynein from rat sperm(21). EHNA was shown to be a mixed-type inhibitor of dynein as it raises dynein's K_m and simultaneously lowers its V_{max}(22). These data raise the possibility that EHNA may bind a site on dynein other than its ATP-binding pocket. However, additional biochemical or structural studies are needed to support this hypothesis. Based on its chemical structure and crystal structures of it bound to adenosine deaminase, we posit that EHNA interacts with the ATP-binding pocket but

can make additional contacts with proximal residues to achieve this complex mode of inhibition(23).

In vitro, EHNA inhibits dynein selectively in comparison to a number of motor proteins and other ATPases(22). As a result, EHNA has seen use as an *in vitro* probe for dynein function. For example, inhibition of MAP1C-driven microtubule gliding by EHNA contributed to the assignment of this minus-end directed motor as a cytoplasmic isoform of dynein(24).

As many cellular proteins bind adenosine-containing compounds, nucleotide analogs such as EHNA are unselective in cells. Indeed, this compound potently inhibits adenosine deaminase (IC_{50} ~20nM), and cyclic-GMP-stimulated phosphodiesterase II (PDE2, IC_{50} ~800nM)(23, 25, 26). As a result, the utility of this compound to probe dynein function in cells is quite limited.

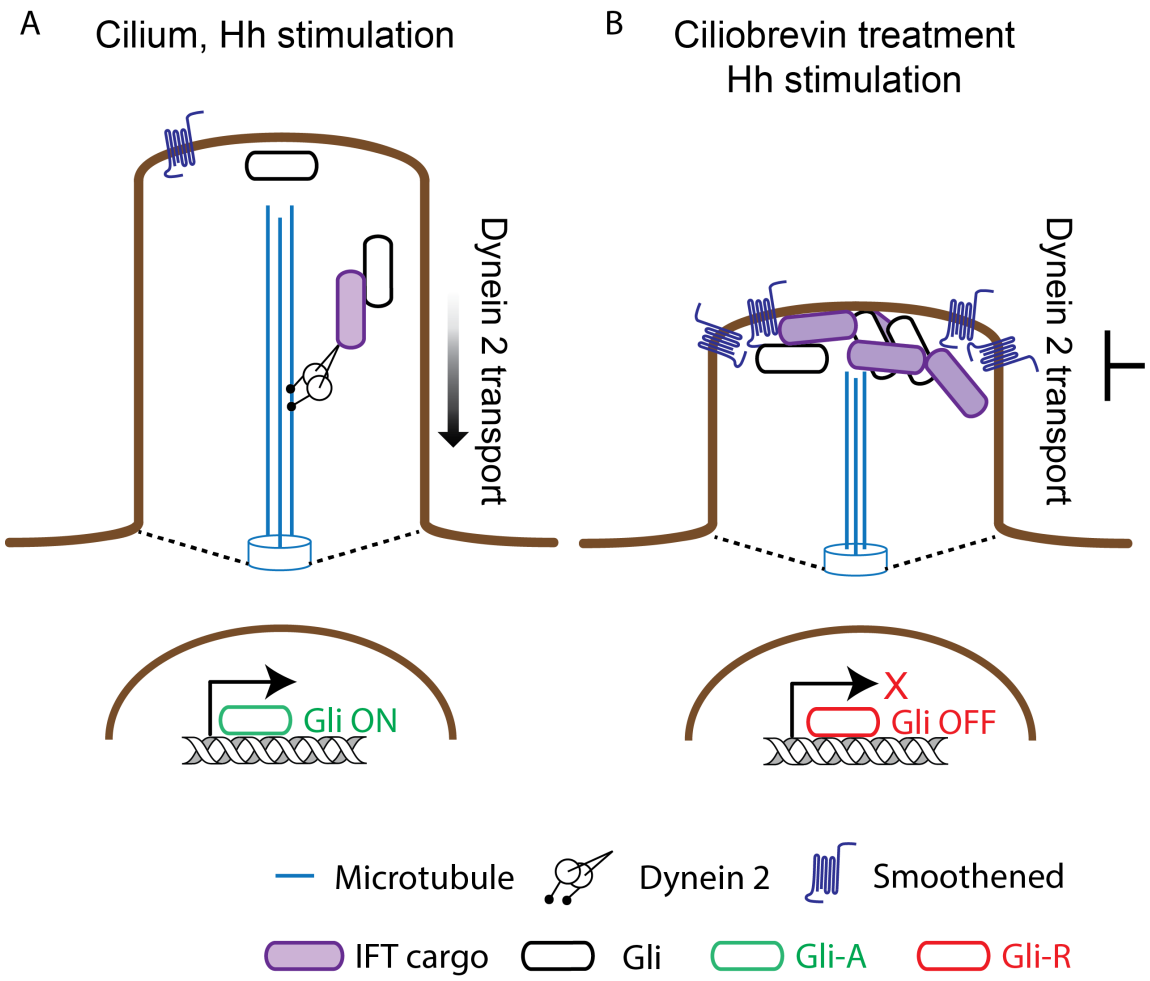

Figure 1.3 Effect of ciliobrevin on the primary cilium and the Hedgehog pathway. (A) Transport of intraflagellar transport cargos (purple) along the cilium is required for proper localization and activation of the Gli transcription factors. (B) Inhibition of dynein leads to shorter cilia, accumulation of IFT cargo and Gli proteins at the ciliary tip, and inhibition of the Hh pathway.

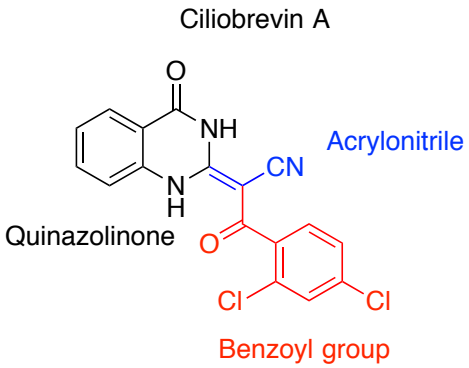

Figure 1.4. Chemical structure of ciliobrevin A, highlighting the components of its scaffold. Quinazolinone-black; acrylonitrile-blue; benzoyl group-red

1.4 The ciliobrevins: cell permeable small-molecule dynein inhibitors

The first dynein inhibitors not based on nucleotides or adenine were discovered in a cell-based screen for Hedgehog (Hh) pathway inhibitors. This screening approach is referred to as 'chemical genetics' as small molecule inhibitors, rather than genetic mutations, are identified that disrupt a cellular process of interest(27). Hh signaling controls development in multicellular organisms and was initially discovered as a regulator of polarity and segmentation in drosophila(28, 29). A vast body of research has led to advanced models for this signaling pathway. Briefly, the binding of a soluble Hedgehog ligand to its receptor Patched leads to the relief of inhibition of the seven-transmembrane protein Smoothened (Smo). Smoothened activity leads to the accumulation of activated Gli transcription factors by altering the balance of proteolytic Gli degradation. Gli then enters the nucleus and activates Hh responsive genes(30). It has been established that Hh activity in vertebrates is dependent on the primary cilium(30, 31).

The primary cilium is an antenna-shaped organelle that protrudes from the cell membrane of vertebrate cells(32). Transport of cargos along its axoneme, termed intraflagellar transport, is required for building and maintaining the cilium, and carries Hh signaling-related cargos. Accumulation of Hh pathway components including Smo, Suppressor of Fused [Su(Fu)], and Gli within the cilium is required for the transcription of Hh responsive genes(33). Dynein 2 is required for assembly of functional cilia and active transport within them(34). In line with these roles, mutations in dynein 2 lead to both Hh pathway disruption and ciliary defects, such as ciliary shortening and accumulation the intraflagellar transport component IFT88(35, 36).

Improper Hh pathway activation can cause cancer in humans. In particular, basal cell carcinoma, one of the most common human cancers, has been shown to be driven by activating mutations in the Hh pathway(37, 38), and considerable effort has focused on discovering chemical inhibitors that block this pathway. With few exceptions, the compounds developed to disrupt the Hh pathway are inhibitors of Smo, and many bind to a common site on this G-protein coupled receptor-like protein(39). These efforts have recently led to approved therapeutics(40). One limitation of these clinical agents is the acquisition of resistance via mutations in Smo itself(41-43). Furthermore, cancer-causing mutations can arise in other Hh pathway proteins, including Patched, Smo, Su(Fu) and Gli. As some of these proteins function downstream of Smo in the signaling cascade these cancers are unlikely to be responsive to drugs that inhibit Smo.

The chemical genetic screen in which ciliobrevin A was discovered was designed to uncover Hh inhibitors that act downstream of Smo(44). For this screen, the Hh pathway was activated using the Smo agonist SAG, a small molecule that competes with other known Smo antagonists at a common binding site(45). This innovation in the screen reduced the likelihood of discovering compounds that directly bind Smo. Of the ~1.2×10^5 compounds screened in this manner, four blocked Hh activity with IC_{50} values < 10 μM.

Ciliobrevin A (or HPI-4, Hedgehog pathway inhibitor-4) was one of these four compounds. The chemical structure of this compound did not imply a mechanism of action, as its core structure, a benzoylacrylonitrile-substituted quinazolinone, differs from those usually observed among common inhibitor classes (e.g. kinase inhibitors). Extensive follow-up work was required to identify dynein as a target of this compound. This work began with validation that ciliobrevin A inhibited a protein in the Hh pathway

that was downstream of Smo. Analyses of reporter cell lines in which Hh signaling was constitutively active, including one expressing inhibitor-resistant allele of Smo, showed that the compound's action is epistatic to, and therefore "downstream" of, Smo.

A clue to the target of this compound came from analysis of its effect on the primary cilium. Extended treatment with HPI-4 resulted in ciliary defects including cells with shortened or no primary cilia. This observation led to HPI-4 being named ciliobrevin(46). Upon closer investigation, it was noted that ciliobrevin A treatment led to Gli2 accumulation at the distal tip of the cilium even in the absence of Hh pathway activation, and caused similar accumulation of IFT88, consistent with inhibition of retrograde intraflagellar transport(46). Together, these data are consistent with ciliobrevin A acting on cytoplasmic dynein 2.

Confirmation that the ciliobrevins were dynein inhibitors came from biochemical experiments showing inhibition of microtubule gliding driven by dynein 1 purified from bovine brain and of the ATPase activity of the recombinant rat dynein 1 motor domain(46). The half-maximal inhibitory concentration (IC_{50}) for dynein in vitro was ~30μM. At the time this research was conducted, dynein 2 was not well characterized biochemically and could not be obtained in quantities sufficient for biochemical assays, but ciliobrevin A has since been shown to block ATP hydrolysis by dynein 2 at low ATP concentrations(47). The ciliobrevins were the first small molecules that gave cellular phenotypes consistent with dynein inhibition and blocked dynein in vitro. As such they were the first selective cell-permeable small molecule probes of dynein function.

Two lines of evidence indicate that the ciliobrevins act at dynein's major ATPase site, AAA1(46). Ciliobrevin D, a close chemical derivative of ciliobrevin A, inhibited dynein in an ATP-competitive manner. Ciliobrevin A blocked vanadate-mediated photocleavage of recombinant dynein, which is consistent with direct displacement by ciliobrevin of ADP-vanadate at AAA1. We note, however, that direct competition cannot readily be distinguished from the effect of slow ADP-vanadate accumulation due to reduced ATPase activity. Furthermore, interpreting ATP-competition experiments is challenging for enzymes with multiple active sites. Additional work is needed to confirm the site(s) of ciliobrevin binding in dynein.

The utility of the ciliobrevins as probes for dynein depends in part on how confidently their cellular effects can be assigned to dynein inhibition. Analysis of other pathways known to interact with the Hh pathway demonstrated that ciliobrevin A does not inhibit signaling associated with protein kinase A, phosphatidylinositol 3-kinase (PI3K)/Akt, mitogen activated protein kinase (MAPK), or the WNT pathway(44). *In vitro*, Ciliobrevin treatment at concentrations that fully inhibited dynein-driven microtubule gliding did not inhibit another microtubule-based motor protein (kinesin) or two other AAA+ proteins (p97, MCM2-7), indicating selective dynein inhibition. Additional studies will be required to determine the full selectivity profile of these first-generation ciliobrevins.

Other dynein inhibitors

In addition to the ciliobrevins, two compounds have been identified as modulators of dynein function. Both compounds described below have seen little use as probes for dynein.

Nordihydroguaiaretic acid (NDGA): This compound, a component of herbal medicines, exhibits pleiotropic activities in cells, which can be ascribed to its anti-oxidant properties or to its inhibition of lipoxygenase(48). Some of the cellular effects of NDGA were noted to be independent of these properties, notably golgi complex disassembly and accumulation of ZW10 and EB1 at the centrosome(49). These effects have been related to potentiation of interactions between dynactin and some dynein-dynactin cargos(50). The mechanistic details of how NDGA alters dynein-dynactin cargo interactions are poorly understood and it is unclear if this effect is direct. Further biochemical characterization of the effect of NGDA is needed before it can be used as a probe of dynein function.

Purealin: This natural product was isolated from a species of sea sponge and shown to inhibit the beating of isolated flagella(51). It was later shown to modestly (up to 50% at the highest concentration tested, 50μM) inhibit the microtubule-stimulated ATPase activity of cytoplasmic dynein *in vitro*. This activity was shown to be ATP-uncompetitive(52).

Use of the ciliobrevins

We highlight a few examples of the use of ciliobrevins as probes of dynein biology. Other studies using ciliobrevins have been recently reviewed elsewhere(53).

Dynein 2 is required to build a primary cilium, and persistent inhibition of its function results in short or ‘stubby’ cilia(30). Acute blockade of dynein 2 can help dissect the role of dynein-driven retrograde intraflagellar transport in signaling dynamics in the intact cilium. In a cell-based assay where intraflagellar transport in a primary cilium could be directly observed using fluorescent tagging of IFT-88, treatment with ciliobrevin A or D blocked retrograde movement within cilia within 3 minutes(47, 54). The ability to rapidly inhibit dynein 2 allowed the uncoupling of intraflagellar transport from maintenance of ciliary architecture, which is largely unperturbed in the short-term inhibitor treatments. The somatostatin receptor (SSTR3), a cilium-based transmembrane protein, continued to move diffusively following acute arrest of intraflagellar transport using ciliobrevin D, indicating that motion of some ciliary signaling proteins is primarily diffusive. This finding was corroborated for both SSTR3 and Smo by rapid depletion of cellular ATP(54) and was later supported by ultra-high resolution tracking of Smo movement(55).

The "immunological synapse" forms between antigen-presenting cells and T lymphocytes following recognition of a stimulatory antigen by the T cell receptor. In order for the T cell to mount a proper response at the immunological synapse, which includes the directed release of cytokines and cytotoxic substances toward the antigen presenting cell, T cells must rapidly rearrange and "polarize" components of their cytoplasm toward the synapse. Two studies elegantly used ciliobrevin D to examine the role of dynein in this dynamic process. In one study, treatment with ciliobrevin D, but not a related inactive control, reduced the polarization induced by T-cell-APC interactions. Addition of an inhibitor of non-muscle myosin further reduced polarization, indicating a

contribution from both dynein and myosin to this process(56). In the other study, ciliobrevin D treatment slowed the velocity at which centrosomes translocated in the cytosol toward the newly formed immunological synapse, and caused centrosomes to pause farther away (~1.5μm) from the synapse compared to treatments with a chemically-related inactive control compound (57). This study showed that dynein has a role in both rapid centrosome movement across the cytoplasm and in positioning the centrosome proximal to the immunological synapse. In both studies, the effect of ciliobrevin D on dynein was shown to be similar to the effect of other dynein disruptions.

Ciliobrevins have also been used to study mechanisms of cell division. Longstanding models indicate that segregation of chromosomes during mitosis depends on microtubules connecting kinetochores to spindle poles. Two studies now show that this may not be absolutely required(58, 59). Using correlative light microscopy and electron microscopy, it was recently shown that, in the course of normal cell division, some chromosomes connected to the mitotic spindle by a microtubule bundle (K-fiber) that did not extend from chromosome to spindle pole(59). Instead these K-fibers ended distal to the pole at an intersection with another microtubule fiber. Such chromosomes continue moving toward the appropriate spindle pole. Though this distal K-fiber attachment occurs in normal cells, it is difficult to detect. Chromosomes attached to the spindle in this manner can be generated by laser microsurgical ablation of a normal K-fiber, after which the free K-fiber stub rapidly (~ 30 s) connects with other microtubule fibers. Inhibition of dynein with a high dose of ciliobrevin (50μM) disrupts spindle pole formation. However, an intermediate ciliobrevin dose in which spindles can form (10μM), delays the resumption of chromosome movement after K-fiber severing(59). Another

study confirmed this finding by overexpressing a dynactin subunit to block dynein-cargo interaction(58). Together, these findings show that dynein is required for the retention and movement of K-fibers that do not extend to the spindle pole and their associated chromosomes.

Finally, ciliobrevins are active in tissue preparations (from mice and chickens, for example)(60, 61). In particular, ciliobrevin was shown to block intra-axonal movement within neurons from chicken egg ganglia and to impair nerve growth factor (NGF) mediated regulation their structure(61).

1.5 Other approaches that allow fast temporal control over dynein function

Recently, two new approaches have been designed to probe dynein function in cells. The first method utilizes chemically induced dimerization to rapidly recruit dynein complexes to a selected cargo(62, 63). Chemical inducers of dimerization (CIDs) were first developed by Schreiber and colleagues based on studies of natural products rapamycin and FK506(64, 65). In particular, addition of rapamycin to cells can induce the dimerization of two proteins, FKBP and FRB (a domain of the mTOR kinase), within seconds(66). This approach, which has been used in a wide-range of cellular contexts, has been adapted to control dynein function(66). Specifically, a dynein cargo adaptor, BicD2, was fused to a FRB and a dynein cargo with known localization (eg. Pex3 for peroxisomal recruitment) was fused to FKBP12. Using this CID-based approach, researchers have studied the effect of rapid recruitment of dynein complexes to membrane-bound organelles such as mitochondria, peroxisomes, and endosomes or to the cell membrane (62, 63, 67, 68). The rapid onset of recruitment and the ability to localize

dynein to a specific cellular compartment allows careful analyses of the contribution of dynein to a given process. In one elegant example, rapamycin derivative-driven localization of dynein to the plasma membrane was used to show that cortical dynein controls the polarity of microtubules in developing axons(67).

The second method combines induced dimerization with optogenetics to enable reversible recruitment of dynein to a defined cargo(68). In this system, illumination with blue light uncages a helix of a Light-Oxygen-Voltage domain (LovPEP), freeing it to bind an engineered PDZ domain (ePDZ)(69). These small (< 20 kDa) protein modules can be fused to proteins of interest and used to rapidly stimulate association upon exposure to the appropriate wavelength of light. In the case of the LovPEP-ePDZ system, association can be reversed (with rapid dissociation kinetics) upon turning off the excitation light. Further, use of precisely focused illumination makes it possible to recruit dynein complexes to a defined subcellular region, enabling spatial and temporal resolution of dynein's activity upon recruitment(68).

These approaches are exciting new developments in the field. However, one limitation of these methods is that the function of engineered protein constructs must be examined, rather than directly probing the activity of the endogenous motor protein, as can be possible with cell-permeable chemical inhibitors.

1.6 Outlook

Ciliobrevins provide a useful starting point to develop new chemical inhibitors with improved properties. Currently, there are two main limitations of ciliobrevins. First, is their micromolar potency. This low potency makes it difficult to achieve target

specificity in cellular contexts, as doses that fully suppress dynein activity may approach ~100 μM, a concentration at which the compound may interact with other proteins and suppress their activities. The second limitation of ciliobrevins is their low aqueous solubility (computed logarithm of the octanol:water partition coefficient [ClogP] ~4-5). This parameter is associated with decreased effective concentrations in cellular contexts and may account for the suppression of ciliobrevin activity by high-serum concentrations, such as those typically used for cell culture (70).

As a first step toward discovering improved dynein inhibitors, we and our collaborators, generated and tested ~50 chemical derivatives of ciliobrevins(47). These compounds were screened for inhibition of purified full-length human cytoplasmic dyneins 1 and 2 with an eye toward the development of selective dynein 2 antagonists. Dynein-2 selective inhibitors could block the Hedgehog signaling pathway without inhibiting the many different cellular processes that depend on dynein 1 function. Most of the compounds synthesized differed from the parental compound at a single position, but left intact the cyano-acrylamide, quinazolinone, and dichlorobenzoyl groups present in ciliobrevins (47). A set of derivatives typified by compound 37 (Figure 1.5A) bearing bulky aryl ethers at the 7 position of the molecule retained activity toward dynein 2 while no longer inhibiting dynein 1, resulting in ~10 to > 20 fold isoform selectivity under the *in vitro* assay conditions, which employed low ATP concentrations (<1μM). It is noteworthy that inhibition of dynein under closer-to-physiologic ATP concentrations was not observed. Cell-based assays using these compounds demonstrated ~1.5 to 6-fold selective inhibition of dynein 2-dependent (e.g. intraflagellar transport, ciliogenesis) relative to dynein 1-associated processes (e.g. mitotic spindle assembly). It is possible

that the diminished selectivity of these compounds in the cellular context is a result of the ATP-sensitive nature of their inhibition or may reflect reduced availability in cytosol due to the high hydrophobicity of these compounds (ClogP for compound 37: ~ 6).

Analysis of the ciliobrevin's chemical structure indicates that it can isomerize about its central double bond (Figure 1.5B). If only a fraction of the ciliobrevins adopt the geometry the inhibits dynein, the overall potency will be proportionately reduced. If chemical modifications of the ciliobrevin scaffold changes the isomer preference of the acrylonitrile double bond, this potential variability in structure can confound structure-activity-relationship analyses that would guide additional chemical modifications to improve properties. Therefore, an important next step is to restrict this potential isomerization, possibly by engineering in an additional cyclization of the core cilibiobrevin scaffold that favors the conformation that inhibits dynein.

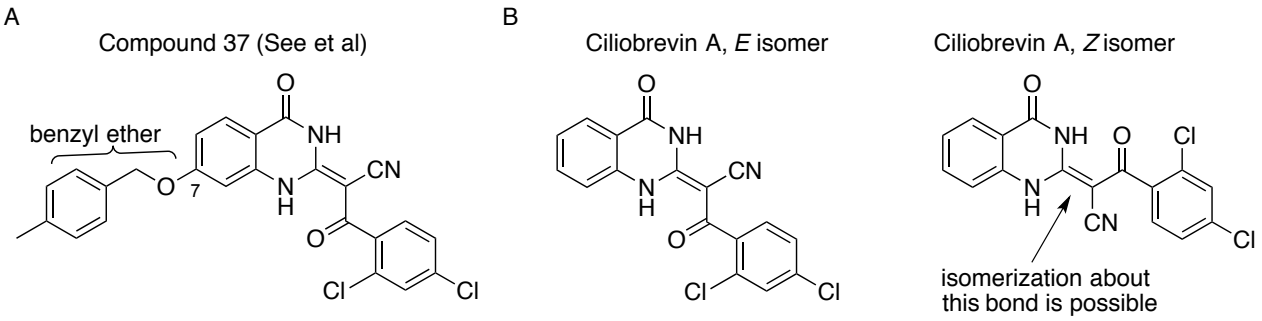

Figure 1.5 Structure of ciliobrevins. (A) Compound 37, a ciliobrevin derivative that selectively inhibits dynein 2. (B) The ciliobrevin scaffold may exist in two isomers about the indicated double bond.

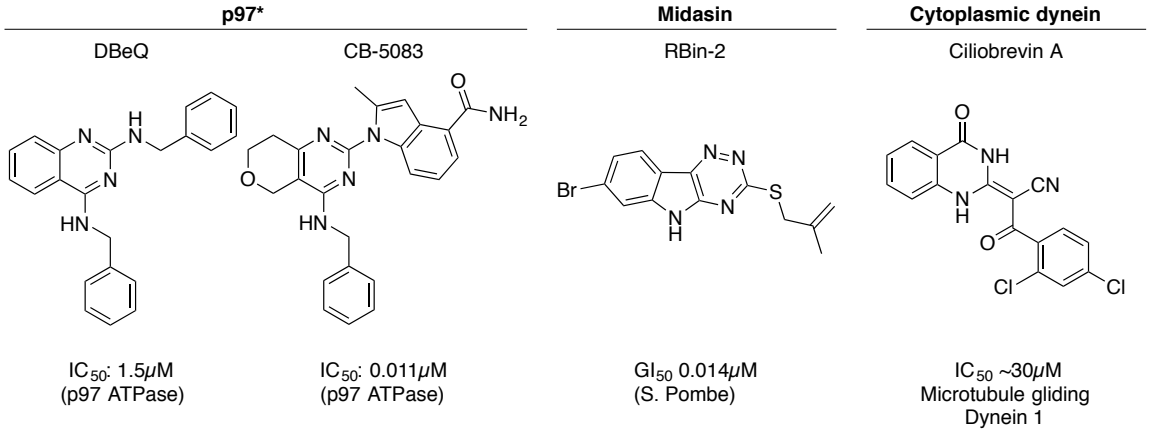

Figure 1.6 Inhibitors of AAA+ proteins. Shown are the structures and inhibitory activities of: the first inhibitor of p97, DBeQ and its derivative CB-5083, the midasin inhibitor RBin-2 and the dynein inhibitor ciliobrevin D. *at least three other classes of compounds that inhibit p97 have been described.

Selectively inhibiting a conserved site: lessons from the development of AAA+ inhibitors

The likelihood that potent and selective probes for dynein can be developed is indicated by the recent discoveries of chemical inhibitors for two other AAA+ proteins, VCP/p97 and midasin.

CB-5083 has been developed as a potent (IC_{50}: 0.01μM) and selective inhibitor of p97 and is the first AAA+ inhibitor to reach clinical trials for treatment of a human disease(71)(72). This compound was developed by iterative modification(73) and testing(74) of hundreds of derivatives of DBeQ (dibenzyl quinazoline-2,4-diamine), a chemical inhibitor of VCP/p97 and was identified via *in vitro* high throughput screening(75, 76). In contrast to dynein, VCP/p97 can be generated in quantities sufficient for a large-scale initial screen and extensive biochemical follow-up work that helped in developing improved inhibitor analogs (77, 78).

Midasin is an AAA+ enzyme required for the process of ribosome biogenesis. Like dynein, all six of its AAA+ subdomains are on a single large polypeptide of mass ~0.5MDa. RBin-1 (ribozinoindole-1), a cell permeable chemical inhibitor, was identified from a high throughput screen of ~10,000 compounds(79). The target of this compound, which is a potent inhibitor of fission yeast *saccharomyces pombe* growth (IC_{50} 0.14μM), was identified by analyses of resistance-conferring mutations. In particular, multiple different point mutations, which clustered near the likely interface of the AAA3-AAA4 domains of midasin, were sufficient to confer resistance to Rbin-1 in cells. Testing of a series of analogs against both sensitive (wild-type) and resistant (midasin mutant) cell lines enabled the discovery of more potent analogs (Rbin-2, IC_{50}: 0.014μM). RBin-2

inhibited the ATPase activity of purified full-length recombinant midasin. Importantly, a mutation in midasin that conferred resistance to Rbins in cells, was sufficient to suppress inhibition of ATPase activity, providing 'gold standard' proof that midasin is RBin's direct physiological target.

In summary, chemical inhibitors of dynein are likely to be powerful tools for dissecting this motor protein's functions across different cell-types and organisms. The work described here suggests that an initial foundation is in place for additional research that will lead to better chemical probes. It is also possible that these studies may lead to new therapeutics that selectively target individual isoforms of these complex cellular motor proteins.

Chapter 2:

Chemical structure-guided design of dynapyrazoles, potent cell-permeable dynein inhibitors with a unique mode of action

Note to readers: the results discussed below arose from a collaborative effort between myself and several colleagues in the Kapoor Lab, at the Tri-Institutional Therapeutics Discovery Institute (TDI), at Stanford University, Northwestern University, and the California Institute of Technology. A closely related version was published in eLife (DOI: DOI: 10.7554/eLife.25174). *With the permission of Prof. Kapoor, I have included work done by others in this thesis as it helps explain the rationale of my work and supports the conclusions I draw. In the body of the text and in the methods section, I have noted who performed each experiment. I have also noted this information in the figure legends, where appropriate. Except for experiments credited explicitly to others, I performed all experiments and analysis. Also please note that all figure supplements are now located in Appendix 2.1.*

2.1 Introduction

The AAA+ (ATPases Associated with diverse cellular Activities) superfamily is comprised of ~100 proteins in humans(5)(80). These ATPases are essential for many cellular processes, including DNA replication, proteostasis, membrane remodeling, and cytoskeletal organization(9). Extensive cell biological and biochemical studies have revealed that these enzymes couple ATP hydrolysis to substrate remodeling and directional transport, processes that can occur on the timescale of seconds or minutes(81). Thus, small molecule inhibitors that can modulate AAA+ activity on similarly fast timescales are likely to be valuable tools to probe their cellular functions(82). Valosin-containing protein(83) and dynein(46) are the only two human enzymes in this large superfamily for which well-characterized small molecule antagonists have been reported.

Dyneins are microtubule-based motor proteins in the AAA+ family that have been divided into two classes, axonemal and cytoplasmic. Axonemal dyneins are required for the beating of flagella. Cytoplasmic dyneins, of which there are two isoforms (hereafter, dynein 1 and 2), are present in metazoan cells and are required for a wide range of

cellular processes(1, 2, 84). Transport of cargo along microtubules requires a balance of forces directed toward either end of the filament. While multiple motor proteins in the kinesin family provide the plus-end directed force to drive this motion, their activity in many contexts is opposed by only two cytoplasmic dyneins, the primary motor proteins transporting cargos towards the minus-end of microtubules(1). Dynein 1 has many functions in the cytoplasm, where it moves diverse cargoes ranging from mRNA molecules to whole organelles. In contrast, dynein 2's functions are restricted to cilia and flagella. The primary cilium is an antenna-like organelle that protrudes from the cell surface, in which dynein 2 drives transport toward the base(34, 85). This process, known as intraflagellar transport, is required for Hedgehog signaling, a developmental signaling pathway(32, 34, 85). Cargos of both dynein isoforms can move at rates of >1 μm/s in cells(2) and therefore, fast-acting, reversible chemical inhibitors are likely to be useful probes for dynamic dynein-dependent cellular processes.

Ciliobrevins were recently reported as the first selective, cell-permeable probes of dynein(46). Although other chemical antagonists of dynein have contributed to understanding the biochemistry of dynein, their use in cell biology has been limited because they are either not cell-permeable (e.g. vanadate) or non-selective in cells (e.g. EHNA)(11, 12, 21). Ciliobrevins were discovered as inhibitors of Hedgehog signaling and shown to block cytoplasmic dynein 1- and 2-dependent transport in cells(44). Ciliobrevins have been used as tools to examine the role of dynein in a number of processes, including formation of the immunological synapse, transport of signaling proteins in the primary cilium, axonal transport of transcription factors, and axon extension and branching in cultured neurons(54, 56, 57, 61). However, the use of

ciliobrevins has been limited by their low potency and suboptimal chemical properties, which is often noted for first-in-class compounds identified through high-throughput screening(53). Complete inhibition of dynein can require high doses (50-100μM) and selective protein target inhibition can be difficult to achieve at these high concentrations.

The ciliobrevins are based on a benzoylacrylonitrile-substituted quinazolinone scaffold (Figure 2.1A). This type of acrylonitrile has the potential to react with nucleophiles, and instability of ciliobrevins during storage has been noted(61). The benzoylacrylonitrile core is required for *in vitro* and cellular activity, but this functional group has the potential to isomerize, and the ciliobrevin scaffold may exist as either of two isomers about the benzoylacrylonitrile olefin (C2 - C9, Figure 2.1A). The preferred isomer of this compound has not been determined and chemical modification of the quinazolinone or acyl groups, even distal to the acrylonitrile functionality, has the potential to affect the geometry of the compound's core. Together, these factors have made activity-guided modifications to improve compound potency challenging. Further, up to ~100-fold differences in potency have been noted between biochemical and cell based assays (0.2 μM – 30 μM for ciliobrevin D), raising concerns about target specificity. Design and chemical synthesis of alternative scaffolds that address these limitations and retain activity against dynein are needed.

Dynein is a large, ~4600 amino acid protein that contains six unique AAA ATPase domains(86). Many AAA+ enzymes function as homohexameric arrays of identical AAA domains, and thus all six of the ATPase sites are biochemically equivalent(87). However, for dyneins, each of the six unique AAA domains resides on a single polypeptide and can have a specialized role in motor protein function(8). In the

case of dynein 1, four of the six AAA domains contain the residues necessary for nucleotide binding; of these, only AAA1 and AAA3 substantially contribute to ATP hydrolysis and have been shown to be required for microtubule motility(8). Dynein's ATPase activity is stimulated by interactions with microtubules and is thought to occur mainly at AAA1, while hydrolysis at AAA3 plays a regulatory role(88-90). Ciliobrevins have been shown to be ATP-competitive inhibitors of dynein(46), but it remains unclear which of the six AAA sites are modulated, adding to the challenges of inhibitor optimization.

Here, we characterize the conformation of ciliobrevins and design tricyclic pyrazoloquinazolinone derivatives that are more potent inhibitors of dynein. One derivative, which we name dynapyrazole-A inhibits dyneins 1 and 2 with similar potencies *in vitro* and in cellular assays. Biochemical analyses of this compound showed that while it inhibits the microtubule-stimulated ATPase activity of dynein, it does not potently block the microtubule-independent basal activity. This mode of activity is unlike that of the ciliobrevins, which inhibit both basal and microtubule-stimulated hydrolysis.

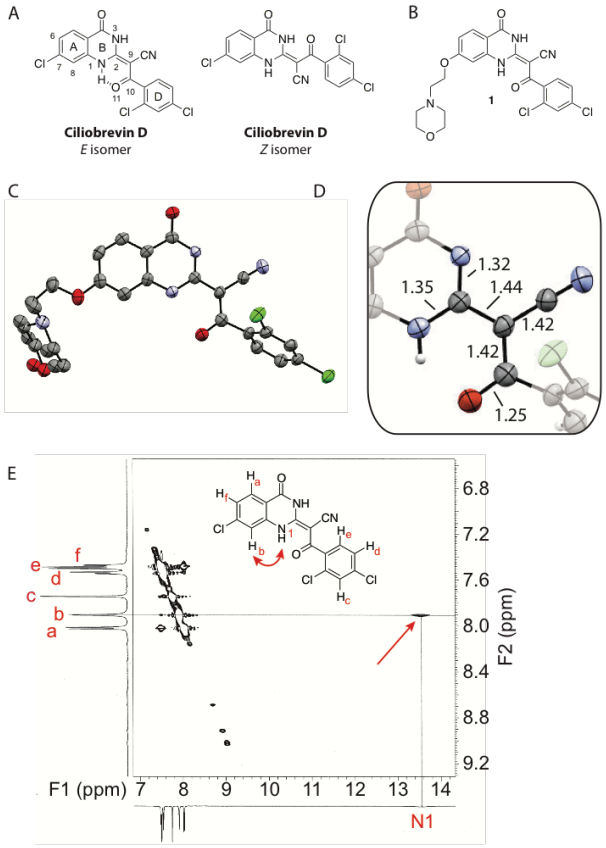

Figure 2.1 Analysis of the conformation of the ciliobrevin scaffold. *Note: this work was done by others: Structural analyses were performed by M. Nishitani (Takeda Pharmaceuticals, Japan), A. Ondrus (California Institutue of Technology), and A. Johnson (Stanford University).* (A) *E* and *Z* isomers about the C2-C9 bond of ciliobrevin D are shown. Possible hydrogen-bond in the *E* configuration is indicated (dashed line). Selected atoms are numbered for reference. (B) Compound **1** was used for x-ray crystallography. (C) X-ray structure of **1**. Displacement ellipsoids are shown at the 50% probability level. (D) Enlarged (2x) image of acrylonitrile moiety with selected bond lengths indicated (Å). Protons are shown to illustrate possible hydrogen-bonding interaction. Color legend: carbon-grey, hydrogen-white, nitrogen-blue, oxygen-red, chlorine-green. (E) Nuclear Overhauser effect spectroscopy (NOESY) spectrum for ciliobrevin D. A broad peak corresponding to interaction between H_b and the N1 proton is indicated. Protons corresponding to peaks in the spectrum of ciliobrevin D are indicated. Coupling is indicated by a double-headed arrow. A 1-dimensional proton NMR spectrum of ciliobrevin D is shown in Figure 1 Figure Supplement 1.

2.2 Results

To design new analogs with improved properties we analyzed the conformation of the ciliobrevin scaffold. For these studies we first used x-ray crystallography. Efforts to crystallize ciliobrevin D were unsuccessful; however compound **1**, a derivative with a 2-morpholinoethyl ether substitution, was synthesized using a previously described procedure and was found to readily crystallize (Figure 2.1B, C, D, crystallography was performed by M. Nishitani, Takeda Pharmaceuticals, Japan)(47). The x-ray data suggested that **1** exists as a single isomer with an *E* olefin configuration of the C2-C9 double bond. The measured bond lengths are consistent with electrons in a π-system delocalized across the benzoylacrylonitrile core (Figure 1D). The C2-C9 bond length (1.44 Å), which is longer than that of a typical olefin, indicates significant single bond character. The proximity between O11 and N1-H suggests that the ciliobrevin structure is stabilized by an intramolecular hydrogen-bond between N1 and O11 (Figure 2.1A, 1D). A closely-related acylacrylonitrile-substituted quinazolinone was found to favor an alternative conformation, corresponding to a Z-olefin at C2-C9, that was also stabilized by intramolecular hydrogen-bonding(91). Taken together, these data indicate that the isomeric preference of the pharmacophore is likely to be sensitive to distal substitutions.

As crystal packing may impact conformation, we turned to NMR spectroscopy to analyze the structure of the ciliobrevin scaffold in solution. A 1-dimensional proton NMR spectrum of ciliobrevin D showed a peak at 13.5 ppm, which could be assigned to a proton at one of the quinazolinone nitrogens(91) (Figure 2.1 Figure Supplement 1). The presence of this broad, downfield peak suggests that one exchangeable N-H proton is stabilized by a hydrogen-bonding interaction. A NOESY spectrum of ciliobrevin D

revealed all the expected resonances (Figure 1E, NOESY experiment was performed by A. Ondrus and A. Johnson, at Stanford University). In addition, we detected a coupling between the proton at 13.5 ppm and the proton at the 8-position of the quinazolinone, consistent with the proton at N1 being involved in hydrogen bonding. Together, these data suggest that ciliobrevin D has similar orientation in solution to that of **1** in the crystal, and the benzoylacrylonitile functional group favors an *E*-isomer configuration that is stabilized by hydrogen bonding (Figure 1E).

We hypothesized that replacing the benzoylacrylonitrile core with a heterocyclic scaffold that maintained the observed ciliobrevin geometry could lead to improved dynein inhibitors. We reasoned that a tricyclic scaffold could replace the non-covalent N1-H-O11 interaction and maintain the overall ciliobrevin pharmacophore. We envisioned replacing the C2-C9 olefin and C10 ketone with either a pyrrole or pyrazole ring to afford such a tricyclic heterocycle (Figure 2.2A-C, synthesis was performed by colleagues at the TDI). We adapted established procedures to synthesize **2** and **3**, which differ from known compounds only in the substitution pattern of the D ring (Figure 2.2A, 2.2B)(92, 93). We also devised a synthetic route to a series of tricyclic analogs exemplified by **4**, which relies on the condensation of a 2-fluorobenzoic acid methyl ester with a 4-cyano-aminopyrazole under basic conditions (Figure 2.2C). This strategy allowed convergent synthesis of the desired cyclized ciliobrevin analogs.

Figure 2.2 Synthesis of ciliobrevin D derivatives and analysis of their activity against dynein 2. *Note: the work shown in A-C was done by others. Synthesis was performed by colleagues at the TDI*. (A - C) Synthesis of ciliobrevin derivatives. (A) Pyrroloquinazolinone derivative. Reagents and conditions: (i) malononitrile, ammonium acetate, toluene, 100 °C, 13h, 72%; (ii) bromine, carbon tetrachloride, 70 °C, 9h, 38%; (iii) methyl anthranilate, isopropanol, 100 °C, 20h, 15%. Selected atoms are numbered for reference. (B - C) Pyrazoloquinazolinone derivatives. Reagents and conditions: (iv) acetic acid, 150 °C (microwave), 30 min, 26%. (v) malononitrile, sodium hydride, tetrahydrofuran, 0 °C, 1h, 96%; (vi) dimethyl sulfate, *N*,*N*-diisopropylethylamine, dioxane, 60 °C, 23h, 27%; (vii) hydrazine hydrate, ethanol, 80 °C, 6h, 82%; (viii) methyl 2-fluoro benzoate (or substituted derivative), potassium carbonate, dimethylformamide, 140 °C, 30 min, 11%. (D) Gel filtration trace (Superose 6) for GFP-dynein 2, with volume at elution peak indicated. V_o, void volume. (E) SDS-PAGE analysis (Coomassie blue stain) of GFP-dynein 2, ~0.5 μg protein loaded. (F) Schematic of microtubule motility assay. Anti-GFP antibody (Ab), GFP-dynein (dyn), and microtubule (MT) are indicated. (G) Time-lapse montage of fluorescent microtubules moving on GFP-dynein 2-coated glass slides in the solvent control (2% DMSO) or in the presence of ciliobrevin D (20 μM). (H) Montages of fluorescent microtubules moving on GFP-dynein 2-coated glass slides in the presence of compounds **2**-**4** (20 μM). (I) Mean velocity of dynein 2-driven microtubule gliding in the presence of control solvent (2% DMSO), ciliobrevin D, or compounds **2**-**4** (mean + S.D., n ≥ 3). Number of microtubules quantified: DMSO-327, Cil. D-85, **2**-98, **3**-90, **4**-77. All motility assays were run at 1mM MgATP, 0.05 mg/mL casein, and 2% DMSO. For all montages, the interval between successive images is 2 seconds and total time elapsed is 20s. Horizontal scale bar, 5 μm.

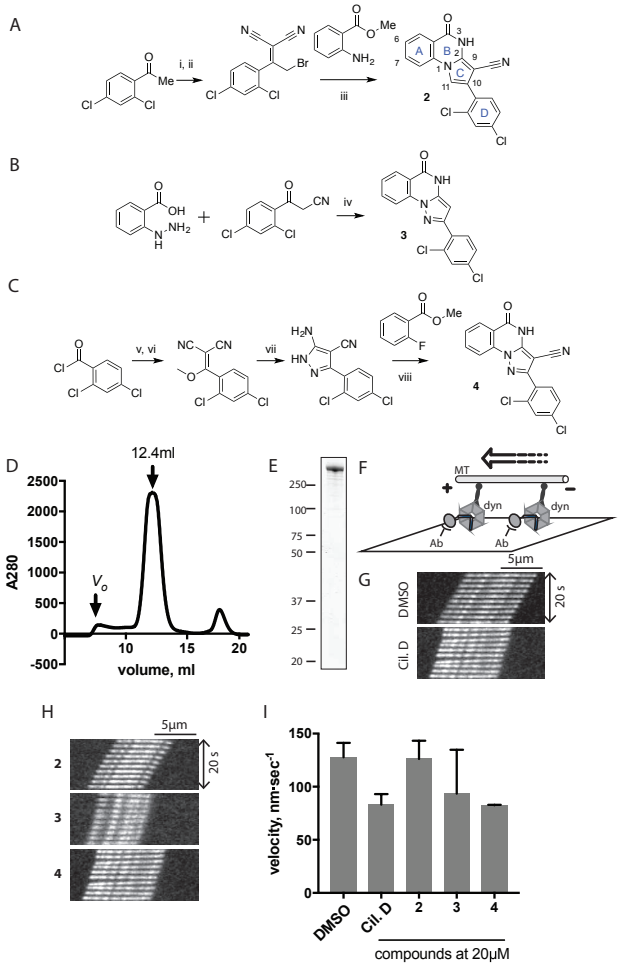
A
i, ii
iii
2
B
iv
3
C
v, vi
vii
viii
4
D
12.4ml
A280
volume, ml
E
250
100
75
50
37
25
20
F
MT
dyn
Ab
5µm
G
DMSO
Cil. D
20 s
H
2
3
4
I
velocity, nm·sec-1
DMSO
Cil. D
compounds at 20µM

To test if these compounds inhibit dynein we employed a microtubule gliding assay. We first focused on human cytoplasmic dynein 2, the isoform involved in ciliary transport and Hedgehog signaling(32), as its inhibition in this assay by ciliobrevin D has not been previously demonstrated. We purified an N-terminally GFP-tagged motor-domain construct of dynein 2 using an insect cell expression system(17). The GFP tag in this construct (GFP-dynein 2, amino acids 1091 - 4307) allowed immobilization on passivated glass coverslips used in microtubule gliding assays. This protein was obtained as a mono-disperse peak by gel filtration (Figure 2.2D, 2.2E). GFP-dynein 2, in the presence of ATP (1mM), moved microtubules with a velocity of 128 ± 14 nm/s (mean ± SD, Figure 2.2G). This activity is readily revealed by a time-series montage, which shows a fluorescently labeled microtubule being displaced ~3μm in 20 seconds (Figure 2.2G). This rate is comparable to previous analyses of this construct(17). Ciliobrevin D (20μM) reduced the microtubule gliding velocity (Figure 2.2G), consistent with its inhibition of dynein 2-dependent processes in cells(46, 54).

We next tested compounds **2** - **4** at 20 μM, a concentration at which ciliobrevin D slowed dynein 2-driven gliding to 83 ± 10 nm/s (Figure 2.2I). Compound **2** did not substantially change microtubule gliding velocity (126 ± 17 nm/s, Figure 2.2H, 2.2I). Compounds **3** and **4** inhibited dynein 2-driven gliding to a velocity comparable to that observed in the presence of ciliobrevin D at this same concentration.

Figure 2.3 Chemical structure analysis, design, and evaluation of pyrazoloquinazolinone derivatives of ciliobrevin. *Note: the work shown in C and I was performed by others. X-ray crystallography was performed by M. Nishitani, Takeda Pharmaceuticals, Japan. Hedgehog pathway analysis was performed by C. Santarossa and L. Yu (graduate student and technician in Kapoor laboratory).* (A) Superposition of the crystal structure of **1** with the computational model of **4** (green). (B) Pyrazoloquinazolinone ciliobrevin derivatives with cyclopropyl group. (C) Crystal structure of **5**. Displacement ellipsoids are shown at the 50% probability level. (D) Superposition of the crystal structure of **1** with the crystal structure of **5** (cyan). (E) Montages of fluorescent microtubules moving on GFP-dynein 2-coated glass slides in the presence of compounds **5** - **8** (20 μM). The interval between successive images is 2 seconds and total time elapsed is 20s. Horizontal scale bar, 5 μm. (F) Mean velocity of dynein 2-driven microtubule gliding in the presence of compounds **5** - **8** (mean + S.D., n ≥ 3). Number of microtubules quantified: **5**-91, **6**-63, **7**-86, **8**-56. (G) Inhibition of GFP-dynein 2-driven motility by **8** and ciliobrevin D. IC_{50} values: **8**: 2.6 ± 1.3 μM (mean ± S.D., n = 3); ciliobrevin D: 20 μM (range: 19-21 μM, n = 2). Velocity distribution histograms for inhibition of dynein-2 driven microtubule motility are presented in Figure 3 Figure Supplement 1. Number of microtubules quantified: **8**: 10μM-36, 5μM-59, 2.5μM-98, 1.3μM-112, 0.6μM-102, 0.3μM-126; Ciliobrevin D: 80μM-10, 40μM-47, 20μM-78, 10μM-85, 5μM-99, 2.5μM-66, 1.3μM-80; (H) Inhibition of GFP-dynein 2-driven motility by **6** and **9**. The chemical structure of **9** is shown. IC_{50} values: **6**: 2.9 ± 0.6 μM (mean ± S.D., n = 3). **9**: 17.7μM (range: 17.2-18.2, n = 2). Number of microtubules quantified: **6**: 20μM-38, 8μM-24, 3.2μM-48, 1.3μM-50, 0.5μM-53; **9**: 20μM-29, 8μM-54, 3.2μM-50, 1.3μM-54, 0.5μM-56. (I) Dose-dependent inhibition of luciferase reporter expression by ciliobrevin D and compound **7**. IC_{50} values (mean ± S.D.): ciliobrevin D: 15.5 ± 3 μM (n = 4); **8**: 1.9 ± 0.6 μM (n = 5). For G, H, and I, IC_{50} values reported reflect the mean (with range or S.D.) of separate IC_{50} values obtained from independent dose-response analyses. Data were fit to a sigmoidal dose-response curve and constrained such that the value at saturating compound = 0. Individual data points presented reflect mean of values determined from n ≥ 2 independent replicates ± S.D. (G, I) or ± range (H). All motility assays were performed at 1mM MgATP, 0.05mg/mL casein, and 2% DMSO.

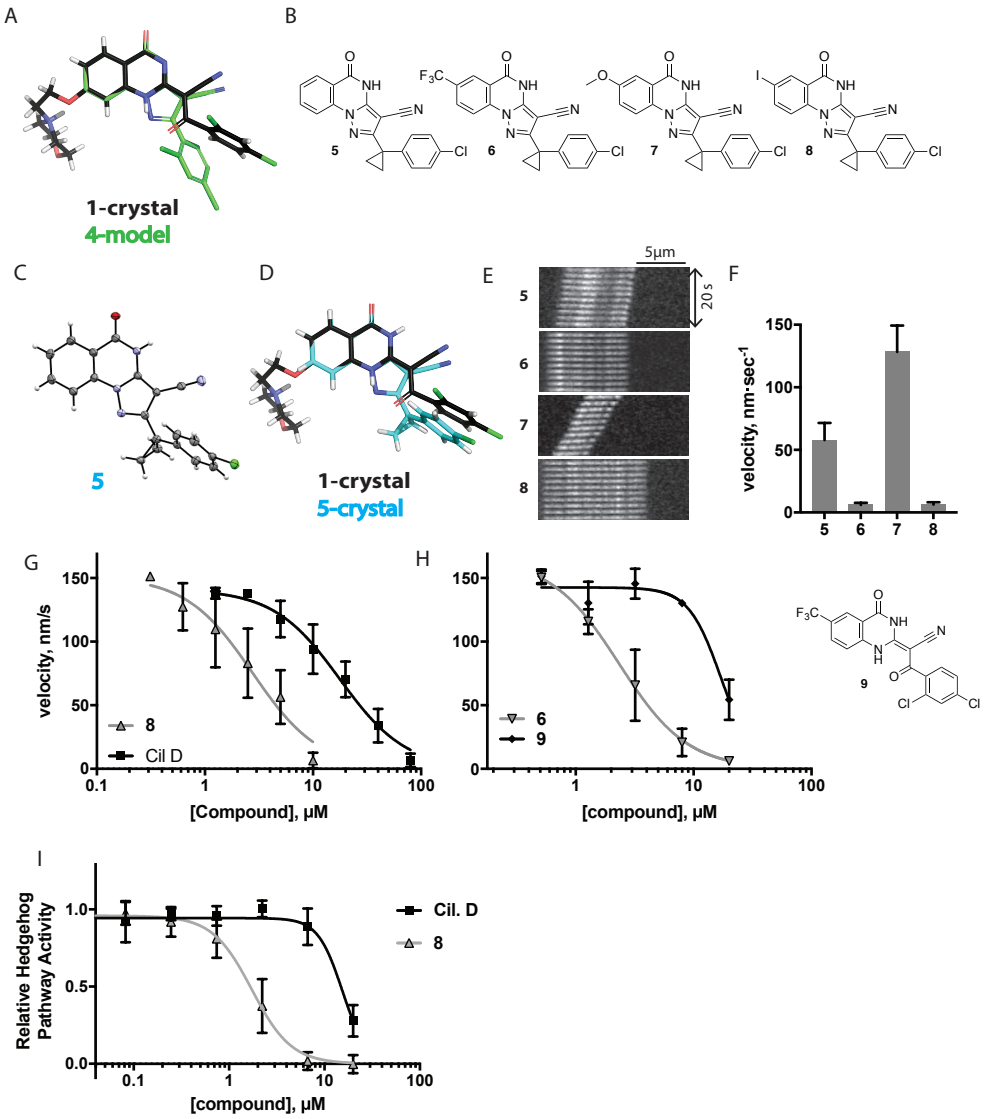
A
1-crystal
4-model
B
5
6
7
8
C
5
D
1-crystal
5-crystal
E
5µm
20 s
5
6
7
8
F
velocity, nm·sec-1
150
100
50
0
5
6
7
8
G
velocity, nm/s
150
100
50
0
8
Cil D
0.1
1
10
100
[Compound], µM
H
150
100
50
0
6
9
1
10
100
[compound], µM
9
I
Relative Hedgehog Pathway Activity
1.0
0.5
0.0
Cil. D
8
0.1
1
10
100
[compound], µM

To improve the potency of compound **4** we compared its structure with that of ciliobrevin analogs. In particular, we superimposed the crystal structure of **1** with an energy-minimized structure of **4** computationally generated using Maestro (Schrödinger). This analysis revealed that the dichlorophenyl D ring of **4** projects from the pyrazoloquinazolinone core such that it is offset from the D ring of the ciliobrevin (Figure 2.3A). We reasoned that adding a single carbon atom between the pyrazoloquinazolinone and the phenyl ring may lead to closer alignment with ciliobrevin and that using a cyclopropyl spacer would restrict rotation of the resulting scaffold. Using our modular synthesis strategy for pyrazoloquinazolinones, we generated a set of ciliobrevin derivatives with this cyclopropyl group separating the aromatic ring systems (**5** - **8**, Figure 2.3B). Three of these compounds had substitutions at the 6-position of the quinazolinone (**6**, **7**, and **8**, Figure 2.3B), a modification that we have previously reported to improve the potencies of ciliobrevins(46). The crystal structure of **5** confirms that its D ring aligns with that of compound **1** better than the chlorophenyl ring of compound **4** (Figure 2.3C, 2.3D).

We tested whether compounds **5** - **8** (20μM) inhibited dynein 2-dependent microtubule gliding (Figure 2.3E, 2.3F). Compound **5** reduced velocity to 58 ± 14 nm/s, while addition of a trifluoromethyl group at the 6 position of the "A" ring in compound **6** led to near-complete inhibition of gliding (6 ± 2 nm/s). By contrast, compound **7**, with a methoxy group at the 6-position of the A ring, did not inhibit dynein 2-driven microtubule gliding (128 ± 21 nm/s, Figure 2.3E, 2.3F). Compound **8**, with a 6-iodo substituent at the A ring, showed comparable activity to **6** (average gliding velocity: 6 ± 2

nm/s). For the two most active compounds (**6**, **8**) as well as ciliobrevin D, we performed dose-dependent analyses. We found 6- to 8-fold increases in potencies of compounds **6** (IC_{50}: 2.9 ± 0.6μM) and **8** (IC_{50}: 2.6 ± 1.3 μM) relative to ciliobrevin D (IC_{50} of 20 ± 1.0 μM) in this assay (Figure 3G, H). To our knowledge, **8** is the most potent inhibitor of dynein 2 published to date. Hereafter, we designate compound **8** as dynapyrazole-A and compound **6** as dynapyrazole-B.

In order to directly test the effect of replacing the benzoylacrylonitrile-quinazolinone system by a pyrazoloquinazolinone we also synthesized uncyclized congeners of dynapyrazoles. Due to poor solubility of a 6-iodo-substituted ciliobrevin derivative it was not possible to test its activity and compare it with that of compound **8**. Comparisons between compound dynapyrazole-B (**6**) and **9**, a 6-CF_3-substituted ciliobrevin derivative (Figure 3H), show that cyclization leads to ~6-fold improvement in the potency of dynein 2 inhibition in the microtubule gliding assay.

We next examined the inhibition of dynein 2 by dynapyrazole-A in cell-based assays. In cell culture, serum starvation results in the formation of primary cilia, which are required for Hedgehog signaling(32). Quiescent cells respond to the Hedgehog ligand or to an agonist and pathway activity can be measured using a Gli-driven luciferase reporter(45, 94). Expression of Hedgehog-driven luciferase reporter was inhibited by dynapyrazole-A (IC_{50}: 1.9 ± 0.6 μM) ~8-fold more potently than ciliobrevin D (IC_{50}: 15.5 ± 3 μM, Figure 3I). Cell death was observed at concentrations 10-fold above the IC_{50} for dynapyrazole-A (20μM) over the 28-hour time course of this experiment. In this assay we have also observed cell death at high ciliobrevin D concentrations (200μM, ~10x above its IC_{50}). To stimulate Hedgehog pathway activity we used the synthetic agonist of

smoothened (SAG)(45), which competes with many known Hedgehog pathway inhibitors for binding to Smoothened, a key protein in this signaling pathway(39). As dynapyrazole-A inhibits Hedgehog signaling at high SAG concentrations (500 nM), it is likely to act downstream of Smoothened, as was previously noted for the ciliobrevins and consistent with inhibition of dynein 2(44, 46).

The Hedgehog signaling pathway depends on dynein 2-driven retrograde intraflagellar transport in the primary cilium(95). We used time-lapse microscopy to examine the dynamics of fluorescently labeled intraflagellar transport protein-88 (mNeonGreen-IFT88, Figure 2.4A; all experimental analysis of intraflagellar transport was performed by C. Santarossa, graduate student in the Kapoor Laboratory), an approach we have previously used to study the effect of ciliobrevins and derivatives(47, 54). Time-lapse recordings of cells treated with control media revealed a steady flow of IFT88 punctae moving from cilium tip to base and vice versa, as expected. The wider end of the cilium was identified as its base, a convention suggested previously by others(96). We find that in cilia treated with dynapyrazole-A (5μM), retrograde-directed IFT88 punctae were markedly slowed. In contrast, anterograde motion did not appear to be substantially altered in the presence of dynapyrazole-A.

Figure 2.4 Analysis of the effect of dynapyrazole-A (8) on intraflagellar transport. *Note: all work in this figure was performed by C. Santarossa (graduate student in Kapoor Laboratory).* (A) Schematic of cilium showing microtubule-based axoneme (blue) and dynein (black), and an intraflagellar transport particle (purple) containing mNeonGreen-IFT88 (green). Anterograde and retrograde transport directions are indicated. (B-C) Images from time-lapse series and associated kymographs showing motion of mNeonGreen-IFT88-containing particles in primary cilia of living murine kidney cells (IMCD3). Cilium tip (red arrowhead) and base (black arrowhead) are indicated. Red (retrograde) and blue (anterograde) traces have been added to one kymograph per condition to illustrate particle tracks. Image scale bar, 3μm; Kymograph horizontal scale bar, 10 seconds; kymograph vertical scale bar, 3μm. (D-E) Velocity distribution histograms showing anterograde and retrograde velocities in the solvent control (0.3% DMSO, D) and in the presence of 5μM **8** (E) at five minutes after initiation of experiment. Analyses of cells treated with 5μM **8** for 10 minutes are shown in Figure 4 Figure Supplement 1. Analyses of cells treated with 10μM **8** are shown in Figure 4, Figure Supplement 2. (F-G). Intraflagellar transport velocities (F) and frequencies (G) after washout of dynapyrazole-A. Bars represent mean + S.D. Data analysis (V_a, anterograde velocity, nm/s; V_r, retrograde velocity, nm/s; F_a, anterograde frequency, counts/minute; F_r, retrograde frequency, counts/minute; values are mean ± S.D. N_a, number of anterograde particles analyzed; N_r, number of retrograde particles analyzed; C, number of cilia analyzed). DMSO, V_a 694 ± 117, V_r 421 ± 156, F_a, 11.3 ± 3, F_r 6.5 ± 4, N_a 429, N_r 244, C 38; 5μM **8**, V_a 566 ± 116, V_r 156 ± 107, F_a, 8.5 ± 5, F_r 4.1 ± 3, N_a 443, N_r 211, C 52; Washout, V_a 697 ± 149, V_r 467 ± 136, F_a, 14.2 ± 6, F_r 9.6 ± 7, N_a 256, N_r 173, C 18.

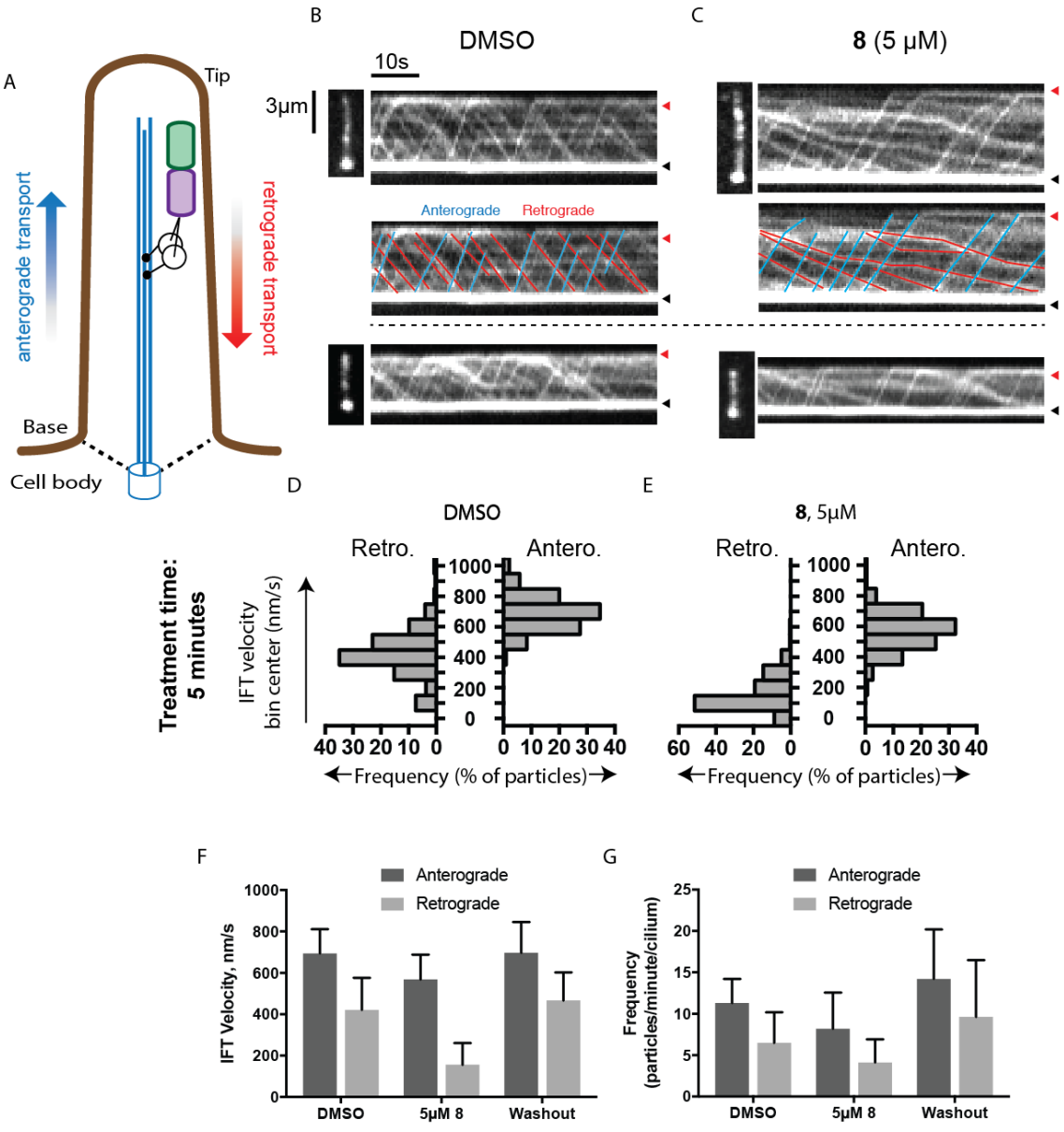
A
Tip
anterograde transport
retrograde transport
Base
Cell body
B
DMSO
10s
3µm
Anterograde
Retrograde
C
8 (5 µM)
D
DMSO
Retro.
Antero.
Treatment time:
5 minutes
IFT velocity
bin center (nm/s)
1000
800
600
400
200
0
40 30 20 10 0
0 10 20 30 40
Frequency (% of particles)
E
8, 5µM
Retro.
Antero.
1000
800
600
400
200
0
60 40 20 0
0 10 20 30 40
Frequency (% of particles)
F
Anterograde
Retrograde
IFT Velocity, nm/s
1000
800
600
400
200
0
DMSO
5µM 8
Washout
G
Anterograde
Retrograde
Frequency
(particles/minute/cilium)
25
20
15
10
5
0
DMSO
5µM 8
Washout

To quantitatively assess the effect of dynapyrazole-A treatment on intraflagellar transport, we analyzed time-lapse images of cilia using KymographDirect, an automated analysis algorithm that extracts particle velocities from kymographs(97). Previous analyses of the effect of dynein 2 inhibition using a temperature-sensitive mutant in *chlamydomonas* revealed that dynein 2 depletion causes a ~60-70% reduction in retrograde velocities and a ~20% reduction in anterograde velocities as well as 30-60% reductions in the frequency of particle transport(98). Under control conditions (0.3% DMSO, Figure 2.4B), anterograde particles moved with a speed of 694 ± 117 nm/s (Figure 2.4D, mean ± S.D., 429 particles, 38 cilia) and retrograde particles moved at 421 ± 156 nm/s (Figure 2.4D, 244 particles, 38 cilia), consistent with previous studies (54). Following addition of dynapyrazole-A to cells, the speed of retrograde particles was markedly reduced at five minutes, the fastest reliable time line for this experiment on our microscopy set-up (Figure 2.4C, 2.4E; 5μM **8**: mean velocity 156 ± 107 nm/s, 211 particles, 52 cilia). In contrast, anterograde particle velocities were only reduced by ~18% (Figure 2.4C and 2.4E, 5μM **8**: 566 ± 116 nm/s, 443 particles, 52 cilia). After 10 minutes of treatment, reductions in velocities were similar to those at the 5 minute time point (Figure 2.4 Figure Supplement 1). Treatment of cilia with a higher dynapyrazole-A concentration (10μM) slowed both retrograde- and anterograde-directed motion. Again, retrograde motion was more strongly inhibited (Figure 2.4 Figure Supplement 2). Dynapyrazole-A treatment (5μM and 10μM) also reduced the frequency, i.e. the number of particles moving across a cilium per minute, in both anterograde and retrograde directions (Figure 2.4G, Figure 2.4 Figure Supplement 2). We note that dynapyrazole-A, at concentrations close to the IC50 for inhibiting microtubule gliding in vitro, alters

intraflagellar transport in a manner similar to what has been observed following dynein 2 loss-of-function in *chlamydomonas*(98).

We next examined whether inhibition of intraflagellar transport by dynapyrazole-A was reversed following washout of the compound. Ciliated cells treated with dynapyrazole-A (5μM, 5 minutes) were transferred to solvent-control media with serum (0.3% DMSO, 10% FBS) and incubated for an additional ten minutes. Both retrograde and anterograde velocities recovered to control levels (Figure 2.4F, retrograde: 467 ±136 nm/s, 173 particles, 18 cilia; anterograde: 697 ± 149 nm/s, 256 particles, 18 cilia) as did transport frequencies (Figure 2.4G). When media with a lower serum concentration was used in washout experiments, retrograde velocities recovered only partially, suggesting that serum may accelerate the partitioning of this compound out of cells (Figure 2.4 Figure Supplement 3). Taken together, our data suggest dynapyrazole-A is a useful reversible probe to study intraflagellar transport.

Figure 2.5. Inhibition of dynein 1 activity by dynapyrazole-A (8). *Note: the work showin in E-O was performed by others. Lysosome motility analysis was performed by A. Serpinskaya and V. Gelfand (Northwestern University, Chicago, IL).* (A) Gel filtration trace (Superose 6) for GFP-dynein 1, with volume at elution peak indicated. V_o, void volume. (B) SDS-PAGE analysis (coomassie blue stain) of GFP-dynein 1, ~0.5 μg protein loaded. (C) Montages of fluorescent microtubules moving on GFP-dynein 1-coated glass slides in the presence of 1mM ATP and either DMSO, ciliobrevin D or **8** (10μM). The interval between successive images is 2 seconds and total time elapsed is 20s. Horizontal scale bar, 5 μm. (D) Inhibition of GFP-dynein 1-driven motility by **8** and ciliobrevin D (mean ± S.D., n = 3). IC_{50} values for **8**: 2.3 ± 1.4 μM (n = 3); ciliobrevin D: 15 ± 2.9 μM (n = 3). Number of microtubules quantified: **8**: 20μM-98, 10μM-105, 5μM-108, 2.5μM-97, 1.3μM-134, 0.6μM-99, 0.3μM-43, 0.2μM-29; ciliobrevin D: 40μM-64, 20μM-74, 10μM-82, 5μM-79, 2.5μM-81, 1.3μM-87. IC_{50} values reported reflect the mean (± S.D.) of separate IC_{50} values obtained from independent dose-response analyses. Data were fit to a sigmoidal dose-response curve and constrained such that the value at saturating compound > 0. All motility assays were performed at 1mM MgATP, 0.05 mg/mL casein, and 2% DMSO. Velocity distribution histograms for inhibition of dynein-1 driven microtubule motility are presented in Figure 5 Figure Supplement 1. Analysis of microtubule attachment to dynein-coated coverslips is presented in Figure 5 Figure Supplement 2. (E - J) Images of CAD cell neurites stained with Lysotracker Red. in the presence of DMSO control (0.1%), 3.5 μM and 5 μM (**8**). Scale bar, 10μm. (E - G) Phase contrast microscopy images of CAD cells. (H-J) Overlay of successive images of lysosome motility in CAD cell neurites. 60 images, spaced 1s apart, are stacked and successive images colored using FIJI according to the temporal color code shown. (K-M) Kymographs corresponding to images in H-J. The kymograph size is 60 seconds (vertical) by 37 μm (horizontal) and the anterograde and retrograde orientations are indicated. (N) Quantitation of lysosome velocity. (O) Quantitation of total lysosome displacement over the time course of imaging (1 min). Data are mean of n ≥ 2 experiments with ≥150 particles counted per experiment. Number of frame-to-frame velocities measured: DMSO-anterograde: 14167, DMSO-retrograde: 14973, 3.5μM **8**-anterograde: 11283, 3.5μM **8**-retrograde: 11340, 5μM **8**-anterograde: 9449, 5μM **8**-retrograde: 10458. For O, number of particles counted: DMSO-3770, 5μM **8**-2400, 3.5μM **8**-840. Error bars: S.D. (DMSO, 5 μM **8**), or range of values (3.5 μM **8**).

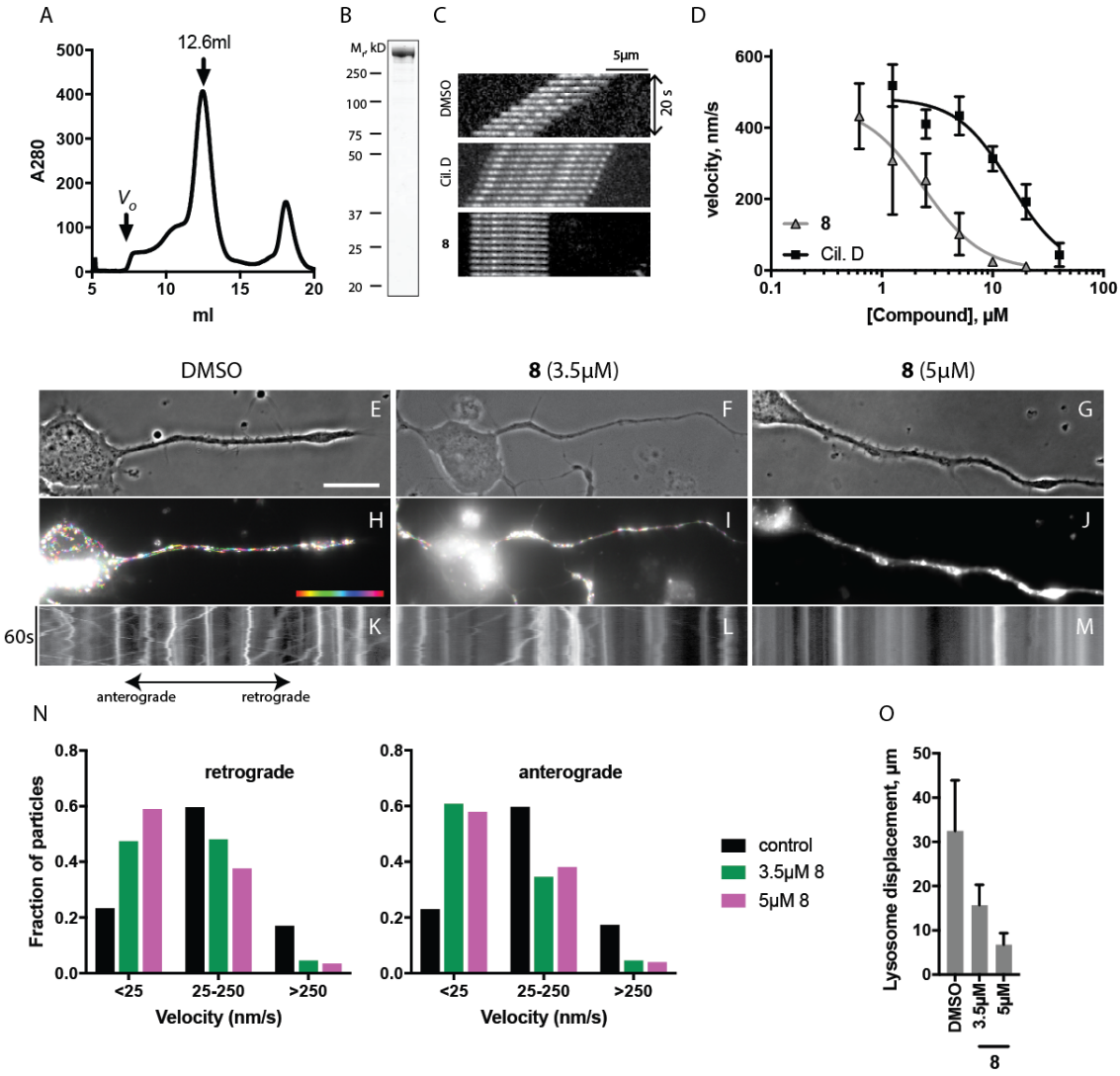
A
12.6ml
A280
V_o
ml
B
M_r kD
250
100
75
50
37
25
20
C
5µm
DMSO
Cil. D
8
20 s
D
velocity, nm/s
8
Cil. D
[Compound], µM
DMSO
8 (3.5µM)
8 (5µM)
E
F
G
H
I
J
K
L
M
60s
anterograde
retrograde
N
retrograde
anterograde
Fraction of particles
<25
25-250
>250
Velocity (nm/s)
control
3.5µM 8
5µM 8
O
Lysosome displacement, µm
DMSO
3.5µM
5µM
8

We predicted that dynapyrazole-A, like ciliobrevin D, should also inhibit cytoplasmic dynein 1(47). To examine the inhibition of dynein 1 by dynapyrazole-A *in vitro* we generated recombinant human protein. We expressed and purified a GFP-tagged human dynein 1 (AA 1320-4646) construct similar to the one we used for GFP dynein 2. This protein migrated with a peak volume of 12.6 mL in size exclusion chromatography and SDS-PAGE analysis showed > 90% purity (Figure 2.5A, B). GFP-dynein 1 moves microtubules at 508 ± 60 nm/s (n = 5 independent experiments, 191 microtubules analyzed), a velocity expected based on studies of other mammalian dynein 1 homologs (99). Under these conditions ~97% of the filaments analyzed had velocities >50nm/s (Figure 2.5 Figure Supplement 1). Time-lapse montages showed that both ciliobrevin D and dynapyrazole-A slowed dynein-dependent microtubule gliding (Figure 2.5C). Dose-dependent analysis indicated that dynapyrazole-A blocked GFP-dynein 1-driven motility with an IC_{50} of 2.3 ± 1.4 μM, ~6-fold more potently than ciliobrevin D (15 ± 2.9 μM, Figure 2.5D). Inhibition of dynein 1-dependent microtubule gliding by dynapyrazole-A was reversed following washout, as is also the case for dynein 2-dependent motility (Figure 2.5 Figure Supplement 3). As has been previously noted for ciliobrevin D, the potency of dynapyrazole-A was sensitive to the protein (e.g. blocking agent, serum) concentration in solution (Figure 2.5, Figure Supplement 4), likely due to the hydrophobicity of these compounds (calculated logarithm of octanol:water partition coefficient [ClogP]: ciliobrevin D: 4.5; dynapyrazole-A: 4.2)(46). We therefore focused our cell-based analyses of dynapyrazole-A on dynein 1-dependent processes in assays that do not require high serum concentrations.

Lysosome transport can be observed in the neurites of CAD cells, a murine cell line that displays neuron-like properties in serum-free cell culture media (Figure 2.5 E-M; all lysosome motion experiments were performed by A. Serpinskaya and V. Gelfand, Northwestern University)(100). This bidirectional transport of lysosomes requires kinesins and dynein 1 and can be observed by imaging live cells stained with the LysoTracker dye (1, 101). A coupling between anterograde and retrograde motion has been described for membrane-bound organelles, with disruption of dynein-driven motion blocking bi-directional organelle motility(102). We imaged control solvent (0.1%DMSO) treated cells and observed bidirectional motion of LysoTracker-labelled puncta (Figure 2.5E, H, K). Overlays of successive images from a time-lapse series, color-coded for displacement, reveal organelle displacements (Figure 2.5 H - J). Quantitative analysis using kymographs shows that ~20% of particles move at speeds below 25 nm/s in both anterograde and retrograde directions under control conditions and a similar fraction of particles have velocities above 250 nm/s (Figure 2.5K, 2.5N). Treatment with dynapyrazole-A suppressed bidirectional motion. In particular, the percentage of retrograde-directed lysosomes moving slower than 25 nm/s increased to ~47% (3.5μM) and ~59% (5μM) and lowered the proportion of lysosomes moving at speeds > 250 nm/s to below 10%. We observed equivalent effects of dynapyrazole-A on anterograde motion (kymographs in 5K, L, M) velocities. In control cells, lysosomes with measureable displacements had trajectories that averaged 32 ± 11 μm (Figure 2.5O)(100). Dynapyrazole-A (3.5 μM, Figure 5I, 5L) reduced the average track length of moving particles to 15.7 ± 4.7 μm, which can be seen as white punctae that result from the overlay of multiple color-coded frames without particle translocation (Figure 2.5J, 2.5M).

A higher dose of dynapyrazole-A (5 μM) shortened the average track length of moving particles to 6.7 ± 2.7 μm. We found that ATP levels in cells treated with dynapyrazole-A at concentrations that inhibited lysosome transport (5μM) were stable for up to 3 hours (Figure 2.5 Figure Supplement 5). Higher concentrations of dynapyrazole-A (15μM) lowered intracellular ATP levels by ~70% at 3 hrs (Figure 2.5 Figure Supplement 5). Together, these data suggest that at concentrations near its *in vitro* IC_{50}, dynapyrazole-A suppresses lysosome transport in cells via inhibition of dynein 1.

Figure 2.6. Analysis of the mechanism of dynein inhibition by dynapyrazole-A (8) (A) Basal ATPase activity of GFP-dynein in the solvent control (2% DMSO, n = 8) and in the presence of **8** (40μM, n = 4) and ciliobrevin D (40μM, n = 4). (B) SDS-PAGE analysis (coomassie blue stain) of His-dynein 1, ~0.5 μg protein loaded. Mass spectrometry showed that the impurity (~15%, triangles) is a fragment of dynein (Figure 6 Figure Supplement 1) (C) Basal ATPase activity of His-dynein in the solvent control (2% DMSO, n = 11) and in the presence of **8** (40μM, n = 11) and ciliobrevin D (40μM, n = 5). (D) Microtubule-stimulated ATPase activity of His-dynein across a range of microtubule concentrations in the solvent control (2% DMSO) or in the presence of 30μM **8** (2.5 μM microtubules, n = 5; 8μM microtubules, n = 4; 8μM microtubules, 30μM **8**, n = 3; 15μM microtubules, 2% DMSO, n = 4; 15μM microtubules, 30μM **8**, n = 3) (E) Dose-dependent inhibition of microtubule-stimulated His-dynein 1 ATPase activity by **8** (2.5 μM microtubules, IC_{50}: 6.2 ± 1.6 μM, n = 3). (F) SDS-PAGE analysis (coomassie blue stain) of dynein following irradiation with ultraviolet light at 365 nm. The components included in the photocleavage reaction loaded into each lane are indicated above the lane. Arrowheads indicate dynein photocleavage products. (G) Analysis of gel band intensity for photocleavage reactions. (H) Gel filtration traces (Superose 6) for His-dynein 1 wild-type and AAA3 Walker A mutant. Peak elution volumes are 12.2, and 12.4 mL, respectively. V_o, void volume. (I) SDS-PAGE analysis (Coomassie blue stain) of Walker A mutant His-dynein 1 protein, ~0.5 μg protein loaded. Mass spectrometry data confirming the presence of the K2601A mutation in this construct is shown in Figure 6 Supplement 5. (J) Basal and microtubule-stimulated ATPase activity of the AAA3 Walker A-mutant His-dynein 1 in the solvent control (2% DMSO) and in the presence of **8** (30μM). (K) Inhibition of the basal ATPase activity of the AAA3 Walker A-mutant His-dynein 1 by **8** (IC_{50}: 5.5 ± 1.6 μM, n = 5) and ciliobrevin D (IC_{50}: 38.4 ± 6.3 μM, n = 3). IC_{50} values reported reflect the mean (±S.D.) of separate IC_{50} values obtained from independent dose-response analyses. For (E) and (K), data were fit to a four-parameter sigmoidal dose-response curve in PRISM and constrained such the value at saturating compound > 0. All ATPase assays were performed at 1mM MgATP and 2% DMSO. All data presented are mean ± S.D. of n ≥ 3 data points, except in K, where replicate numbers for individual datapoints were as follows. **8**: 80μM-2, 40μM-5, 20μM-5, 10μM-5, 5μM-5, 2.5μM-5, 1.3μM-5, 0.6μM-2. Ciliobrevin D: 80μM-2, 40μM-3, 20μM-3, 10μM-3, 5μM-3, 2.5μM-3.

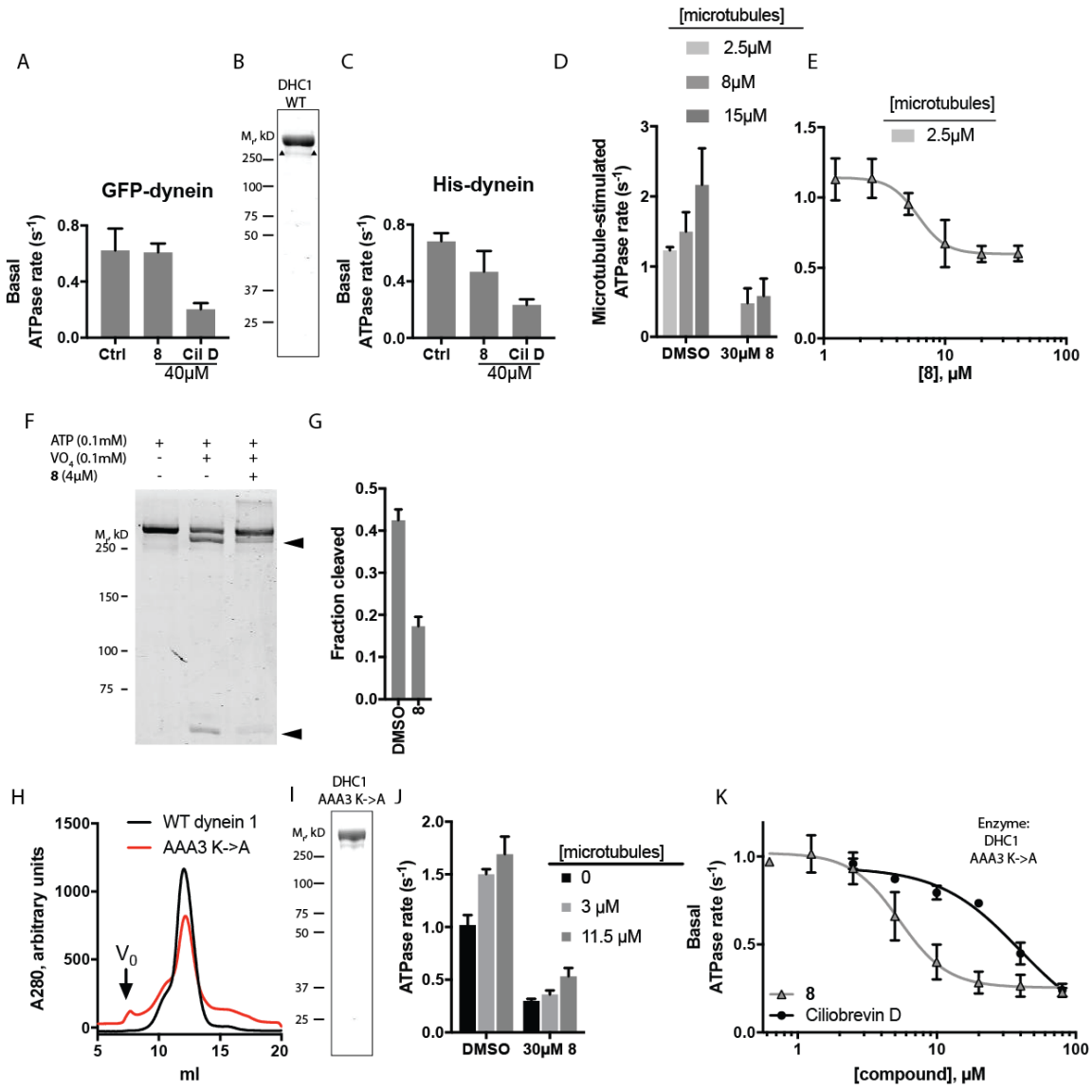
A
GFP-dynein
Basal ATPase rate (s-1)
Ctrl
8
Cil D
40μM
B
DHC1 WT
Mr kD
250
100
75
50
37
25
C
His-dynein
Basal ATPase rate (s-1)
Ctrl
8
Cil D
40μM
D
[microtubules]
2.5μM
8μM
15μM
Microtubule-stimulated ATPase rate (s-1)
DMSO
30μM 8
E
[microtubules]
2.5μM
[8], μM
F
ATP (0.1mM)
VO4 (0.1mM)
8 (4μM)
Mr kD
250
150
100
75
G
Fraction cleaved
DMSO
8
H
WT dynein 1
AAA3 K->A
A280, arbitrary units
V0
ml
I
DHC1 AAA3 K->A
Mr kD
250
100
75
50
37
25
J
ATPase rate (s-1)
[microtubules]
0
3 μM
11.5 μM
DMSO
30μM 8
K
Enzyme: DHC1 AAA3 K->A
Basal ATPase rate (s-1)
8
Ciliobrevin D
[compound], μM

Dynein 1, whose biochemical activity has been extensively characterized, serves as a model for the mechano-chemistry of this motor protein family. Therefore, to dissect the mechanism of inhibition of dynein by dynapyrazole-A, we focused on this isoform. The basal ATPase activity of GFP-dynein was 0.62 ± 0.2 s^{-1} (Figure 2.6A, n = 8 independent experiments, mean ± S.D.). We also purified an N-terminally polyhistidine (His)-tagged dynein motor domain construct (AA 1320 - 4646) that was routinely obtained in five-fold higher yield than the GFP-tagged construct (Figure 2.6B). Following a three-step purification protocol, we obtained this protein with >80% purity. The specific activity of His-dynein 1 (0.66 ± 0.1 s^{-1}, mean ± S.D. Figure 2.6C) was similar to that of GFP-dynein. The basal ATPase rates of these human dynein constructs were within the range observed by others for mammalian dyneins(103-105). We examined the inhibition of dynein 1's ATPase activity by dynapyrazole-A. Remarkably, a high concentration of dynapyrazole-A (40μM) did not inhibit the basal ATPase activity of GFP-dynein 1 (Figure 6A) and weakly inhibited His-dynein 1 (~30% inhibition Figure 2.6C). Under similar conditions, ciliobrevin D (40 μM) inhibited the ATPase activity of both GFP-dynein 1 and His-dynein 1 by ~70% (Figure 2.6A, 2.6C). The rather modest inhibition of dynein's ATPase activity by dynapyrazole-A was unexpected, as dynapyrazole-A can inhibit microtubule gliding at a 20-fold lower concentration.

We next examined if dynapyrazole-A inhibits dynein 1's microtubule-stimulated ATPase activity. We find that human dynein's ATP hydrolysis rate is stimulated in a microtubule concentration-dependent manner (Figure 2.6D, 2.5 μM: 1.2 ± 0.05 s^{-1}, n = 3; 8μM: 1.5 ± 0.3 s^{-1}, n = 4; 15μM: 2.2 ± 0.5 s^{-1}, n = 4). At high microtubule concentrations dynapyrazole-A (30μM) inhibited the microtubule-stimulated ATPase activity to a

residual rate of ~0.5 s^{-1} (8 or 15 μM microtubules, Figure 2.6D). Dose-dependent analysis was carried out at a microtubule concentration (2.5μM) that gave two-fold stimulation of dynein. At increasing concentrations of dynapyrazole-A dynein's microtubule-stimulated ATPase activity saturated at ~0.5s^{-1}, despite the expected nearly complete occupancy of dynein molecules with dynapyrazole A at the enzyme concentrations used (Assuming K_i values in the ~2-5 μM range and with protein concentrations of <0.1 μM, occupancy of dynein should be 88-95% at 40 μM; Figure 2.6E). Fitting to this non-zero plateau value gave an IC_{50} of dynapyrazole-A of 6.2 ± 1.6 μM. In comparison, dose-dependent inhibition of dynein 1's microtubule-stimulated ATPase activity by ciliobrevin D did not reveal a plateau up to the highest concentrations the compound remained soluble in these assay conditions (Figure 6 Figure Supplement 2).

To better understand how dynapyrazole-A inhibits dynein activity, we monitored its effect on ADP-vanadate dependent photocleavage of dynein. In this assay, an established read-out of nucleotide binding at dynein's AAA1 site(19, 20), ultraviolet irradiation leads to ADP-vanadate-dependent photocleavage of dynein at the AAA1 site, resulting in two protein fragments(106). Using His-dynein 1, 100µM ATP, and 100µM vanadate, we consistently observed ~40% photocleavage of His-dynein 1 (Figure 2.6F, 2.6G) and fragments consistent with cleavage at AAA1, as expected(19, 20). At a dynapyrazole-A concentration near its IC_{50} for *in vitro* dynein inhibition (4µM), ADP-vanadate dependent photocleavage of dynein was reduced ~2.5 fold relative to controls (~17% photocleavage). These data are consistent with dynapyrazole-A binding at the AAA1 site.

To further dissect how dynein is inhibited by dynapyrazole we expressed and purified a construct with a Walker A lysine-to-alanine substitution at AAA3 (K2601A), a mutation that disrupts nucleotide binding at AAA3(20, 107). We found that the mutant protein eluted during size exclusion chromatography with a major peak at a similar elution volume to that for the wild-type construct (12.4 mL for the mutant, 12.2 mL for wild-type, Figure 2.6H, I), suggesting that the mutations do not disrupt overall protein folding. We also purified a comparable AAA1 (K1912A) mutant, but this protein had ~80-90% reduced ATPase activity, making analysis of its ATPase activity difficult (Figure 2.6 Figure Supplement 3). We found that the AAA3 mutant had basal activity that was elevated relative to wild-type (1.1 ± 0.2 s^{-1}, n = 5), as has been previously shown for yeast dynein with a similar mutation(89). The ATPase activity of this mutant was stimulated by microtubules to $1.5s^{-1}$ (3μM microtubules) and 1.7 s^{-1} (11.5μM microtubules) (Figure 2.6J). The reduced microtubule stimulation of the ATPase activity is consistent with findings for comparable dynein constructs from other organisms(20, 89).

Across the range of microtubule concentrations tested, dynapyrazole-A reduced the AAA3 mutant dynein's ATPase activity by 70-80% (Figure 6J). Surprisingly, unlike what we observed for the wildtype protein, strong inhibition of the basal activity of this mutant construct was also observed (~ 70% inhibition; 30μM dynapyrazole-A). A dose-dependent analysis showed that dynapyrazole-A inhibits the basal activity of the AAA3 mutant with an IC_{50} of $5.5 \pm 1.6\mu$M while ciliobrevin D has an IC_{50} of 38 ± 6 μM (Figure 2.6K). Even in the context of the AAA3 mutant enzyme, a residual ATPase activity of ~$0.2s^{-1}$ was observed at the highest dynapyrazole-A concentrations tested (Figure 2.6K).

It is noteworthy that dynapyrazole-A inhibits basal activity of the AAA3 mutant and the microtubule-stimulated ATPase activity of the wild-type enzyme with similar potency, suggesting that a common ATPase site, likely AAA1, might be inhibited in both contexts.

2.3 Discussion

In this study, we analyzed the structure of the ciliobrevins and designed tricyclic derivatives in which the benzoylacrylonitrile of ciliobrevin was replaced with a cyanopyrazole. These compounds inhibited dynein *in vitro* and in cells more potently than ciliobrevins and have improved chemical properties. We also find that dynapyrazole-A inhibits dynein by a mechanism that is distinct from that of ciliobrevins.

We find that the pyrazoloquinazolinone scaffold of the dynapyrazoles addresses many of the limitations of the ciliobrevins. First, activated acrylonitriles, such as the benzoylacrylonitrile at the core of the ciliobrevin scaffold, have been shown to be susceptible to attack by intracellular nucleophiles, raising the possibility of unwanted reactivity of these dynein inhibitors(108). While ciliobrevins have been observed to be unstable under standard laboratory storage conditions, the pyrazoloquinazolinone of the dynapyrazoles is unlikely to be reactive or unstable but retains many of the electrostatic and steric elements present in ciliobrevin(61). Second, the potency of dynapyrazole-A is similar across *in vitro* and cell-based assays, consistent with dynein being its cellular target. This was not consistently observed for ciliobrevin analogs. Dynapyrazole-A and -B inhibited dynein-dependent microtubule gliding six- to eight-fold more potently than ciliobrevins, however different mechanisms of inhibition make it difficult to relate this change in potency directly to an increased binding affinity. Third, the ciliobrevin scaffold

is present in chemical screening libraries and a close derivative has annotated anti-malarial activity(109). In contrast, to our knowledge, the 2-aryl-substituted cyano-pyrazoloquinazolinone structure of **4** has not previously been reported in a bioactive compound. The hydrophobicity of the dynapyrazoles remains a limitation that needs to be addressed. We note that the high ClogP value of dynapyrazole-A, which is similar to that of ciliobrevins, may explain why this compound, like ciliobrevin D, has reduced activity in the presence of high protein concentrations (eg. serum). Likewise, acute reversal of intraflagellar transport inhibition was most effective using cell culture medium with serum. We believe that the dynapyrazole scaffold will be valuable for further optimization of these chemical probes.

In current models, the motion of membrane-bound organelles requires a balance of motors moving toward microtubule plus- and minus-ends (102). Studies across several cell types of different organelles have established that depletion or inhibition of dynein reduces bidirectional organelle motion(110-112). Remarkably, organelle motion following dynein depletion can be restored by add-back of a minus-end directed kinesin, suggesting that micromechanical coupling is involved and an opposing force is needed to activate directional motion of the motor proteins needed for the directional motion of these cellular cargoes (102, 113). These observations provide a plausible explanation for the bi-directional inhibition of lysosome motility upon dynapyrazole-A treatment. Although the individual cargos in the cilium are not likely membrane-bound, this intracellular transport is no less complex than organelle movement in the cytoplasm(114). We believe that dynapyrazole-A will be a useful tool to dissect how the length and shape

of the cilium is linked to directional transport and to tease apart the contributions of active transport and passive diffusion of proteins to Hedgehog signaling.

Dynapyrazole-A blocks both dynein 1 and dynein 2. As dynein 1 plays a critical role in numerous cellular processes, its persistent inhibition is expected to be toxic to cells (Figure 2.6 Figure Supplement 5). However, acute inhibition may be useful in deciphering dynein function in different contexts. Can dynapyrazoles be chemically modified to develop inhibitors that are selective for dynein 1 or 2? Previously, we found that modest selectivity for inhibition of dynein 2 relative to dynein 1 can be achieved under certain conditions ([ATP] < 1 μM) by appending tolyl ethers at the 7-position of the ciliobrevin quinazolinone(47). However, inhibition of dynein's ATPase activity by these ciliobrevin analogs is suppressed at higher ATP concentrations (e.g. 100μM) *in vitro*. Studies of mammalian dynein 1 indicate that there are two ATP-binding sites with K_m values separated by two orders of magnitude (~2 μM and ~600 μM(115)). It is possible that the observed selectivity is achieved by targeting the high-affinity ATPase site and therefore, at higher, close to physiologic ATP concentrations, the inhibition by these ciliobrevin analogs would be suppressed. In contrast, dynapyrazoles inhibit dynein at high ATP concentrations (1 mM), consistent with a different mode of inhibition. Also, substitution of this compound with a methyl ether at the 6-position abrogated dynein inhibition. These data suggest that the selectivity gains observed from appending tolyl ethers to the ciliobrevin scaffold are unlikely to be applicable to dynapyrazole and developing a dynein isoform-selective dynapyrazole derivative will require more extensive structure-activity relationship studies.

Of the six AAA sites in dynein, only mutations at AAA1 and AAA3 have been found to block motility(116). In current models, ATPase activity at AAA1 is linked to rigid-body movements of subdomains during individual steps of the motor protein along microtubule tracks, while nucleotide state at AAA3 modulates the activity at AAA1 (8). Three lines of evidence indicate that dynapyrazole-A targets the AAA1 site. First, dynapyrazole-A blocks ADP-vanadate dependent photocleavage at site 1. Second, dynapyrazole-A inhibits the activity of a dynein 1 construct with a mutation in the AAA3 domain (Walker A lysine). In this construct, the ATPase activity is expected to be mainly due to the AAA1 site. Third, sequence comparisons indicate that the AAA1 sites in dynein 1 and 2 are highly conserved, while the other AAA sites are less conserved. In fact, the residues within 4Å of the bound nucleotide in AAA1 are identical between dynein 1 and 2 (Figure 6 Figure Supplement 5). This sequence similarity and our observation that dynapyrazole-A inhibits dynein 1 and 2 with comparable potency are consistent with a model in which this compound selectively inhibits hydrolysis of dynein's AAA1 site. However, further biophysical and structural studies will be required to determine whether dynapyrazole-A binds at or near the AAA1 site.

Our finding that dynapyrazole-A does not substantially inhibit ATP hydrolysis in the absence of microtubules suggests that, for dynein 1, the AAA1 site contributes to only a small fraction of this enzyme's basal activity. We posit that a separate site, likely AAA3, accounts for the majority of dynein's ATPase activity in the absence of microtubule. This site likely remains active even when ATPase activity at AAA1 is inhibited by dynapyrazoles. Currently, we cannot exclude the possibility that additional ATPase sites, such as AAA4, may also contribute partially to the basal ATPase activity

of dynein. The nucleotide state at AAA3 is known to regulate the ATPase cycle of AAA1 when microtubules are present, with the apo- and ATP-bound states of AAA3 slowing overall hydrolysis and the ADP-bound state of AAA3 leading to rapid hydrolysis at AAA1 in wild-type dynein(88, 89). Our finding that the AAA3 mutant has elevated basal activity relative to the wild-type is consistent with the protein being in a state that mimics one in which hydrolysis at AAA1 is activated. While additional biophysical studies are needed to analyze this further, dynapyrazole-A is likely to be useful as tool for chemical "separation of function" to distinguish between dynein's microtubule stimulated and basal activities in different contexts.

While restricting conformational flexibility of ligands is a well-established strategy for improving potency, its successful application typically depends on structural data that reveal the compound conformation required for activity(117). In the case of the ciliobrevins the geometric constraints we designed were guided by conformational analysis of the compounds alone and afforded ~6-8-fold improvement in potency. We note that replacement of a scaffold prone to isomerization with a fixed tricyclic pyrazoloquinazolinone did not lead directly to improved potency. Rather, incorporation of a cyclopropyl group into the dynapyrazole scaffold was required, likely by better matching the shape of the ciliobrevin pharmacophore. Our unexpected finding that conformational restriction led to changes both in potency and mechanism of inhibition raises the question of whether alternative scaffolds with different conformational constrains could reveal still other modes of dynein inhibition. More broadly, conformational restriction may be an effective strategy for improving the few AAA+ inhibitors described to date. Compounds with distinct mechanisms of action, which may

result from these efforts, will be especially valuable for these multi-site enzymes whose activity is often regulated by intricate allosteric communication.

2.4 Methods

1. Chemical Synthesis: *All chemical synthesis and structural characterization work was performed by colleagues at the Tri-Institutional Therapeutics Discovery Institute (TDI) and at Takeda Pharmaceuticals, Japan.*

General chemical methods: Solvents and reagents were purchased from VWR or Sigma Aldrich. All reactions involving air- or moisture-sensitive compounds were performed under nitrogen atmosphere using dried glassware. ^{1}H NMR spectra were recorded at 500MHz on a Bruker Advance III HD 500 MHz NMR spectrometer equipped with a TCI cryogenic probe with enhanced ^{1}H and ^{13}C detection. Chemical shifts are reported in parts per million (ppm) and coupling constants (J) are expressed in hertz (Hz). All data were collected at 298K, and internally referenced for ^{1}H to the residual chloroform signal at 7.26 ppm; to DMSO signal at 2.50 ppm; or to TMS at 0 ppm. Flash chromatography purifications were performed on CombiFlash Rf (Teledyne ISCO) as the stationary phase. The LC-MS was performed on a Waters ACQUITY H-Class UPLC/MS with a PDA eLambda detector and QDa mass spectrometer. And the reactions under microwave irradiation were performed on a CEM Explorer 48 System.

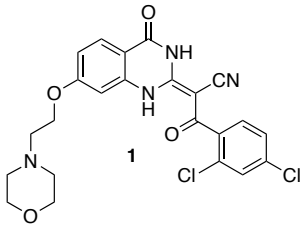

1

(2*E*)-3-(2,4-dichlorophenyl)-2-[7-(2-morpholinoethoxy)-4-oxo-1H-quinazolin-2-ylidene]-3-oxo-propanenitrile (1)

To a mixture of (2E)-3-(2,4-dichlorophenyl)-2-(7-hydroxy-4-oxo-1H-quinazolin-2-ylidene)-3-oxo-propanenitrile (82mg, 219μmol, synthesized as described previously)(47) and potassium carbonate (48.7mg, 351μmol) in dimethylformamide (10ml) was added 4-(2-chloroethyl)morpholine hydrochloride (37.13mg, 200μmol), and the resulting mixture was stirred at 80°C for 18h. The mixture was allowed to cool, and the filtrate was concentrated in vacuo. The residue was purified by column chromatography (ethyl acetate/methanol) to give (2E)-3-(2,4-dichlorophenyl)-2-[7-(2-morpholinoethoxy)-4-oxo-1H-quinazolin-2-ylidene]-3-oxo-propanenitrile (50.20 mg, 103.01 μmol, 52% yield). ^{1}H NMR (500 MHz, DMSO-d_6) δ 13.36 (s, 1H), 9.88 (s, 1H), 7.95 (d, J = 8.8 Hz, 1H), 7.66 (d, J = 2.0 Hz, 1H), 7.50-7.41 (m, 2H), 7.05-6.95 (m, 1H), 6.94-6.86 (m, 1H), 4.50 (s, 2H), 4.09-3.93 (m, 2H), 3.68 (d, J = 33.0 Hz, 2H), 3.57 (s, 2H), 3.24 (s, 2H). LCMS m/z: 487.1 $[M+H]^+$.

*Supplemental Scheme 1: Synthesis of **2** based on literature precedent.(92)*

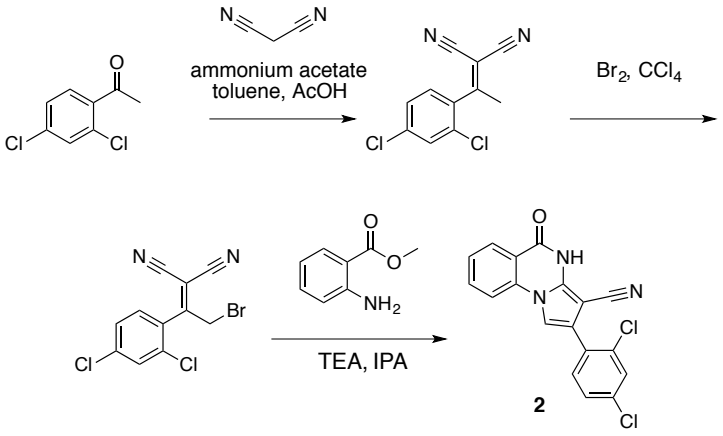

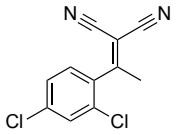

2-[1-(2,4-dichlorophenyl)ethylidene]propanedinitrile

To a solution of 1-(2,4-dichlorophenyl)ethanone (1.00 g, 5.29 mmol) in toluene (20 mL) - acetic acid (2 mL) were added malononitrile (349.45 mg, 5.29 mmol) and ammonium acetate (407mg, 5.29 mmol) at room temperature. The mixture was stirred at 100 °C for 13 h. The mixture was neutralized with sat. $NaHCO_3$ (aq). and extracted with ethyl acetate. The combined organic layer was washed with water and brine, dried over $MgSO_4$,

filtered and concentrated in vacuo. The residue was purified by column chromatography (hexane/ethyl acetate) to give 2-[1-(2,4-dichlorophenyl)ethylidene]propanedinitrile (907 mg, 3.83 mmol, 72% yield) as a colorless oil. ^{1}H NMR (500 MHz, Chloroform-d) δ 7.57 (s, 1H), 7.43 (d, J = 8.3 Hz, 1H), 7.19 (d, J = 8.3 Hz, 1H), 2.62 (s, 3H). LCMS m/z: 235.1 $[M-H]^-$.

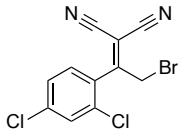

2-[2-bromo-1-(2,4-dichlorophenyl)ethylidene]propanedinitrile

To a solution of 2-[1-(2,4-dichlorophenyl)ethylidene]propanedinitrile (310.50 mg, 1.31 mmol) in carbon tetrachloride (4.00 mL) was added bromine (230 mg, 1.44 mmol) at room temperature. The mixture was stirred at room temperature for 15 min and at 70 °C for 8.5 h. The starting material remained, so bromine (620mg, 200μL, 3.88mmol) was added. The mixture was stirred at 70 °C for 21 h. The mixture was diluted with sat. NaS_2O_3 (aq). and extracted with dichloromethane. The combined organic layer was washed with sat. NaS_2O_3 (aq). and brine, dried over $MgSO_4$, filtered and concentrated in vacuo. The residue was purified by column chromatography (hexane/ethyl acetate) to give 2-[2-bromo-1-(2,4-dichlorophenyl)ethylidene]propanedinitrile (157 mg, 497 μmol, 38% yield) as a colorless oil. ^{1}H NMR (500 MHz, Chloroform-*d*) δ7.59 (s, 1H), 7.47 (d, *J*=8.3 Hz, 1H), 7.34 (d, *J*=8.3 Hz, 1H), 4.58 (s, 2H). LCMS m/z: 314.856 $[M-H]^-$.

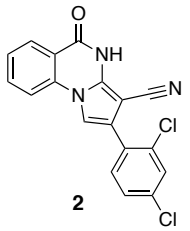

2

2-(2,4-dichlorophenyl)-5-oxo-4H-pyrrolo[1,2-a]quinazoline-3-carbonitrile (2)

To a solution of 2-[2-bromo-1-(2,4-dichlorophenyl)ethylidene]propanedinitrile (73.70 mg, 233.24 μmol) in isopropyl alcohol (3.00 mL) was added methyl 2-aminobenzoate (70.51 mg, 466.48 μmol) at room temperature. The mixture was stirred at 100 °C for 20 h. The mixture was concentrated. The residue was purified by column chromatography (hexane/ethyl acetate) to give 2-(2,4-dichlorophenyl)-5-oxo-4H-pyrrolo[1,2-a]quinazoline-3-carbonitrile (12.4 mg, 35 μmol, 15% yield) as a colorless solid. ^{1}H NMR (500 MHz, Chloroform-*d*) δ 8.81 (s, 1H), 8.40 (d, *J* = 7.8 Hz, 1H), 7.84 (t, *J* = 7.8 Hz, 1H), 7.66 (d, *J* = 8.3 Hz, 1H), 7.57 – 7.46 (m, 3H), 7.40 (s, 1H), 7.36 (d, *J* = 8.2 Hz, 1H). LCMS m/z: 354.1 $[M+H]^+$.

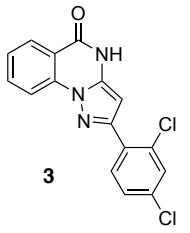

3

2-(2,4-dichlorophenyl)-4H-pyrazolo[1,5-a]quinazolin-5-one (3)

A mixture of 2-hydrazinobenzoic acid (43.32 mg, 284.7 μmol), 3-(2,4-dichlorophenyl)-3-oxo-propanenitrile (41.20 mg, 192.48 μmol) and acetic acid (2.00 mL) was stirred at 150°C under microwave irradiation for 30 min. The mixture was diluted with water and ethyl acetate, the insoluble material was collected by filtration to give the desired

compound as a colorless solid (7.5 mg). The filtrate was extracted with ethyl acetate. The combined organic layer was washed with water and brine, dried over MgSO4, filtered and concentrated in vacuo. The solid was washed wth ethyl acetate to give the desired compound (9.4 mg). The combined solid was washed with hexane to give 2-(2,4-dichlorophenyl)-4H-pyrazolo[1,5-a]quinazolin-5-one (16.4 mg, 49.7 μmol, 26% yield) as a colorless solid.^{1}H NMR (500 MHz, DMSO-d6) δ 12.34 (s, 1H), 8.19 (dd, J = 11.4, 8.2 Hz, 2H), 7.99 (d, J = 8.4 Hz, 1H), 7.94 (t, J = 7.7 Hz, 1H), 7.80 (s, 1H), 7.61 – 7.53 (m, 2H), 6.42 (s, 1H). LCMS m/z: 329.9 $[M+H]^{+}$.

*Supplemental Scheme 2: Synthesis of aminopyrazole precursor for **4** based on literature precedent for related compounds.(118)*

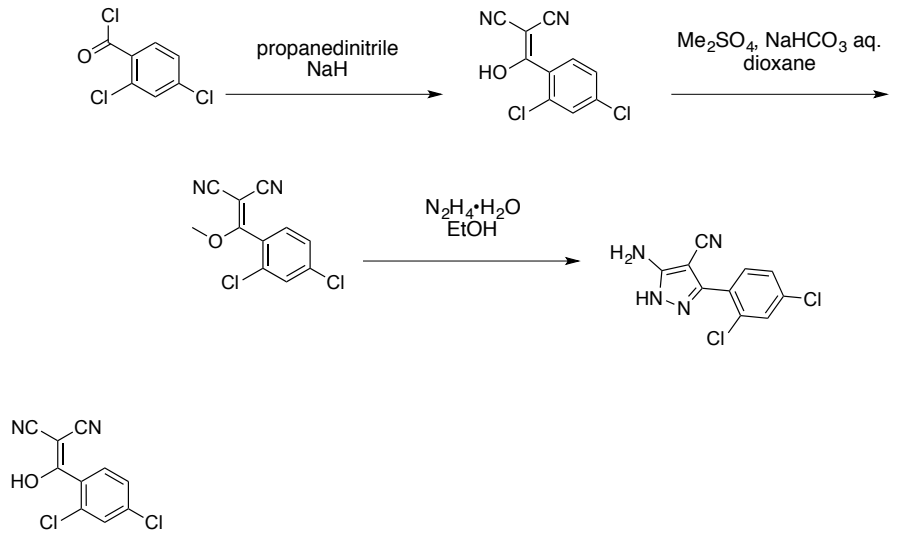

2-[(2,4-dichlorophenyl)-hydroxy-methylene]propanedinitrile

To a stirred solution of propanedinitrile (4.71 g, 71.33 mmol) in THF (150.00 mL) were added sodium hydride (5.71 g, 142.66 mmol, 60% purity) at 0 °C. The mixture was stirred at room temperature for 1 h. The solution of 2,4-dichlorobenzoyl chloride (14.62 g,

69.8 mmol, 10 mL) in THF (50 mL) was added to the mixture at 0 °C. The mixture was stirred at room temperature for 4 h. The mixture was diluted with 1N HCl (aq.) and extracted with ethyl acetate. The combined organic layer was washed with water and brine, dried over $MgSO_4$, filtered and concentrated in vacuo. The residue was purified by column chromatography (ethyl acetate/hexanes) to give 2-[(2,4-dichlorophenyl)-hydroxy-methylene]propanedinitrile (17.38 g, 72.70 mmol, 104% yield) as light yellow amorphous powder. This product was subject to the next reaction. ^{1}H NMR (500 MHz, Chloroform-*d*) δ7.55 (s, 1H), 7.46-7.38 (m, 2H). LCMS m/z: 236.992 $[M-H]^-$.

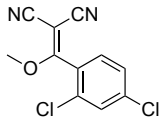

2-[(2,4-dichlorophenyl)-methoxy-methylene]propanedinitrile

A mixture of 2-[(2,4-dichlorophenyl)-hydroxy-methylene]propanedinitrile (17.38 g, 72.70 mmol), dimethyl sulfate (18.34 g, 145.40 mmol, 13.79 mL) and N-ethyl-N-isopropyl-propan-2-amine (28.19 g, 218.10 mmol, 38.09 mL) in dioxane (200 mL) was stirred at 60 °C for 23 h. The reaction was cooled to room temperature and concentrated in vacuo. The residue was dissolved with ethyl acetate and quenched with water. The organic layer was separated, washed with brine, dried over $MgSO_4$, filtered and concentrated in vacuo. The residue was purified by column chromatography (hexane/ethyl acetate) to give 2-[(2,4-dichlorophenyl)-methoxy-

methylene]propanedinitrile (3.19 g, 12.60 mmol, 17% yield) as a brown solid. (Known compound, cas: 1188083-55-7). ^{1}H NMR (500 MHz, Chloroform-*d*) δ 7.62 (d, *J*=1.9 Hz, 1H), 7.49 (dd, *J*=8.3, 1.9 Hz, 1H), 7.34 (d, *J*=8.3 Hz, 1H), 3.85 (s, 3H).

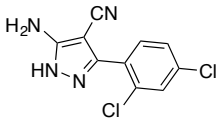

5-amino-3-(2,4-dichlorophenyl)-1H-pyrazole-4-carbonitrile

The mixture of 2-[(2,4-dichlorophenyl)-methoxy-methylene]propanedinitrile (3.19 g, 12.60 mmol) and hydrazine hydrate (694 mg, 13.86 mmol, 672 μL) in ethanol (50.00 mL) was stirred at 80 °C for 4.5 h. Additional hydrazine hydrate (252.30 mg, 5.04 mmol, 244.48 uL) was added to the mixture and it was stirred at 80 °C for 1.5 h. The reaction was concentrated *in vacuo*. The residue was washed with ethanol to give 5-amino-3-(2,4-dichlorophenyl)-1H-pyrazole-4-carbonitrile (1.73 g, 6.84 mmol, 54% yield) as an off-white solid. ^{1}H NMR: (500MHz, DMSO-d_6) δ 12.31 (s, 1H), 7.76 (s, 1H), 7.58-7.41 (m, 2H), 6.49 (s, 2H). LCMS m/z: 253.184 $[M+H]^+$.

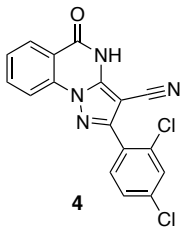

2-(2,4-dichlorophenyl)-5-oxo-4H-pyrazolo[1,5-a]quinazoline-3-carbonitrile, 4

A mixture of 5-amino-3-(2,4-dichlorophenyl)-1H-pyrazole-4-carbonitrile (100.00 mg, 395.12 μmol), dipotassium carbonate (81.91 mg, 592.68 μmol) and methyl 2-fluorobenzoate (73.08 mg, 474.14 μmol, 60.40 μL) in dimethylformamide (1.00 mL) was stirred at 140 °C for 30 min. The mixture was poured into water, and extracted with ethyl acetate. The organic layer was washed with water and brine respectively, dried over $MgSO_4$ and concentrated in vacuo. The residue was purified by silica-gel column chromatography (hexane/ethyl acetate) to give 2-(2,4-dichlorophenyl)-5-oxo-4H-pyrazolo[1,5-a]quinazoline-3-carbonitrile (14.2 mg, 39.98 μmol, 10% yield) as a white solid. ^{1}H NMR: (500MHz, DMSO-d_6) δ 8.09 (d, *J*=7.8Hz, 1H), 7.94 (d, *J*=8.2Hz 1H), 7.83 (d, *J*=2.0Hz 1H), 7.73-7.56 (m, 3H), 7.40 (t, *J*=7.5Hz, 1H). LCMS m/z: 353.136 $[M-H]^-$.

*Supplemental Scheme 3: Synthesis of cyclopropyl-substituted aminopyrazole precursor for **5**, **6**, **7**, and **8**.*

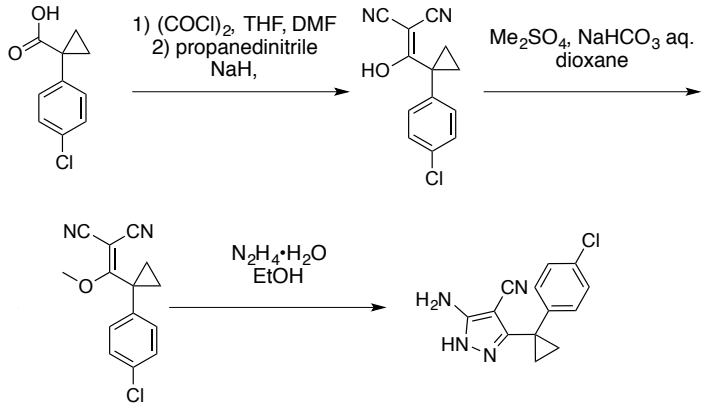

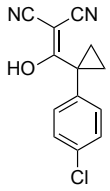

2-((1-(4-chlorophenyl)cyclopropyl)(hydroxy)methylene)malononitrile

To a solution of 1-(4-chlorophenyl)cyclopropanecarboxylic acid (**1**, 10.00 g, 50.86 mmol) in THF (100.00 mL) were added oxalyl chloride (7.75 g, 61 mmol, 5.33 mL) and dimethylformamide (37.17 mg, 508.60 μmol, 39.54 uL). The mixture was stirred at room temperature for 0.5h. The mixture was concentrated in vacuo. The mixture was added to a solution of propanedinitrile (3.36 g, 50.86 mmol) and sodium hydride (4.07 g, 101.72 mmol, 60% purity) in THF (100 ml) at 0 °C. The mixture was stirred at room temperature for 1 h. The mixture was diluted with 1N HCl and extracted with ethyl acetate. The combined organic layer was washed with water and brine, dried over Na_2SO_4, filtered and concentrated under reduced pressure. The residue was purified by column chromatography (hexane/ethyl acetate) to give 2-((1-(4-chlorophenyl)cyclopropyl)(hydroxy)methylene)malononitrile (12 g, 49 mmol, 96% yield) as a light yellow oil. ^{1}H NMR (500 MHz, DMSO-d_6) δ 7.36 – 7.30 (m, 2H), 7.22 (dd, J = 7.8, 2.0 Hz, 2H), 1.22 – 1.16 (m, 2H), 0.97 (d, J = 3.6 Hz, 2H). LCMS m/z: not detected.

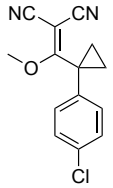

2-((1-(4-chlorophenyl)cyclopropyl)(methoxy)methylene)malononitrile

To a solution of 2-[1-(4-chlorophenyl)cyclopropanecarbonyl]propanedinitrile (**2**, 12.00 g, 49.0 mmol) in dioxane (200 mL) and H_2O (20 mL) were added dimethyl sulfate (18.56 g, 147.1 mmol, 13.9 mL) and $NaHCO_3$ (20.60 g, 245.20 mmol). The mixture was stirred at 100 °C for 5 hour. The mixture was poured into water, and extracted with ethyl acetate. The organic layer was washed with brine, dried over Na_2SO_4 and concentrated in vacuo. The residue was purified by column chromatography (hexane/ethyl acetate) to give 2-((1-(4-chlorophenyl)cyclopropyl)(methoxy)methylene)malononitrile (3.38 g, 13.1 mmol, 27% yield) as a yellow oil. ^{1}H NMR (500 MHz, DMSO-d_6) δ 7.55 – 7.45 (m, 2H), 7.33 – 7.22 (m, 2H), 4.04 (s, 3H), 1.80 – 1.71 (m, 2H), 1.68 – 1.61 (m, 2H). LCMS m/z: not detected.

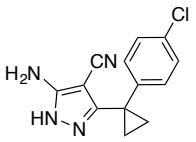

5-Amino-3-[1-(4-chlorophenyl)cyclopropyl]-1H-pyrazole-4-carbonitrile

To a solution of 2-[[1-(4-chlorophenyl)cyclopropyl]-methoxy-methylene]propanedinitrile (**3**, 3.38 g, 13.07 mmol) in ethanol (100.00 mL) was added hydrazine hydrate (981.43 mg, 19.61 mmol). The mixture was stirred at 80 °C for 2 hour. The mixture was concentrated in vacuo. The residue was purified by column chromatography (hexane/ethyl acetate) to give 5-amino-3-[1-(4-chlorophenyl)cyclopropyl]-1H-pyrazole-4-carbonitrile (2.77 g,

10.71 mmol, 82% yield) as a white powder. ^{1}H NMR (500 MHz, DMSO-d_6) δ 11.73 (s, 1H), 7.35 (d, J = 8.0 Hz, 2H), 7.27 – 7.16 (m, 2H), 6.28 (s, 2H), 1.43 – 1.13 (m, 4H). LCMS m/z: 259 $[M+H]^+$.

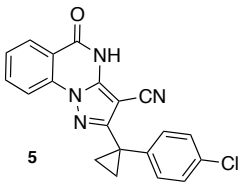

5

2-[1-(4-chlorophenyl)cyclopropyl]-5-oxo-4H-pyrazolo[1,5-a]quinazoline-3-carbonitrile (5)

A mixture of 5-amino-3-[1-(4-chlorophenyl)cyclopropyl]-1H-pyrazole-4-carbonitrile (100.00 mg, 386.53 μmol), dipotassium carbonate (80.13 mg, 579.80 μmol) and methyl 2-fluorobenzoate (71.50 mg, 463.84 μmol, 59.09 uL) in dimethylformamide (1.00 mL) was stirred at 140 °C for 30 min. The mixture was poured into water, and extracted with ethyl acetate. The organic layer was washed with water and brine respectively, dried over $MgSO_4$ and concentrated in vacuo. The residue was purified by flash chromatography (ethyl acetate/hexane) to give 2-[1-(4-chlorophenyl)cyclopropyl]-5-oxo-4H-pyrazolo[1,5-a]quinazoline-3-carbonitrile (16 mg, 44μmol, 11% yield) as a white solid. ^{1}H NMR (500 MHz, DMSO-d_6) δ 13.23 (s, 1H), 8.17 (d, J=7.9 Hz, 1H), 8.10 (d, J=8.2 Hz, 1H), 7.95 (t, J=7.8 Hz, 1H), 7.59 (t, J=7.6 Hz, 1H), 7.38 (d, J=8.2 Hz, 2H), 7.32 (d, J=8.3 Hz, 2H), 1.55 (q, J=4.6 Hz, 2H), 1.42 (q, J=4.6 Hz, 2H). LCMS m/z: 361.233 $[M+H]^+$.

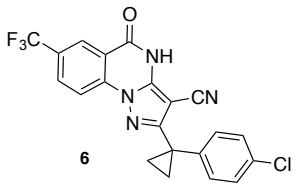

6

2-(1-(4-chlorophenyl)cyclopropyl)-5-oxo-7-(trifluoromethyl)-4,5-dihydropyrazolo[1,5-*a*]quinazoline-3-carbonitrile (6)

A mixture of 5-amino-3-[1-(4-chlorophenyl)cyclopropyl]-1H-pyrazole-4-carbonitrile (80.00 mg, 309.23 μmol) , methyl 2-fluoro-5-(trifluoromethyl)benzoate (75.56 mg, 340.15 μmol) and dipotassium;carbonate (64.11 mg, 463.85 μmol) in dimethylformamide (1.00 mL) was stirred at 140 °C for 30 min under microwave irradiation. The mixture was poured into water, and extracted with ethyl acetate. The organic layer was washed successively with water and brine, dried over $MgSO_4$ and concentrated in vacuo. The residue was purified by column chromatography (ethyl acetate/hexane) to give a mixture. The amorphous material was triturated with acetonitrile and the white precipitate was collected to give 2-[1-(4-chlorophenyl)cyclopropyl]-5-oxo-7-(trifluoromethyl)-4H-pyrazolo[1,5-a]quinazoline-3-carbonitrile (26.20 mg, 61.10 μmol, 19.76% yield) as a white solid. ^{1}H NMR (500 MHz, DMSO-d_6) δ 13.49 (s, 1H), 8.36 (s, 1H), 8.25 (d, *J*= 1.3 Hz, 2H), 7.42 – 7.35 (m, 2H), 7.35 – 7.27 (m, 2H), 1.63 – 1.52 (m, 2H), 1.48 – 1.38 (m, 2H). LCMS m/z: 429.2 $[M+H]^+$.

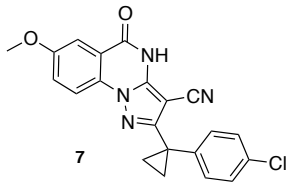

7

2-[1-(4-chlorophenyl)cyclopropyl]-7-methoxy-5-oxo-4H-pyrazolo[1,5-a]quinazoline-3-carbonitrile (7)

A mixture of 5-amino-3-[1-(4-chlorophenyl)cyclopropyl]-1H-pyrazole-4-carbonitrile (127.71 mg, 493.65 μmol), dipotassium;carbonate (102.34 mg, 740.47 μmol) and methyl 2-fluoro-5-methoxy-benzoate (100.00 mg, 543.01 μmol) in dimethylformamide (3.00 mL) was stirred at 140 °C for 40 hours. The mixture was poured into water, and extracted with ethyl acetate. The organic layer was washed with water and brine respectively, dried over $MgSO_4$ and concentrated in vacuo. The residue was purified column chromatography (ethyl acetate/hexane) to give 2-[1-(4-chlorophenyl)cyclopropyl]-7-methoxy-5-oxo-4H-pyrazolo[1,5-a]quinazoline-3-carbonitrile (9 mg, 24 μmol, 5% yield) as a white solid. ^{1}H NMR (500 MHz, DMSO-d_6) δ 13.24 (s, 1H), 8.03 (d, *J*= 9.0 Hz, 1H), 7.61 – 7.48 (m, 2H), 7.39 – 7.23 (m, 4H), 3.89 (s, 3H), 1.52 (q, *J*= 4.5 Hz, 2H), 1.39 (q, *J*= 4.5 Hz, 2H). LCMS m/z: 391.30 $[M+H]^+$.

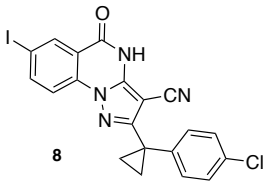

8

2-[1-(4-chlorophenyl)cyclopropyl]-7-iodo-5-oxo-4H-pyrazolo[1,5-a]quinazoline-3-carbonitrile (8)

A mixture of 5-amino-3-[1-(4-chlorophenyl)cyclopropyl]-1H-pyrazole-4-carbonitrile (498.89 mg, 1.93 mmol), methyl 2-fluoro-5-iodo-benzoate (600.00 mg, 2.14 mmol) and dipotassium carbonate (444.20 mg, 3.21 mmol) in dimethylformamide (10.00 mL) was stirred at 150 °C for 1 h under microwave irradiation. The reaction was cooled to room temperature and poured into water. The white precipitate was collected and washed with ethyl acetate to give 2-[1-(4-chlorophenyl)cyclopropyl]-7-iodo-5-oxo-4H-pyrazolo[1,5-a]quinazoline-3-carbonitrile (400 mg, 822 μmol, 38% yield) as a white solid. ^{1}H NMR (500 MHz, Chloroform-*d*) δ 9.78 (s, 1H), 8.65 (d, *J*= 2.0 Hz, 1H), 8.15 (dd, *J*= 8.7, 2.0 Hz, 1H), 7.91 (d, *J*= 8.6 Hz, 1H), 7.43 – 7.32 (m, 4H), 1.64 (d, *J*= 2.4 Hz, 2H, overlaps with a peak for residual water), 1.41 (q, *J*= 4.6 Hz, 2H). LCMS m/z: 487.0 $[M+H]^+$.

*Supplemental Scheme 4: Synthesis of **9**.*

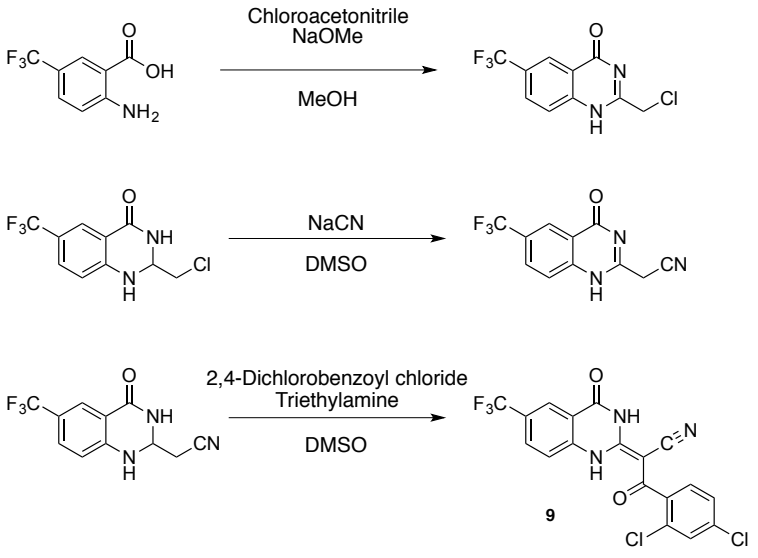

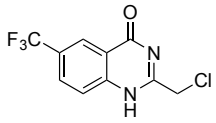

2-(chloromethyl)-6-(trifluoromethyl)-2,3-dihydroquinazolin-4(1*H*)-one

To a solution of sodium methoxide (0.5 M, 2.44 mL) was added 2-chloroacetonitrile (423 mg, 5.6 mmol). The mixture was stirred at 25 °C for 30 min. A solution of 2-amino-5-(trifluoromethyl)benzoic acid (1.00 g, 4.9 mmol) in MeOH (7.0 mL) was added to the mixture. The mixture was stirred at rt for 12 h. The resulting solid was collected by filtration to give 2-(chloromethyl)-6-(trifluoromethyl)-1H-quinazolin-4-one (422 mg, 1.61 mmol, 33% yield) as a white solid. ^{1}H NMR (500 MHz, DMSO-d6) δ 12.98 (s, 1H), 8.38 (s, 1H), 8.17 (d, J = 8.4 Hz, 1H), 7.90 (dd, J = 8.6, 2.4 Hz, 1H), 4.61 (d, J = 2.6 Hz, 2H). LCMS m/z: 263.03 $[M+H]^+$.

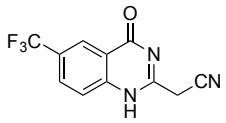

2-(4-oxo-6-(trifluoromethyl)-1,4-dihydroquinazolin-2-yl)acetonitrile

To a solution of 2-(chloromethyl)-6-(trifluoromethyl)-1H-quinazolin-4-one (410 mg, 1.56 mmol) in DMSO (5.0 mL) was added sodium cyanide (153 mg, 3.12 mmol). The mixture was stirred at 25 °C for 3 hour. The mixture was poured into aqueous ammonium chloride, and extracted with ethyl acetate. The organic layer was washed with brine, dried over Na_2SO_4 and concentrated in vacuo. The residue was purified by column chromatography (ethyl acetate/hexane) to give 2-[4-oxo-6-(trifluoromethyl)-1H-quinazolin-2-yl]acetonitrile (145 mg, 573 μmol, 37% yield) as a pale yellow solid. ^{1}H NMR (500 MHz, DMSO-d6) δ 12.83 (s, 1H), 8.37 (s, 1H), 8.16 (d, J = 8.6 Hz, 1H), 7.93

– 7.86 (m, 1H), 4.26 (d, J = 2.6 Hz, 2H). LCMS m/z: 254.13 $[M+H]^+$.

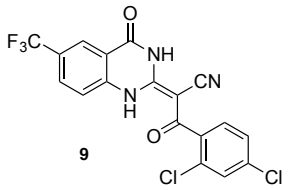

9

(*E*)-3-(2,4-dichlorophenyl)-3-oxo-2-(4-oxo-6-(trifluoromethyl)-3,4-dihydroquinazolin-2(1*H*)-ylidene)propanenitrile (9)

To a mixture of 2-[4-oxo-6-(trifluoromethyl)-3H-quinazolin-2-yl]acetonitrile (145 mg, 573 μmol)in dioxane (4.0 mL) were added 2,4-dichlorobenzoyl chloride (144 mg, 687 μmol) and triethylamine (64 mg, 630umol) at 100 °C . The mixture was stirred for 15 hour at 100 °C. The mixture was poured into water, and extracted with EtOAc. The organic layer was washed with brine, dried over Na_2SO_4 and concentrated in vacuo. The resulting solid was collected by filtration using ethyl acetate to give (2E)-3-(2,4-dichlorophenyl)-3-oxo-2-[4-oxo-6-(trifluoromethyl)-1H-quinazolin-2-ylidene]propanenitrile (159 mg, 373 μmol, 65% yield) as a pale yellow solid. ^{1}H NMR (500 MHz, DMSO-d6) δ 13.66 (s, 1H), 8.23 (s, 1H), 7.91 (d, J = 8.5 Hz, 1H), 7.67 (q, J = 1.9 Hz, 1H), 7.56 (d, J = 8.7 Hz, 1H), 7.47 (tdd, J = 8.8, 5.8, 1.7 Hz, 2H). LCMS m/z: 428.08 $[M+H]^+$.

2. X-ray Crystallography of compounds **1** and **5**: *X-ray crystallography was performed by colleagues at Takeda Pharmaceuticals, Japan.*

For compound **1**, measurements were made on a Rigaku R-AXIS RAPID-191R diffractometer using graphite monochromated Cu-K irradiation. The structure was solved

by direct methods with SIR2008(119) and was refined using full-matrix least-squares on F^2 with SHELXL-2013.(120) All non-H atoms were refined with anisotropic displacement parameters. The solvent area was disordered, no satisfactory model could be refined. This disordered density was taken into account with the SQUEEZE procedure, as implemented in PLATON.(121) For compound **5**, measurements were made on a Rigaku XtaLAB P200 diffractometer using graphite monochromated Cu-K ✔radiation. The structure was solved by direct methods with SIR2008(119) and was refined using full-matrix least-squares on F^2 with SHELXL-2014/7.(120) All non-H atoms were refined with anisotropic displacement parameters. Supplementary crystallographic data for compound **1** and **5** have been deposited in the Cambridge Crystallographic Data Centre (CCDC) with accession numbers CCDC 1510769 (**1**) and CCDC 1510770 (**5**), respectively. These data can be obtained free of charge from the CCDC via the internet: http://www.ccdc.cam.ac.uk/Community/Requestastructure/Pages/DataRequest.aspx?.

ORTEP drawing of **1**, thermal ellipsoids are drawn at 20% probability. Color code: black: carbon; blue: nitrogen; yellow: chlorine; red: oxygen.

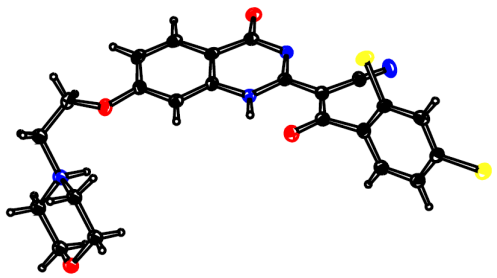

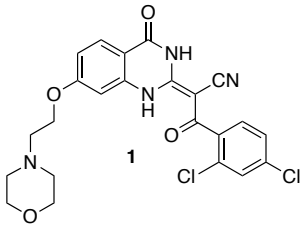

1

Crystal data for **1**: $C_{23}H_{20}Cl_2N_4O_4$, *MW* = 487.34; crystal size, 0.21 x 0.10 x 0.07 mm; colorless, block; monoclinic, space group $P2_1/c$, a = 14.2322(6) Å, b = 6.7917(3) Å, c = 25.2715(18) Å, $\alpha = \gamma = 90°$, β = 90.494(6)°, V = 2442.7(2) Å^3, Z = 4, Dx = 1.325 g/cm^3, T = 100 K, μ = 2.698 mm^{-1}, λ = 1.54187 Å, R_1 = 0.098, wR_2 = 0.201.

ORTEP of **5**, thermal ellipsoids are drawn at 30% probability. Color code: black: carbon; blue: nitrogen; yellow: chlorine; red: oxygen.

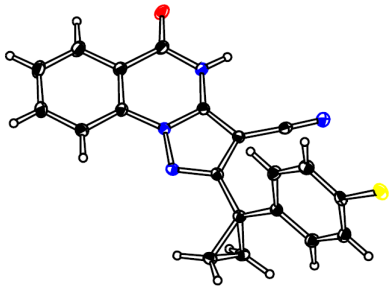

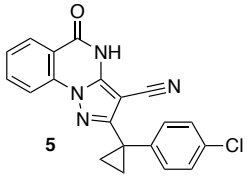

5

Crystal data for **5**: $C_{20}H_{13}ClN_4O$, *MW* = 360.80; crystal size, 0.23 x 0.05 x 0.03 mm; colourless, needle; monoclinic, space group $P2_1/c$, a = 10.32080(19) Å, b = 4.91042(7) Å, c = 34.5332(5) Å, β = 90.6463(16)°, $\alpha = \gamma = 90°$, V = 1750.01(5) Å^3, Z = 4, Dx = 1.369 g/cm^3, T = 100 K, μ = 2.067 mm^{-1}, λ = 1.54187 Å, R_1 = 0.037, wR_2 = 0.096.

3. Protein expression and purification: *I performed all protein purification*.

GFP-human cytoplasmic dynein 2 (AA 1091-4307, uniprot: Q8NCM8), which bears an N-terminal protein A tag, followed by tobacco etch virus (TEV) protease-cleavable linker, followed by a GFP tag, was expressed using the baculovirus/insect cell expression system and purified as described previously(17) with a number of modifications. An Sf9 insect cell pellet was resuspended in lysis buffer (30 mM HEPES pH with KOH to 7.4, 50 mM KOAc, 2 mM $MgOAc_2$, 0.2 mM EGTA, 10% (v/v) glycerol, 300 mM KCl, 0.2 mM ATP, 1 mM DTT and 2 mM PMSF+ protease inhibitor cocktail (cOmplete^{TM} Roche) and lysed using a dounce homonizer. The lysate was clarified by centrifugation at 160,000g and then incubated with IgG-sepharose beads beads for 90 minutes at 4°. The beads were washed with 12 bed volumes of lysis buffer and 12 bed volumes of buffer B (50 mM Tris HCl pH 8.0, 150 mM KOAc, 2 mM $MgOAc_2$, 1 mM EGTA, 10% v/v glycerol, 1 mM DTT, and 0.2 mM ATP). TEV protease was added to the bead slurry and incubated at 4° for 8 hours with rotation. Cleaved soluble protein was collected, concentrated, and loaded onto a gel filtration chromatography column (Superose 6, GE Healthcare). The protein was eluted in buffer C (20 mM Tris HCl pH 8.0, 100 mM KOAc, 2 mM $MgOAc_2$, 1 mM EGTA, 10% v/v glycerol, 1 mM DTT, 50 μM ATP), peak fractions were collected, concentrated, aliquoted, and then frozen in liquid nitrogen.

GFP-human cytoplasmic dynein 1 (AA 1320-4646 with additional valine [at position 4647], uniprot Q14204), which, like the GFP-dynein 2 construct, bears N-terminal protein A tag, followed by a TEV-cleavable linker, followed by a GFP tag, was expressed

using the baculovirus/insect cell expression system and purified using a similar procedure to that described for GFP-dynein 2 with the following modifications:

- The lysis buffer was: 30 mM HEPES (pH 7.5 with KOH), 200 mM NaCl, 1 mM DTT, 1 mM PMSF, protease inhibitor cocktail (Halt™, Thermo).
- Lysis was accomplished by addition of 0.2% triton X-100 followed by incubation on ice for 15 minutes.
- Buffers B and C were replaced with a buffer with the following composition: 50 mM Tris HCl (pH 7.8),150 mM KOAc, 2 mM $Mg(OAc)_2$, 1 mM EGTA, 1 mM EDTA, 10% glycerol, 0.1 mM ATP, 1 mM DTT.
- TEV protease was incubated with the bead slurry for 90 minutes on wet ice without agitation.
- The protein was not concentrated.

6x-His-tagged human cytoplasmic dynein 1 (wild-type, K1912A, K2601A, AA 1320-4646, uniprot: Q14204), proteins which contain N-terminal hexahistixine (6x-His), followed by tobacco etch virus (TEV) protease-cleavable linker were expressed using the baculovirus/insect cell expression system and purified as follows. An Sf9 cell pellet was resuspended in a buffer containing, 30mM HEPES pH 7.6, 200mM NaCl, 10mM imidazole, 1mM TCEP, 2mM PMSF, and protease inhibitor cocktails (HALT, Thermo-Fisher and cOmplete™, Roche) and lysed by the addition of Triton X-100 to a final concentration of 0.2%. The lysate was clarified by centrifugation at 140,000g and then incubated with Ni-NTA beads for 2h at 4°. The beads were washed with 75 bed volumes of lysis buffer and bound proteins were eluted with buffer containing 30mM HEPES pH

7.5, 100mM NaCl, 500mM imidazole, and 1mM TCEP. Eluate fractions containing protein were diluted into buffer B (50mM Tris HCl pH7.8, 150mM KOAc, 2mM $Mg(OAc)_2$, 1mM EGTA, 1mM EDTA, 0.1mM ATP, 1mM DTT) and loaded onto a Mono Q anion exchange column (GE Healthcare). The column was eluted using a salt gradient from 150 to 750mM KOAc over 20 column volumes. Peak fractions were concentrated using a centrifugal concentrator (Amicon) and subjected to size exclusion chromatography on a Superose 6 column using buffer B. For K1912A and K2601A proteins, the ion exchange chromatography step was omitted and NiNTA-eluate fractions were pooled and subjected directly to size exclusion chromatography. Gel filtration revealed a monodisperse peak at an elution volume of 12.2 mL (wild-type) 12.3ml (K1912A), and 12.4ml (K2601A), consistent with the expected molecular weight. Peak fractions were pooled, supplemented with glycerol to a final concentration of 20%, and snap frozen. The protein yield was ~1-2 mg of dynein 1 wild-type or mutants per 1L of Sf9 culture. Cleavage of the TEV-cleavable linker following binding to Ni-NTA beads lead to protein precipitation.

4. Microtubule motility assays: *I performed all microtubule motility assays*

Reaction setup: A coverslip-based motility assay was adapted from similar assays reported previously.(17, 46) A flow chamber assembled on a pre-cleaned microscope coverslide (3-5 μl chamber volume) was hydrated with buffer A (25 mM PIPES, 30 mM KCl, 5 mM $MgCl_2$, 1 mM EGTA, 0.01% Triton X-100, 1 mM DTT, 20 μM taxol, pH 7.0 with KOH). Anti-GFP antibody (0.4 mg/ml, affinity purified rabbit antibody) was flowed into the chamber and allowed to adhere non-specifically to the glass for 20 seconds. The

surface was blocked using 0.5 mg/ml α-casein in buffer A. Excess protein was then washed away with buffer A. GFP-dynein motor domain was diluted in buffer A supplemented with 1 mM DTT and 0.1 mM ATP (2 mM DTT final; GFP-dynein 2 diluted to: 180 nM; GFP-dynein 1 diluted to: 60 nM), flowed into the chamber and allowed to bind for 20 seconds. Excess protein was washed away with buffer A. Reaction mix (25 mM PIPES, 90 mM KCl, 6 mM $MgCl_2$, 1 mM EGTA, 0.01% Triton X-100, 3 mM DTT, 20 μM taxol, 1 mM ATP, 1x oxygen scavenging system components [4.5 mg/ml glucose, 35 μg/ml catalase, 200 μg/ml glucose oxidase], 2% final DMSO [v/v] with compounds at appropriate concentrations, 0.05 mg/ml α-casein, microtubules, pH 7.0 with KOH) was flowed into the chamber using ~4 chamber volumes. For experiments shown in Figure 4 Supplement 1, α-casein concentration in reaction mix was 0.5 mg/ml and all other parameters were held constant.

For reversibility experiments, motility in the presence of 5μM **8** was observed as above, and upon completion of imaging, the chamber, fresh buffer A supplemented with 1mM ATP was flowed into the chamber and incubated for one minute; this wash and incubation cycle was repeated twice. Reaction mix containing DMSO (no compound) was flowed into the chamber using ~4 chamber volumes. The chamber was sealed with valap and returned to the microscope.

Microscopy conditions: Following addition of reaction mix, microtubules were allowed to bind for 5 minutes before imaging. For reversibility experiments, microtubules were allowed to bind for 10 minutes before imaging. Videos were taken on a Zeiss Axiovert

200M wide-field microscope equipped with a Zeiss 100x/1.45 NA α-Plan-Fluar objective. Data were captured with an EM-CCD camera (iXon DU-897, Andor Technology) with a 0.2-second exposure time and frame rate of 0.25-0.5/second. Four 10-20 second videos were captured per experimental condition. Velocities were measured using the kymograph tool in FIJI.(122) Data analysis is discussed below under "8. General data analysis procedures."

5. ATPase Assays: *I performed all ATPase assays*

ATPase activity of dynein

ATPase assays using recombinant Dynein 1 (wild-type and mutants) were performed in a buffer containing 25mM PIPES pH7.0, 30mM KCl, 1mM EGTA, 5mM MgCl2, 0.01% triton X-100, 1mM DTT, and 20-30μM taxol (if microtubules were present). For typical conditions, enzyme was incubated with varying concentrations of inhibitor in buffer containing 2% DMSO for 10 minutes in a volume of 10 µL. When microtubules were present, they were polymerized by stepwise addition of taxol and high concentrations of DMSO (30% final during polymerization reactions), and re-suspended following centrifugation in ATPase buffer to a concentration up to 3-fold above the final concentration used in the reaction. For microtubule-stimulated reactions in dose-response format, reactions were assembled by 1:1:1 mixture of 3x enzyme stock, 3x compound stock (in buffer with 6% DMSO), and 3x microtubule stock to each well. For microtubule-stimulated ATPase assays at tubulin concentrations >2.5μM, enzyme stock was supplemented with compound stock in pure DMSO (resulting in an intermediate DMSO concentration of 6%), and then the microtubule stock was added. Final enzyme

concentrations were 30-100nM for GFP-dynein 1, wild-type 6x-His-dynein 1, and K2601A 6x-His-dynein 1 and up to 500nM for K1912A 6x-His-dynein 1. The final DMSO concentration was 2% in all ATPase assays performed.

Assembled reaction mixtures (including enzyme, compound, and microtubules, if present) were incubated for 10 minutes before addition of ATP. Each ATPase reaction was initiated by addition of 2 μL of a 6x ATP stock containing trace γ-^{32}P ATP (6000 Ci/mmol, 10mCi/mL, Perkin Elmer) and allowed to proceed for a time predetermined to lie within the linear range of the assay (20-30 minutes). For typical conditions, ATP was used at a final concentration of 1 mM. Reactions were quenched by the addition of 12μL 100 mM EDTA, and 2 μL of each quenched reaction was spotted onto PEI-cellulose TLC plates (Millipore). Plates were developed in a glass chamber with a freshly prepared solution of 150 mM formic acid and 150 mM LiCl, dried, exposed to a storage phosphor tray (GE Healthsciences), and scanned on a Typhoon imaging system (GE Healthsciences). The fraction of γ-phosphate hydrolyzed in each condition was quantified using ImageJ.

6. Ultraviolet light and ADP-vanadate-dependent photocleavage of dynein: *I performed all ADP-vanadate photocleavage assays*.

30μL reactions were prepared in 96-well plates as follows. ATPase buffer was supplemented with concentrated stocks of His-dynein 1 (90nM final), compound **8** (4μM final) or an equivalent amount of solvent carrier (3.3% DMSO), followed by a 10 minute incubation at room temperature. ATP (0.1mM final) was added and the mixtures were incubated 5 minutes at room temperature. $NaVO_3$ (0.1mM final) was added and the mixtures were again incubated 5 minutes at room temperature. Vanadate was deliberately

omitted from one well. The plate was then transferred to ice and irradiated with 365 nm light for 15 minutes with the lamp positioned 10cm above the plate (Spectroline Maxima ML-3500S lamp). Following addition of SDS-PAGE loading buffer and heating (95°, 5 minutes), individual reactions were resolved on hand-poured 8% tris-glycine polyacrylamide gels. Gels were stained (Coomassie blue), imaged using a Li-Cor Odyssey, and band intensities were analyzed using FIJI.

7. Assays of hedgehog pathway activity: *Assays of Hedgehog pathway activity were performed by Cristina Santarossa and Lola Yu.*

NIH-3T3 cells stably expressing a luciferase reporter downstream of a Gli binding site (Shh-Light2 cells, RRID: CVCL_2721) were maintained in DMEM with 10% bovine calf serum (BCS). Cells were seeded at a density of 30,000 cells/well in 96-well tissue culture-treated plates (Corning, cat #353072) in 100 µL in DMEM + 10% BCS, and incubated for 48 hours(94). Wells were washed briefly with PBS. Next 100 µL of low serum media (DMEM + 0.5% BCS) containing either 0.2% DMSO, 500 nM of smoothened agonist (SAG), or 500 nM SAG in the presence of serial threefold dilutions of each inhibitor starting from 20 µM were added to the wells. After 28 - 32 hours of inhibitor treatment, cells were washed with 50 µL PBS and lysed for > 30 min in 30 µL Passive Lysis Buffer (Promega Dual Luciferase kit, cat E1910). 5 µL of each lysate was transferred to white, solid-bottom 96-well plates (Greiner, cat #655075), followed by rapid addition (within 30 s) of 30 µL of Luciferase Assay Reagent using a multichannel pipette. Luminescence for each condition was read using a Synergy Neo plate reader (5 s

integration time per well). Cell line identity was confirmed by measurement of the degree of response to Hedgehog pathway stimulation by the synthetic agonist SAG and using previously-published values from our groups and others as references(44, 46).

8. Cytotoxicity assays: *I performed cytotoxicity assays.*

Murine inner medullary collecting duct (IMCD3) cells stably expressing mNeonGreen-IFT88 were maintained in DMEM/F12 supplemented with 10% FBS. Cells were described previously(54) and cell line identity was confirmed by the proper localization and motility of mNeonGreen IFT88 puncta, in reference to published analyses from our groups and from the work of others(54, 96). Cells were seeded in a 96 well plate at a density of 5 x 10^3 cells / well. Following overnight incubation, low-serum media (0.2% FBS) containing solvent control (0.3% DMSO) or compound. At fixed time points, CellTiter-Glo 2.0 (Promega) reagent was added to the wells, mixed by pipetting, and transferred to a white, opaque 96 well plate. After a 10-minute incubation, luminescence for each condition was read using a Synergy Neo plate reader (1 s integration time per well).

9. Intraflagellar transport assays: *Intraflagellar transport assays were performed by Cristina Santarossa.*

Murine inner medullary collecting duct (IMCD3) cells stably expressing mNeonGreen-IFT88 were maintained in DMEM/F12 supplemented with 10% FBS. Cells were typically passaged fewer than 10 times following thawing of frozen stocks. Cells were described previously(54). 6 x 10^5 cells were seeded onto 22mm coverslips in a 6 well

plate and incubated for 24 hours at 37°C. The media was then replaced with DMEM/F12 + 0.2% FBS and cells were incubated 24 hours to promote cilium formation. Immediately prior to imaging, media was replaced with phenol red-free media (Leibovitz's L-15 + 0.2% FBS) containing either carrier solvent control (0.3% DMSO) or compound. IFT88 transport was observed using a TE2000-E spinning disk confocal microscope (Nikon PlanApo 100x/1.45 objective lens) fitted with a Photometrics Cascade II (EMCCD 512) camera and imaged at a frame rate of 2 frames/second. Kymographs were generated in ImageJ using *KymographClear* and the velocities of mNeonGreen-IFT88 foci movements were quantified by *KymographDirect*(97).

For washout experiments, cells were exposed to a 5 minute compound treatment as described above. Cells were then washed twice with 5 mL of L-15 supplemented with 10% FBS (or 0.2% FBS) and 0.3% DMSO. A five minute incubation followed each wash. For short term washout experiments, imaging was performed as described above immediately after the second five minute wash and incubation step had been completed. For longer-duration washout experiments, following the second wash incubation, cells were incubated at 37° a further 50 minutes and then imaged.

10. Lysosome motility assays: *These assays were performed by Dr. Anna Serpinskaya and Dr. Vladimir Gelfand at Northwestern University.*

CAD cells (catecholaminergic neuronal tumor cell line, RRID:CVCL_0199) were maintained in DMEM/F12 medium with 10% Fetal Bovine Serum(100). Cell line identity was confirmed by the morphological response to serum withdrawal (i.e. neurite formation), a previously-documented characteristic of this cell line(100). 24 hours before

the experiment cells were plated on coverslips in serum-free medium to induce neurite formation. Cells were treated with inhibitors or control solvent (0.1% DMSO final in all experiments) for 60 min, then lysosomes were labeled with 0.1 μM (final concentration) LysoTracker Red DND-99 (Molecular Probes) and used for microscopy immediately after LysoTracker addition.

Microscopy was performed using a Nikon TE-2000 inverted microscope equipped with a LED X-Cite illuminator (Lumen Dynamics) at 37 degrees. Images were acquired with a Hamamatsu ORCA-Flash 4.0 camera driven by MetaMorph software at a rate of 1 frame per second for 1 minute. Lysosome motility in neurites was analyzed using Diatrack software (http://www.diatrack.org/), particle velocities were measured from frame to frame and the total length of trajectories divided by the number of analyzed organelles was calculated for every experimental condition.

11. General data analysis procedures:

Microtubule velocity measurements: the tracks of microtubules were traced and converted to kymographs (x axis-displacement, y axis-time) using the kymograph function of FIJI (RRID: SCR_002285). The angle formed between an edge of a microtubule and the horizontal was measured. This angle, θ, was converted into velocity using the following relationship:

$$\text{velocity} = 1/|\text{tangent}(\theta)| * (\text{unit pixel distance})/(\text{time interval between frames})$$

The calibrated pixel distance was 0.152 μm and the time interval between frames was either 2 or 4 seconds. The velocities of at least 7 microtubules were measured per field of view, if sufficient tracks could be found. In cases where fewer than 7 microtubules were found in a field of view, velocities of all microtubules on the coverslip were measured. ~30 microtubule velocities were measured for a given condition and their mean was reported as the average microtubule velocity.

Microtubule number counting: The number of microtubules bound to a coverslip in the first frame of a movie were counted manually.

Curve fitting: Where dose-response experiments are fit and IC_{50}values given, these are obtained as follows: Individual experiments are treated as separate. The data are fit to a sigmoidal dose-response curve of the form (Y=Bottom + (Top-Bottom)/(1+10^((LogIC50-X)*HillSlope)). All variables were allowed to float freely with the exception of the variable denoted "bottom", which was constrained to be > 0. The separate IC_{50} values obtained from fits to each individual experiment's dataset were averaged together and presented as a mean with range (Figure 3G, 3H) or standard deviation (Figure 3I, 5D, 6E, 6K).

Statistical analysis of intraflagellar transport frequencies: Run frequencies output directly from *KymographDirect* were tabulated across all cilia imaged in a given condition (see Figure 4, Figure Supplement 2). For each of two experimental conditions (5μM **8**, 10μM **8**) and the respective controls, an un-paired T-test was performed for the difference of

means control and compound treatment. This analysis was performed for each direction of motion.

Quantification of ADP-vanadate dependent photocleavage of dynein was performed as follows: Scanned gels were analyzed with FIJI, and fraction cleaved quantified as follows:

Fraction cleaved = (intensity of band at 250kDa) /

(intensity of band at 250kDa + intensity of band at ~350kDa)

Chapter 3:

Dynapyrazole and its chemical derivatives inhibit dynein via distinct mechanisms

Note to readers: the results discussed below arose from a collaborative effort between myself and several colleagues in the Kapoor Lab and at the Tri-Institutional Therapeutics Discovery Institute (TDI). I have included this work as it helps explain the rationale of my work and supports the conclusions I draw. In the body of the text and in the methods section, I have noted who performed each experiment. I have also noted this information in the figure legends, where appropriate. Except for experiments credited explicitly to others, I performed all experiments and analysis.

3.1 Introduction

While the dynapyrazoles constitute a step toward the improvement of cytoplasmic dynein 1 and 2 antagonists, a number of limitations remain. The activity of dynapyrazoles is reduced in settings with high protein concentrations, which restricts their use in many cell culture settings, where the use of serum is often required. Furthermore, the potency of dynapyrazoles A and B remains modest, with concentrations in the 3-10μM range typically required to observe cellular phenotypes. Cytotoxicity is another limitation of the dynapyrazoles. Treatment at a dynapyrazole A concentration of 15μM depletes cellular ATP levels within hours. This toxicity may represent an inherent limitation of inhibition of cytoplasmic dynein 1, which plays multiple roles in cellular physiology(123). A consequence of the cytotoxicity is that it limits the window of time and the concentration range over which these compounds can be used to study the cell-biological roles of the cytoplasmic dyneins.

3.2 Chemical analysis of ciliobrevins and dynapyrazoles inform synthesis of new inhibitors

As a first step toward addressing the liabilities of the dynapyrazoles, I sought to identify dynapyrazole derivatives with improved potency. I revisited the chemical analysis that led to the design and synthesis of this compound class, incorporating structure-activity data from both the ciliobrevins and its pyrrolo- and pyrazoloquinazolinone derivatives(46, 47, 124). The structure-activity-relationship analysis of the ciliobrevin and pyrrolo/pyrazoloquinazolinone scaffolds with respect to cytoplasmic dynein 2, as judged by inhibition of purified proteins or of the Hedgehog signaling pathway, is summarized in Figure 3.1. Overall, the structure-activity-relationship landscape for the ciliobrevin scaffold showed that substitutions of the nitrile or the carbonyl groups at C4 and C10 led to loss of inhibition (Figure 3.1A). Modifications at the D ring were tolerated only if they retained halogens at the 2 and 4 positions of the ring. Compounds with modifications at C6 and C7 were generally active inhibitors some had improved potency and selectivity(47). A caveat to interpreting these data is that it is unknown whether any of these changes alter the preferred olefin isomer at C2-C9

In contrast, fewer analogs in the pyrrolo/pyrazoloquinazolinone compound series have been synthesized, making analysis of structure-activity-relationship trends more difficult. Features that could be assigned as important for activity include a nitrogen at position 11, without which inhibition of dynein 2 was abolished, and the cyclopropyl-phenyl substituent at C10, which improved inhibition relative to the 2,4-dichlorphenyl substituent at the same position (See data in Chapter 2). A pyrazoloquinazolinone lacking

a nitrile at C9 inhibited dynein 2, however the contribution of the nitrile group in the context of more potent compounds such as dynapyrazoles A and B was not assessed. Synthesis and testing of additional analogs will be required to more clearly assign the fragments of the dynapyrazole scaffold that are critical for dynein inhibition.

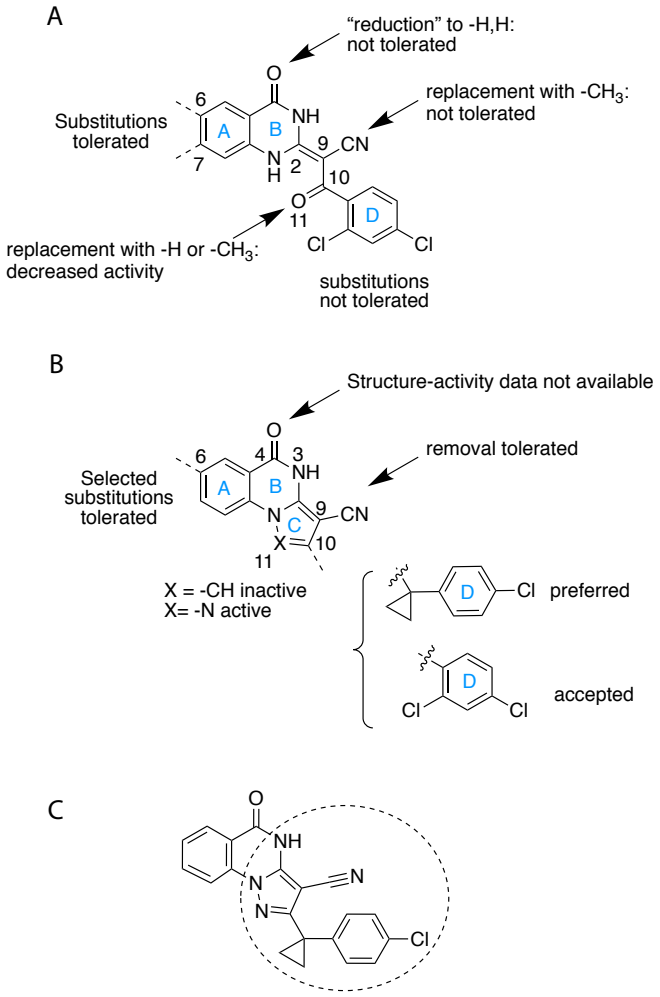

Figure 3.1 Analysis of ciliobrevin and dynapyrazole structure-activity trends and proposed core pharmacophore. (A) Ciliobrevin compounds and activity trends with position numbers indicated. (B) Dynapyrazole componds and activity trends with position numbers indicated. (C) The chemical structure of the dynapyrazoles, with dotted circle indicating proposed aminopyrazole-cyclopropyl-chlorophenyl pharmacophore. (A) and (B) are based on analysis of data from Firestone *et al*., See *et al*., and Chapter 2.

As analysis of the effect of specific substitutions on dynapyrazoles did not give rise to predictions for how to improve compound potency, likely because too few analogs were available for analysis, I next examined the differences between the ciliobrevin and dynapyrazole scaffolds. When substitutions at the A and B rings were held constant, the a compound with the pyrazoloquinazolinone-cyclopropyl-chlorophenyl scaffold (dynapyrazole B) inhibited dynein 2 ~6 fold more potently than the comparable ciliobrevin derivative (Figure 2.3H, Chapter 2). This key observation suggested that the cyclopropyl-chlorophenyl substituted cyano-aminopyrazole fragment of the dynapyrazoles may constitute an improved pharmacophore for dynein inhibition relative to the benzoylarylonitrile of the ciliobrevins (proposed pharmacophore highlighted in Figure 3.1C). This fragment contains or mimics several of the elements of the ciliobrevin scaffold identified as important for inhibition. However, the spatial relationship among these groups differs slightly (Chapter 2, Figure 3D), which could account for improved inhibition, as has been observed previously in efforts increase inhibitor potency by synthesis of geometrically constrained derivatives(117).

This chapter describes progress toward improved derivatives of the dynapyrazoles discovered through a chemical-synthesis campaign focused on elaboration of the proposed aminopyrazole pharmacophore. The biochemical mode of inhibition of dynein by these dynapyrazole derivatives is analyzed and compared with that of the dynapyrazole A. The majority of synthesis was conducted in collaboration with our colleagues at the Tri-Institutional Therapeutics Discovery Institute (TDI). This effort led to biochemical and structural characterization of a new pyrazolo-pyrimidinone dynein inhibitor, which is discussed in this chapter.

3.3 Identification and biochemical characterization of TDI 3016

To test if aminopyrazole-containing dynapyrazole derivatives could more potently inhibit dynein, a set of compounds bearing a 3-alkyl, 4-cynao, 5-amino pyrazole core were synthesized. AP-1 was identified as a starting point for compounds containing this aminopyrazole core, a synthetic route was developed to bicyclic derivatives with a dihydropyrazolo[1,5-*a*]pyrimidine-3-carbonitrile core (Figure 3.2A; synthesis was performed by colleagues at the TDI). 20 compounds in this series (2μM) for were tested for inhibition of Hedgehog pathway activity using a Gli-driven luciferase reporter system that has previously been used to identify and characterize inhibitors of cytoplasmic dyneins (Figure 2B, compound structures and screening data are tabulated in Appendix Table 3.1, Hedgehog assays were performed by Lola Yu and Cristina Santarossa, technician and graudate student in the Kapoor Laboratory)(46, 124). Within this series, compounds with aryl or aryl-ether substitutions at the 6 position of the pyrazolopyrimidine core were identified as the strongest inhibitors of Hedgehog pathway activity. The most potent compound in this series, TDI 3016, inhibited Hedgehog pathway activity with an IC_{50} of 1.57 ± 1.2 μM (Figure 3.2C, mean ± S.D., n = 3.).

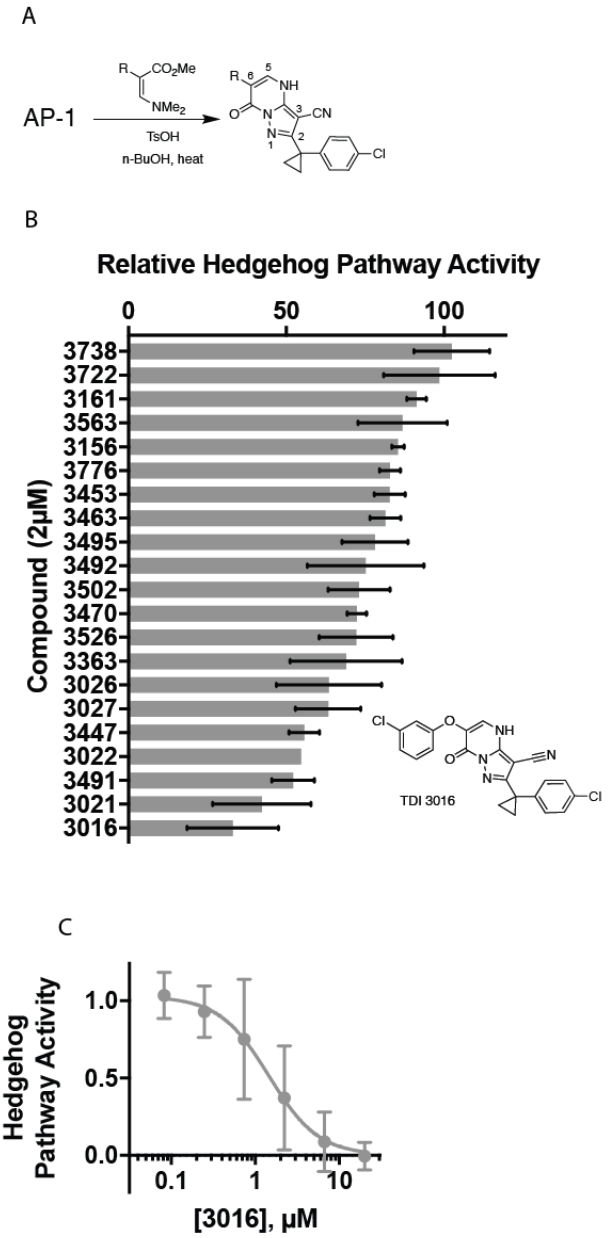

Figure 3.2 Synthesis and testing of pyazolopyrimidine-containing dynapyrazole derivatives. *Note: experiments shown in this figure were performed by others. Synthesis was performed at the TDI. C. Santarossa and L. Yu performed Hedgehog pathway assays.* (A) Synthesis of bicyclic dynapyrazole derivatives from common precursor AP-1. TsOH: paratoluenelsulfonic acid. n-BuOH: n-butanol. (B) Effect of bicyclic dynapyrazole derivatives of Hedgehog pathway activity in a Gli-driven luciferase reporter assay system. Compounds were tested at 2μM. Data are mean ± range of n = 2 independent experiments. The structure of TDI 3016 is shown. Appendix 3.1 shows structures of individual compounds showin in historgram. (C) Analysis of Hedgehog pathway inhibition by TDI 3016. Data are mean ± S.D. of n = 3 separate experiments and were fit to a sigmoidal dose-response curve using Prism. Data for this figure were generated by collaborators.

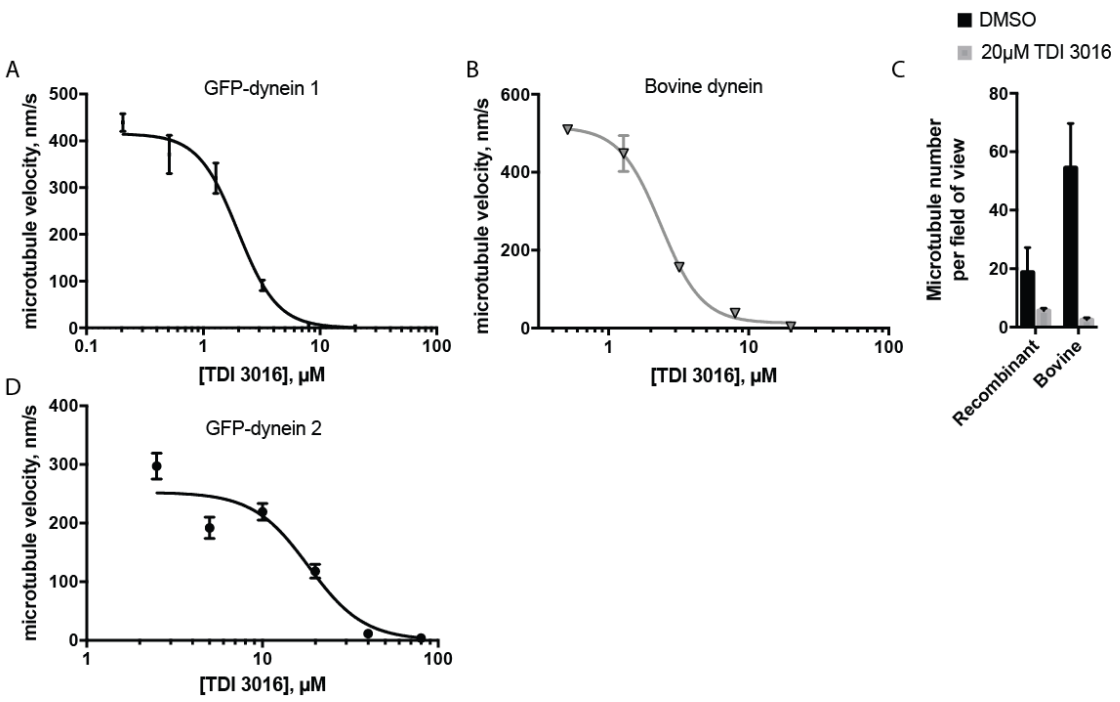

Figure 3.3 Effect of TDI 3016 on dynein 1-driven microtubule glding. Inhibition of (A) recombinant GFP-dynein-1 or (B) bovine dynein 1-driven motility by TDI 3016. Data are mean ± range of n = 2 separate experiments and were fit to a sigmoidal dose-response curve using Prism. (C) Analysis of the number of microtubules associated with coverslips in microtubule gliding assays. The number of microtubules was counted in four separate fields of view in each experiment. (D) Inhibition of recombinant GFP-dynein 2-driven motility by TDI 3016. Data are mean ± range of n = 2 separate experiments and were fit to a sigmoidal dose-response curve using Prism. Motility assays in (A) and (B) were performed at 1mM MgATP and 0.05mg/ml casein, while those in (D) were performed at 2mM MgATP and 0.5mg/ml casein.

3.4 Analysis of TDI 3016 in biochemical assays

Several biochemical assays were used to characterize the effect of TDI 3016 on cytoplasmic dynein 1. This dynein isoform was selected for comparison because it is a model for dyneins in general and results could be compared to previous analyses of the ciliobrevins and the dynapyrazoles. Microtubule gliding assays were used first, as they represent a biochemical reconstitution of dynein's cellular function, namely, to drive motion along microtubules. Subsequently, the effect of TDI 3016 on dynein's ATP hydrolysis was assessed using both wild-type and mutant dynein constructs. Finally, the effect of this compound on ADP-vanadate-dependent photocleavage of dynein by ultraviolet light was tested. This assay enables dissection of the effect of nucleotide engagement at dynein's AAA1 ATPase site. Together, these assays can illuminate the mode of dynein inhibition, and were previously used to demonstrate that Dynapyrazole A and ciliobrevins inhibit dynein via a distinct mechanism (Chapter 2).

In the microtubule gliding assay, recombinant human dynein motor domains or purified bovine brain dynein are immobilized to glass coverslips. Addition of microtubules and ATP leads to translocation of microtubules toward their plus-ends as a consequence of ensembles of dynein heads moving toward the minus ends. I first assessed the effect of TDI 3016 on microtubule motion driven by recombinant human dynein 1 motor domain with an N-terminal GFP tag (GFP-dynein). Under solvent control conditions (1mM ATP, 2% DMSO), this enzyme moved microtubules with an average velocity of 434 nm/s (432-436, n = 2), in line with previous analyses (Chapter 2, Figure 2.5C). TDI 3016 (0.2-20μM) blocked GFP-dynein 1-driven microtubule gliding with an IC_{50} of 2.0μM (1.9-2.1, n = 2, Figure 3.3C). A decrease in the number of microtubules

bound to the coverslip was noted at higher concentrations of TDI 3016, in contrast to previous observations with dynapyrazole A in similar assays (Figure 3.3C).

I next tested the effect of TDI 3016 on microtubule gliding driven by bovine dynein. This preparation from brain extracts contains full-length dynein (~4600 amino acids, ~500KDa) and ~10 accessory factors(125). In this setting, dynein is expected to exist as a complex containing two heavy chains and several accessory proteins (molecular weight >1MDa). However, despite the differences between this preparation and the GFP-dynein 1 preparation, bovine dynein drives microtubule guiding at 537nm/s (518-556, n = 2, Figure 3.3B), a velocity comparable to the isolated recombinant GFP-dynein 1 motor domain. Microtubule gliding driven by bovine dynein was inhibited by TDI 3016 with an IC_{50} of 2.4μM (2.3-2.5, n = 2). The number of microtubules bound to the coverslide was decreased at high TDI 3016 concentrations (20μM). A similar pattern was observed for inhibition of GFP-dynein 2-driven microtubule gliding, namely, that the number of microtubules bound to the coverslip was decreased at concentrations of TDI 3016 at or above 20μM. The IC_{50} for inhibition of dynein 2 by TDI 3016 was 16μM (14.5-17.5, n = 2, Figure 3.3D), however this value is not directly comparable to the values measured for dynein 1, as the assays were performed at higher [ATP] and higher [casein], and the latter has caused 3-5-fold decreases in potency for related compounds (e.g. dynapyrazole A), as may be expected for compounds with high ClogP values (ClogP for TDI 3016: 4.2). If microtubule binding were suppressed by TDI 3016, then it is possible that the decrease in microtubule velocity is related to a decrease in the number of available binding sites. Such a decrease in binding sites has been shown to reduce microtubule gliding velocity even if the translocation rate associated with any individual dynein motor is not

reduced(126, 127). In order to dissect the contribution of dynein-microtubule affinity changes caused by TDI 3016 from direct effects on dynein-driven microtubule gliding velocity, it will be necessary to perform a deeper biophysical analysis that allows the direct measurement of binding affinity.

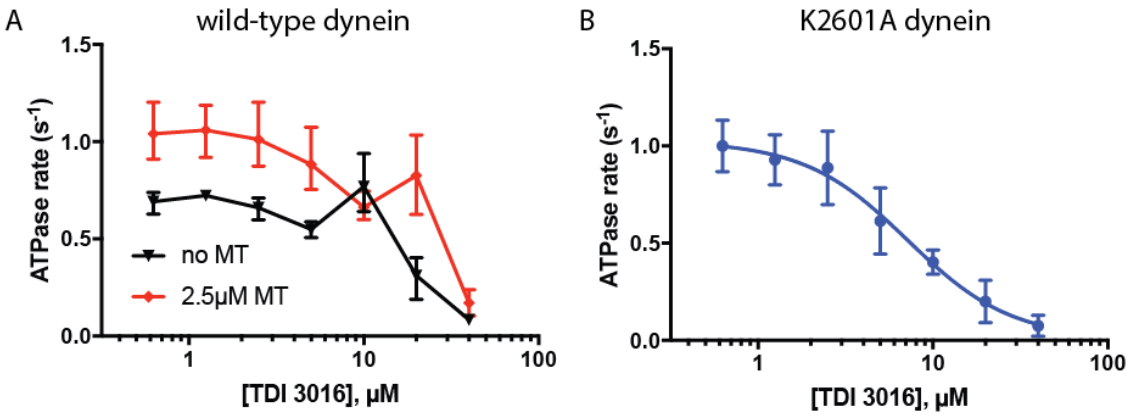

Figure 3.4 Effect of TDI 3016 on the ATPase activity of dynein 1. (A) Dose-dependent inhibition of basal (black) and microtubule-stimulated (red) ATPase activity of wild-type His-dynein 1 by TDI 3016. (B) Dose-dependent inhibition of AAA3 mutant His-dynein 1 by TDI 3016. Data are mean ± S.D. of n = 3 experiments and were fit to a sigmoidal dose-response curve in Prism. ATPase assays were performed at 1mM Mg-ATP and 2% DMSO.

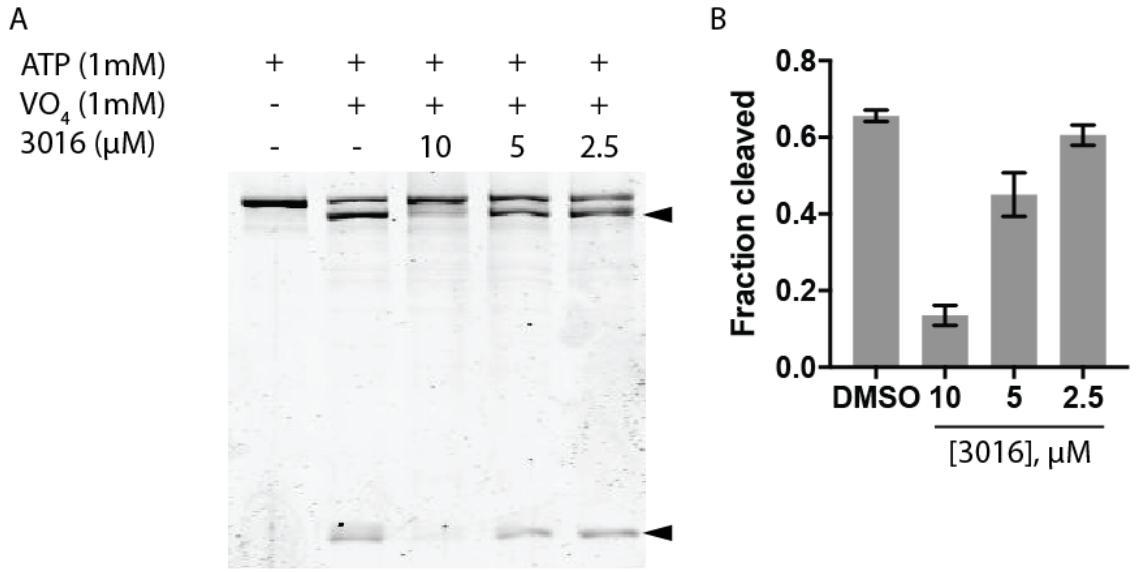

Figure 3.5 Effect of TDI 3016 on ADP-vanadate-dependent photocleavage of dynein 1. (A) SDS-PAGE analysis (Coomassie blue) of dynein 1 following irradiation with ultraviolet light at 365nm. Components of reaction loaded into each lane are noted above gel. Arrowheads indicate proteolysis products. (B) Analysis of gel band intensity for photocleavage reactions.

While microtubule gliding assays report on dynein's ability to cause directional motion of microtubules, they do not directly reflect ATP hydrolysis rates. I therefore analyzed the effect of TDI 3016 (0.6-40μM) on the basal and microtubule-stimulated ATPase activities of an N-terminally hexahistidine tagged human dynein 1 motor domain (His-dynein 1). Doses up to 10μM did not decrease His-dynein 1's basal ATPase activity, but higher concentrations (20μM and 40μM) reduced the basal activity to $0.31 \pm 0.11 s^{-1}$ and $0.06 \pm 0.02 s^{-1}$, respectively (Figure 3.4A). Microtubules (2.5μM) stimulated dynein's ATPase activity to $\sim 1 s^{-1}$. TDI 3016 (0.6-40μM) reduced dynein's microtubule-stimulated ATPase activity, with inhibition to a rate of $0.2 s^{-1}$ at the highest concentration tested (40μM). It is notable that, in the presence of microtubules, an intermediate concentration of TDI 3016 (10μM) reduced dynein's ATPase activity to $0.66 \pm 0.08 s^{-1}$, a value similar to the basal ATPase rate ($0.68 \pm 0.03 s^{-1}$, Figure 3.4A). Next, I tested whether TDI 3016 inhibits a dynein 1 construct with a Walker A lysine-to-alanine mutation in its AAA3 binding site. The basal ATPase activity of this construct is expected to arise mostly from hydrolysis at AAA1(20, 89). TDI 3016 inhibited this mutant with an IC_{50} of $6.7 \pm 0.7\mu$M (Figure 3.4B, n = 3, mean ± S.D.) For another compound with a similar scaffold, TDI 4692, I observed similar patterns of biochemical activity with ~3-4 fold higher potency (Data presented in Appendix 3.2). As it was not consistently active in cell-based assays, this compound is not likely to be suitable as a probe for dynein, and subsequent analysis focused on TDI 3016.

To further examine the mechanism of dynein inhibition by TDI 3016, I assessed whether it blocks ADP-vanadate-dependent photocleavage. Thas assay has previously utilized to monitor nucleotide engagement at dynein's AAA1 ATPase site(20, 46, 106,

124). When dynein was treated with control solvent (3% DMSO) and incubated with 1mM ATP and 1mM vanadate, 15 minute ultraviolet irradiation caused 66 ± 1% cleavage (3.3A, B, n = 3, mean ± S.D.). Pre-treatment with TDI 3016 (10μM) reduced photocleavage to 13 ± 3%. Lower concentrations of TDI 3016 blocked photocleavage to a lesser degree (3.5A, B).

3.5 Negative stain electron microscopy analysis of the effect of compounds on dynein structure

Decades of research into the structure of dynein have shed light on a series of mechanical movements of domains within the dynein heavy chain and illustrated how these are coupled to and regulated by nucleotide occupancy at dynein's ATPase sites, primarily AAA1(8, 86). The linker region of dynein has been identified as central element in dynein's chemomechanical cycle. This bundle composed primarily of overlapping α-helices emanates from the AAA ring of dynein, crosses above it, making interactions with AAA subdomains, and then extends toward the N-terminal tail of dynein. A key step in dynein's chemomechanical cycle is the "power stroke" in which the linker transitions from a bent, "pre-powerstroke" geometry, to a straight "post-powerstroke" geometry. ATP binding at AAA1 is proposed to induce the bent pre-powerstroke state, while phosphate release following ATP hydrolysis is associated with straightening of the linker(86). The combination of this linker motion with binding and unbinding to the microtubule track (also a nucleotide-state-dependent process) leads to overall translocation of dynein and its cargo.

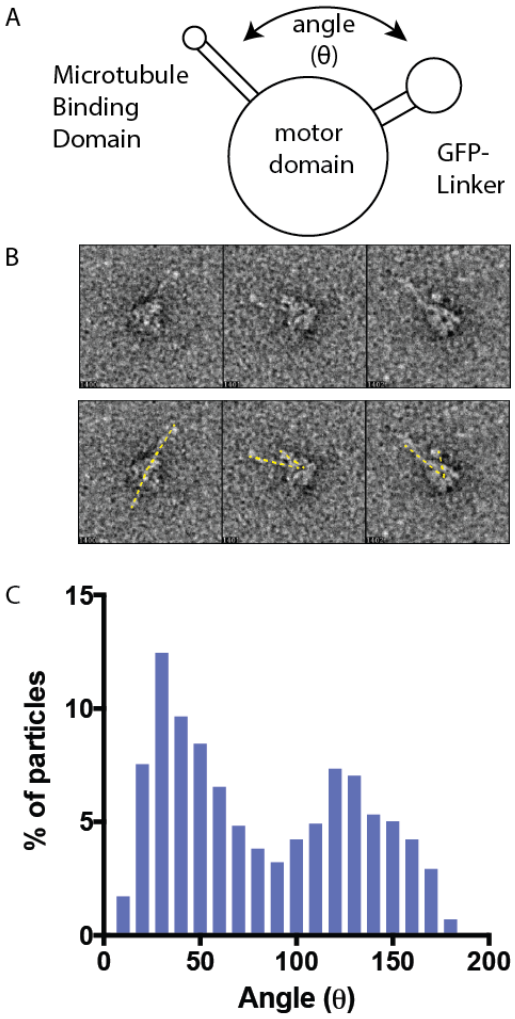

Figure 3.6 Structural analysis dynein using negative stain electron microscopy. *Electron microscopy grid preparation and image acquisition were performed by Zhen Chen (graduate student in Kapoor Laboratory).* (A) Schematic depiction of the dynein motor domain illustrating the protruding microtubule binding domain and GFP-linker. (B) Images from negative stain electron microscopy. GFP-dynein 1 was pre-incubated with control solvent (0.5% DMSO), ATP (1mM), and sodium vanadate (1mM) before fixation. Top row: raw images of individual particles. Bottom row: vector pointing to each protrusion is emphasized in yellow. The angle between these two vectors is measured. (C) Histogram showing distribution of angles. θ was measured for 1000 particles.

Structural studies using negative stain electron microscopy provided an early view into this nucleotide state-dependent regulation of dynein's conformation(128). The microtubule binding domain and the linker/tail of dynein protrude from the ring-shaped AAA domain. Using a GFP-labeled dynein motor domain construct with a ~500 amino acid long linker, it is possible to observe both structures emanating from the AAA+ ring by negative stain electron microscopy and measure the angle between them (θ, Figure 3.6A). Previous studies have shown that the nucleotide-free (apo) and ADP-bound states are characterized by a small θ (~40°), which corresponds with a post-powerstroke linker state(128). In contrast, binding of ADP-vanadate, an ATP hydrolysis transition-state mimetic, is associated with a bimodal distribution of θ, with peaks at ~40° and ~145° in an approximate ratio of 3:2, with the large-angle component reflecting the pre-powerstroke state of dynein. I sought to use a similar electron microscopy-based assay to determine the impact of compound treatment on the chemomechanical cycle of dynein. I performed electron microscopy on GFP-dynein 1 samples stained with uranyl formate (Figure 3.6B, all electron microscopy image acquisition and grid preparation was performed by Zhen Chen; I performed image analysis and sample preparation). In the ADP-V state (obtained by incubation with 1mM ATP and 1mM Na_3VO_4, solvent control: 0.5% DMSO), I observed a bimodal distribution of angles, with one peak at 37° accounting for ~60% of particles and a second peak at 125° accounting for the remaining 40% of particles (Figure 3.4C). These distributions are similar to those previously observed for dynein 1 from dictyostelium(128).

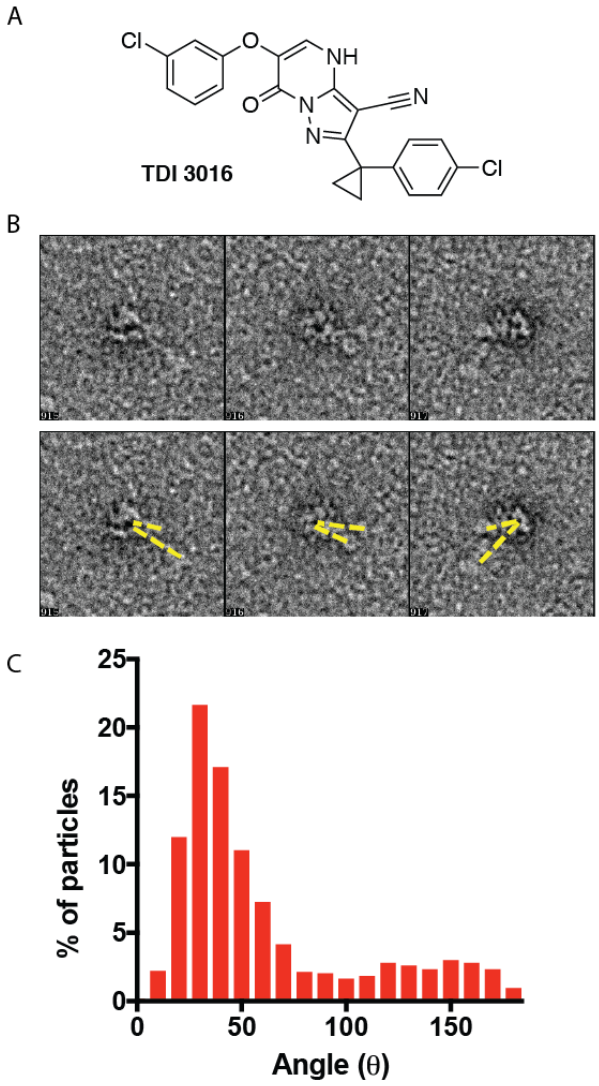

Figure 3.7 Analysis of the effect of TDI 3016 on dynein structure using negative stain electron microscopy. *Electron microscopy grid preparation and image acquisition were performed by Zhen Chen (graduate student in Kapoor Laboratory).* (A) Structure of TDI 3016. (B) Images from negative stain electron microscopy. GFP-dynein 1 was pre-incubated with TDI 3016 (10μM), ATP (1mM), and sodium vanadate (1mM) before fixation. Top row: raw images of individual particles. Bottom row: vector pointing to each protrusion is emphasized in yellow. The angle between these two vectors is measured. (C) Histogram showing distribution of angles. θ was measured for > 1000 particles.

I next analyzed the effect of TDI 3016 and dynapyrazole A on the structure of GFP-dynein 1. Dynein was treated with TDI 3016 (10μM) before addition ATP and vanadate and subsequent fixation. The angle separating the two protrusions was measured for ~1000 particles. A unimodal distribution of angles was observed, with a peak frequency at ~35° (Figure 3.7C). 79.7% of particles had $\theta < 90°$. In contrast, for the solvent control condition, 58.3% of particles had $\theta < 90°$. The distribution of angles between the microtubule binding domain and liker of dynein 1 in the presence of TDI 3016 and ADP-vanadate was similar to that observed by others for ADP- and apo-states, and are in line with the observation that this compound blocks ADP-vanadate dependent photocleavage of dynein (Figure 3.5). (A comparable experiment performed for TDI 4692 and a similar structural effect was observed, see Appendix 3.2.) Taken together, these data suggest that TDI 3016 prevents dynein from adopting a pre-powerstroke geometry.

A similar analysis was performed for dynapyrazole A. Unlike TDI 3016, the distribution of angles was bimodal, with frequency peaks at ~37° and ~140° (Figure 3.9C). 49.0% of particles had microtubule binding domain-linker angles < 90°, a value slightly smaller than observed in the solvent control. The bimodal distribution of angles suggested that dynapyrazole A did not block the ability of dynein to adopt a pre-powerstroke geometry, which was unexpected, as this compound also blocked ADP-vanadate dependent photocleavage. Experiments are ongoing to determine the effect of both dynapyrazole A and TDI 3016 on the geometry of dynein 1 in other nucleotide states.

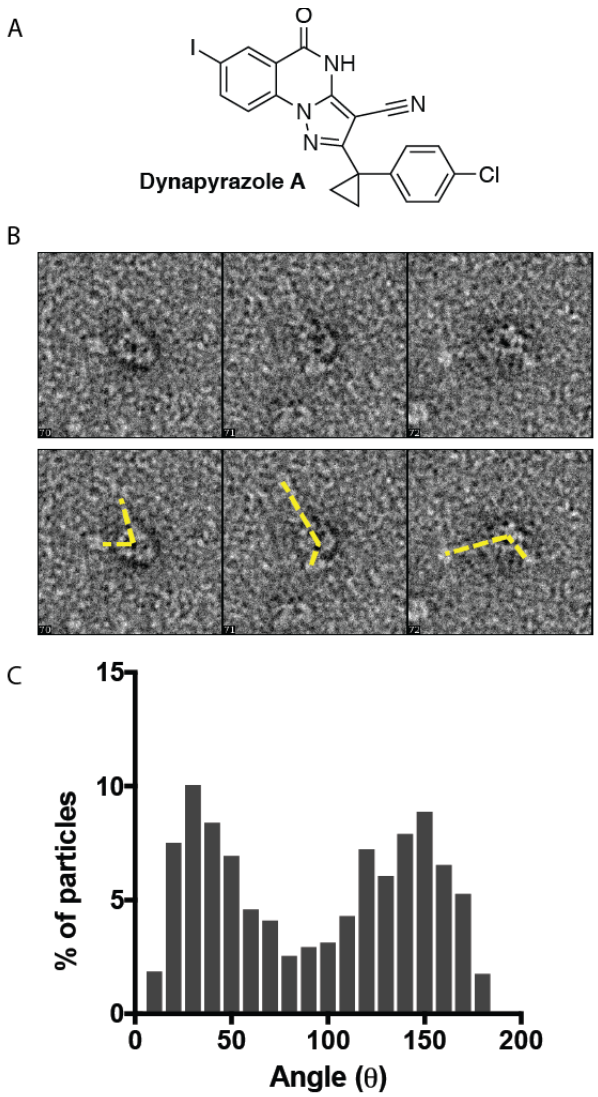

Figure 3.8 Analysis of the effect of dynapyrazole A on dynein structure using negative stain electron microscopy. *Electron microscopy grid preparation and image acquisition were performed by Zhen Chen (graduate student in Kapoor Laboratory).* (A) Structure of dynapyrazole A. (B) Images from negative stain electron microscopy. GFP-dynein 1 was pre-incubated with dynapyrazole A (10μM), ATP (1mM), and sodium vanadate (1mM) before fixation. Top row: raw images of individual particles. Bottom row: vector pointing to each protrusion is emphasized in yellow. The angle between these two vectors is measured. (C) Histogram showing distribution of angles. θ was measured for > 1000 particles.

3.6 Discussion

The work described in this chapter centers on the re-analysis of the structure of the dynapyrazoles. These compounds, in turn, were synthesized as part of an effort to create "locked" derivatives of the first cell-permeable dynein inhibitors, the ciliobrevins. In considering the fusion of isomerizable benzoylacrylonitrile scaffold of the ciliobrevins as a pyrazoloquinazolinone that could not isomerize, it was assumed that the spatial relationship between all four newly-formed rings (A-D, see figure 3.1B) was necessary for dynein inhibition. The results obtained in this chapter challenge this assumption and suggest instead that the cyanoaminopyrazole-cyclopropyl group-phenyl ring system (C-D rings in the dynapyrazole nomenclature) is essential for dynein binding and that structural variation is tolerated at the sites of the A and B rings. In combination with the previous findings for the dynapyrazole scaffold, I now find that two different heterocyclic scaffolds based on this cyanoaminopyrazole core have bioactivity consistent with dynein 1 inhibition, as summarized in Figure 3.7. The biochemical and structural analyses performed for these compounds suggest that the mechanism of inhibition by these two compound classes are different. A caveat to the classification proposed in Figure 3.7 is that these trends have been established across a limited subset of compounds within a given structural class. Comparison of more compounds within each scaffold class would be required in order to better demarcate the boundaries between the two classes and the structural determinants of the two different patterns of bioactivity shown in Figure 3.9.

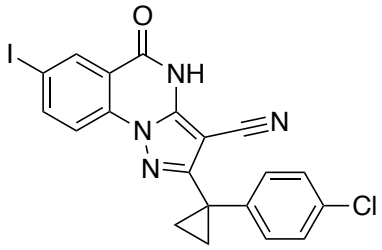

Dynapyrazole A

-Hedgehog pathway inhibition
-Intraflagellar transport inhibition
-Lysosome motion inhibition
-Cytotoxic
-ATPase inhibition to basal level (dynein 1 IC_{50} ~5μM)
-Microtubule gliding inhibition (dynein 1 and 2 IC_{50} ~3μM)
-EM: no effect on distribution of angles in ADP-V state.

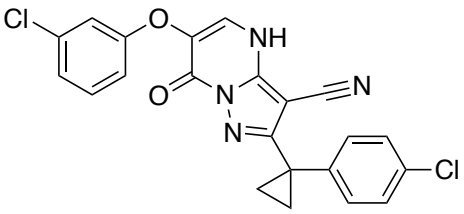

TDI 3016

-Hedgehog pathway inhibition
-Cytotoxic
-ATPase inhibition to near-zero (dynein 1)
-Microtubule gliding inhibition (dynein 1 IC_{50} ~2μM)
-EM: blocks ADP-V induced change in dynein structure.

Figure 3.9 Overview aminopyrazole-containing dynein inhibitors.

The set of bicyclic compounds similar to TDI 3016 inhibit the Hedgehog pathway and block dynein 1 and 2 *in vitro* in a number of assays, but show biochemical behavior separate from that of the dynapyrazoles. (Another compound with a similar bicyclic scaffold showed similar activity, see Appendix 3.2.) The most prominent difference between these compounds is their effect on the structure of dynein, as observed by negative stain electron microscopy. TDI 3016 caused the enzyme to be locked in an ADP or apo-like state in the presence of ATP and vanadate. In contrast, dynapyrazole A did not substantially alter the distribution of dynein geometries compared to the DMSO control in the ADP-vanadate state; experiments in other nucleotide states will be required to observe whether this compound alters dynein's structure. Other biochemical assays were also consistent with different mechanisms of inhibition. For instance, while the dynapyrazoles inhibit the microtubule stimulated ATPase activity dynein to a residual activity of ~0.5s^{-1} and do not show substantial inhibition of the basal activity (at concentrations up to 40μM), TDI 3016 inhibits both the basal and microtubule-stimulated ATPase activity to nearly zero at high concentrations (e.g. 40μM). Furthermore, while the dynapyrazoles inhibit motility, ADP-vanadate dependent photocleavage, and microtubule-stimulated ATP hydrolysis at low-micromolar concentrations (~3-5μM), TDI 3016 more potently inhibited microtubule gliding than ATP hydrolysis or vanadate-dependent photocleavage. Finally, dynapyrazole A did not significantly reduce microtubule binding in motility assays while TDI 3016 did. Taken together, these data suggest that TDI 3016 and dynapyrazoles both act at dynein 1's AAA1 site, but inhibit dynein by different mechanisms. Nucleotide occupancy at AAA1 is known to affect both dynein's microtubule affinity and its linker geometry(86), so it is possible that upon

binding of each of these compounds, dynein mimics a different nucleotide state (e.g. ATP bound vs. ADP bound). Further structural analyses are ongoing and will be valuable to elucidate the commonalities and differences between inhibition of dynein by dynapyrazoles and pyrazolopyrimidines such as TDI 3016.

This effort would benefit especially from development of an assay that allows measurement of binding affinity between compounds and dynein. To date, all assays used to observe dynein inhibition *in vitro* have been activity-based: basal and microtubule-stimulated ATPase activity, motility, and ADP-vanadate dependent photocleavage. These assays do not report directly on binding affinity and their outcome may be misleading—e.g. failure of dynapyrazole A to inhibit the basal ATPase activity of dynein 1 could be taken to mean that dynapyrazole A does not substantially inhibit dynein unless multiple other assay types are performed. In contrast, a binding assay would measure a biophysical parameter that is less likely to report on the convolution of multiple biochemical and structural transitions. This would be particularly valuable in the case of dynein 2, an enzyme for which it has been difficult to identify conditions that lead to consistent microtubule stimulation, likely reflecting poor understanding of how to mimic the complex interplay between dynein 2, its cargo, any opposing motors, and the cellular/ciliary milieu in biochemical settings(129). With a readout of compound binding affinity, it would be possible to more confidently ascertain whether the different patterns of inhibition caused by the dynapyrazoles and TDI 3016 reflect bona fide differences in mechanism or, alternatively, reflect the combined effects of differences in affinity and solubility in the setting of a complex multi-site enzyme.

3.7 Materials and methods:

Several experiments were performed as reported in Chapter 2. These include: protein purification, motility assays with recombinant GFP-dynein 1, ATPase assays, and ADP-vanadate dependent photocleaveage assays.

Motility assays with bovine dynein: motility assays were performed essentially as described in Chapter 2, with the exception that bovine dynein was used and was immobilized directly on the glass coverslips, without the use of antbodies. Bovine dynein was the "sucrose fraction" from the preparation described by Bingham and colleagues(125), and was prepared by previous members of the Kapoor laboratory.

Electron microscopy: GFP-dynein 1 protein was expressed in insect cells and purified as described previously (Chapter 2). Following elution from IgG sepharose beads, ~300μl aliquots were frozen in liquid nitrogen. On the day of electron microscopy experiments, one aliquot was thawed and subjected to size exclusion chromatography (Superose 6) using the following gel filtration buffer: 50 mM TrisHCl pH 8.0, 150mM KOAc, 2mM MgOAc, 1mM EGTA, 0.1mM DTT. The peak fraction was collected and diluted in gel filtration buffer; dilution factors were determined empirically at the outset of each grid preparation session. 20μl eactions were set up in Eppendorf tubes as follows. Protein and buffer were added, to an initial volume of 14μl. Next, 2μl buffer containing 5% DMSO (either control solvent or with appropriate compounds at 100μM) was added, the reaction mixed by pipetting up and down, and the reaction allowed to mix for 3 minutes. 2μl of ATP at 10mM in buffer was added, mixed by pipetting up and down, and the reaction allowed to mix for 3 minutes. Finally, 2μl sodium vanadate at 10mM in buffer was added

mixed by pipetting up and down, and the reaction allowed to mix for 3 minutes. Samples were then added to copper-coated grids (Part number, company). Grids were dried with filter paper, then stained by dipping in uranyl formate solution two times. Grids were washed two times with deionized water and then dried. Images were acquired using a Philips CM10 electron microscope. Grid preparation and image acquisition were performed by Zhen Chen.

Image analysis was performed as follows: particles for which two protrusions could be observed extending from a central ring-shaped structure were selected using Boxer (EMAN)(130). Stacks of particles selected in this manner were analyzed manually using FIJI. The angle between the tip of one protrusion, the center of the ring and the tip of the other protrusion was measured using the Angle Tool.

Work done by collaborators:

Work performed by collaborators included: chemical synthesis and Hedgehog pathway activity assays.

Chapter 4:
Discovery of quinazoline-based dynein inhibitors

Note to readers: screening library synthesis and assembly were performed by Tommaso Cupido (Postodoctoral fellow in the Kapoor Laboratory) while some ATPase assays were performed by Lola Yu (technician in the Kapoor Laboratory). In the body of the text and in the methods section, I have noted contributions by others to this work where appropriate. I have also noted this information in the figure legends, where appropriate. Except for experiments credited explicitly to others, I performed all experiments and analysis.

4.1 Introduction

The discovery of new small-molecule ligands for proteins frequently relies on screening of large (often ~10^4) sets of small molecules in search of compounds that cause desired chemical or biochemical outcomes. The chances of success of such a high-throughput screening campaign becomes likelier as library diversity and size increase(131). Indeed, many validated probes and clinical drugs have been developed following initial discovery via high-throughput screening(131). However, in the case of human cytoplasmic dynein 1, a large enzyme with a relatively low ATP hydrolysis rate (<$1s^{-1}$), limited protein availability can restrict screening throughput. For instance, a protein preparation yielding 1mg of dynein (molecular weight $5x10^5$) is sufficient for 800 assay wells (assuming enzyme concentration of 100nM and assay volume of 25μl). Thus, a protein preparation larger than most routinely performed for recombinant human cytoplasmic dynein 1 is only sufficient to screen ~400 compounds (assuming assays are run in duplicate), making it operationally challenging to screen even modest size commercial screening libraries of 10^3-10^4 compounds.

When screening large libraries is intractable, focused libraries enriched with

"privileged" scaffolds are a valuable alternative. This term was coined in 1988 to mean "a single molecular framework able to provide ligands for diverse receptors"(132). Screening libraries can be designed to incorporate only compounds with a desired chemical feature known to be privileged, which is expected to raise the screening hit rate(133, 134). Privileged features in compound libraries can include as a heterocycle or hydrogen-bonding motif already known to bind a certain protein type or cause a desired cellular phenotype. We focused our library on a set of 2,4-diaminoquinazolines chemically similar to DBeQ (N^2,N^4- dibenzylquinazoline-2,4-diamine), the first potent small molecule antagonist of the AAA+ enzyme P97(75). We and others had identified this compound as an antagonist of other enzymes in the AAA+ enzyme family, including Vps4, RuvBL1(76), and spastin (Tommaso Cupido, manuscript in preparation). We hypothesized that a compound library composed of quinazolines with substitutions at the 2- and 4-positions of the quinazoline core would be likely to contain antagonists ofhuman cytoplasmic dyneins 1 and 2.

4.2 Results

Screening plates were assembled containing compounds synthesized in-house following established procedures (compound synthesis and plate assembly was performed by Dr. Tommaso Cupido) as well as commercially-availiable compounds. Two compound plates with ~160 2,4-diaminoquinazolines were screened for inhibition of the basal ATPase activity of cytoplasmic dynein 1. The inter-replicate reproducibility values (r^2) were 0.63 and 0.76 for plates one and two, respectively (See Table 4.1 and Chapter 4 Methods for other screening parameters). For dynein 1, plate 1, three compounds showed >30% inhibition at 10μM. Due to the low number of active

compounds identified in plate 1, a higher compound concentration (20μM) was used for the screen of plate 2. Six compounds on this plate inhibited dynein 1 by >50% at 20μM. A higher screening concentration (50μM) was used for dynein 2 against plate 1 and four compounds caused >40% inhibition at 50μM.

Table 4.1 Statistical parameters of screens for inhibitors of cytoplasmic dyneins.

Plate #	# total compounds #diaminoquinazolines	Z' values	Concentration tested	Inter-replicate reproducibility (r^2)
1	95 82	D1-0.68, 0.79 D2-0.71, 0.82	D1-10μM D2-50μM	D1-0.61 D2-0.30
2	96 83	D1-0.80, 0.51 D2- not tested	D1-20μM D2-not tested	D1-0.76 D2-not tested

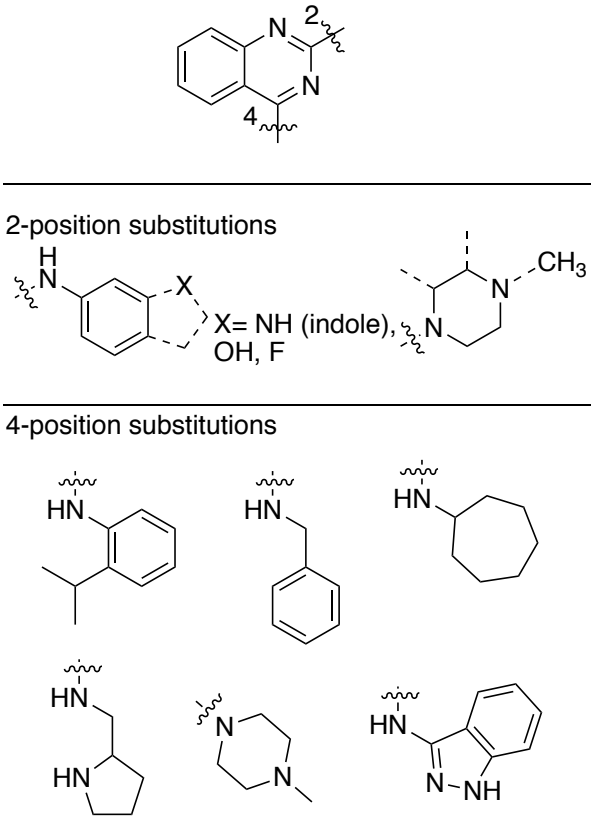

Figure 4.1 Structure-activity trends for inhibitors of cytoplasmic dynein 1

Analysis of the overall structure-activity relationship across the quinazolines on the two plates revealed a number of recurring motifs in the hit compounds that inhibited dynein 1 (Figure 4.1; full screening dataset is provided in Appendix 4.1). At the 2-position of the quinazoline, aniline-like substitutions bearing electronegative groups at the 3-position were common among screening hits. Recurring groups at the quinazoline 2-position included 6-aminoindoles, 3-hydroxy anilines, and 3-fluoroanilines. The piperazine moiety, both methylated and non-methylated at the distal amine was found in multiple screening hits. In contrast, because of the lower degree of variability at the quinazoline 4-position within the compounds screened, it was more difficult to describe a trend at this position. However, hits tended to have hydrophobic substituents at the 4-position, including multiple hits containing a benzyl group (which was the most common 4-position substituent within the screening library), as well as o-isopropyl-phenyl, and cycloheptyl. Other substituents at the 4-position of hit compounds included piperadyl, pyrrolidyl, and indazolyl moieties. Finally, almost all screening hits had unsubstituted quinazoline phenyl rings, although it should be noted that this was the most common quinazoline type within the screening collection. The only hit with a substituted quinazoline phenyl ring contained a fluorine substituent at the quinazoline 8-position (see below, TC183b). Of note, only one compound with a core hetererocycle that was not a quinazoline was identified as a hit for dynein 1: JNJ7706621, a compound which has shown inhibition of a number of other AAA+ enzymes (Appendix 4.2 shows measured IC_{50} values inhibition of other AAA+ enzymes by this compound).

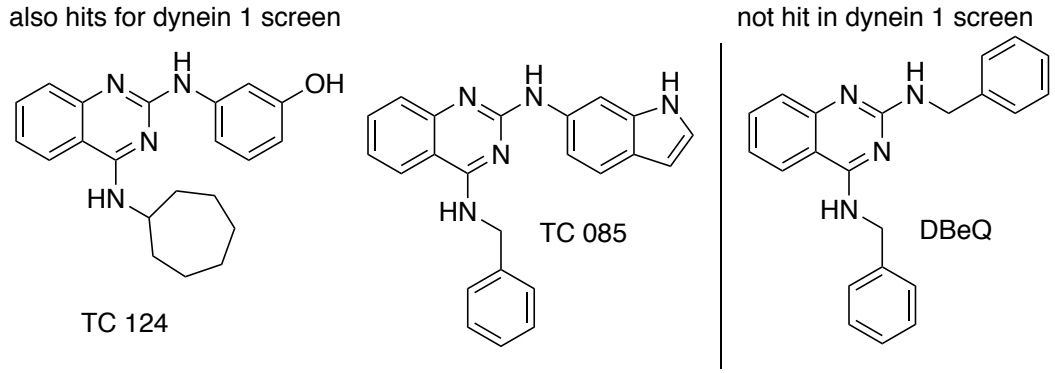

Figure 4.2 Structure-activity trends for inhibitors of cytoplasmic dynein 2

Table 4.2 Analysis of inhibition of dynein 1 by diaminoquinazolines. *Note: a subset of ATPase assay experiments summarized here were performed by L. Yu (technician in Kapoor Laboratory)*. ATPase assays were performed at 0.3mM ATP using the NADH-coupled enzyme assay system. IC_{50} values were obtaining by fitting dose-response data to a four-parameter sigmoidal curve of the mathematical form: Y=Bottom + (Top-Bottom)/(1+10^((LogIC50-X)*HillSlope)). All compounds shown were screening hits except TC 416, which was synthesized in the course of follow-up studies. TC 212 is a mixture of two isomers at position R2.

Compound designation	R1	R2	R3	Steady state IC_{50} μM (individual measured values)
TC097	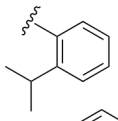	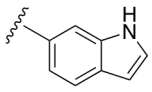	-	7.0 (4.9, 5.1, 6.6, 8.1, 8.6, 8.4)
TC085	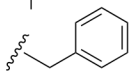	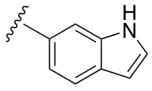	-	10.1 (8.3, 13.4, 8.5)
TC212	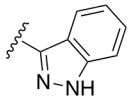	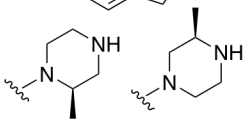	-	15.2 (10.3, 20.2)
TC124	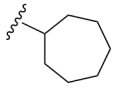	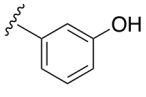	-	19.3 (18.2, 20.3)
TC183b	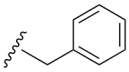	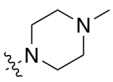	8-F	35.9 (26.7, 45.1)
TC 416	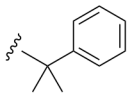	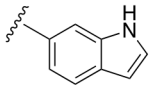	-	7.16 (7.15, 7.18)

Of the four compounds that showed >40% inhibition of cytoplasmic dynein 2, two were also identified as hits in the screen of AAA plate 1 against cytoplasmic dynein 1, while one, DBeQ, is a known antagonist of several other AAA+ ATPases (Figure 4.2). The fourth compound was excluded from further examination after routine LC/MS analysis to confirm compound identity and purity showed that the compound had degraded.

Screening follow-up

For the most active hits identified through screening assays, preliminary follow-up consisted of performing 6-8 point dose-response curves for inhibition of dynein 1 (some ATPase assays were performed by Lola Yu, technician in Kapoor Laboratory). Emphasis was placed on dynein 1 because, at the time of these experiments, this isoform was more readily available. These analyses are summarized in Table 4.2. Limited additional follow-up was also performed for dynein 2, which shall be described below.

In the course of the dose-dependent analyses, TC 097 was identified as the most potent compound discovered in the screen, with an IC_{50} value of 7.0 ± 1.5μM (mean ± S.D., n = 6). This compound did not inhibit dynein 2 in screening assays (100% residual activity, range 90%-110%, n = 2). The rank ordering of IC_{50} values matched the activities observed across both screening plates. The modest potency of inhibition motivated the synthesis of more diaminoquinazoline derivatives, in search of dynein inhibitors with improved potency. Additionally, it was noted that inhibition by the diaminoquinazolines was more pronounced in the presence of 25-50mM ammonium sulfate, and that inhibition was diminished in the absence of this salt.

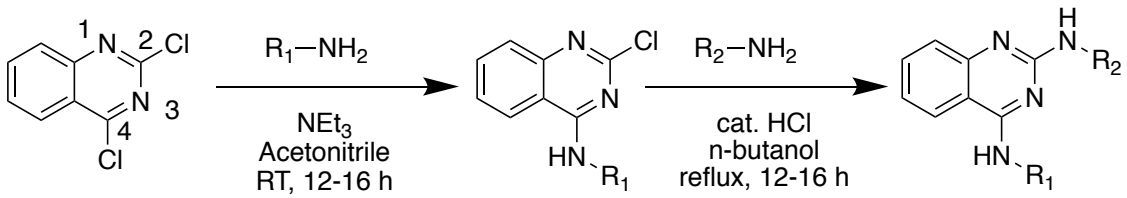

Figure 4.3 Synthetic approach to 2, 4-diaminoquinazolines
Synthesis details are provided in Appendix 4.3.

Compound synthesis and evaluation

A number of structure-activity relationship trends were evident from the screen of ~160 2,4-diaminoquianzolines against dynein 1. I hypothesized that combining the features that tended to be found in active molecules would lead to compounds with improved potency. To test this hypothesis, I synthesized a focused set of 2,4-diaminoquinazolines with combinations of substituents found among the most active screening hits.

Figure 4.2 shows the synthetic approach used to synthesize 2,4-diaminoquinazolines (full synthesis details are provided in appendix 4.3). The 4-position chlorine was first replaced by reaction with the desired R_1-substituent amine at room temperature under basic conditions. The product, a 2-chloro, 4-aminoquinazoline, generally precipitated and could be recovered by filtration. The second substituent was appended by reaction of an R_2-substituted amine with the 2-chloro, 4-aminoquinazoline intermediate in refluxing n-butanol. Products generally precipitated upon cooling or following addition of hexane to the reaction mixture. Though 2-piperazine-substituted compounds (such as TC 421, 423, 424 and 425) were an exception to this trend, these could also be purified without the need for column chromatography. This approach enabled synthesis of desired diaminoquinaozlines, with yields of ~1 - 80% over 2 steps from commercially-accessible starting materials. Compounds with alternative heterocyclic cores (eg. pyrido-pyrimidines, pyrazolo-pyrimidines, purines, and thieno-pyrimidines) could also be synthesized in a similar fashion.

Following synthesis and chemical characterization, compounds were screened for inhibition of the ATPase activity of dynein 1. 27 of 28 compounds screened showed < 50 % inhibition at or near 10μM (8μM was used for 4 of these compounds) and only 7 of 28 compounds screened showed > 25% inhibition at 10μM. The only compound that caused >50% inhibition was TC416, a quinazoline with a 6-aminoindole substituent at the 2 position and a cumylamine substituent at the 4 position. This compound was analyzed in a dose-response format and had an IC_{50} value for inhibition of dynein 1 of 7.16μM (7.15-7.18, n = 2, Table 4.2), which was comparable to TC085, the most closely-related initial screening hit. As no diaminoquinazoline could be identified with improved potency relative to TC 097/ TC 085, these two screening hits were selected for further analysis.

Motility assays

To better understand the effect dynein inhibition by TC 097 and other diaminoquinazoline inhibitors, I turned to a microtubule motility assay. In this assay, dynein is immobilized on a microscope coverslide and ensembles of dynein molecules translocate microtubules in an ATP hydrolysis-dependent manner (Figure 4.4A). I first assessed the effect of TC 097 on microtubule motility driven by bovine dynein. This enzyme preparation contains the native dynein 1 heavy chain as well as 10-15 of accessory factors identifiable by SDS-PAGE and Coomassie staining ("sucrose fraction")(125). Further purification of the semi-pure sucrose fraction dynein complex is possible, and yields dynein heavy chain with a minimal set of two to three accessory factors. However, because of the high yields and ready availability of the sucrose fraction,

this preparation was used to test whether diaminoquinazolines inhibit dynein-driven microtubule motility.

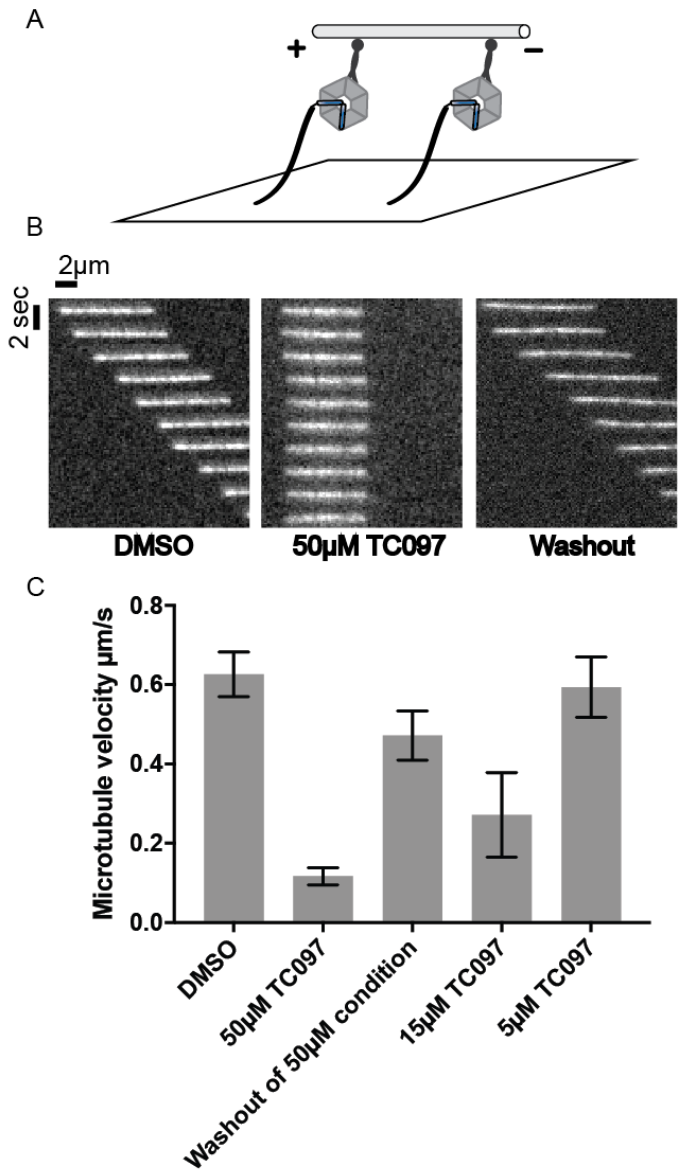

Figure 4.4 Analysis of effect of TC 097 on dynein-driven microtubule gliding. (A) Schematic of motility assay with bovine dynein. Dynein is directly immobilized on the coverslip. (B) Time-lapse montages of fluorescent microtubules moving on bovine dynein-coated glass slides in the presence of control solvent (2% DMSO), TC 097 (50μM) or following washout of TC 097. (C) Mean microtubule velocities in the presence of solvent control (2% DMSO), a range of TC 097 concentrations, or following washout. Values are given as mean ± range for n = 2 independent experiments. Motility assays were run at 0.3mM MgATP, with 0.5mg/ml casein.

Under control conditions, bovine dynein moved microtubules at an average velocity of 0.62 ± 0.06 μm/s (ATP = 2mM, mean ± S.D., n = 3, Figure 4.4B and 4.4C), which was comparable to the velocity observed for other preparations of mammalian brain dynein(24, 104). Addition of TC 097 (50μM) slowed the average microtubule velocity to 0.12 ± 0.02 μm/s (n = 3). Washout of the reaction chamber with buffer containing solvent control only (DMSO, 2%) followed by addition of control reaction mix containing microtubules, ATP, but no inhibitor, led to recovery of microtubule gliding velocity (0.47 μm/s, range: 0.43 - 0.52 μm/s, n = 2). Approximately 50% microtubule gliding inhibition was observed at an intermediate concentration of TC 097 (15μM), while no inhibition was observed at a lower concentration (5μM, Figure 4.4C).

Analysis of the mechanism of dynein inhibition by 2,4-diaminoquinazolines

To determine which of dynein's ATPase sites was inhibited by TC 097, I utilized a dynein construct with a mutation in its AAA3 site (Chapter 2). In this construct the Walker A lysine of this site, was replaced with alanine. This mutation is known to disrupt nucleotide binding within a given ATPase site, and similar mutations have previously been introduced in dyneins from other species to study the role of nucleotide binding at AAA3 on the mechanochemical properties of dynein (purification details and extended discussion can be found in chapter 2)(20, 89). TC097 inhibited both wild-type and AAA3 mutant dynein enzymes with comparable potency (Figure 4.5A, IC_{50} for AAA3 mutant enzyme is 10.3 ± 2.3μM, n = 3, two tailed Student's T-test with Welch's correction for difference between mean IC_{50} values: P = 0.12). This finding is consistent with a common ATPase site being inhibited by TC097 in both wild-type and AAA3 mutant enzyme constructs.

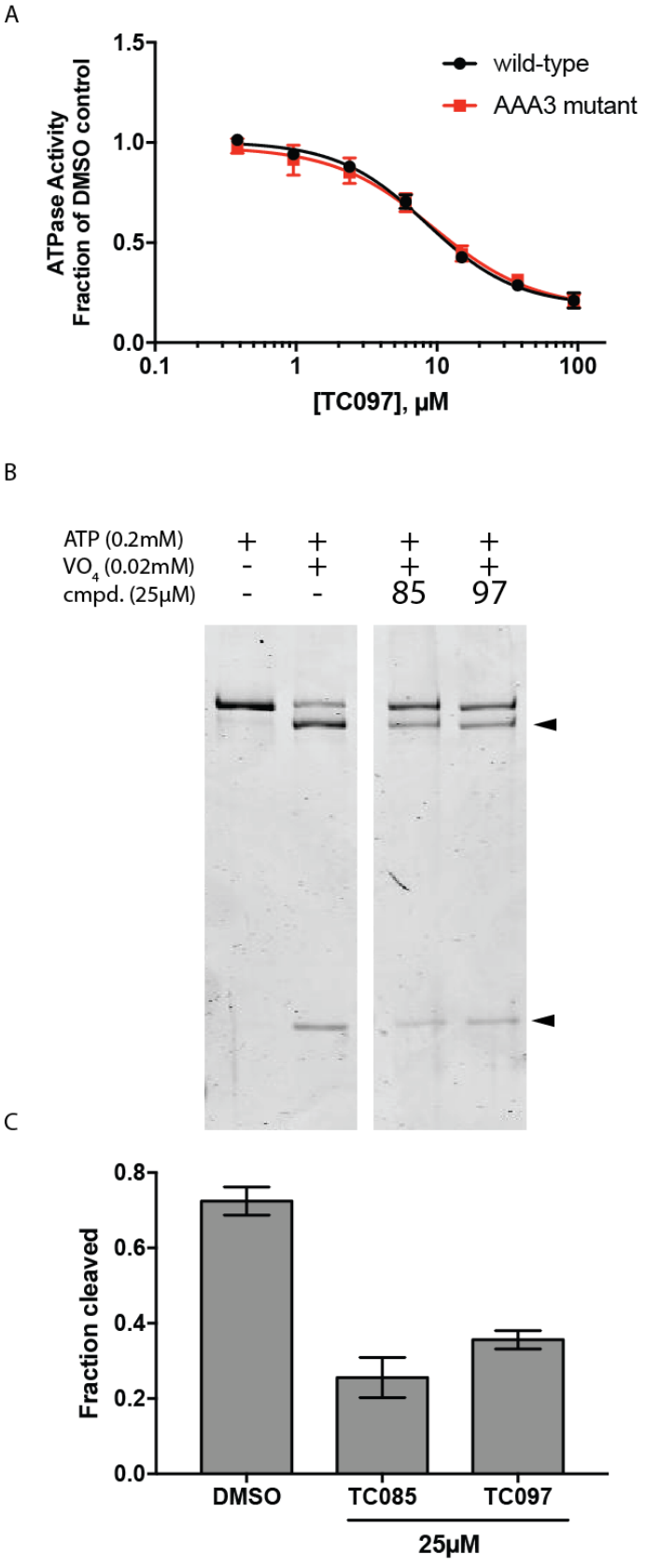

Figure 4.5 Analysis of the mechanism of inhibition of dynein by diaminoquinazolines. (A) Comparison of inhibiton of wild-type and AAA3 mutant His-dynein by TC097. Assays were performed at 0.3mM MgATP in a steady state ATPase assay. Values are mean ± range for n ≥ 2 independent experiments and were fit to a sigmoidal dose-response curve using Prism. IC_{50} values: wild-type His-dynein-8.5μM (8.4-8.6, n = 2). AAA3 mutant His-dynein-10.3μM (8.3-12.9, n = 3). (B) SDS-PAGE analysis (Coomassie blue) of dynein 1 following irradiation with ultraviolet light at 365nm. Components of reaction loaded into each lane are noted above gel. Arrowheads indicate proteolysis products. (C) Analysis of gel band intensity for photocleavage reactions. Values are mean ± range.

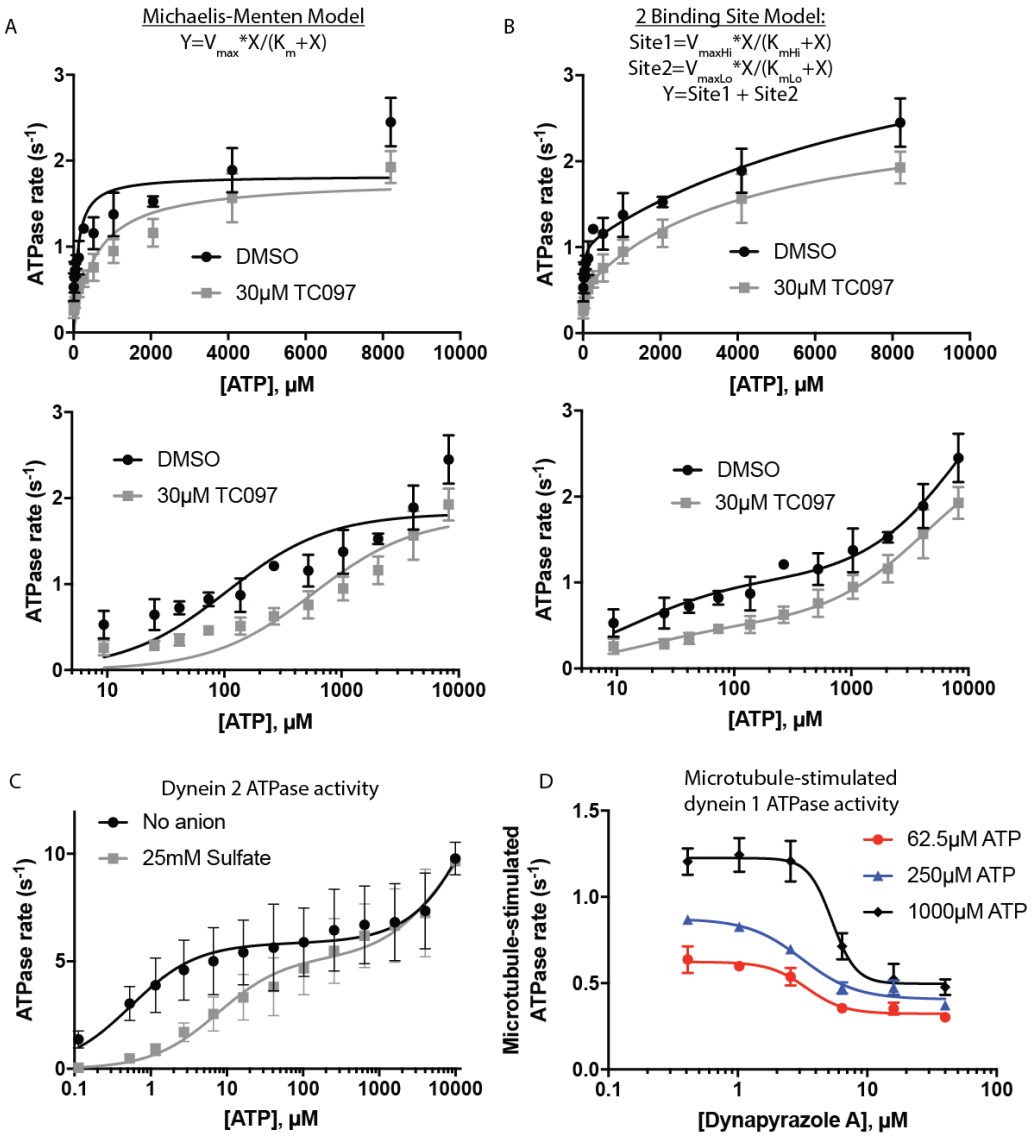

Figure 4.6 Inhibition of dynein across a range of ATP concentrations. (A) Plot of His-dynein 1 ATPase activity across a range of ATP concentrations. Data are fit to the Michaelis-Menten model. (B) Same data as (A) but data are fit to a two active site model, whose mathematical expression is shown. For both (A) and (B), lower plot represents same data as upper plot, but X-axis values are shown on a logarithmic scale. ATPase rates were measured using a steady-state assay system in the absence of ammonium sulfate. (C) Plot of GFP-dynein 2 ATPase activity across a range of ATP concentrations. Data were fit to a two active site model, as in (B). ATPase rates were measured using a steady-state assay system in the presence (25mM) or absence of ammonium sulfate. (D) Effect of dynapyrazole A on the microtubule-stimulated ATPase activity of His-dynein 1 at three ATP concentrations. Rates were measured using a non-steady state radioactive ATPase assay and values were fit to a sigmoidal dose-response curve. All ATPase activity values are presented as mean ± range for n = 2 experiments.

To further characterize the site of inhibition by 2,4-diaminoquinazolines, we examined the effect of the two most potent compounds on ADP-vanadate-dependent photocleavage of dynein 1. This assay has been used over decades of research into the biochemistry of dynein as a readout of nucleotide engagement in dynein's AAA1 ATPase site(106). Briefly, when incubated in buffer containing ATP (or ADP) and vanadate, dynein binds to a covalent adduct formed by ADP and vanadate. Irradiation with ultraviolet light leads to oxidative photocleavage of dynein into two peptides that occurs at AAA1. When dynein 1 was incubated with solvent control (5% DMSO), 200μM ATP, and 20μM vanadate, 72% photocleavage was observed (69-76%, n = 2), and cleaved peptide masses were consistent with photolysis of dynein at AAA1 (Figure 4.5B and 4.5C). Treatment with either TC085 or TC097 (25μM each) reduced photocleavage to 26% (20-31%, n = 2) and 36% (33-38%, n = 2) respectively, suggesting that these compounds act by inhibiting nucleotide association with AAA1 of dynein.

Diaminoquinazolines have been shown by others to be ATP-competitive inhibitors of AAA+ proteins(75), so I tested whether TC 097 inhibited dynein in an ATP-competitive fashion. Using a steady state ATPase assay, I measured the ATPase activity of dynein 1 across a range of ATP concentrations (~10μM-8mM). In the solvent control, dynein ATPase activity ranged from ~0.3s^{-1} to ~2.5s^{-1} (Figure 4.6A and B). Two models were fit to the data: the Michaelis-Menten model (4.6A) and a 2-site binding model (with an expression given mathematically by the addition of two separate Michaelis-Menten expressions 4.6B). Comparison of these two models using the extra sum-of-squares F test, which corrects for the effect of additional fitting parameters, indicated that the data are better fit by a two binding site model ($P < 0.0001$, Figure 4.6A vs. 4.6B, data presented in

logarithmic scale, 4.6A and B, bottom panels). Fit to a two-site binding model revealed a high affinity binding site ($K_{m, Hi}$: 14μM $V_{Max, Hi}$: 1.0s^{-1}) and a low-affinity binding site ($K_{m, Lo}$: >10,000μM $V_{Max, Lo}$: 3.2s^{-1}). Addition of TC097 (30μM) to the [ATP] *versus* ATPase activity titrations for dynein 1 decreased hydrolysis activity across the range of ATP concentrations tested, although it should be noted that decreases in ATPase activity were less pronounced than in previous dose-response analyses, likely as a result of the omission of ammonium sulfate from these titrations. Data were again better fit by a two-site binding model (P = 0.0001).

A similar trend was observed for ATP titrations with dynein 2: activity trends were consistent with two binding sites with K_m values separated by >2 orders of magnitude. For dynein 2 it was further noted that addition of ammonium sulfate (~25mM) to the ATPase assay shifted the K_m of the high affinity ATPase site by ~10-fold without shifting the apparent $V_{max, Hi}$ (4.6C). Finally, to establish a basis for comparison, the effect of dynapyrazole A on dynein's microtubule-stimulated ATPase activities was measured at three ATP concentrations (Figure 4.6D, 62.5μM, 250μM, and 1000μM). Inhibition was partial at the highest dynapyrazole A concentration tested (40μM), as had been previously noted. Fitting to the residual ATPase activities revealed that IC_{50} values for inhibition were 3.8μM (1.9-5.7), 3.0μM (2.8-3.3), and 5.5μM (5.1-6.0) at 62.5μM, 250μM, and 1000μM, respectively (mean and range, n = 2). Thus, a clear trend toward decreased inhibition was not observed as ATP concentrations increased, although the resolution of this analysis is limited.

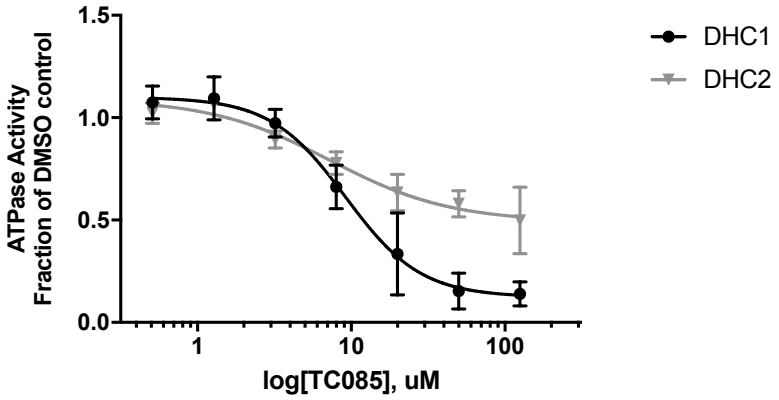

Figure 4.7 Comparison of the effect of TC 085 on the ATPase activities of dynein 1 and dynein 2. *Note: a subset of the ATPase assays shown in this figure were performed by L. Yu (technician in the Kapoor Laboratory)*. The ATPase activities of His-dynein 1 and GFP-dynein 2 were measured in the presence of TC 085 (0.5-125μM) using a steady-state ATPase assay in the presence of 25mM ammonium sulfate. Values represent mean ± S.D. of n ≥ 3 separate experiments. Data were fit to a sigmoidal dose-response curve using Prism.

Inhibition of dynein 2

To characterize the effect of diaminoquinazolines on dynein 2, dose-response assays were performed with TC085, one of the three hit compounds for this isoform. This compound reduced dynein 2 ATPase activity by ~48% at the highest dose tested (125μM, Figure 4.7). When the dose-response data were fit to a sigmoidal curve with lower plateau allowed to float freely, an IC_{50} value of 8.0μM was obtained. The difference between residual activities of dynein 1 and dynein 2 at the highest compound concentration tested was statistically significant (P = 0.007). Further analysis will be required to understand why the effect of TC085 inhibits these two dynein isoforms with comparable IC_{50}s but with different residual activities at high compound concentrations.

4.3 Discussion

In this chapter I report the results of a screen of a focused library of ~160 diaminoquinazoline-based compounds for inhibitors of the basal ATPase activity of cytoplasmic dynein 1. Of the compounds screened, two were validated as dynein inhibitors with IC_{50} values at or below 10μM and activity across two or more complementary biochemical assays of dynein inhibition. Three other compounds identified through the screen inhibited dynein 1 with IC_{50} values below 40μM. Thus, defining a "hit" as a compound that can be starting point for further chemical inhibitor optimization, the hit rate for this assay was ~3%, well above the hit rate expected for conventional high-throughput screening of a large compound library(0.1-1%)(135). This can be interpreted as evidence in support of the hypothesis that diaminoquinazolines are a privileged scaffold for inhibition of enzymes in the AAA+ protein family.

Although the privileged scaffold-based approach to dynein inhibitor discovery has shown early promise, much additional work lies ahead. Further development of any diaminoquinazoline as a probe for dynein 1 will likely require careful counter-screening against other AAA+ proteins to exclude compounds that inhibit multiple enzymes in the family. I note that diaminoquinazoline analogs generated based on the structure-activity data arising from this screen did not yield any compounds with improved potency. However, these synthetic efforts were limited (<30 compounds). It is probable that more extensive analog synthesis efforts with TC 097/085 as starting points can lead to more potent inhibitors. This is especially true if additional structural and biochemical data can be integrated into the iterative process of design, synthesis, and testing.

Two lines of evidence support a model in which TC097 and TC085 inhibit the ATP hydrolysis at AAA1 of dynein 1. First, these compounds block ADP-vanadate dependent photocleavage of dynein, suggesting they disrupt nucleotide binding at AAA1. Second, they block the ATP hydrolysis of the AAA3 walker A lysine-to-alanine mutant, a construct whose ATPase activity is expected to arise mostly from AAA1.

If both the dynapyrazoles and the diaminoquinazolines act at AAA1, then why do dynapyrazoles show modest inhibition of the basal ATPase rate of dynein (~30%) while the diaminoquinazolines show near >80% inhibition? One explanation may be that the conditions under which these assays were performed were different: the dynapyrazoles were tested in a radioactive ATPase assay while the diaminoquinazolines were tested in a steady-state ATPase assay containing a coupled-enzyme system and high concentrations of ammonium sulfate (25-50mM). When TC 097 was tested in an otherwise-similar buffer without ammonium sulfate, the degree of inhibition at ~30μM TC097 was reduced

from ~80% (25mM ammonium sulfate, see Figure 4.5A) to ~35% (0 ammonium sulfate, see Figure 4.6A/B, note concentrations in the 0.1-1mM ATP range). I propose that ammonium sulfate may modulate the basal activity of dynein, raising the relative contribution of AAA1 to the basal hydrolysis. This could be due to the sulfate anion, which can mimic phosphate, inhibiting the AAA3 site via product inhibition. Direct evidence of the diaminoquinazoline binding site (eg. via structural or crosslinking-and-proteomics approaches) will be critical to fully understand the mechanism of inhibition of these compounds.

Another question raised by the mechanistic analysis of diaminoquinazoline inhibition is whether these compounds can be said to be ATP-competitive. In the well-established model of substrate competitive enzyme inhibition for single-site enzymes, such an inhibitior would be expected to shift the enzyme's K_m without affecting its V_{max}. IC_{50} values would be expected to increase with increasing substrate concentration. When ATP titration data in the presence and absence of compound are fit to the Michaelis-Menten model for a single site enzyme, TC 097 appears to be simply ATP competitive, with 30μM TC097 raising the K_m from ~100μM to ~500μM without significantly altering the V_{max}. However, the data do not appear to be well-fit by the Michaelis-Menten expression, and are better fit by a two-site model. When this model is applied, the inhibition pattern is less clear, with TC 097 causing changes to the K_m and V_{max} of both high- and low-affinity sites. In comparison, ammonium sulfate causes a ~10 fold decrease in the $K_{m,hi}$ of dynein 2, without shifting the $V_{max,hi}$ or either K_m or V_{max} of the low-affinity site (see figure 4.6 C). These data suggest that some compounds do cause "simple" substrate competitive inhibition (analogous to what would be expected from interaction

with a single-site enzyme) in the setting of dynein's two active sites. However when the two-site model is considered, both TC097 and dynapyrazole A do not show ATP-competitive patterns of inhibition, despite both blocking ADP-vanadate photocleavage, consistent with disruption of nucleotide binding at AAA1. It is possible that the complex allosteric regulation of AAA1 by other ATPase sites on dynein, which has been demonstrated by multiple other groups(88, 89), obscures ATP competition with inhibitor binding as nucleotide concentrations are titrated up. However, the possibility of other non-nucleotide competitive mechanisms of inhibition for both diaminoquinazolines and dynapyrazoles has not been rigorously excluded.

A longstanding goal has been to develop isoform-selective dynein 2 inhibitors. Although this screen and subsequent biochemical characterization did not yield any compounds fitting this profile, they did uncover three dynein 2 antagonists and principles that could raise the chance of success in the future. Dose-response analysis for one of these compounds, TC 085, revealed a plateau of ~50% inhibition that was not exceeded up to the limit of compound solubility (~125μM). Taking this non-zero residual activity into account, the IC_{50} of TC 085 was found to be similar between dynein 1 and dynein 2 (8μM). One plausible explanation for this is that the high affinity ATPase site identified for dynein 2 (for which the measured K_m is ~200nM in the absence of ammonium sulfate and 8μM at 25mM ammonium sulfate) may contribute a larger fraction of overall ATPase activity than the comparable site on dynein 1 at the ATP concentration at which dose-response assays were conducted (300μM). It is likely that screens can be adapted to capitalize on the apparent two-site nature of dynein 2. For instance, more screening hits might be expected, counterintuitively, by performing screening assays at higher [ATP].

This is because as a larger fraction of ATPase activity would be expected to come from the low-affinity site, and it is more likely to identify compounds that can compete with binding at a site with ATP affinity >1mM than at a site with ATP affinity <1μM. Finally, the finding that TC 097 shows dynein 1 selective inhibition while TC 085 inhibits both dyneins 1 and 2 with similar potency suggests that the binding sites on each enzyme for diaminoquinazolines have slightly different structure-activity-relationship landscapes. These differences can be likely be exploited through an iterative process of analog synthesis and isoform selectivity testing.

4.4 Methods

Library assembly: ~200 compounds were synthesized or purchased from commercial sources and arrayed in two 384-well plates at stock concentrations of 5, 1, and 0.2mM. Compound synthesis and plate assembly were performed by Dr. Tommaso Cupido. Compound identities and their locations on screening plates are presented in Appendix 4.1.

Protein purification: Wild-type and AAA3 mutant His-dynein 1, motor domain constructs of wild-type human dynein 1 with hexahistidine tags at their N-termini, were purified as described in previous chapters (chapter 2). Bovine brain dynein was purified by previous members of the Kapoor laboratory following the procedure of Bingham *et al*(125).

ATPase assays

Screens and follow-up ATPase assays were performed using an NADH-coupled assay system.

The ATPase activity of each of dynein 1 or dynein 2 was measured using an NADH-coupled assay in which ATP was regenerated and kept at a constant concentration with concomitant oxidation of NADH to NAD^+. NADH fluorescence was monitored and its rate was an indirect readout of ATP hydrolysis. Assays were performed with final NADH-coupled assay components as follows: pyruvate kinase (Sigma Aldrich cat. P1506 for reactions with ammonium sulfate, P9136 for reactions without ammonium sulfate) 5 U/ml, lactate dehydrogenase (Sigma Aldrich cat. L1254) 5U/ml, potassium phosphoneolpyruvate 0.8 - 1mM, disodium nicotinamide adenine dinucleotide (Sigma Aldrich, N7140) 150 – 210 μM.

Final reaction mixes contained 50-150nM dynein 1 or 25-50nM dynein 2. The buffer composition was: 25mM PIPES pH7, 30mM KCl, 1mM EGTA, 5mM $MgCl_2$, 0.01% triton-X-100, 1mM DTT. Because pyruvate kinase was obtained as a suspension in 3.2M ammonium sulfate, final concentrations of ammonium sulfate were 25mM (except for reactions shown in Figure 4.6, which for which an alternative pyruvate kinase source was used). Reaction mixes all contained bovine serum albumin at 0.1mg/ml and MgATP at 0.3mM (or variable ATP for reactions shown in 4.6), 2% (v/v) DMSO in the presence or absence of test compounds. NADH fluorescence was measured at 10-45 second intervals over a 20-30 minute time course using a synergy NEO microplate reader. The rate of NADH consumption was determined from a linear regression of the NADH fluorescence data. The rate of NADH consumption was used as a measure of ATP hydrolysis activity and was converted to ATPase rate using conversion factors determined from analysis of the decrease in NADH fluorescence caused by addition of known amounts of ADP.

Screening was performed using the above-described ATPase assay conditions, but buffers and compounds were dispensed using automated robotics, with the assistance of staff at the High Throughput Resource Center (Rockefeller University). For each plate screened, eight wells were used as solvent (un-inhibited) controls and eight wells were used as no-enzyme controls. Screening data is presented in Appendix 4.1.

ATPase assays for dynapyrazole A were performed as described in Chapter 2.

Calculation of Z': Z', a measure of the effect size within a screening assay, was calculated as follows:

$$Z' = 1 - [3*(s.d._{no\text{-}inhibitor} + s.d._{no\ enzyme})/(mean_{no\text{-}inhibitor} - mean_{no\ enzyme})]$$

Conditions were optimized such that Z' values were > 0.5.

Assays performed as described in previous chapters: ADP-vanadate dependent photocleavage assays and bovine dynein-driven motility assays were performed essentially as described in previous chapters.

Chapter 5:

Conclusion and outlook—toward chemical genetics of dynein

5.1 Dynein inhibitor trends

Reviewing the data for the three classes of dynein antagonists disclosed in this work within in the context of the four dynein antagonists described previously by others (vanadate(11, 12), EHNA(21, 22), ciliobrevins(46), and tolyl-ether substituted-ciliobrevins(47)) can help illuminate general features and underlying principles relevant to dynein inhibition (data summarized in Table 5.1). *In vitro* IC_{50} values for dynein inhibition ranged from ~1μM (vanadate) to >200μM (EHNA), but using these values to compare inhibitors is complicated by the variable conditions and under which inhibition was measured and the different dynein sources used. A K_i value was only estimated for one of these dynein antagonists (EHNA, ~74μM)(22).

Table 5.1 Analysis of dynein inhibitors in the literature and in this work.

Compound (year discovered as dynein inhibitor)	Potency (assay type)	Cell permeable ?	Site/Mechanism of inhibition
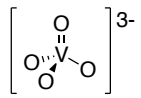 Vanadate (1978)	~1μM IC_{50} for mammalian dyneins	No	Covalent ADP-VO_4 adduct binds at AAA1 (uncompetitive)
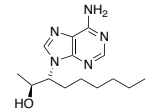 EHNA (1981)	0.25-1mM for mammalian dyneins K_i 74μM (sea urchin dynen)	Yes (non-selective)	Site: unknown (partial competitive inhibition)
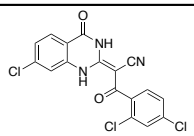 Ciliobrevin D (2012)	~20-30μM for mammalian dynen microtubule gliding	Yes	Site: Likely AAA1 (ATP competitive)
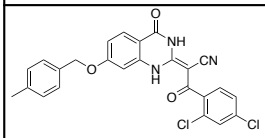 #37—See *et al* (2016)	10μM (mammalian dynein 2 ATPase activity at [ATP] < 1μM, ~10x selective dynein2 vs 1)	Yes	Site: unknown (Mechanism not established)
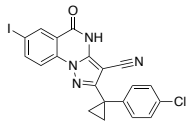 Dynapyrazole A (this work)	~3μM mammalian dynein microtubule gliding	Yes	Site: AAA1 (no direct evidence of ATP competition)
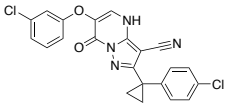 TDI 3016 (this work)	~2μM mammalian dynein microtubule gliding	Yes	Site:AAA1 (no direct evidence of ATP competition)
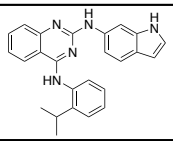 TC 097 (this work)	~8μM dynein 1 ATPase inhibition	No data	Site: AAA1 (no direct evidence of ATP competition)

With regard to the *mechanism* of inhibiton, nucleotide-competitive inhibition consistent with the Cheng-Prusoff relationship was not observed for any of the compounds, with the exception of ciliobrevin D(46, 136). The un-competitive mechanism of inhibition for vanadate may be explained by a requirement for ADP to be bound in the AAA1 site before vanadate binding can occur(11). Vanadate is known to inhibit dynein via formation of an ADP-vanadate adduct that mimics the transition state of ATP hydrolysis at AAA1 of dynein(17). However, the absence of substrate-competitive inhibition noted for the other dynein antagonists is surprising in light of two previous observations. First EHNA inhibits another enzyme (adenosine deaminase) in a substrate-competitive manner(137), in line with what might be anticipated for a compound that contains the adenine nucleobase. Second, diaminoquinazolines have been shown to be ATP-competitive inhibitors of AAA+ ATPases(75). It is possible that multiple compounds with known substrate-competitive mechanisms (for other enzymes) bind dynein at allosteric sites distant from dynein's nucleotide binding pockets, and only direct binding site identification (see below) will be able to conclusively exclude this alternative. However, taking all the available mechanistic data together, I propose that in the case of dynein, apparently non-ATP-competitive inhibition may occur even when the mechanism involves inhibitor binding at the nucleotide binding site. This may be a feature of dynein, a multi-active-site enzyme whose ATPase sites can regulate one another's activity(88, 89), and potentially other enzymes like it.

Across the seven dynein inhibitors in Table 5.1, the *site* of binding is only known conclusively for one compound, vanadate, for which x-ray crystallography and complementary biochemical evidence indicate binding to AAA1(17, 20). Biochemical

data including experiments comparing basal and microtubule-stimulated hydrolysis, analyses of inhibition of mutant dynein enzymes, and ADP-vanadate photocleavage assays suggest that four other compounds (ciliobrevins, dynapyrazoles, TDI-3016 and its relatives, and diaminoquinazolines), also act by inhibiting AAA1. This is consistent with, but does not guarantee *binding to* AAA1. Data for EHNA and tolyl-ether substituted ciliovrevins do not support assignment of a site of inhibition.

Why is inhibition at AAA1 a common feature of dynein inhibitors characterized to date? Two explanations seem most plausible.

First, AAA1 may be the only site with low enough ATP affinity to be readily inhibited. Several lines of evidence support this suggestion. Nucleotide binding at both AAA1 and AAA3 has been shown to be required for dynein 1 activity(20). Some analyses (including those shown in Chapter 4) are consistent with those two sites having nucleotide affinities separated by ~2 orders of magnitude(115), although other analyses have not found such behavior(104, 105), and affinities have not been conclusively assigned to either site. It has also been proposed that tight binding to ADP is required for full dynein activity(138). More recent analyses using yeast dyneins have made clear that the presence of ADP in AAA3 is required for dynein to undergo a productive chemomechanical cycle(88) and have further shown that binding of ADP to AAA3 can persist through multiple (~20) cycles of ATP hydrolysis at AAA1(89), implying relatively slow release of ADP from AAA3 compared to AAA1. The slow release of ADP may drive high nucleotide affinity at AAA3 ($K_d = K_{off}/K_{on}$). AllFrom the perspective of inhibitor identification, tight binding of either ATP or ADP to AAA3, would make finding an antagonist of this site within a collection of screening compounds

considerably less likely than identifying one that blocks a site with 20-1000-fold lower nucleotide affinity.

A second explanation for why dynein inhibitors discovered to date tend to inhibit AAA1 is that when AAA1 is blocked the effect is easy to appreciate—dynein driven motion stops—and that the effect of AAA3 inhibition is likely to be more nuanced. Perturbations at AAA3 have been analyzed by multiple research groups across different biochemical assay systems. Replacement of the AAA3 Walker A lysine with threonine slowed dynein driven motility but did not affect ADP-vanadate dependent photocleavage at AAA1 and, unexpectedly, potentiated photocleavage at AAA4(20). Mutation of the same residue to alanine increased dynein's basal ATPase activity (116)(Chapter 2). While this mutation slowed dynein motion, the velocity recovered as salt concentrations were raised to physiologic levels(89). In the course of the same analysis, the slowly-hydrolyzable nucleotide mimetic was shown to inhibit AAA3 and to be hydrolyzed by AAA1 at ~1/4 the rate of ATP hydrolysis. Analysis of processive dynein motion revealed that AAA3 inhibition by ATPγS caused an increase in the likelihood of pausing, and only partially slowed running velocities between pauses(89). Taking these biochemical observations together, it is clear that inhibitor binding at AAA3 could cause biochemical effects that do not, at first pass, appear to be inhibition, such as activation of dynein's basal ATPase activity. While the effect on simpler assays of dynein activity (eg. ATPase, ADP-vanadate photocleavage) may be difficult to discern, inhibition of dynein at AAA3 would be expected to cause a measureable effect on the processive motility of the human dynein holo-complex, as was noted in the analysis of disease-causing mutations occurring outside of AAA1(139). Assaying processive motility of human dynein is technically

complex and not likely to be a viable approach to inhibitor discovery. Despite the biochemical nuances surrounding AAA3 inhibition, a compound that blocks activity of this site is likely to disrupt dynein function in cells(107). Researchers performing phenotype-based screens for compounds that inhibit dynein would do well to remember the complexities associated with AAA3 inhibition before discarding a compound with promising cellular activity that does not cause straightforward effects when tested for dynein inhibition *in vitro*.

5.2 Future directions

In the following section, I propose a few lines of research that may help address the open questions arising from the work described in this thesis, and in doing so, could improve the utility of known dynein inhibitors and spur advances toward development of new inhibitors.

In the short term, carefully sorting out the differences in the effect of inhibition by dynapyrazoles and pyrazolopyrimdinone-based derivatives such as TDI 3016 is a top priority. TDI 3016 causes dynein 1 to adopt a post-powerstroke state even in the presence of ADP-vanadate while dynapyrazole does not. As a next step, the effect of these compounds should be tested in other nucleotide states. Is the apo-like state induced by TDI 3016 maintained in the absence of nucleotide? Can a nucleotide state be found in which the dynapyrazole changes dynein geometry relative to the DMSO control? One possibility is that, in the nucleotide-free state, where a small angle is expected between the microtubule binding domain and the linker, dynapyrazole A treatment might dynein to adopt a geometry with a large θ. In parallel, it will be valuable to assess if TDI 3016

and dynapyrazole A affect dynein's affinity for microtubules using an assay that more robustly measures this interaction—as multiple factors can confound the interpretation of the number of microtubules bound to the coverslip in microtubule gliding assays. If the compounds do indeed cause different effects on dynein's affinity to microtubules, it would be tantalizing to dissect the cellular effects of compounds acting with these two separate mechanisms.

Conclusively identifying the binding site of either dynapyrazoles or TDI 3016 will help clarify the mechanistic distinctions between these two compound classes. While present data are consistent with inhibition occurring at AAA1, it is not certain that either compound binds within the ATP binding site or even in this domain. Incorporating binding site information with available structural information, and modeling techniques, it may be possible to develop an accurate model that could then be refined using structure-activity data, and directed mutagenesis. One of the most direct approaches to identifying the binding site of dynein inhibitors is to covalently bind a compound to dynein, proteolytically digest the enzyme, the and then to "fish" the peptide-compound adduct out of the resulting complex mixture of peptides using affinity precipitation and/or proteomic deconvolution approaches(140). Generally, the disadvantage of binding site identification via formation of a covalent bond followed by proteomic analysis is the requirement that a compound be modified with both a reactive group and a chemical handle for affinity tagging (often diazirines and alkynes, respectively) while retaining the bioactivity of the parental compound(140). Identifying and synthesizing active compounds with the appropriate groups can often be limiting and can require extensive structure-activity relationship data. Fortunately, the structure-activity data already in hand

suggest that such could be identified using TDI 3148, which contains an alkyne and has comparable activity to TDI 3016 in terms of Hedgehog pathway inhibition, as a starting point (Figure 5.1).

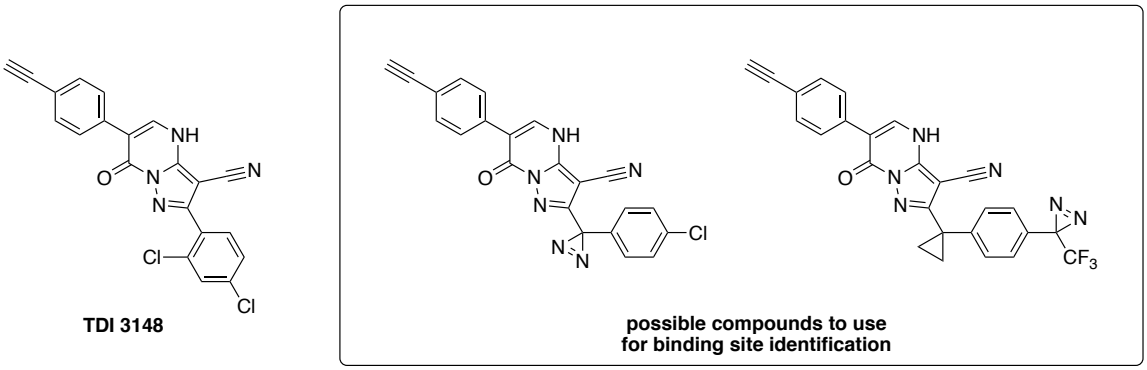

Figure 5.1 Proposed compounds to use for binding site identification using proteomic approaches. TDI 3148 inhibits Hedgehog pathway activity and is structurally related to TDI 3016. Compounds in box are proposed based on established structure-activity relationships.

A valuable step beyond locating the dynapyrazole/TDI 3016 binding site on dynein will be to identify mutations that confer resistance to compound binding. Ideally, this mutation should be "silent" in that it blocks compound binding to dynein but does not otherwise affect dynein's function. Resistance-conferring mutations have been identified using structural(141), genetic (e.g. analysis of sequence conservation across enzyme families)(142), and selection-based approaches(42, 143). In the case of dynein, where structural data regarding compound binding are still lacking and the putative compound binding site (AAA1) is conserved (see Chapter 1 Figure 1 and Appendix 2.1, Figure 6-5), selection-based approaches to identifying resistance mutations are the most promising. If a resistance-conferring mutation can be shown to decrease compound binding to a given target *in vitro* and insertion of that mutation into an otherwise-sensitive cell line blocks the effect of compound treatment, then the mutation has been shown to be sufficient for resistance and the compound's effect can be confidently assigned as due to binding of the sensitive enzyme. In the case of dynein, identification of a resistance-conferring mutation could be used to distinguish whether the cytotoxicity observed at high concentrations of dynapyrazole A (eg. 15μM, 3 hour treatment, see Chapter 2) is due to dynein inhibition or engagement of another target. If treatment of cells expressing the resistant dynein allele with dynapyrazole A does not cause cytotoxicity, then the toxicity would be understood to be a consequence of dynein inhibition. This approach has been referred to as the "gold standard" for validation of physiologic target engagement by a small molecule inhibitor(79, 144).

Finally, it will be valuable to continue exploring the chemical space surrounding the dynapyrazole and TDI 3016 scaffolds. Doing so may help to identify compounds with

improved potency or solubility. Increased potency and solubility will, in turn decrease the likelihood that compound activity is reduced in the presence of high protein concentrations (i.e. in cell culture conditions with 10% serum), which at present is a major limitation for both compound classes. Progress toward any of the four interlocking goals described above will solidify the foundation necessary to use these compounds to study dynein with precision, and, will constitute progress toward the ultimate goal of testing the therapeutic utility of dynein inhibitors.

Appendices

Appendix 2.1: Supplemental figures associated with chapter 2— Chemical structure-guided design of dynapyrazoles, potent cell-permeable dynein inhibitors with a unique mode of action

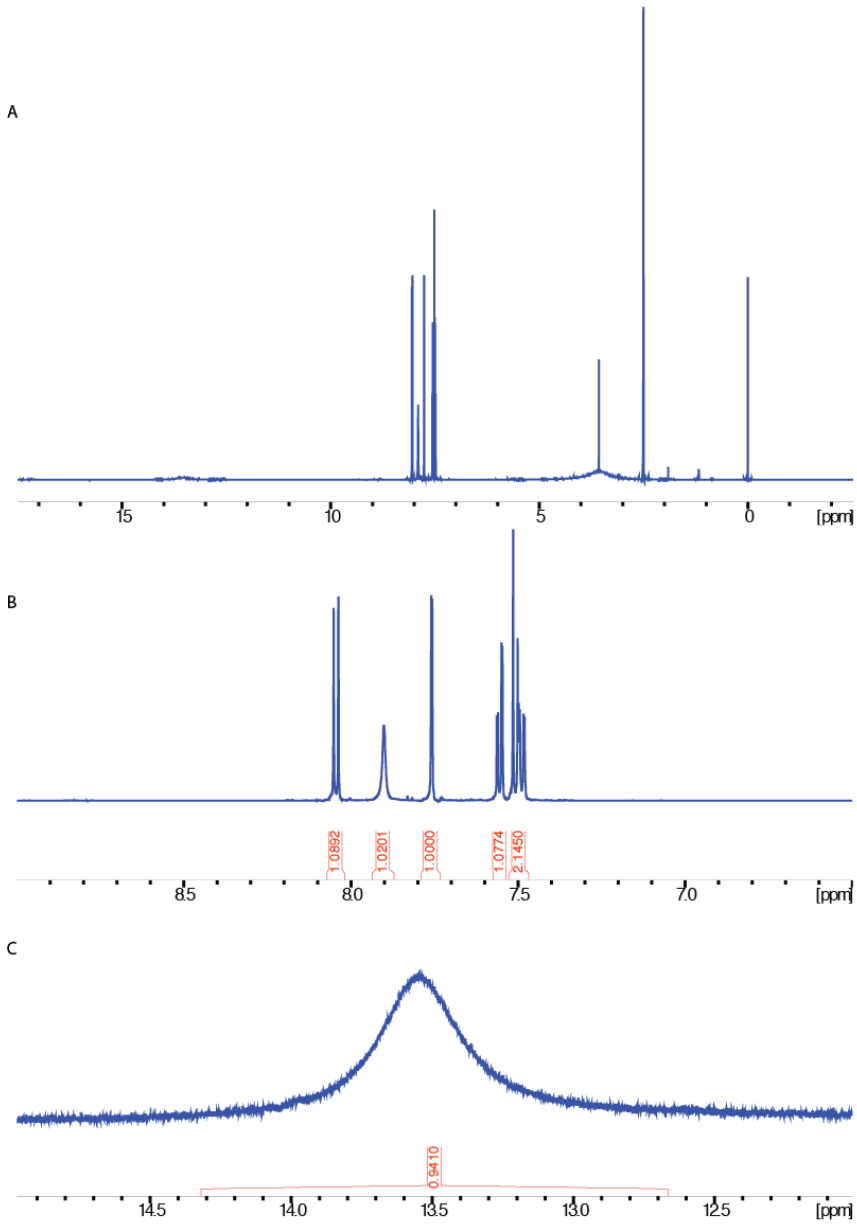

Figure 1 Figure Supplement 1: ^{1}H NMR spectrum of ciliobrevin D. NMR taken on a 600 MHz instrument, DMSO-d_6. (A) Full spectrum. (B) Enlarged view of the aromatic region. (C) Enlarged view highlighting peak at 13.5 ppm.

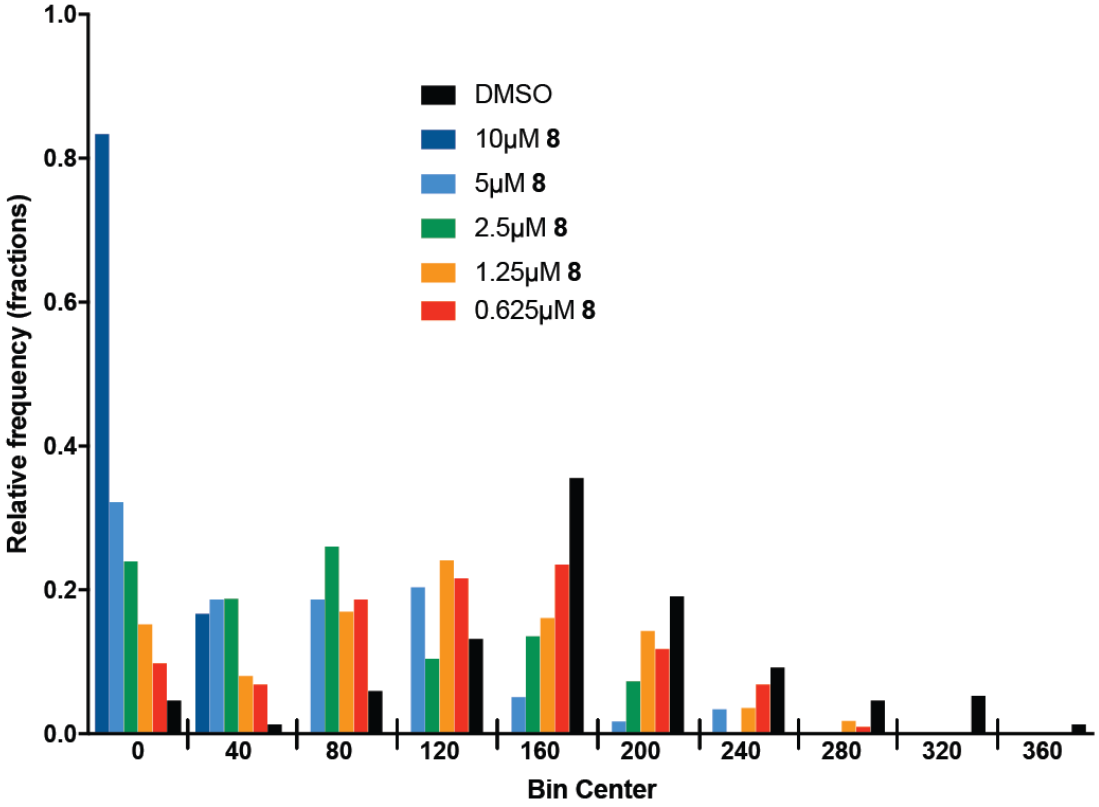

Figure 3 Figure Supplement 1: Microtubule velocity distribution histograms for dynein-2 driven motion in the presence of different concentrations of **8**. At least 36 microtubules were analyzed per experimental condition.

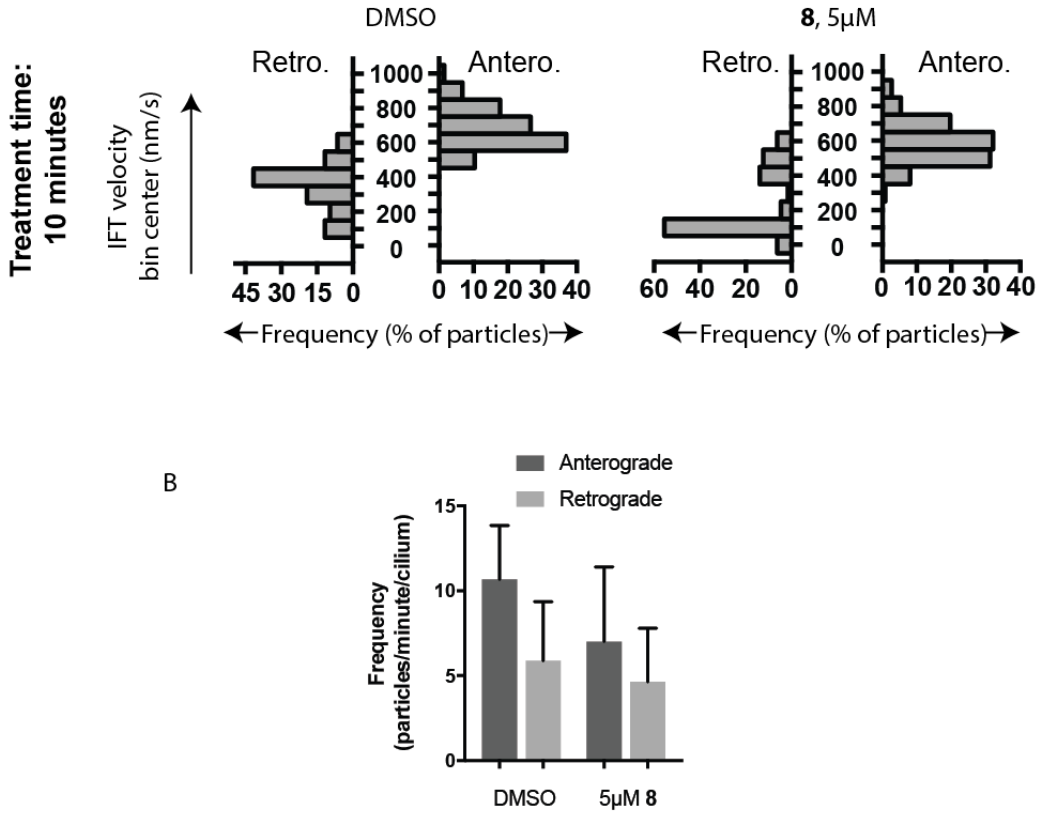

Figure 4 Figure Supplement 1: Analysis of intraflagellar transport following 10-minute exposure to dynapyrazole-A. (A) Velocity distribution histograms showing anterograde and retrograde velocities in the solvent control (0.3% DMSO) and in the presence of 5μM **8** (B) at 10 minutes after treatment. (C) Analysis of intraflagellar transport particle frequencies. Data analysis (V_a, anterograde velocity, nm/s; V_r, retrograde velocity, nm/s; F_a, anterograde frequency, counts/minute; F_r, retrograde frequency, counts/minute; values are mean ± S.D. N_a, number of anterograde particles analyzed; N_r, number of retrograde particles analyzed; C, number of cilia analyzed). DMSO, V_a 655 ± 124, V_r 354 ± 134, F_a 10.2 ± 3, F_r 5.9 ± 3, N_a, 276; N_r 145, C 18; 5μM **8**, V_a 572 ± 121, V_r 202 ± 180, F_a 6.9 ± 4, F_r 4.2 ± 3, N_a 125, N_r 75, C 18.

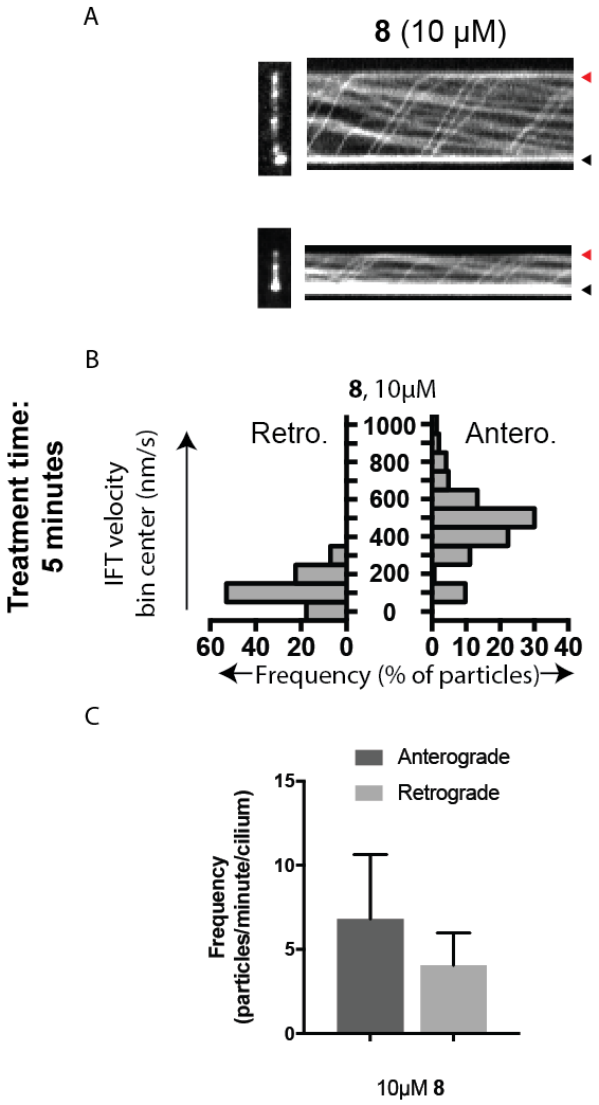

Figure 4 Figure Supplement 2: Analysis of intraflagellar transport at higher dynapyrazole-A concentrations. (A) Still images from time-lapse series and associated kymographs showing motion of mNeonGreen-IFT88-containing particles in representative primary cilia treated with 10μM **8**. Still image scale bar, 3μm; interval between frames, 0.5 seconds. Kymograph horizontal scale bar, 10 seconds; vertical scale is identical to cilium image. (B) Velocity distribution histograms for anterograde and retrograde motion. (C) Analysis of particle frequency in the presence of 10μM **8**. Data analysis (V_a, anterograde velocity, nm/s; V_r, retrograde velocity, nm/s; F_a, anterograde frequency, counts/minute; F_r, retrograde frequency, counts/minute; values are mean ± S.D. N_a, number of anterograde particles analyzed; N_r, number of retrograde particles analyzed; C, number of cilia analyzed). 10μM **8**, V_a 466 ± 183, V_r 121 ± 78, F_a 6.8 ± 4, F_r 4.0 ± 2, N_a 143, N_r 85, C 21.

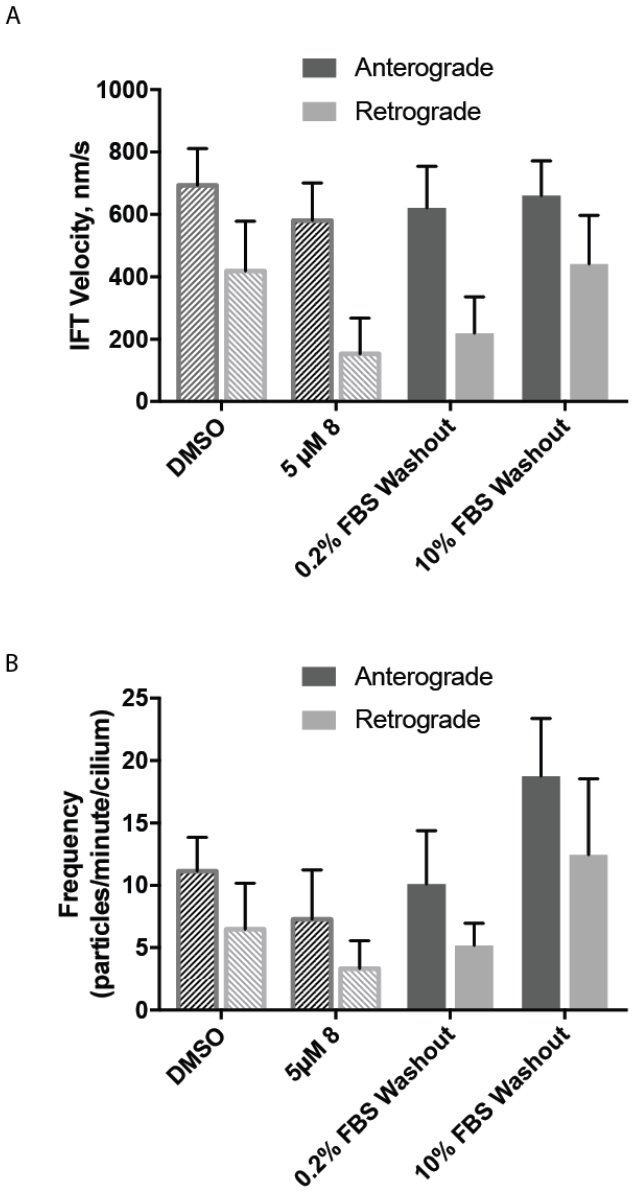

Figure 4 Figure Supplement 3: The effect of serum concentration on washout of dynapyrazole-A in intraflagellar transport assays. (A) mNeonGreen-IFT88 particle velocities following washout of dynapyrazole-A for 1 hour in media with either low serum (0.2% FBS) or high serum (10% FBS). (B) Particle frequencies following low-serum and high-serum washout. Reference values for solvent control (0.3% DMSO) and inhibited/pre wash-out (5μM **8**) states are shown as checked bars in both (A and B). These values are also shown in Figure 4F and 4G, respectively, and are included here for reference. Bars represent mean ± S.D. Data analysis (V_a, anterograde velocity, nm/s; V_r, retrograde velocity, nm/s; F_a, anterograde frequency, counts/minute; F_r, retrograde frequency, counts/minute; values are mean ± S.D. N_a, number of anterograde particles analyzed; N_r, number of retrograde particles analyzed; C, number of cilia analyzed). 0.2% FBS washout, V_a 620 ± 134, V_r 219 ± 117, F_a 10.1 ± 4, F_r 5.2 ± 2, N_a 111, N_r 57, C 11. 10% FBS washout, V_a 660 ± 112, V_r 441 ± 156, F_a 18.8 ± 5, F_r 12.4 ± 6, N_a 283, N_r 186, C 16.

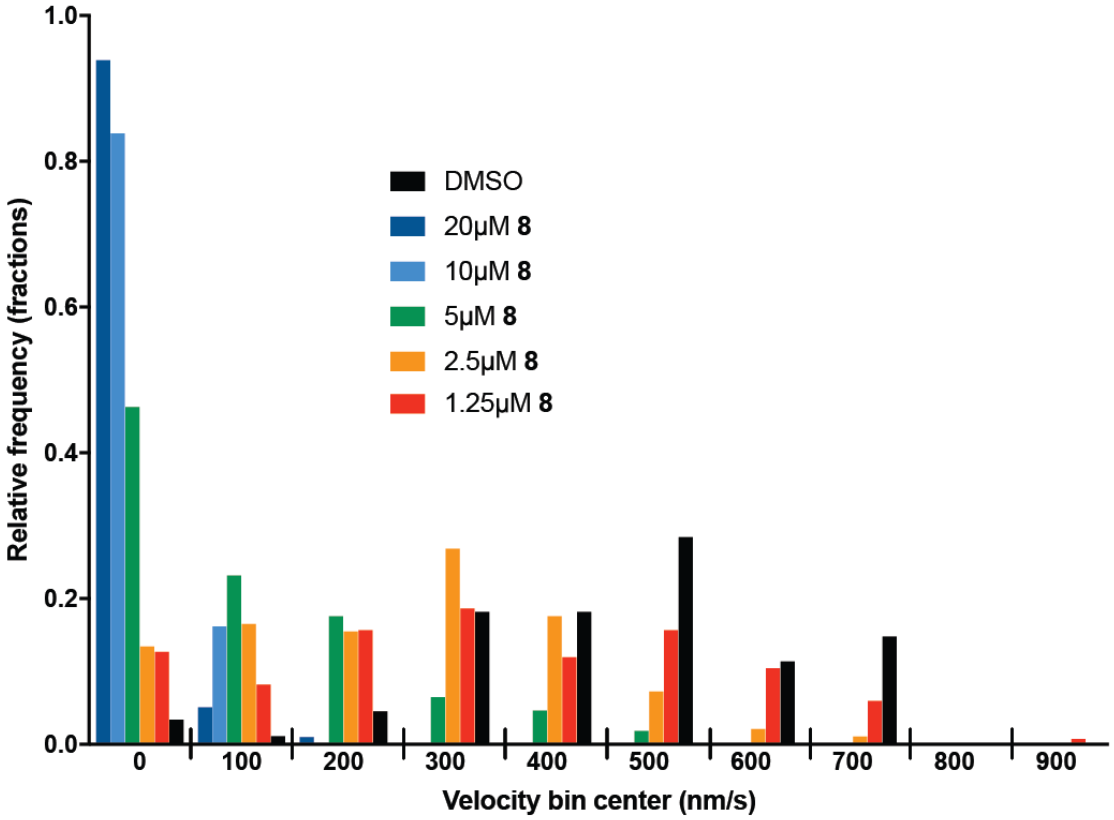

Figure 5 Figure Supplement 1: Microtubule velocity distribution histograms for dynein-1 driven motion associated with different concentrations of **8**. At least 88 microtubules were analyzed per experimental condition.

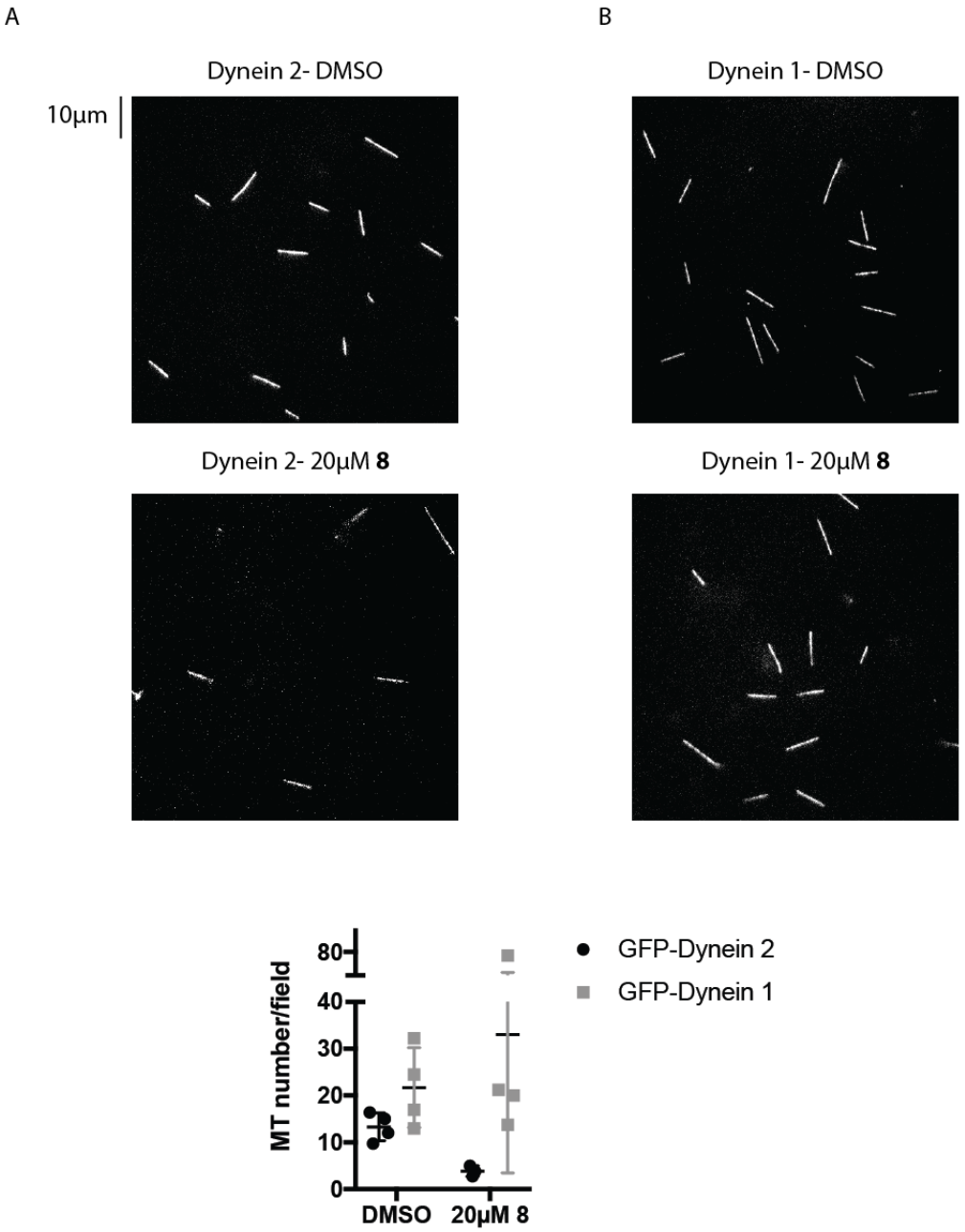

Figure 5 Figure Supplement 2: Analysis of the number of microtubules associated with coverslips in microtubule gliding assays. (A, B) Images from time-lapse movies of microtubule motility driven by GFP-dynein 2 (A) or GFP-dynein 1 (B) at 1 mM MgATP. Scale bar, 10 μm. (C) Quantification of microtubule number. Each data point represents the average count of microtubules in 4 fields of view in a single independent experiment. Mean ± S.D from n ≥ 3 experiments.

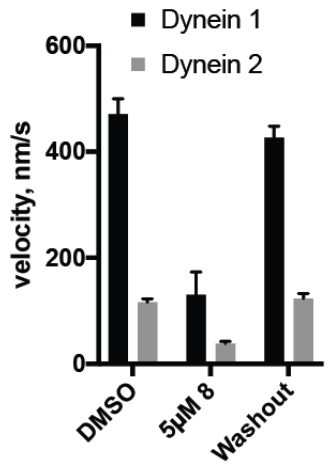

Figure 5 Figure Supplement 3: Reversibility of inhibition by **8**. The GFP-dynein 1 and GFP-dynein 2 motility assays were conducted at 1mM ATP and 0.05mg/ml casein. Chambers exposed to inhibitor (5μM **8**) were imaged and then buffer A (see motility methods) supplemented with 1mM ATP was flowed into the chamber, followed by a one minute incubation. This process was repeated twice and then reaction mix containing 2% DMSO and 1mM ATP was flowed into the chamber using ~4 chamber volumes and the chambers were then sealed. Time-lapse movies of the washout condition were taken 10-15 minutes after last addition of reaction mix. Data shown reflect average of n = 3 washout experiments (± S.D.) and n = 2 for the DMSO controls (± range).

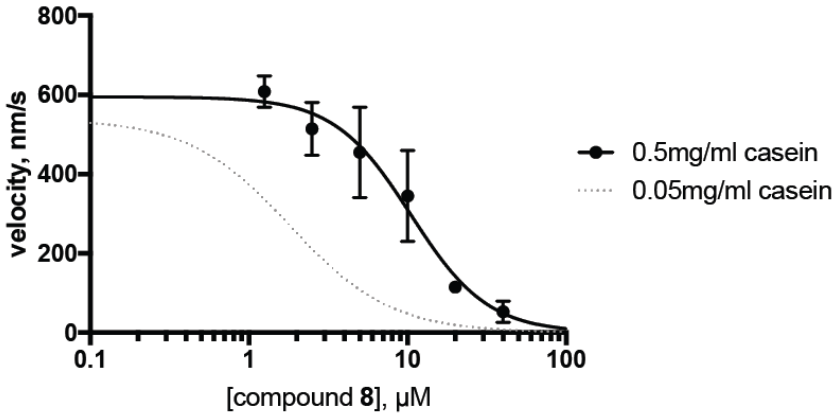

Figure 5 Figure Supplement 3: Analysis of the effect of blocking agent on inhibition. The GFP-dynein 1 motility assay was conducted at 1mM ATP in a reaction mix containing 0.5 mg/ml casein. Mean data from 3 experiments are shown (± S.D). In the presence of 0.5mg/ml casein, the IC_{50} was 10.5 ± 4.6 μM (n = 3, mean of 3 separate IC_{50} fits, ± S.D.). Curves shown represent fit to average value for a given compound concentration. The curve shown in grey reflects the same data as used in Figure 5D (IC_{50} = 2.3 μM).

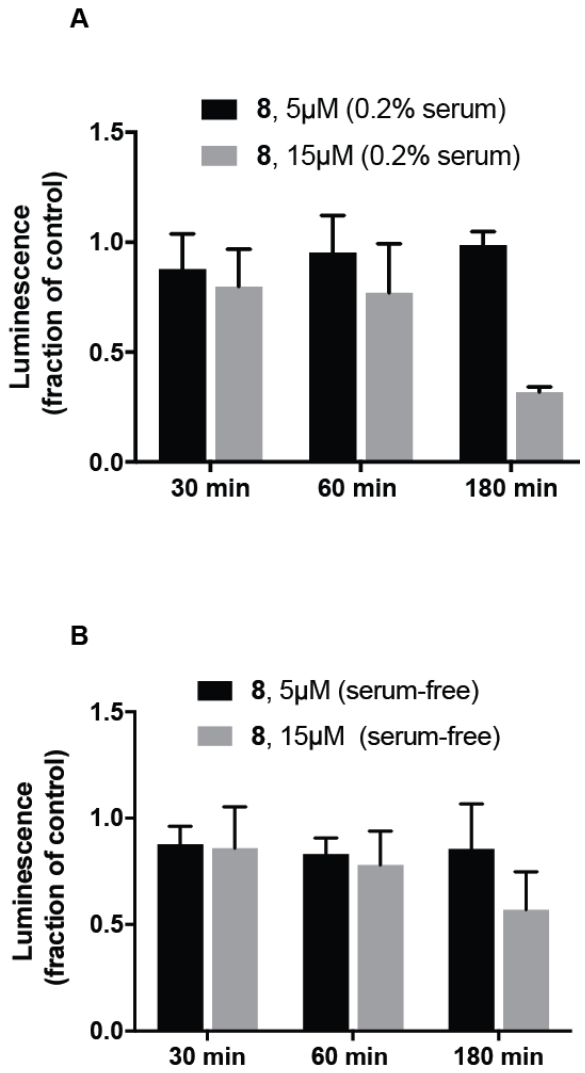

Figure 5 Figure Supplement 5: Analysis of the effect of dynapyrazole-A on intracellular ATP concentrations. IMCD3 cells incubated in either low-serum (A-0.2% FBS) or serum-free (B) media were treated with dynapyrazole-A (5μM, 15μM) over the course of 3 hours. Cellular ATP content was measured using the CellTiter-glo assay system. Bars represent mean ± S.D. of n = 3 independent replicates.

Dynein 1 WT, main band: 243 unique peptides, 80% sequence covereage

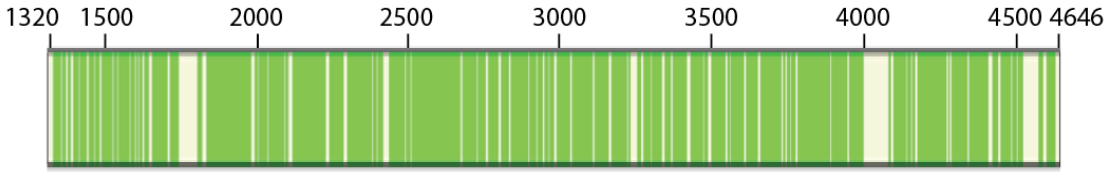

Dynein 1 WT, lower (proteolytic) band: 189 unique peptides, 62% sequence covereage

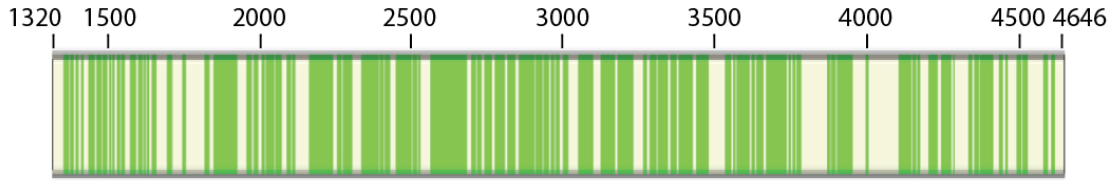

	Top (Main) Band	Lower (Proteolytic) Band
Proteins identified with Uniprot accession code (# of unique peptides identified if > 10)	Human Cytoplasmic Dynein 1 Heavy Chain Q14204 (243)	Human Cytoplasmic Dynein 1 Heavy Chain Q14204 (189)
		Human Desmoplakin P15924 (16)

Figure 6 Figure Supplement 1: Mass spectrometry-based analysis of wild-type His-dynein 1. Protein sample was run on an SDS-PAGE gel. The largest band at >350KDa and a minor band (indicated with triangles in Figure 6B) were excised from a gel separately and analyzed. Peptides identified by mass spectrometry are indicated (green bars, schematic generated using Proteome Discoverer 1.4, Thermo Scientific). Common contaminants are excluded (e.g. trypsin, keratin). The minor band was also identified as His-dynein 1, and is likely a product of partial proteolysis.

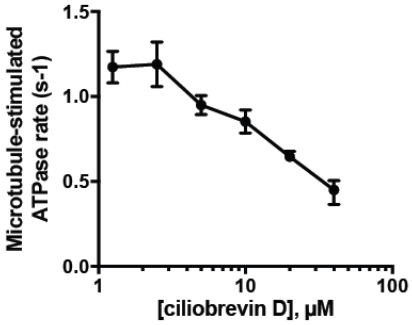

Figure 6 Figure Supplement 2: Dose-dependent inhibition of microtubule-stimulated His-dynein 1 ATPase activity by ciliobrevin D (2.5 μM microtubules). Data are presented as mean ± range, n ≥ 2.

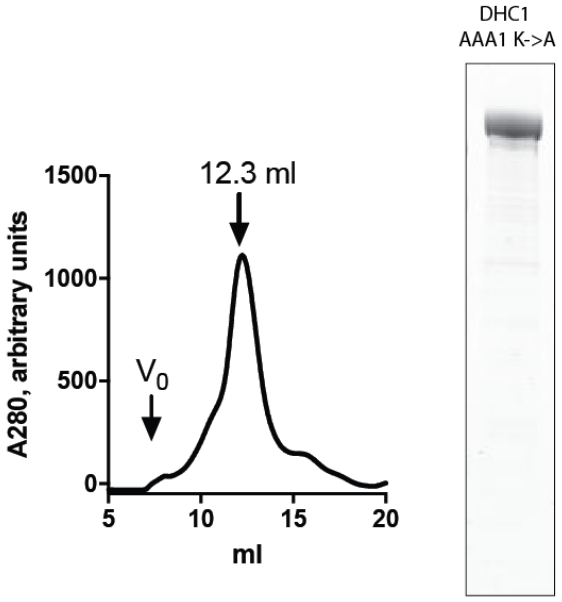

Figure 6 Figure Supplement 3: Purification and testing of His-dynein 1 with Walker A mutation in AAA1. Gel filtration trace (Superose 6) for His-dynein 1 with K1912A (AAA1 Walker A lysine to alanine), with volume at elution peak indicated. SDS-PAGE analysis (Coomassie stain) of this protein, ~0.5 μg protein loaded. V_o, void volume. The ATPase activity for this enzyme was measured as 0.05-0.1s^{-1}, and was < 2x above background hydrolysis in the absence of enzyme.

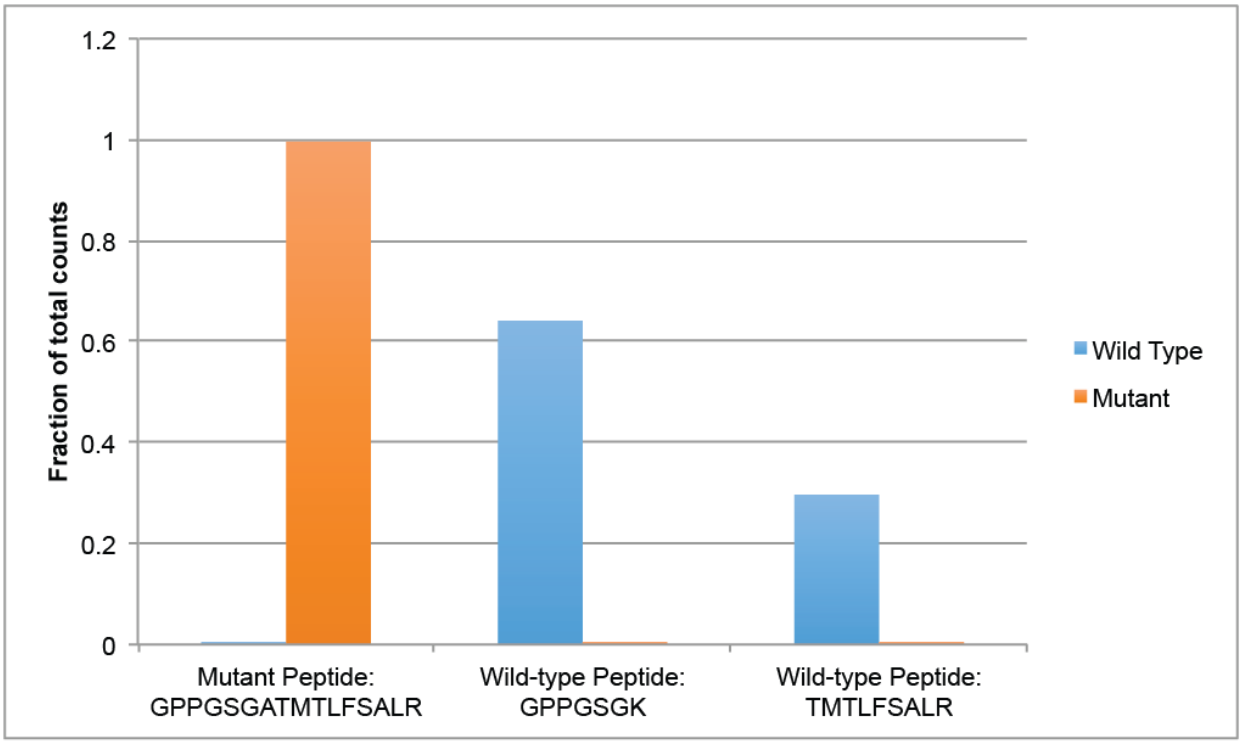

Figure 6 Figure Supplement 4: Mass spectrometry-based analysis of His-dynein 1 with Walker A mutation in AAA3. Protein samples of wild-type and mutant (K2601A, AAA3 Walker A lysine to alanine) were run in separate lanes of an SDS-PAGE gel. Gel bands for each protein were excised, trypsinized, and peptides allowing for the differentiation of dynein 1 wild-type and mutant (all in the Walker A region) as were peptides that could serve as a loading control were targeted in a parallel reaction monitoring experiment(145). Data were analyzed using Skyline(146) combined with ProteomeDiscoverer 1.4 (Thermo Fisher) and Mascot (Matrix Science). For each protein, peptide counts for the peptides GPPGSGATMTLFSALR, GPPGSGK, and TMTLFSALR, were divided by the sum of counts for all three peptides and this value is presented below. GPPGSGATMLFSALR peptide is expected in the AAA3 mutant while GPPGSGK and TMTLFSALR are expected in the wild-type enzyme.

Figure 6 Figure Supplement 5: Sequence analysis of human cytoplasmic dynein isoforms 1 and 2. Alignments were performed using the ClustalW algorithm for the following protein fragments: (A) human dynein 1 AAA1 (T1882-Y2193) and human dynein 1 AAA3 (T2571-L2911) (B) human dynein 1 AAA1 (T1882-Y2193) and human dynein 2 AAA1 (T1665-I1954). Residues in in black boxes are identical across isoforms. Red stars denote residues < 4Å from the nucleotide (ADP-Vanadate) in AAA1 of human dynein 2 (PDB 4RH7). Some residues within this 4Å shell are not included in this sequence alignment because they are located in adjacent AAA domains. Domain boundaries were chosen based on analysis of available crystal structures and sequence alignments. Uniprot accession numbers: dynein 1-Q14204 dynein 2-Q8NCM8.

A

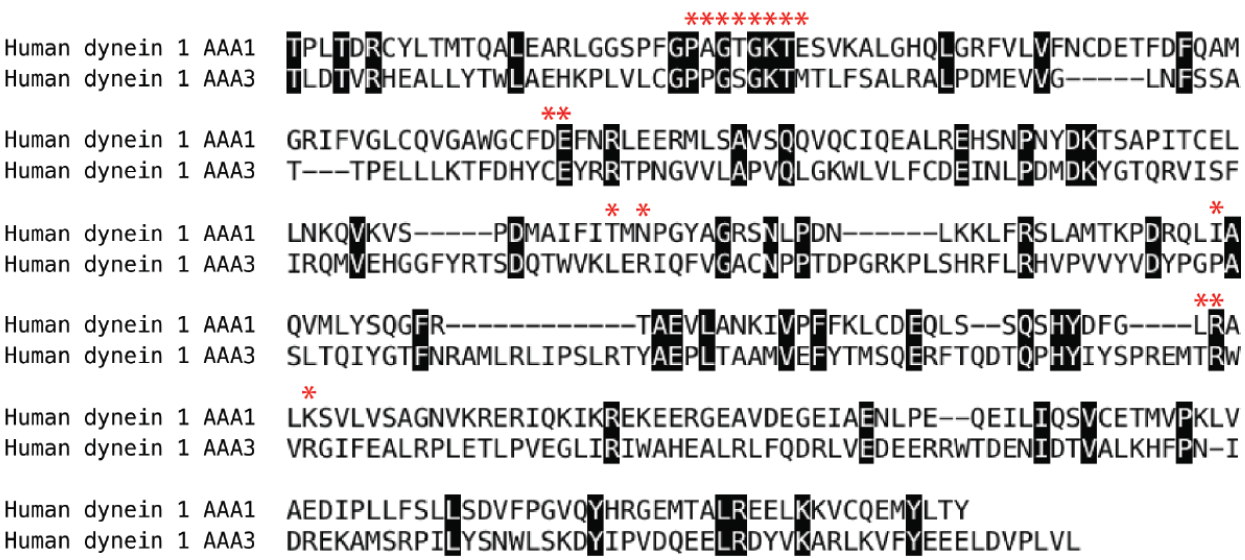
Human dynein 1 AAA1
Human dynein 1 AAA3

B

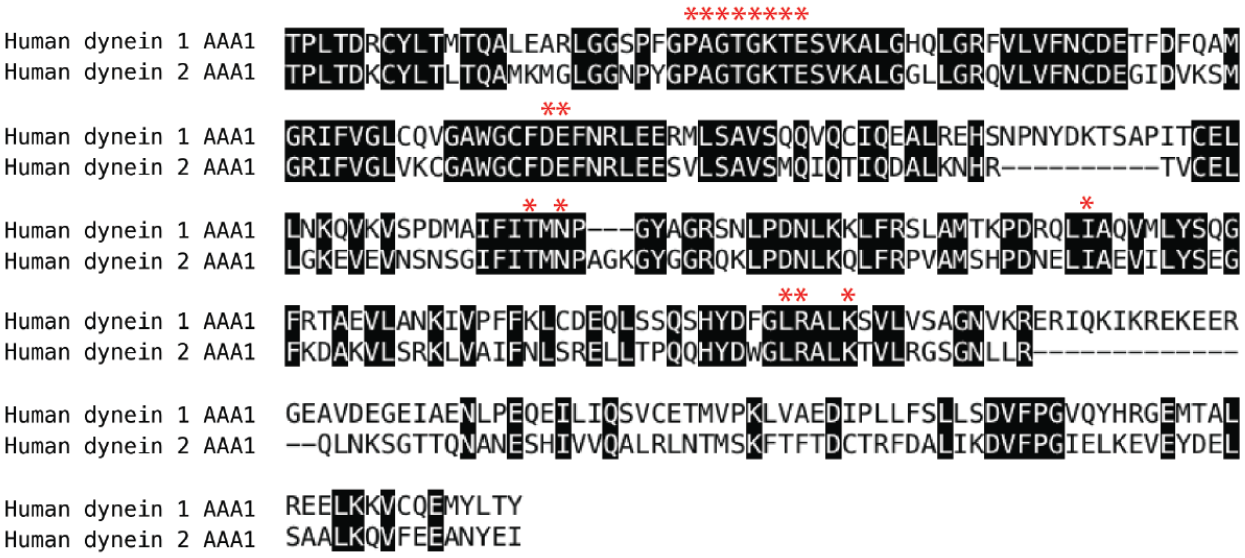
Human dynein 1 AAA1
Human dynein 2 AAA1

Appendix 3.1

Structure-activity trends for compounds with aminopyrazole core

Appendix 3.1

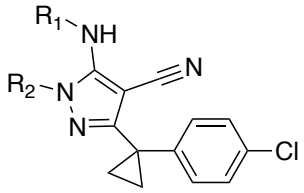

R_1/R2	TDI number	% Resid. Hh. Activity at 2μM (range)
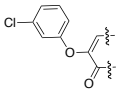	3016	33.1 (19-48)
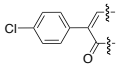	3021	42.3 (27-57)
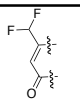	3491	52.2 (45-59)
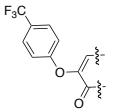	3022	54.7 (53-57)
	3447	55.7 (51-60)
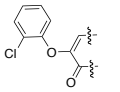	3027	63.3 (53-74)
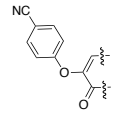	3026	63.5 (47-80)
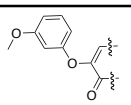	3363	68.9 (51-87)
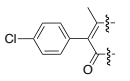	3526	72.1 (60-84)
	3470	72.4 (69-75)

Appendix 3.1
continued

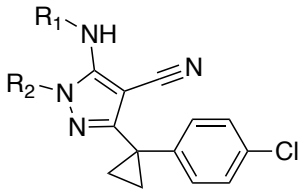

R_1/R2	TDI number	% Resid. Hh. Activity at 2μM (range)
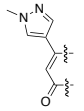	3502	73.1 (63-83)
	3492	75.1 (57-94)
	3495	78.1 (68-89)
	3463	81.4 (77-86)
	3453	82.8 (78-88)
	3776	82.9 (80-86)
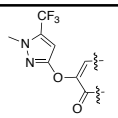	3156	85.4 (83-87)
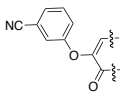	3563	86.9 (73-101)
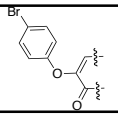	3161	91.3 (88-94)
	3722	98.5 (81-116)
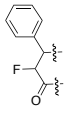	3738	102.4 (90-114)

Appendix 3.2:

Biochemical analysis of the effect of TDI 4692 on dynein 1

Legend for appendix 3.2: (A) Chemical structure of TDI 4692. (B) Dose-dependent inhibition of basal (black) and microtubule-stimulated (grey) ATPase activity of wild-type His-dynein 1 by TDI 4692. Data are mean ± range. of n = 2 experiments and were fit to a sigmoidal dose-response curve in Prism. ATPase assays were performed at 1mM Mg-ATP and 2% DMSO. (C) SDS-PAGE analysis (Coomassie blue) of dynein 1 following irradiation with ultraviolet light at 365nm. Components of reaction loaded into each lane are noted above gel. Arrowheads indicate proteolysis products. (D) Analysis of gel band intensity for photocleavage reactions. Data are mean ± S.D. of n = 3 experiments. (E) Inhibition of recombinant GFP-dynein 1. Data are mean ± S.D. of n = 3 separate experiments and were fit to a sigmoidal dose-response curve using Prism. (F) Reversibility of inhibition by TDI 4692 in microtubule gliding assay. Data are mean + range of n = 2 experiments. (G-H) Images from negative stain electron microscopy. GFP-dynein 1 was pre-incubated with TDI 4692 (4μM), ATP (1mM), and sodium vanadate (1mM) before fixation. (G) raw images of individual particles. (H) vector pointing to each protrusion is emphasized in yellow. The angle between these two vectors is measured. (I) Histogram showing distribution of angles. θ was measured for > 1000 particles. *Electron microscopy grid preparation and image acquisition were performed by Zhen Chen*.

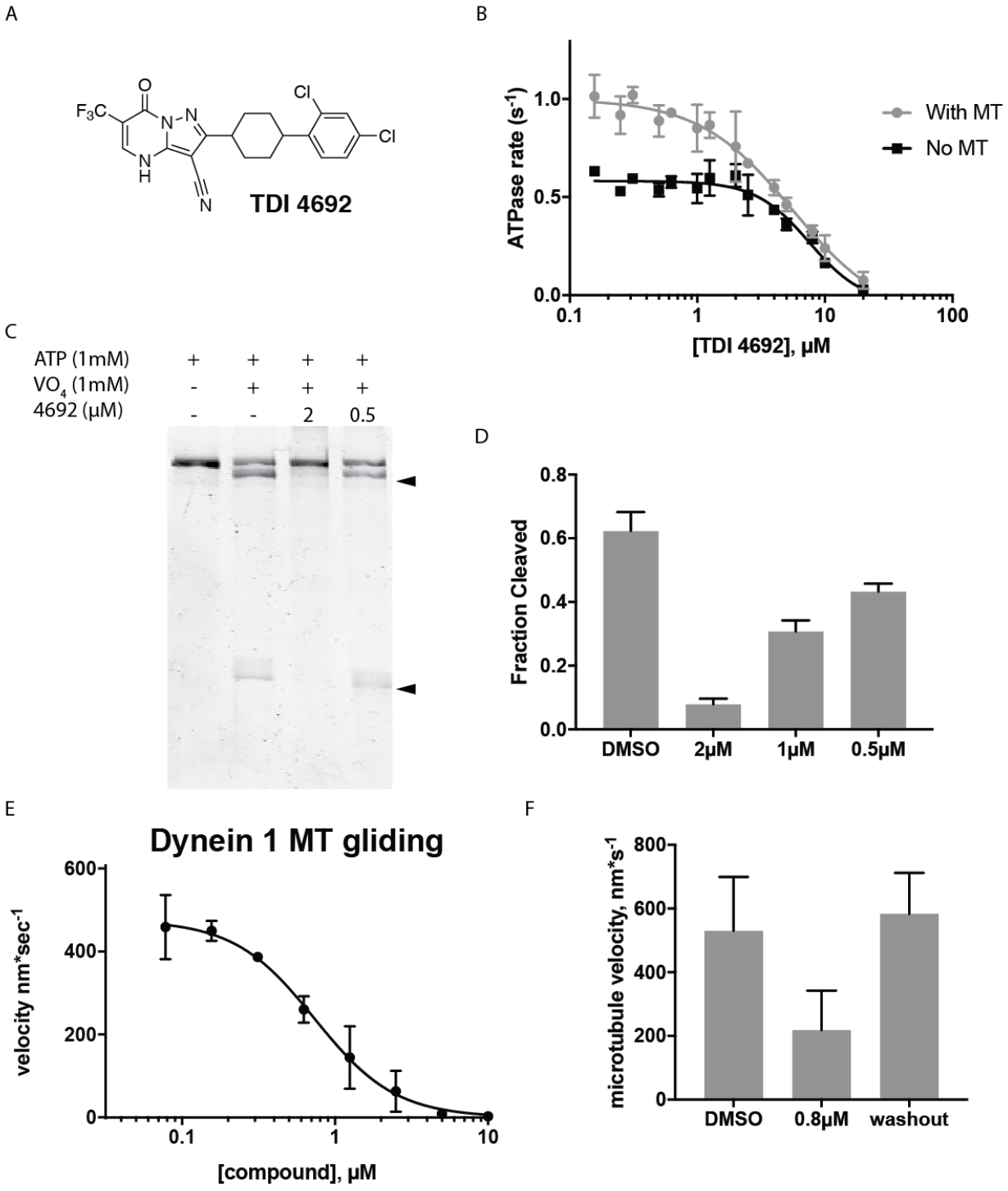

(continued on following page)

G

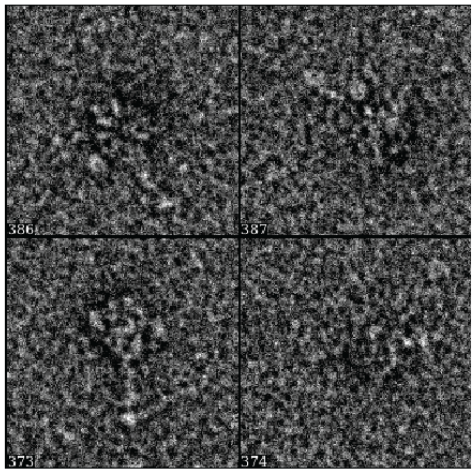
386
387
373
374

H

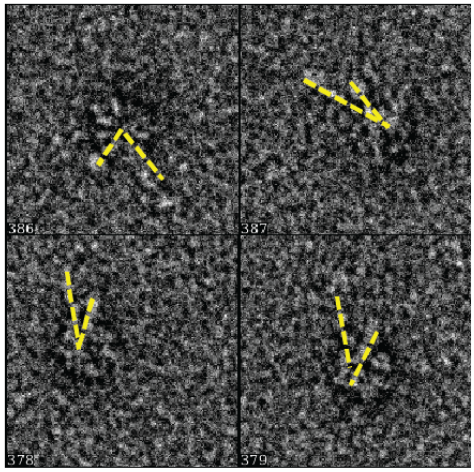
386
387
378
379

I

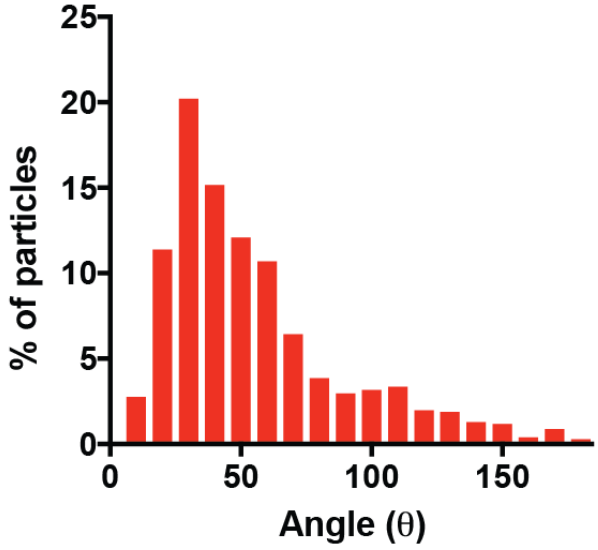
25
20
15
10
5
0
% of particles
0
50
100
150
Angle (θ)

Appendix 4.1

Screening for inhibitors of the ATPase activity of dynein

Plate maps: Compounds were arrayed in triplicate, with each well for a given compound containing a different concentration. DMSO stock concentrations were 5mM, 1mM, and 0.2mM. For every set of three boxes for a given compound, the compound name is given in the leftmost, and the compound number is given in the other two. Compound identities are tabulated at the end of this appendix.

Plate 1:

	1	2	3	4	5	6	7	8	9	10	11	12	13	14	15	16	17	18	19
A	Linsitinib	1	1	GDC-0941	3	3	Dactolisib	5	5	RIBIN-ZC3	7	7	CilD	9	9	DBeQ	11	11	dmso
B	Sorafenib	2	2	Iniparib	4	4	Vemurafenib	6	6	RIBIN-ZC1-3	8	8	HPI-102	10	10	TC12	12	12	dmso
C	TC13	13	13	TC17	15	15	TC19	17	17	TC25	19	19	TC28	21	21	ML240(TC31)	23	23	dmso
D	TC16	14	14	TC18	16	16	TC20	18	18	TC27	20	20	TC30	22	22	TC34	24	24	dmso
E	TC39	25	25	TC43	27	27	TC50	29	29	TC54	31	31	TC56	33	33	TC58	35	35	dmso
F	TC40	26	26	TC44	28	28	TC53	30	30	TC55	32	32	TC57	34	34	TC59	36	36	dmso
G	TC60	37	37	TC62	39	39	TC64	41	41	TC66	43	43	TC68	45	45	TC70	47	47	dmso
H	TC61	38	38	TC63	40	40	TC65	42	42	TC67	44	44	TC69	46	46	TC73	48	48	dmso
I	TC76	49	49	TC78	51	51	TC82	53	53	TC84	55	55	TC86	57	57	TC88	59	59	dmso
J	TC77	50	50	TC80	52	52	TC83	54	54	TC85	56	56	TC87	58	58	TC90	60	60	dmso
K	TC91	61	61	TC96	63	63	TC97	65	65	TC100	67	67	TC104	69	69	TC108	71	71	dmso
L	TC95	62	62	TC98	64	64	TC108SYM	66	66	TC103	68	68	TC107	70	70	TC111	72	72	dmso
M	TC108re	73	73	TC116	75	75	TC126	77	77	TC131	79	79	TC140	81	81	TC142	83	83	dmso
N	TC114	74	74	TC124	76	76	TC129	78	78	TC136	80	80	TC141	82	82	TC143	84	84	dmso
O	TC144	85	85	TC147	87	87	TC149	89	89	TC151	91	91	RAF-265	93	93	TC155	95	95	dmso
P	TC146	86	86	TC148	88	88	TC150	90	90	TC153	92	92	dmso	dmso	dmso	TC156	96	96	dmso

Plate 2:

	1	2	3	4	5	6	7	8	9	10	11	12	13	14	15	16	17	18
A	TC-165	1	1	TC-187	3	3	TC-211	5	5	TC-250	7	7	TC-267	9	9	JNJ 7706621	11	11
B	TC-184	2	2	TC-197	4	4	TC-236	6	6	TC-259	8	8	TC-275	10	10	PI-103	12	12
C	TC-168	13	13	TC-188	15	15	TC-212	17	17	TC-251	19	19	TC-268	21	21	NSC 693868	23	23
D	TC-185	14	14	TC-199	16	16	TC-237	18	18	TC-260	20	20	TC-276	22	22	DYNACICLIB	24	24
E	TC-171	25	25	TC-189	27	27	TC-213	29	29	TC-252	31	31	TC-269	33	33	II-62	35	35
F	TC-159	26	26	TC-201	28	28	TC-240	30	30	TC-261	32	32	TC-277	34	34	ROSCOVITINE	36	36
G	TC-172	37	37	TC-190	39	39	TC-226	41	41	TC-253	43	43	TC-270	45	45	II-65	47	47
H	TC-160	38	38	TC-202	40	40	TC-243	42	42	TC-262	44	44	TC-278	46	46	PP3	48	48
I	TC-173	49	49	TC-191	51	51	TC-227	53	53	TC-255	55	55	TC-271	57	57	II-66	59	59
J	TC-162	50	50	TC-201F	52	52	TC-244	54	54	TC-263	56	56	TC-280	58	58	HESPERADIN	60	60
K	TC-177	61	61	TC-166	63	63	TC-230	65	65	TC-256	67	67	TC-272	69	69	BIX 01294	71	71
L	TC-163	62	62	TC-206	64	64	TC-247	66	66	TC-264	68	68	TC-282	70	70	SUNITINIB	72	72
M	TC-179	73	73	TC194	75	75	TC-231	77	77	TC-257	79	79	TC-273	81	81	CRIZOTINIB	83	83
N	TC-183	74	74	TC-207	76	76	TC-245	78	78	TC-265	80	80	TC-300	82	82	ZM 447439	84	84
O	TC-181	85	85	TC-195	87	87	TC-234	89	89	TC-258	91	91	TC-274	93	93	ARQ197	95	95
P	TC-186	86	86	TC-210	88	88	TC-249	90	90	TC-266	92	92	TC-301	94	94	VX680	96	96

Screening results: Data presented on the following pages are the mean residual ATPase activity value of replicate screens. Value is presented as a fraction of enzyme activity in the DMSO control wells. Please note that for plate 1, the compound in B16/17 is at 10x the intended concentration. In light of this error, this compound was not considered a screening hit and was not examined in follow-up assays.

Dynein 1 screen, plate 1 (compounds at 10μM):

	column ->	2	5	8	11	14	17
row	a	1.08	1.18	1.54	1.10	0.75	0.74
	b	1.08	1.05	1.05	1.10	0.92	0.33
	c	1.02	1.03	1.12	0.86	0.89	0.97
	d	1.08	0.90	0.95	0.94	0.85	0.84
	e	0.92	0.88	0.89	0.94	0.79	0.77
	f	0.82	0.75	0.85	0.82	0.81	0.87
	g	0.96	0.83	0.97	0.95	0.98	0.74
	h	0.85	0.92	0.95	0.76	0.89	0.82
	i	1.05	1.07	1.00	0.98	1.00	1.03
	j	0.81	1.06	0.76	0.61	0.98	0.84
	k	1.18	1.15	0.50	0.93	1.08	0.94
	l	1.12	0.83	0.94	1.12	0.93	0.90
	m	1.00	1.10	1.13	1.08	0.85	0.94
	n	1.12	0.78	1.12	0.97	1.01	0.92
	o	1.15	1.00	1.13	1.00	1.00	0.86
	p	0.93	0.85	0.98	0.97	0.99	0.75

Dynein 1 screen, plate 2 (compounds at 20μM)

	column->	2	5	8	11	14	17
row	a	1.16	0.94	0.92	0.81	0.63	0.39
	b	0.93	0.86	0.60	0.83	0.73	0.87
	c	0.80	0.57	0.21	0.74	0.61	0.71
	d	1.18	0.58	0.76	0.47	0.72	0.85
	e	1.08	0.78	0.99	0.83	0.81	0.64
	f	0.77	0.82	0.73	0.77	1.00	0.87
	g	1.10	0.60	0.95	0.83	0.81	0.61
	h	0.92	0.84	0.70	0.59	0.71	0.81
	i	0.87	0.86	0.96	0.66	0.80	0.74
	j	0.78	0.38	0.83	0.58	0.83	0.76
	k	0.87	0.81	0.93	0.74	0.71	0.49
	l	0.66	0.74	0.90	0.72	0.85	0.68
	m	0.86	0.83	0.94	0.71	0.70	0.87
	n	0.45	0.75	0.65	0.72	0.91	0.83
	o	0.76	0.91	1.00	0.91	0.86	0.78
	p	0.84	0.68	0.82	0.92	0.37	0.80

Dynein 2 screen, plate 1 (compounds at 50μM)

	column->	1	4	7	10	13	16
row	a	0.94	0.88	1.18	0.99	0.98	0.57
	b	1.02	1.00	0.99	1.10	1.10	0.09
	c	1.15	0.99	0.89	0.96	0.68	0.98
	d	1.10	0.62	1.00	0.99	0.94	0.77
	e	0.77	0.77	0.93	0.89	1.08	0.93
	f	0.69	0.93	0.87	0.93	0.89	1.00
	g	0.93	0.80	0.83	1.02	0.97	0.97
	h	0.97	0.80	0.82	0.63	0.79	0.89
	i	1.06	0.80	0.99	0.93	0.99	0.97
	j	0.90	1.14	0.83	0.57	1.00	0.02
	k	0.88	0.96	1.00	0.95	1.00	0.97
	l	1.02	0.94	0.92	0.96	0.95	0.92
	m	0.98	1.04	1.02	0.91	0.95	0.98
	n	1.12	0.37	0.96	0.99	1.04	1.00
	o	1.04	0.97	0.83	0.92	1.02	0.87
	p	1.14	0.97	0.96	0.97	1.02	0.63

Compound identity: Tables presented on the following pages contain structural information as well as plate locations for all compounds in screening plates.

Compound identities, plate 1

Kapoor LAB -80C freezer G

Chem ID	n	structure	scaffold typ	Position (f
TC-165	1	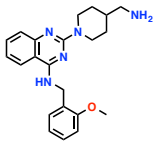	2,4 amino-quin	1A
TC-168	2	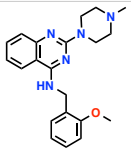	2,4 amino-quin	1B
TC-171	3	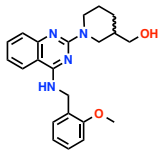	2,4 amino-quin	1C
TC-172	4	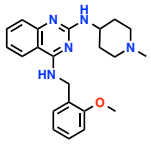	2,4 amino-quin	1D
TC-173	5	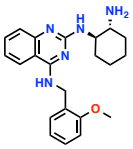	2,4 amino-quin	1E
TC-177	6	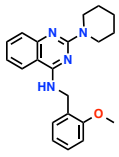	2,4 amino-quin	1F
TC-179	7	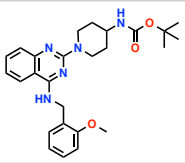	2,4 amino-quin	1G
TC-181	8	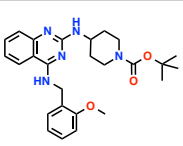	2,4 amino-quin	1H
TC-184	9	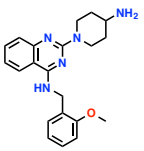	2,4 amino-quin	2A
TC-185	10	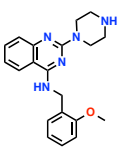	2,4 amino-quin	2B
TC-159	11	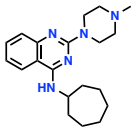	2,4 amino-quin	2C
TC-160	12	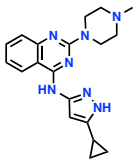	2,4 amino-quin	2D
TC-162	13	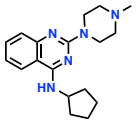	2,4 amino-quin	2E
TC-163	14	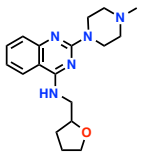	2,4 amino-quin	2F
TC-183	15	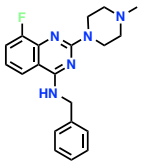	2,4 amino-quin	2G
TC-186	16	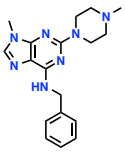	2,6 amino- pu	2H
TC-187	17	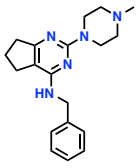	2,4 amino-cyclope	3A
TC-188	18	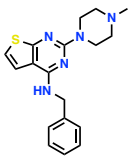	2,4 amino-thienc	3B
TC-189	19	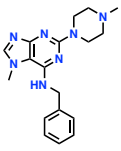	2,6 amino- pu	3C
TC-190	20	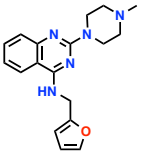	2,4 amino-quin	3D

Compound identities, plate 1

TC-191	21	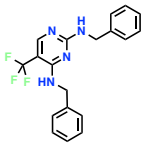	2,4 amino-p	3E
TC-166	22	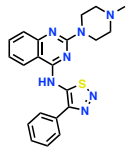	2,4 amino-c	3F
TC194	23	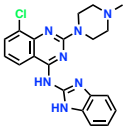	2,4 amino-c	3G
TC-195	24	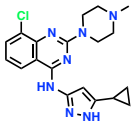	2,4 amino-c	3H
TC-197	25	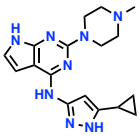	2,4 amino-py	4A
TC-199	26	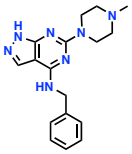	4,6 amino-py	4B
TC-201	27	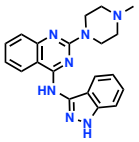	2,4 amino-c	4C
TC-202	28	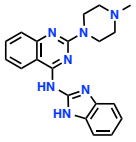	2,4 amino-c	4D
TC-201F	29	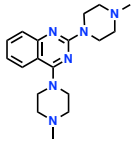	2,4 amino-c	4E
TC-206	30	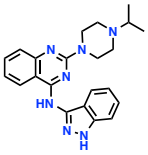	2,4 amino-c	4F
TC-207	31	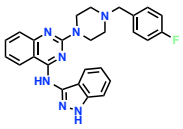	2,4 amino-quin	4G
TC-210	32	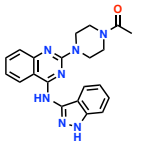	2,4 amino-quin	4H
TC-211	33	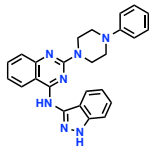	2,4 amino-quin	5A
TC-212	34	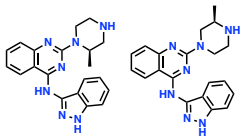	2,4 amino-quin	5B
TC-213	35	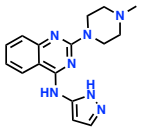	2,4 amino-quin	5C
TC-226	36	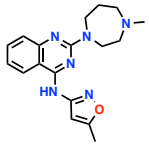	2,4 amino-quin	5D
TC-227	37	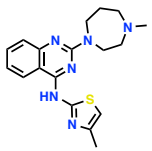	2,4 amino-quin	5E
TC-230	38	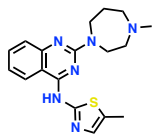	2,4 amino-quin	5F
TC-231	39	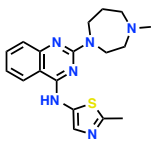	2,4 amino-quin	5G
TC-234	40	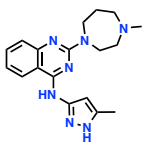	2,4 amino-quin	5H

Compound identities, plate 1

TC-236 (CYM50354)	41	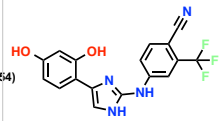	phenylimida	6A
TC-237	42	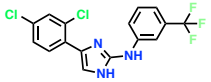	phenylimida	6B
TC-240	43	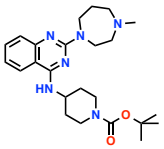	2,4 amino-c	6C
TC-243	44	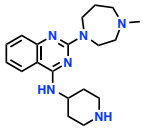	2,4 amino-c	6D
TC-244	45	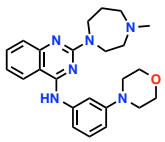	2,4 amino-c	6E
TC-247	46	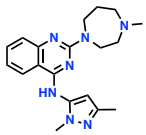	2,4 amino-c	6F
TC-245	47	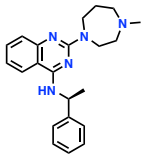	2,4 amino-c	6G
TC-249	48	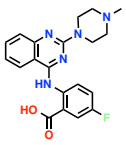	2,4 amino-c	6H
TC-250	49	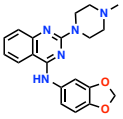	2,4 amino-c	7A
TC-251	50	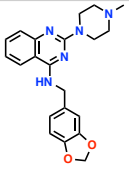	2,4 amino-c	7B
TC-252	51	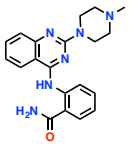	2,4 amino-quin	7C
TC-253	52	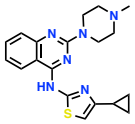	2,4 amino-quin	7D
TC-255	53	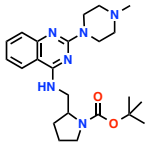	2,4 amino-quin	7E
TC-256	54	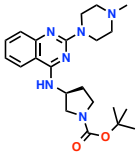	2,4 amino-quin	7F
TC-257	55	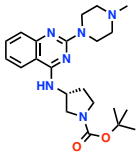	2,4 amino-quin	7G
TC-258	56		2,4 amino-quin	7H
TC-259	57	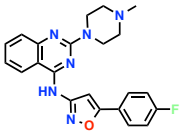	2,4 amino-quin	8A
TC-260	58	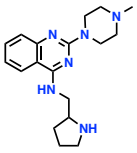	2,4 amino-quin	8B
TC-261	59	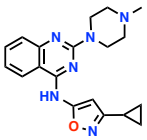	2,4 amino-quin	8C
TC-262	60		2,4 amino-quin	8D

Compound identities, plate 1

TC-263	61	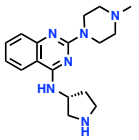	2,4 amino-c	8E
TC-264	62	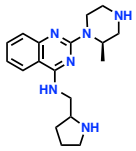	2,4 amino-c	8F
TC-265	63	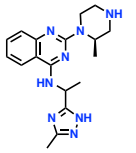	2,4 amino-c	8G
TC-266	64	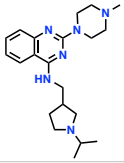	2,4 amino-c	8H
TC-267	65	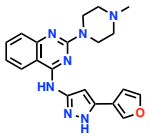	2,4 amino-c	9A
TC-268	66	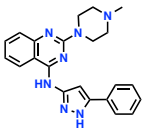	2,4 amino-c	9B
TC-269	67	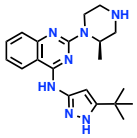	2,4 amino-c	9C
TC-270	68	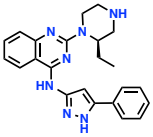	2,4 amino-c	9D
TC-271	69	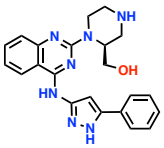	2,4 amino-c	9E
TC-272	70	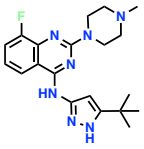	2,4 amino-c	9F
TC-273	71	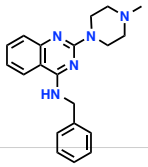	2,4 amino-c	9G
TC-274	72	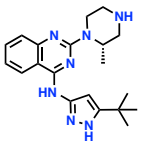	2,4 amino-c	9H
TC-275	73		2,4 amino-c	10A
TC-276	74	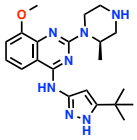	2,4 amino-c	10B
TC-277	75	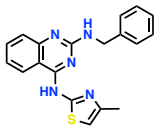	2,4 amino-c	10C
TC-278	76	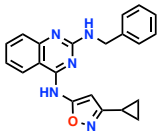	2,4 amino-c	10D
TC-280	77	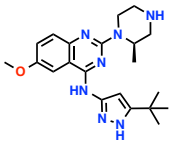	2,4 amino-c	10E
TC-282	78	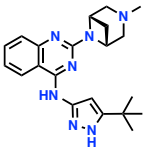	2,4 amino-c	10F
TC-300 Diazaborine	79	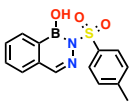	2,4 amino-c	10G
TC-301	80	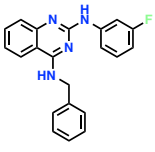	diazaborin	10H

Compound identities, plate 1

JNJ 7706621	81	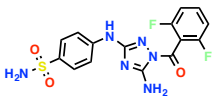	3,5-diamino tr	11A
NSC 693868 (AA	82	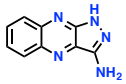	pyrazolo [3,4] qu	11B
II-62	83	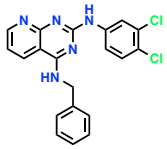	2,4 amino- pyrido	11C
II-65	84	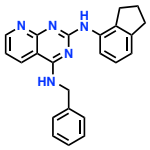	2,4 amino- pyrido	11D
II-66	85	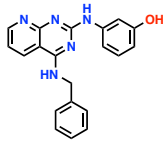	2,4 amino- pyrido	11E
BIX-01294	86	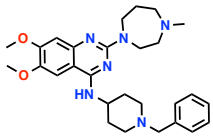	2,4 amino-quin	11F
Crizotinib	87	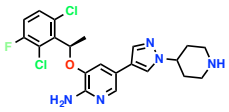	2-amino pyrazol	11G
ARQ-197 Kapoor Lab	88	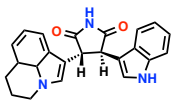	Bis-indolyl pyrr	11H
PI-103 (LC Labs)	89	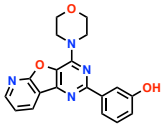	pyrido-furo-pyri	12A
Dinaciclib (LC Labs)	90	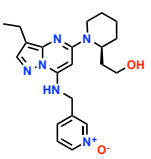	pirazolo-[1,5]a p	12B
Roscovitine (LC Labs)	91	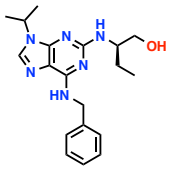	Purine-2,6-dia	12C
PP3 (Acros)	92	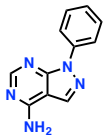	pirazolo-[3,4]d p	12D
Hesperadine Kapoor Lab	93	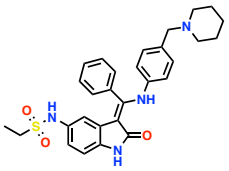	oxoindolin-3-ber	12E
Sunitinb	94	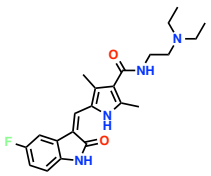	oxoindolin-3-yl	12F
ZM-447439 Kapoor Lab	95	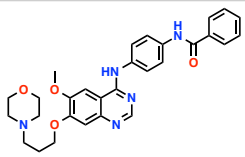	2-amino benzylo	12G
Tozasertib (LC Labs)	96	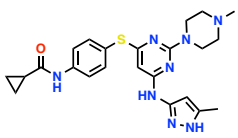	Phenylthio-pyrin amine	12H

Compound identities, plate 2

Chem ID	n	structure	scaffold type
TC-165	1	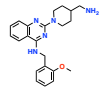	2,4 amino-quinazoline
TC-168	2	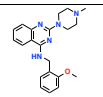	2,4 amino-quinazoline
TC-171	3	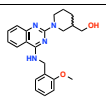	2,4 amino-quinazoline
TC-172	4	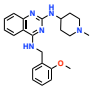	2,4 amino-quinazoline
TC-173	5	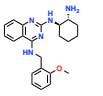	2,4 amino-quinazoline
TC-177	6	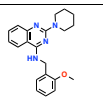	2,4 amino-quinazoline
TC-179	7	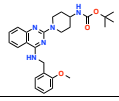	2,4 amino-quinazoline
TC-181	8	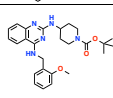	2,4 amino-quinazoline
TC-184	9	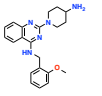	2,4 amino-quinazoline
TC-185	10	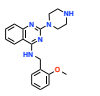	2,4 amino-quinazoline
TC-159	11		2,4 amino-quinazoline
TC-160	12	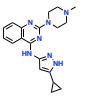	2,4 amino-quinazoline
TC-162	13	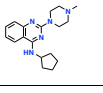	2,4 amino-quinazoline
TC-163	14	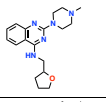	2,4 amino-quinazoline
TC-183	15	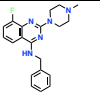	2,4 amino-quinazoline
TC-186	16	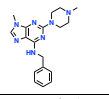	2,6 amino-purine
TC-187	17	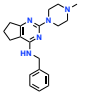	2,4 amino-cyclopenta pyrimidine
TC-188	18		2,4 amino-thieno pyrimidine
TC-189	19		2,6 amino-purine
TC-190	20	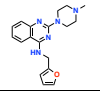	2,4 amino-quinazoline
TC-191	21	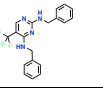	2,4 amino-pyrimidine
TC-166	22	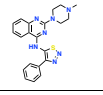	2,4 amino-quinazoline
TC194	23	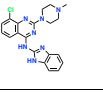	2,4 amino-quinazoline
TC-195	24	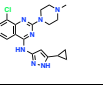	2,4 amino-quinazoline
TC-197	25	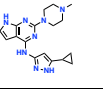	2,4 amino-pyrrolo pyrimidine
TC-199	26	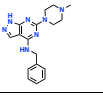	4,6 amino-pyrazolo pyrimidine
TC-201	27	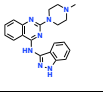	2,4 amino-quinazoline
TC-202	28	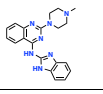	2,4 amino-quinazoline
TC-201F	29	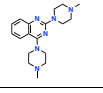	2,4 amino-quinazoline
TC-206	30	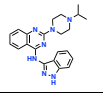	2,4 amino-quinazoline
TC-207	31	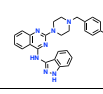	2,4 amino-quinazoline
TC-210	32	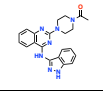	2,4 amino-quinazoline
TC-211	33	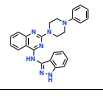	2,4 amino-quinazoline
TC-212	34	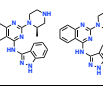	2,4 amino-quinazoline
TC-213	35	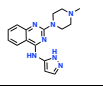	2,4 amino-quinazoline
TC-226	36	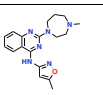	2,4 amino-quinazoline
TC-227	37	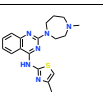	2,4 amino-quinazoline
TC-230	38	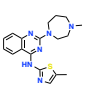	2,4 amino-quinazoline
TC-231	39	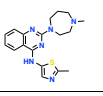	2,4 amino-quinazoline
TC-234	40	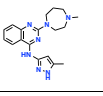	2,4 amino-quinazoline
TC-236 (CYM5654)	41	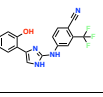	phenylimidazol-2-amine
TC-237	42	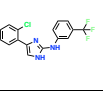	phenylimidazol-2-amine
TC-240	43	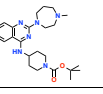	2,4 amino-quinazoline
TC-243	44	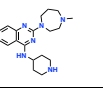	2,4 amino-quinazoline
TC-244	45	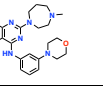	2,4 amino-quinazoline
TC-247	46	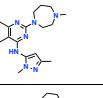	2,4 amino-quinazoline
TC-245	47	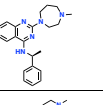	2,4 amino-quinazoline
TC-249	48	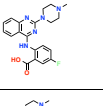	2,4 amino-quinazoline
TC-250	49	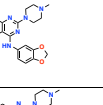	2,4 amino-quinazoline
TC-251	50	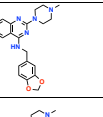	2,4 amino-quinazoline
TC-252	51	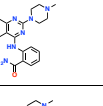	2,4 amino-quinazoline
TC-253	52	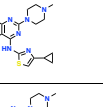	2,4 amino-quinazoline
TC-255	53	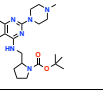	2,4 amino-quinazoline
TC-256	54	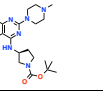	2,4 amino-quinazoline
TC-257	55	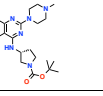	2,4 amino-quinazoline
TC-258	56	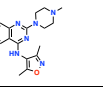	2,4 amino-quinazoline
TC-259	57	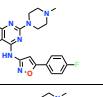	2,4 amino-quinazoline
TC-260	58	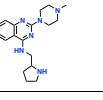	2,4 amino-quinazoline
TC-261	59	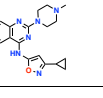	2,4 amino-quinazoline
TC-262	60	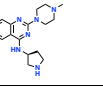	2,4 amino-quinazoline
TC-263	61	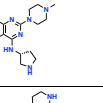	2,4 amino-quinazoline
TC-264	62	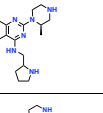	2,4 amino-quinazoline
TC-265	63	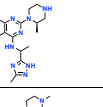	2,4 amino-quinazoline
TC-266	64	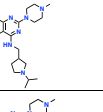	2,4 amino-quinazoline
TC-267	65	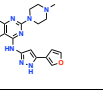	2,4 amino-quinazoline
TC-268	66	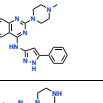	2,4 amino-quinazoline
TC-269	67	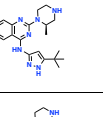	2,4 amino-quinazoline
TC-270	68	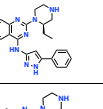	2,4 amino-quinazoline
TC-271	69	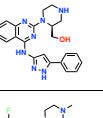	2,4 amino-quinazoline
TC-272	70	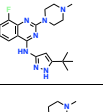	2,4 amino-quinazoline
TC-273	71	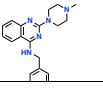	2,4 amino-quinazoline

Compound identities, plate 2, continued

TC-274	72	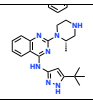	2,4 amino-quinazoline
TC-275	73	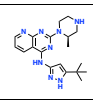	2,4 amino-quinazoline
TC-276	74	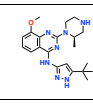	2,4 amino-quinazoline
TC-277	75		2,4 amino-quinazoline
TC-278	76	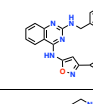	2,4 amino-quinazoline
TC-280	77	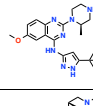	2,4 amino-quinazoline
TC-282	78		2,4 amino-quinazoline
-300 Diazoborin	79	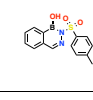	2,4 amino-quinazoline
TC-301	80	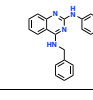	diazaborinine
JNJ 7706621	81	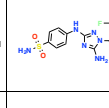	3,5-diamino triazol
NSC 693868 (AA ChemBio)	82	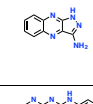	pyrazolo [3,4] quinoxaline
II-62	83	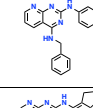	2,4 amino-pyrido pyrimidine
II-65	84	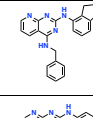	2,4 amino-pyrido pyrimidine
II-66	85	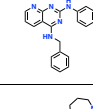	2,4 amino-pyrido pyrimidine
BIX-01294	86	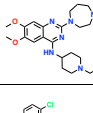	2,4 amino-quinazoline
Crizotinib	87	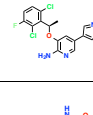	2-amino pyrazolyl pyrimidine
ARQ-197 Kapoor Lab	88	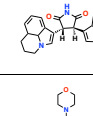	Bis-indolyl pyrrolidine
PI-103 (LC Labs)	89	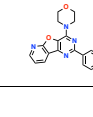	pyrido-furo-pyrimidine
Dinaciclib (LC Labs)	90	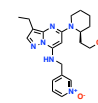	pirazolo-[1,5]a pyrimidine
Roscovitine (LC Labs)	91	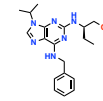	Purine-2,6-diamine
PP3 (Acros)	92	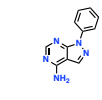	pirazolo-[3,4]d pyrimidine
Hesperadine Kapoor Lab	93	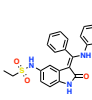	oxoindolin-3-benzylidene
Sunitinb	94	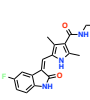	oxoindolin-3-ylidene
ZM-447439 Kapoor Lab	95		2-amino benzoylquinazolin e
Tozasertib (LC Labs)	96	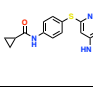	Phenylthio-pyrimidine- 2,4 amine

Appendix 4.2

Inhibition of AAA+ proteins by JNJ7706621

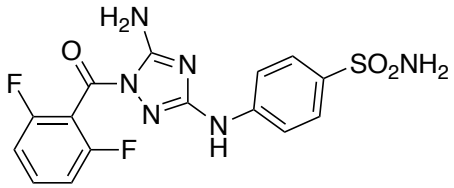

JNJ 7706621

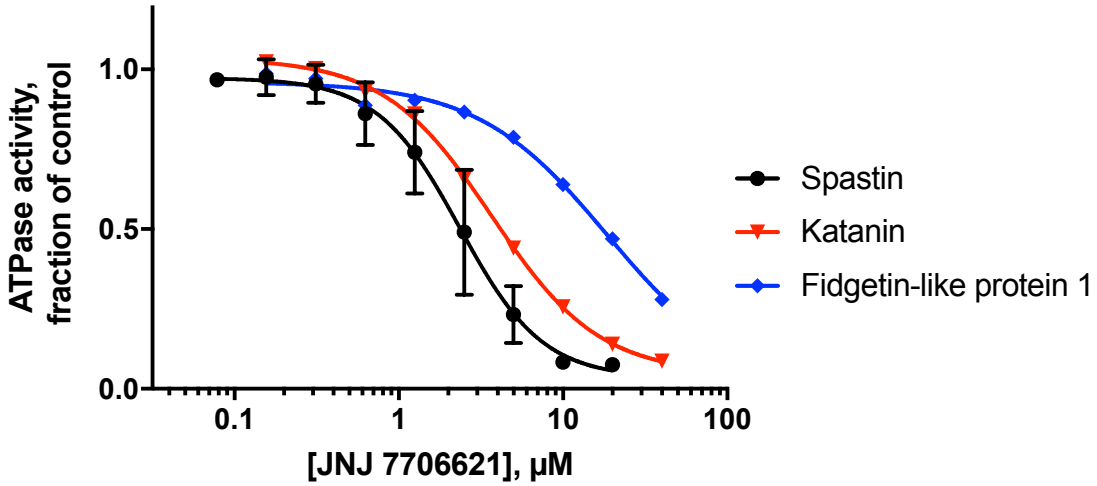

Legend: Top, chemical structure of JNJ7706621. Bottom dose-response analysis for effect of JNJ 7706621 on ATPase activity of AAA+ proteins. ATPase activity was measured using NADH-coupled ATPase assay system at 500μM ATP. Where shown, error bars reflect range. Values were fit to a sigmoidal dose-response curve in prism and fits were constrained such that the value at saturating compound concentrations > 0. IC_{50} values: spastin-2.4μM, katanin-3.7μM, fidgetin-like protein 1-18.7. *Enzyme preparation was performed by Tommaso Cupido*.

Appendix 4.3

Synthesis and characterization of compounds informed by screen of diaminoqunazolines for inhibitors of dynein

General synthetic methods: Reagents and solvents were used as received. Unless otherwise specified, precautions were not taken to exclude oxygen or moisture from reactions. LC/MS analysis was performed using a Waters MicroMassZQ mass spectrometer, with an electron spray ionization (ESI) probe. Liquid chromatographic separation was performed with a Symmetry® C18 column. Analysis was performed using MassLynx. ^{1}H NMR data was acquired using a varian (400MHz) or Bruker (600MHz) device and analyzed using MestreNova® or TopSpin®. NMR data have been collected and analysis and assignment of spectra are ongoing. Assignments can be provided in an addendum to this thesis.

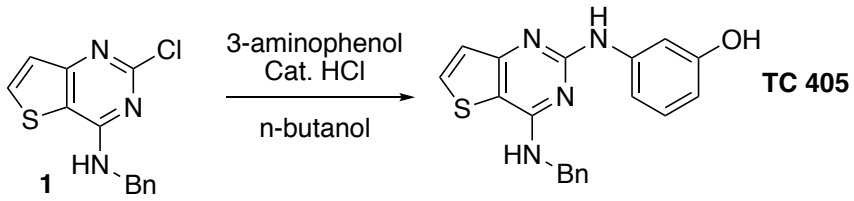

3-((4-(benzylamino)thieno[3,2-*d*]pyrimidin-2-yl)amino)phenol, TC 405. A mixture of **1** (25mg, 0.09mmol, synthesized by T. Cupido), 3-aminophenol (20mg, 0.18mmol), and concentrated hydrochloric acid (10μl) were refluxed in n-butanol (1ml) overnight. After cooling, hexane was added and a precipitate formed. The precipitate was collected by filtration and washed with water and methanol and then dried under vacuum. 9.8mg of **TC 405** were obtained (31% yield). LC/MS: 349.82 $[M+H]^{+}$.

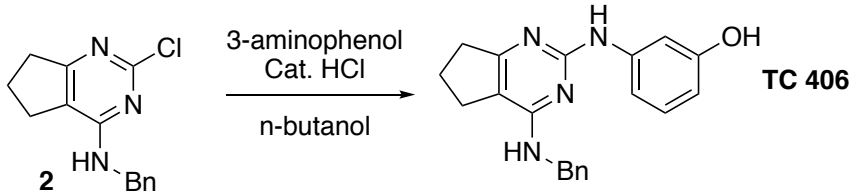

3-((4-(benzylamino)-6,7-dihydro-5*H*-cyclopenta[*d*]pyrimidin-2-yl)amino)phenol, TC 406. A mixture of **2** (25mg, 0.1mmol, synthesized by T. Cupido), 3-aminophenol (20mg, 0.18mmol), and concentrated hydrochloric acid (10μl) were refluxed in n-butanol (1ml) overnight. After cooling, hexane was added and a precipitate formed. The precipitate was

collected by filtration and washed with water and methanol and then dried under vacuum. 4.5mg of **TC 406** were obtained (14% yield). LC/MS: 333.85 $[M+H]^+$.

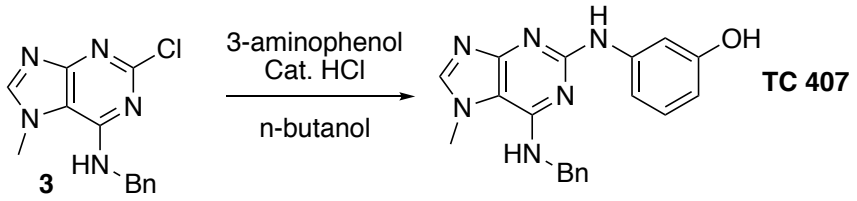

3-((6-(benzylamino)-7-methyl-7*H*-purin-2-yl)amino)phenol, TC 407. A mixture of **3** (25mg, 0.09mmol, synthesized by T. Cupido), 3-aminophenol (20mg, 0.18mmol), and concentrated hydrochloric acid (10μl) were refluxed in n-butanol (1ml) overnight. After cooling, hexane was added and a precipitate formed. The precipitate was collected by filtration and washed with water and methanol and then dried under vacuum. 20.7mg of **TC 407** were obtained (66% yield). LC/MS: 347.87 $[M+H]^+$.

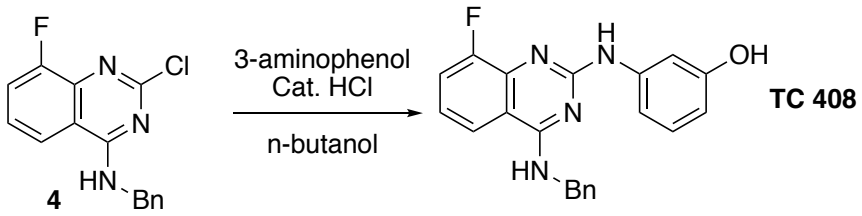

3-((4-(benzylamino)-8-fluoroquinazolin-2-yl)amino)phenol, TC 408. A mixture of **4** (25mg, 0.09mmol, synthesized by T. Cupido), 3-aminophenol (20mg, 0.18mmol), and concentrated hydrochloric acid (10μl) were refluxed in n-butanol (1ml) overnight. After cooling, hexane was added and a precipitate formed. The precipitate was collected by filtration and washed with water and methanol and then dried under vacuum. 11.5mg of **TC 408** were obtained (35% yield). LC/MS: 361.81 $[M+H]^+$.

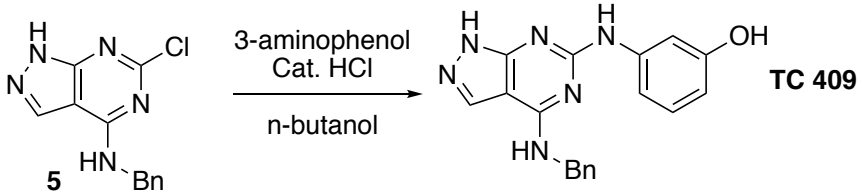

3-((4-(benzylamino)-1*H*-pyrazolo[3,4-*d*]pyrimidin-6-yl)amino)phenol, TC 409. A mixture of **5** (25mg, 0.09mmol, synthesized by T. Cupido), 3-aminophenol (20mg, 0.18mmol), and concentrated hydrochloric acid (10μl) were refluxed in n-butanol (1ml) overnight. After cooling, hexane was added and a precipitate formed. The precipitate was collected by filtration and washed with water and methanol and then dried under vacuum. 4.8mg of **TC 409** were obtained (16% yield). LC/MS: 333.85 $[M+H]^+$.

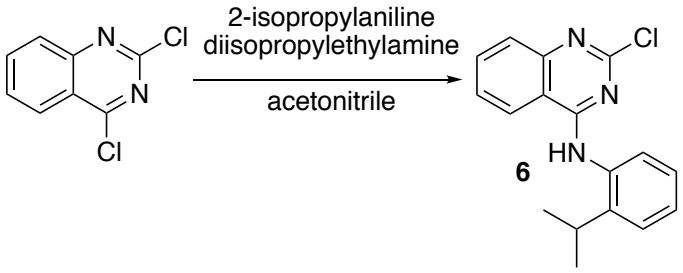

2-chloro-*N*-(2-isopropylphenyl)quinazolin-4-amine, 6. 2,4-dichloroquinazoline (200mg, 1mmol), 2-isopropylaniline (158mg, 1.2mmol), and diisopropylethylamine (258mg, 2mmol), were stirred at 70 °C in acetonitrile (4ml) for five days. Reaction was cooled to room temperature, then water (4ml) was added. A precipitate formed and was recovered by filtration. The precipitate was washed with cold acetonitrile:water, then with water and then dried under vacuum. 240mg of **6** were obtained (80% yield). LC/MS: 298.71 $[M+H]^+$.

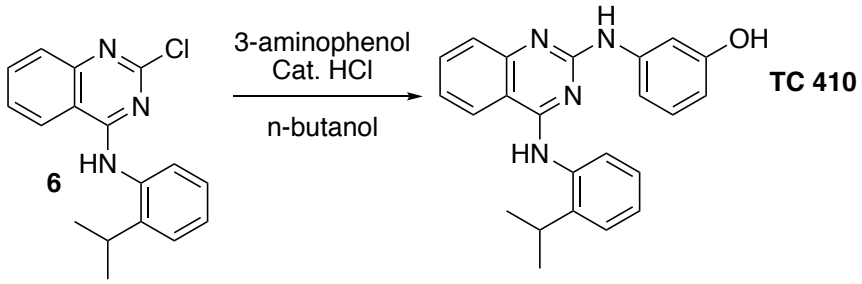

3-((4-((2-isopropylphenyl)amino)quinazolin-2-yl)amino)phenol, TC 410. A mixture of **6** (25mg, 0.09mmol), 3-aminophenol (20mg, 0.18mmol), and concentrated hydrochloric acid (10μl) were refluxed in n-butanol (1ml) overnight. After cooling, hexane was added and a precipitate formed. The precipitate was collected by filtration and washed with water and methanol and then dried under vacuum. 4.8mg of **TC 409** were obtained (16% yield). LC/MS: 333.85 $[M+H]^+$.

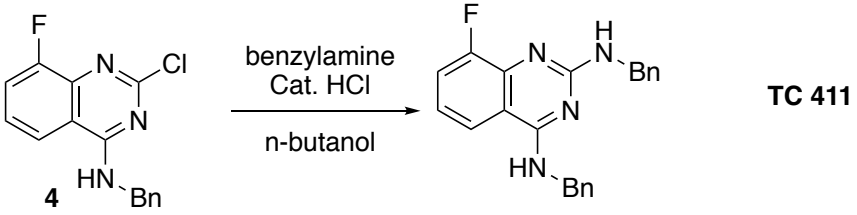

***N*^{2},*N*^{4}-dibenzyl-8-fluoroquinazoline-2,4-diamine, TC 411.** A mixture of **4** (25mg, 0.09mmol, synthesized by T. Cupido), benzylamine (20mg, 0.18mmol), and concentrated hydrochloric acid (10μl) were refluxed in n-butanol (1ml) overnight. After cooling, water was added and a precipitate formed. The precipitate was collected by filtration and washed with water, 1M hydrochloric acid (aq), and hexane and then dried under vacuum. 22mg of **TC 411** were obtained (68% yield). LC/MS: 359.86 $[M+H]^+$.

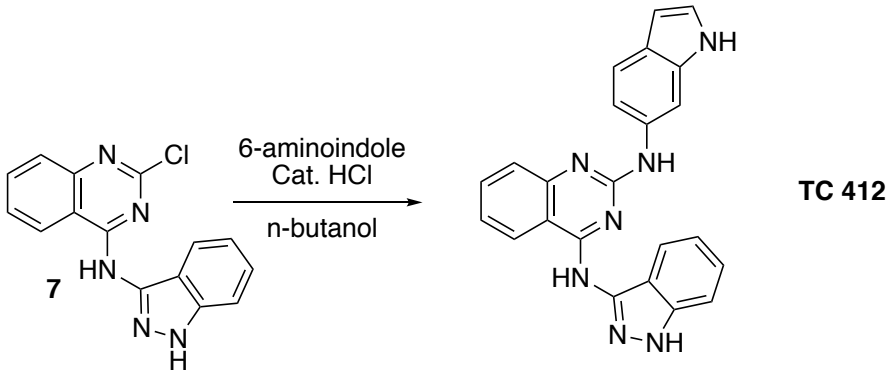

N^4-(1H-indazol-3-yl)-N^2-(1H-indol-6-yl)quinazoline-2,4-diamine, TC 412. A mixture of **7** (67mg, 0.23mmol, synthesized by T. Cupido), 6-aminoindole (40mg, 0.3mmol), and concentrated hydrochloric acid (10μl) were refluxed in n-butanol (0.8ml) overnight. After cooling, a precipitate formed. The precipitate was collected by filtration and washed with water, 1M hydrochloric acid (aq), and hexane and then dried under vacuum. 63mg of **TC 412** were obtained (70% yield). LC/MS: 392.70 $[M+H]^+$.

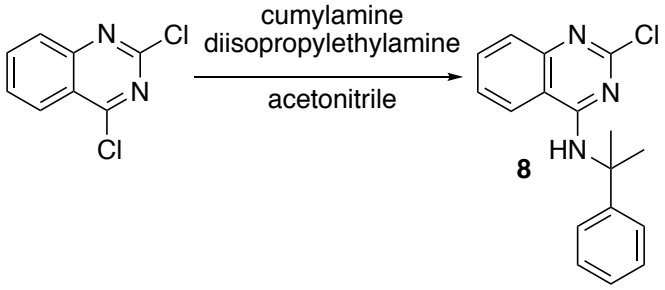

2-chloro-*N*-(2-phenylpropan-2-yl)quinazolin-4-amine, 8. 2,4-dichloroquinazoline (200mg, 1mmol), 2-isopropylaniline (149mg, 1.1mmol), and diisopropylethylamine (258mg, 2mmol), were stirred at room temperature in acetonitrile (4ml) for seven days. The yellow precipitate was collected by filtration, washed with water, and dried under vacuum. 160mg of **8** were obtained (54% yield). LC/MS: 298.71 $[M+H]^+$.

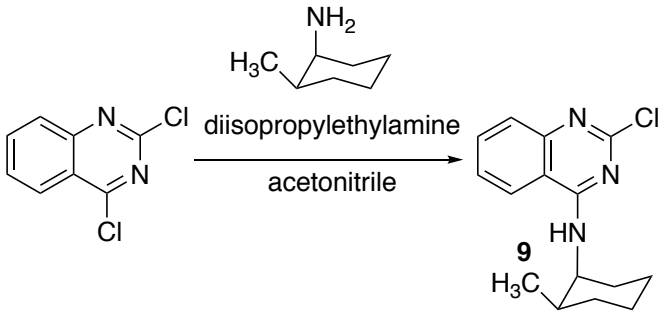

2-chloro-*N*-((1*S*,2*R*)-2-methylcyclohexyl)quinazolin-4-amine, 9. 2,4-dichloroquinazoline (200mg, 1mmol), (1*S*,2*R*)-2-methylcyclohexan-1-amine (124mg, 1.1mmol), and diisopropylethylamine (258mg, 2mmol), were stirred at room temperature

in acetonitrile (4ml) for two hours. The yellow precipitate was collected by filtration, washed with water, and dried under vacuum. 262mg of **9** were obtained (95% yield). LC/MS: 276.67 $[M+H]^+$.

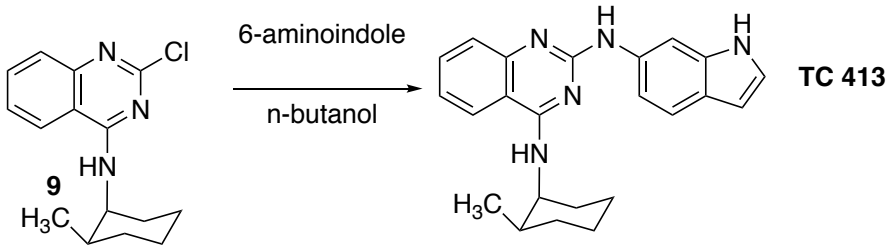

N^2-(1H-indol-6-yl)-N^4-((1S,2R)-2-methylcyclohexyl)quinazoline-2,4-diamine, TC 413. A mixture of **9** (28mg, 0.1mmol), 6-aminoindole (20mg, 0.15mmol) was refluxed in n-butanol (1ml) overnight. After cooling, hexane was added and a precipitate formed. The precipitate was collected by filtration and washed with hexane, water, and methanol and then dried under vacuum. 0.7mg of **TC 413** were obtained (2% yield). LC/MS: 372.90 $[M+H]^+$.

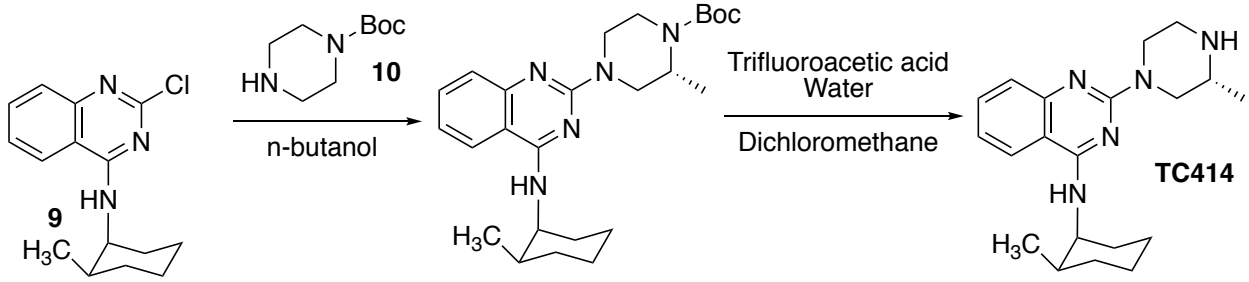

N-((1S,2R)-2-methylcyclohexyl)-2-((R)-3-methylpiperazin-1-yl)quinazolin-4-amine, TC 414. A mixture of **9** (28mg, 0.1mmol), **10** (as the HCl salt, 35mg, 0.15mmol) was refluxed in n-butanol (1ml) overnight. After cooling, hexane and concentrated hydrochloric acid were added and a precipitate formed. The precipitate was collected centrifugation and removal of the supernatant, and was used without further purification. Trifluoroacetic acid (500μl), dichloromethane (400μl), and water (100μl) were added to the precipitate. This mixture was stirred at room temperature for 1 hour. Solvent was removed under reduced pressure, the resulting slurry resuspended in diethyl ether, and the solvent removed again. This process was repeated two times. The resulting amorphous solid was dissolved in 1M sodium hydroxide (aq.) and the aqueous was extracted with ethyl acetate. The organic layer was washed with brine, dried over sodium sulfate, and the solvent was evaporated. The resulting oil was treated with ~5ul of concentrated hydrochloric acid (aq.), which caused precipitaton. This precipitate was collected by centrifugation, washed twice with acetone, and dried under vacuum. 1mg of **TC 414** was obtained (3% yield). LC/MS: 340.89 $[M+H]^+$.

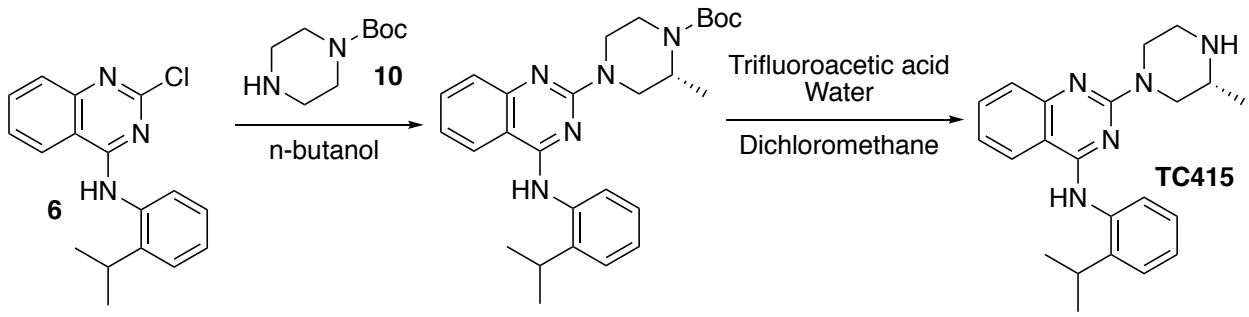

(*R*)-*N*-(2-isopropylphenyl)-2-(3-methylpiperazin-1-yl)quinazolin-4-amine, TC 415. A mixture of **6** (28mg, 0.15mmol), **10** (as the HCl salt, 53mg, 0.23mmol) was refluxed in n-butanol (1ml) overnight. After cooling, hexane and concentrated hydrochloric acid were added and a precipitate formed. The precipitate was collected centrifugation and removal of the supernatant, and was used without further purification. Trifluoroacetic acid (500μl), dichloromethane (400μl), and water (100μl) were added to the precipitate. This mixture was stirred at room temperature for 1 hour. Solvent was removed under reduced pressure, the resulting slurry resuspended in diethyl ether, and the solvent removed again. This process was repeated two times. The resulting amorphous solid was dissolved in 1M sodium hydroxide (aq.) and the aqueous was extracted with ethyl acetate. The organic layer was washed with brine, dried over sodium sulfate, and the solvent was evaporated. The resulting oil was treated with ~5ul of concentrated hydrochloric acid (aq.), which caused precipitaton. This precipitate was collected by centrifugation, washed twice with acetone, and dried under vacuum. The precipitate was dissolved in 85:15 dichloromethane:methanol and purified by preparative-scale thin-layer chromatography. The plate was developed using 85:15 dichloromethane:methanol. The desired band (R_f 0.15 in 85:15 dichloromethane:methanol) was excised with a razor and the product removed by addition of 85:15 dichloromethane:methanol to the collected silica powder and removal of the powder by filtration. 3mg of **TC 415** were obtained (6% yield). LC/MS: 362.86 $[M+H]^+$.

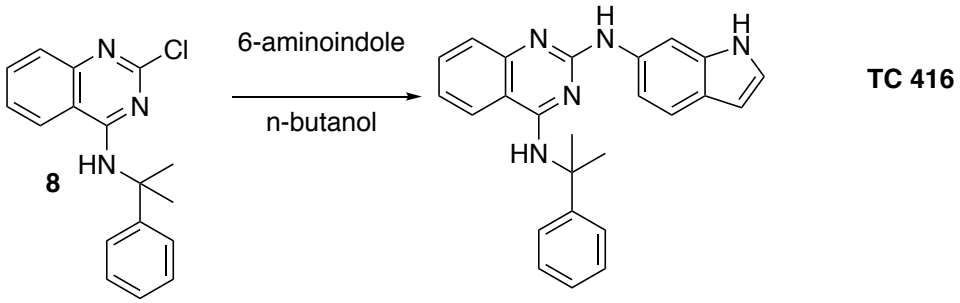

N^2-(1H-indol-6-yl)-N^4-(2-phenylpropan-2-yl)quinazoline-2,4-diamine, TC 416. A mixture of **8** (30mg, 0.1mmol) and 6-aminoindole (20mg, 0.15mmol) was refluxed in n-butanol (1ml) overnight. After cooling and addition of hexane, a precipitate formed. The precipitate was collected by filtration and washed with water and ethanol and then dried under vacuum. 26.6mg of **TC 415** were obtained (68% yield). LC/MS: 394.79 $[M+H]^+$.

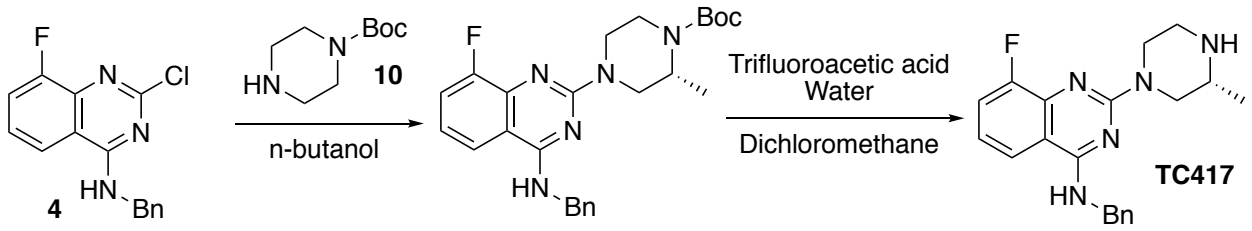

(*R*)-*N*-benzyl-8-fluoro-2-(3-methylpiperazin-1-yl)quinazolin-4-amine, TC 417. A mixture of **9** (29mg, 0.1mmol), **10** (as the HCl salt, 35mg, 0.15mmol) was refluxed in n-butanol (1ml) overnight. After cooling, hexane and concentrated hydrochloric acid were added and a precipitate formed. The precipitate was collected centrifugation and removal of the supernatant, and was used without further purification. Trifluoroacetic acid (500μl), dichloromethane (400μl), and water (100μl) were added to the precipitate. This mixture was stirred at room temperature for 1 hour. Solvent was removed under reduced pressure, the resulting slurry resuspended in diethyl ether, and the solvent removed again. This process was repeated two times. The resulting amorphous solid was dissolved in 1M sodium hydroxide (aq.) and the aqueous was extracted with ethyl acetate. The organic layer was washed with brine, dried over sodium sulfate, and the solvent was evaporated. The resulting oil was treated with ~5ul of concentrated hydrochloric acid (aq.), which caused precipitaton. This precipitate was collected by centrifugation, washed twice with acetone, and dried under vacuum. 25.7mg of **TC 417** were obtained (73% yield). LC/MS: 352.82 $[M+H]^+$.

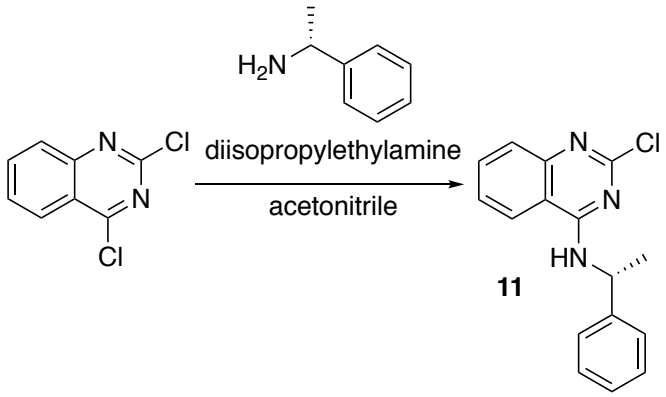

(*R*)-2-chloro-*N*-(1-phenylethyl)quinazolin-4-amine, 11. 2,4-dichloroquinazoline (200mg, 1mmol), (R)-1-phenylethan-1-amine (133mg, 1.1mmol), and diisopropylethylamine (258mg, 2mmol), were stirred at room temperature in acetonitrile (4ml) for 24 hours. Water was added and the solution was cooled at -20°. Following phase separation, ethyl acetate and 0.1M hydrochloric acid (aq.) were added. The organic layer was collected, washed with 1M sodium hydroxide (aq.), and brine, then dried over sodium sulfate. The solvent was evaporated under reduced pressure. 205mg of **11** were obtained (72% yield).

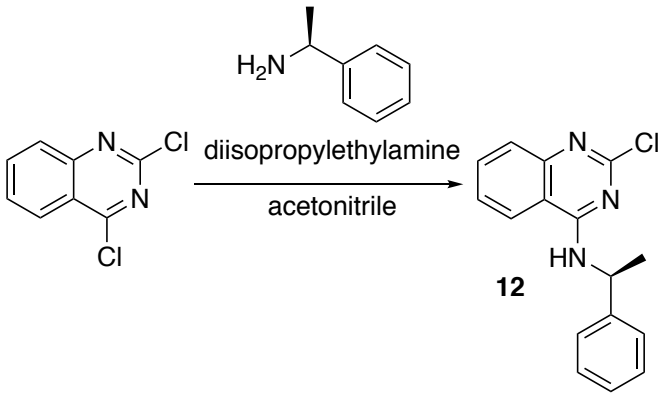

(*S*)-2-chloro-*N*-(1-phenylethyl)quinazolin-4-amine, 11. 2,4-dichloroquinazoline (200mg, 1mmol), (S)-1-phenylethan-1-amine (133mg, 1.1mmol), and diisopropylethylamine (258mg, 2mmol), were stirred at room temperature in acetonitrile (4ml) for 24 hours. Water was added and the solution was cooled at -20°. Following phase separation, ethyl acetate and 0.1M hydrochloric acid (aq.) were added. The organic layer was collected, washed with 1M sodium hydroxide (aq.), and brine, then dried over sodium sulfate. The solvent was evaporated under reduced pressure. 246mg of **12** were obtained (86% yield).

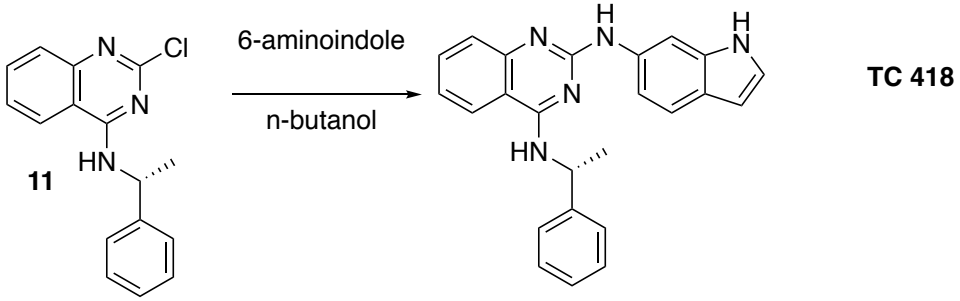

(R)-N^2-(1H-indol-6-yl)-N^4-(1-phenylethyl)quinazoline-2,4-diamine, **TC 418.** A mixture of **11** (28mg, 0.1mmol) and 6-aminoindole (20mg, 0.15mmol) was refluxed in n-butanol (1ml) overnight. After cooling and addition of hexane, a precipitate formed. The precipitate was collected by filtration and washed with water and then dried under vacuum. 22.3mg of **TC 418** were obtained (59% yield). LC/MS: 380.78 $[M+H]^+$.

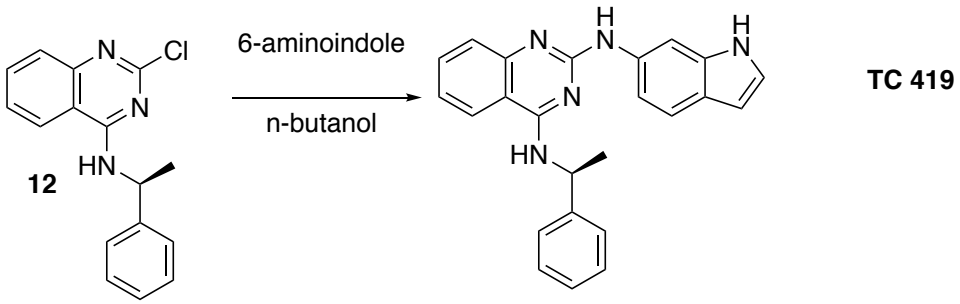

(S)-N^2-(1H-indol-6-yl)-N^4-(1-phenylethyl)quinazoline-2,4-diamine, **TC 419.** A mixture of **12** (28mg, 0.1mmol) and 6-aminoindole (20mg, 0.15mmol) was refluxed in n-butanol (1ml) overnight. After cooling and addition of hexane, no precipitate formed. Amorphous material formed in the reaction vessel. The solvent was removed under reduced pressure. The solid residue was dissolved in ethyl acetate and the resulting solution was washed with 0.1M HCl (aq.) and brine, dried over sodium sulfate, and the solvent was removed under reduced pressure. . The precipitate was collected by filtration and washed with water and then dried under vacuum. 26.9mg of **TC 419** were obtained (71% yield). LC/MS: 380.79 $[M+H]^+$.

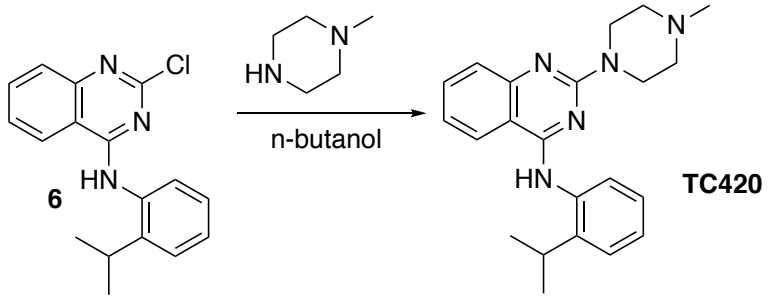

N-(2-isopropylphenyl)-2-(4-methylpiperazin-1-yl)quinazolin-4-amine, TC 420. A mixture of **6** (30mg, 0.1mmol) and 1-methylpiperazine (15mg, 0.15mmol) was refluxed in n-butanol (1ml) overnight. Solvent was removed under reduced pressure. Hexane and concentrated hydrochloric acid were added to the resulting oil. A precipitate formed, which was collected by filtered and washed with basic water (pH 10) and then neutral water then dried overnight under vacuum. 18.4mg of **TC 420** were obtained (51% yield). LC/MS: 362.79 $[M+H]^+$.

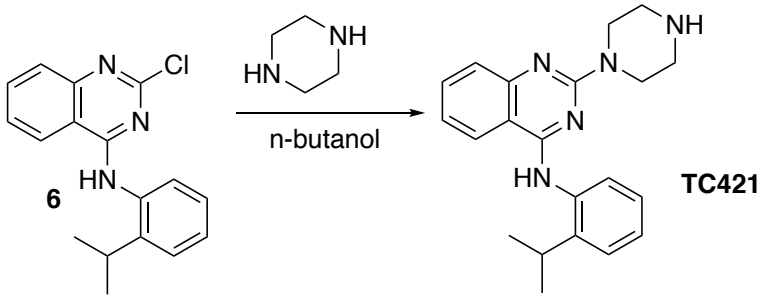

N-(2-isopropylphenyl)-2-(piperazin-1-yl)quinazolin-4-amine, TC 421. A mixture of **6** (30mg, 0.1mmol) and piperazine (258mg, 3mmol) was refluxed in n-butanol (6ml) overnight. The solvent was removed by evaporation at reduced pressure and the resulting oil was dissolved in basic water (pH 10). The aqueous was extracted with ethyl acetate. The organic was washed with brine and dried over sodium sulfate. Solvent was removed under reduced pressure. The resulting oil was dissolved in 9:1 dichloromethane:methanol and purified by preparative-scale thin-layer chromatography. The plate was developed using 9:1 dichloromethane:methanol. The desired band (R_f 0.1 in 9:1 dichloromethane:methanol) was excised with a razor and the product removed by addition of 9:1 dichloromethane:methanol to the collected silica powder and removal of the powder by filtration. 5.2mg of **TC 421** were obtained (15% yield).

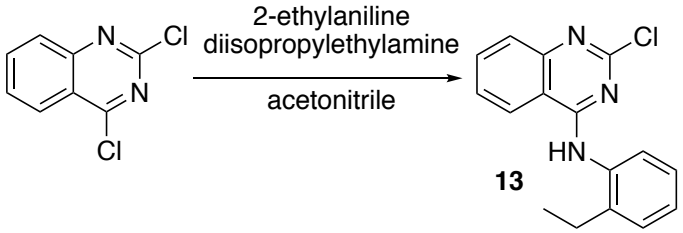

2-chloro-N-(2-ethylphenyl)quinazolin-4-amine, 13. 2,4-dichloroquinazoline (200mg, 1mmol), 2-ethylaniline (133mg, 1.1mmol), and diisopropylethylamine (258mg, 2mmol), were stirred at room temperature in acetonitrile (4ml) for 80 hours. Water was added and a precipitate formed. The precipitate was collected by filtration and washed with cold 2:1 water:acetonitrile, then with water and then dried under vacuum. 291mg of **13** were obtained (>99% yield). LC/MS: 284.62 $[M+H]^+$.

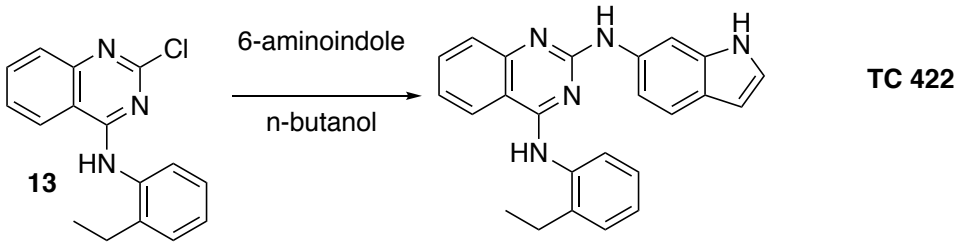

***N*^{4}-(2-ethylphenyl)-*N*^{2}-(1*H*-indol-6-yl)quinazoline-2,4-diamine, TC 422.** A mixture of **13** (28mg, 0.1mmol) and 6-aminoindole (20mg, 0.15mmol) was refluxed in n-butanol (1ml) overnight. After cooling and addition of hexane, a precipitate formed. The precipitate was collected by filtration and washed with water and then dried under vacuum. 5mg of **TC 422** were obtained (13% yield). LC/MS: 380.78 $[M+H]^+$.

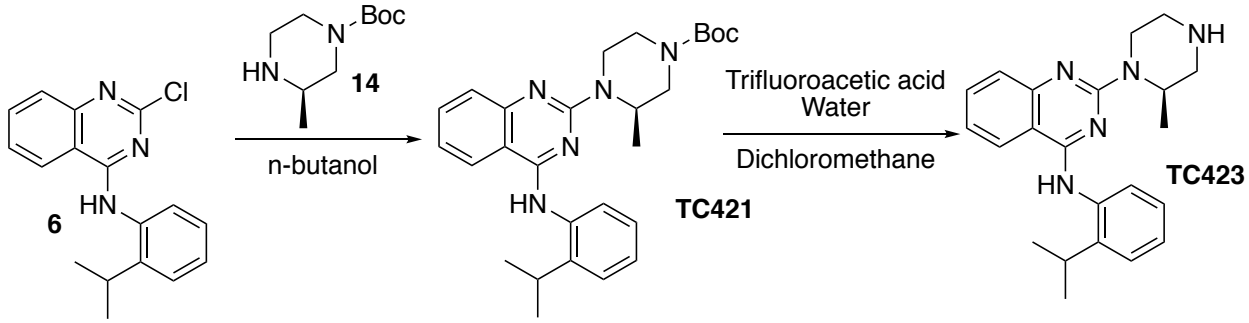

(R)-N-(2-isopropylphenyl)-2-(2-methylpiperazin-1-yl)quinazolin-4-amine, TC 423. A mixture of **6** (29mg, 0.1mmol) and **14** (30mg, 0.15mmol) was refluxed in n-butanol (1ml) overnight. After cooling, hexane and concentrated hydrochloric acid but no precipitation occurred. Solvent was removed under reduced pressure and the residue was used without further purification. Trifluoroacetic acid (500μl), dichloromethane (400μl), and water (100μl) were added to the precipitate. This mixture was stirred at room temperature for 1 hour. Solvent was removed under reduced pressure, the resulting slurry resuspended in diethyl ether, and the solvent removed again. This process was repeated two times. The resulting amorphous solid was dissolved in 1M sodium hydroxide (aq.) and the aqueous was extracted with ethyl acetate. The organic layer was washed with brine, dried over sodium sulfate, and the solvent was evaporated. The resulting oil was treated with ~5ul of concentrated hydrochloric acid (aq.), which caused precipitaton. This precipitate was collected by centrifugation, washed twice with acetone, and dried under vacuum. 22.6mg of **TC 423** were obtained (62% yield). LC/MS: 362.86 $[M+H]^+$.

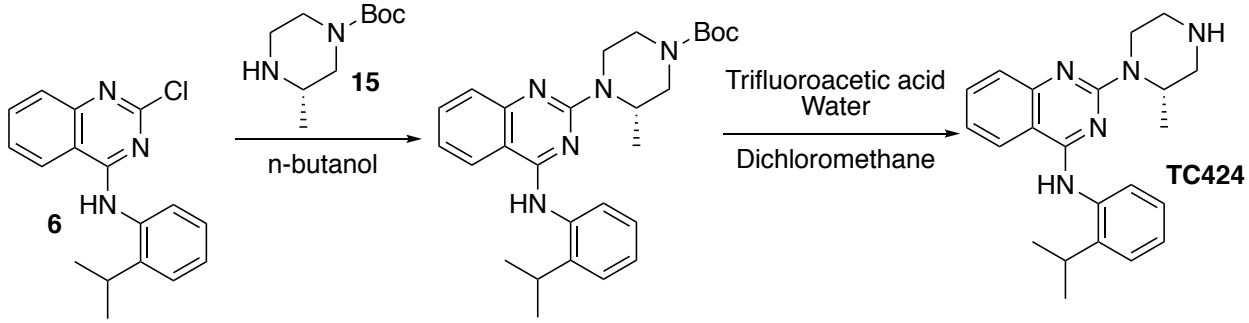

(*S*)-*N*-(2-isopropylphenyl)-2-(2-methylpiperazin-1-yl)quinazolin-4-amine, TC 424. A mixture of **6** (29mg, 0.1mmol) and **15** (30mg, 0.15mmol) was refluxed in n-butanol (1ml) overnight. After cooling, hexane and concentrated hydrochloric acid but no precipitation occurred. Solvent was removed under reduced pressure and the residue was used without further purification. Trifluoroacetic acid (500μl), dichloromethane (400μl), and water (100μl) were added to the precipitate. This mixture was stirred at room temperature for 1 hour. Solvent was removed under reduced pressure, the resulting slurry resuspended in diethyl ether, and the solvent removed again. This process was repeated two times. The resulting amorphous solid was dissolved in 1M sodium hydroxide (aq.) and the aqueous was extracted with ethyl acetate. The organic layer was washed with brine, dried over sodium sulfate, and the solvent was evaporated. The resulting oil was treated with ~5ul of

concentrated hydrochloric acid (aq.), which caused precipitaton. This precipitate was collected by centrifugation, washed twice with acetone, and dried under vacuum. 28.4mg of **TC 424** were obtained (78% yield). LC/MS: 362.86 $[M+H]^+$.

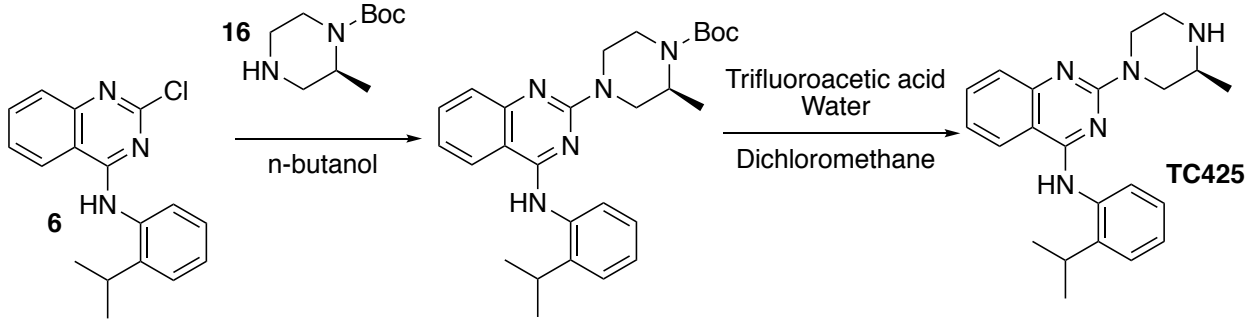

(*S*)-*N*-(2-isopropylphenyl)-2-(3-methylpiperazin-1-yl)quinazolin-4-amine, TC 425. A mixture of **6** (45mg, 0.15mmol) and **16** (45mg, 0.23mmol) was refluxed in n-butanol (1ml) overnight. After cooling, hexane and concentrated hydrochloric acid but no precipitation occurred. Solvent was removed under reduced pressure and the residue was used without further purification. Trifluoroacetic acid (500μl), dichloromethane (400μl), and water (100μl) were added to the precipitate. This mixture was stirred at room temperature for 1 hour. Solvent was removed under reduced pressure, the resulting slurry resuspended in diethyl ether, and the solvent removed again. This process was repeated two times. The resulting amorphous solid was dissolved in 1M sodium hydroxide (aq.) and the aqueous was extracted with ethyl acetate. The organic layer was washed with brine, dried over sodium sulfate, and the solvent was evaporated. The resulting oil was treated with ~5ul of concentrated hydrochloric acid (aq.), which caused precipitaton. This precipitate was collected by centrifugation, washed twice with acetone, and dried under vacuum. 38.4mg of **TC 425** were obtained (70% yield). LC/MS: 362.86 $[M+H]^+$. ^1H NMR (400MHz) was acquired, analysis is ongoing.

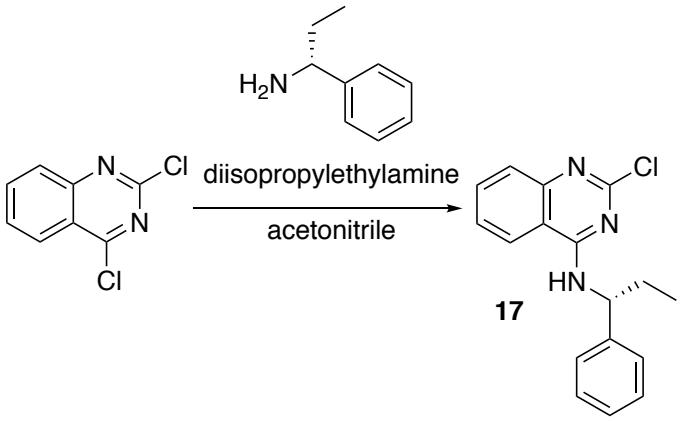

(*R*)-2-chloro-*N*-(1-phenylpropyl)quinazolin-4-amine, 17. 2,4-dichloroquinazoline (200mg, 1mmol), (*R*)-1-phenylpropan-1-amine (148mg, 1.1mmol), and diisopropylethylamine (258mg, 2mmol), were stirred at room temperature in acetonitrile (4ml) for 72 hours. Hydrochloric acid (0.3M, aq) and the solution was extracted with ethyl acetate. The organc layer was washed with 1M sodium hydroxide (aq.) and brine, dried over sodium sulfate, and the solvent was removed under reduced pressure. 224mg of **13** were obtained (75% yield). LC/MS: 298.64 $[M+H]^+$.

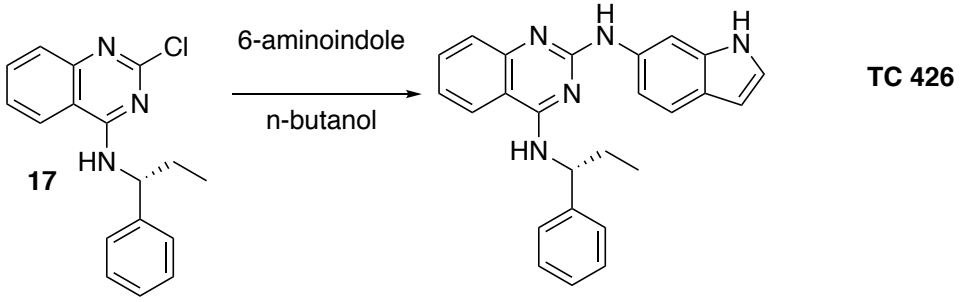

(*R*)-N^2-(1*H*-indol-6-yl)-N^4-(1-phenylpropyl)quinazoline-2,4-diamine, TC 426. A mixture of **17** (28mg, 0.1mmol) and 6-aminoindole (20mg, 0.15mmol) was refluxed in n-butanol (1ml) overnight. After cooling and addition of hexane, a precipitate formed. The precipitate was collected by filtration and washed with water and then dried under vacuum. 6.6mg of **TC 426** were obtained (16% yield). LC/MS: 394.80 $[M+H]^+$.

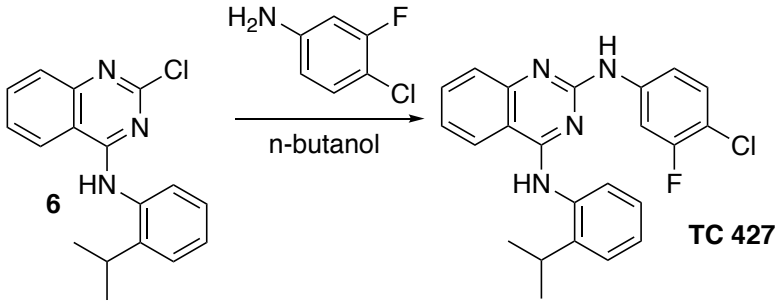

N^2-(4-chloro-3-fluorophenyl)-N^4-(2-isopropylphenyl)quinazoline-2,4-diamine, TC 427. A mixture of **17** (28mg, 0.1mmol) and 6-aminoindole (20mg, 0.15mmol) was refluxed in n-butanol (1ml) overnight. After cooling and addition of hexane, a precipitate formed. The precipitate was collected by filtration and washed with water and methanol, then dried under vacuum. 24.1mg of **TC 427** were obtained (60% yield). LC/MS: 394.80 $[M+H]^+$.

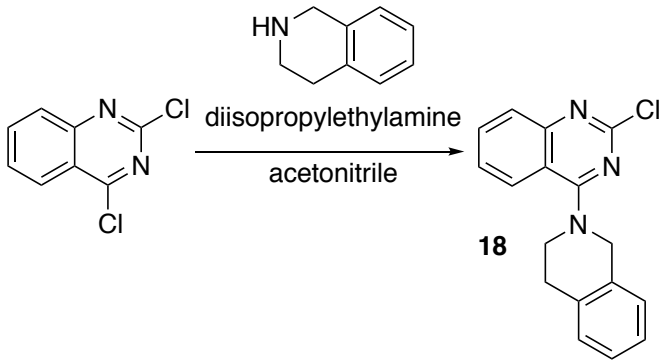

2-chloro-4-(3,4-dihydroisoquinolin-2(1*H*)-yl)quinazoline, 18. 2,4-dichloroquinazoline (200mg, 1mmol), 1,2,3,4-tetrahydroisoquinoline (147mg, 1.1mmol), and diisopropylethylamine (258mg, 2mmol), were stirred at room temperature in acetonitrile (4ml) for 48 hours. Hydrochloric acid (0.3M, aq) and the solution was extracted with ethyl acetate. The organc layer was washed with 1M sodium hydroxide (aq.) and brine, dried over sodium sulfate, and the solvent was removed under reduced pressure. 202mg of **18** were obtained (68% yield). LC/MS: 292.62 $[M+H]^+$.

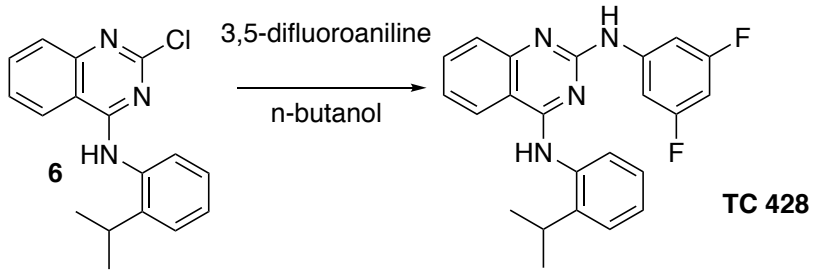

***N*^{2}-(3,5-difluorophenyl)-*N*^{4}-(2-isopropylphenyl)quinazoline-2,4-diamine**, **TC 428.** A mixture of **6** (30mg, 0.1mmol) and 6-aminoindole (26mg, 0.2mmol) was refluxed in n-butanol (1ml) overnight. After cooling and addition of hexane, a precipitate formed. The precipitate was collected by filtration and washed with water and methanol, then dried under vacuum. 12.6mg of **TC 428** were obtained (32% yield). LC/MS: 391.73 $[M+H]^+$.

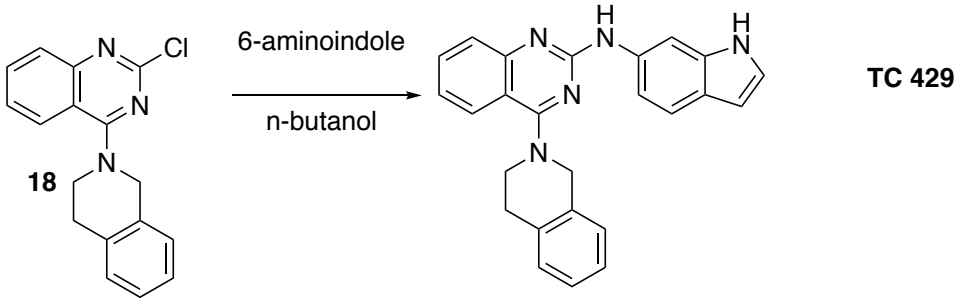

4-(3,4-dihydroisoquinolin-2(1*H*)-yl)-*N*-(1*H*-indol-6-yl)quinazolin-2-amine, TC 429. A mixture of **18** (30mg, 0.1mmol) and 6-aminoindole (20mg, 0.15mmol) was refluxed in n-butanol (1ml) overnight. After cooling and addition of hexane, a precipitate formed.

The precipitate was collected by filtration and washed with water and then dried under vacuum. 27mg of **TC 429** were obtained (69% yield). LC/MS: 392.69 $[M+H]^+$.

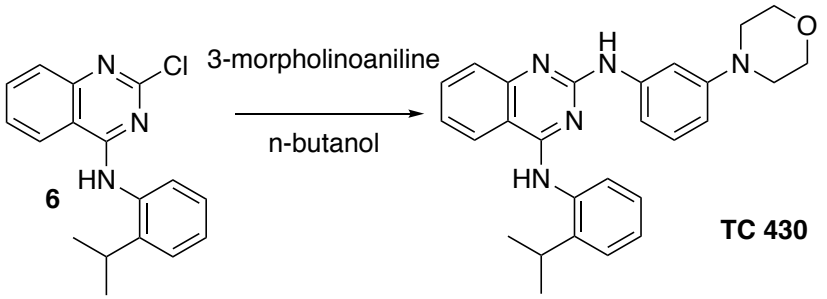

N^4-(2-isopropylphenyl)-N^2-(3-morpholinophenyl)quinazoline-2,4-diamine, TC 430. A mixture of **6** (30mg, 0.1mmol) and 6-aminoindole (32mg, 0.17mmol) was refluxed in n-butanol (1ml) overnight. After cooling and addition of hexane, a precipitate formed. The precipitate was collected by filtration and washed with water. The precipitate was lost upon washing with water, so the filtrate was acidified with hydrochloric acid and extracted with ethyl acetate. The organic layer was washed with brine, dried over sodium sulfate, and solvent removed under reduced pressure. 10mg of **TC 430** were obtained (23% yield). LC/MS: 440.68 $[M+H]^+$.

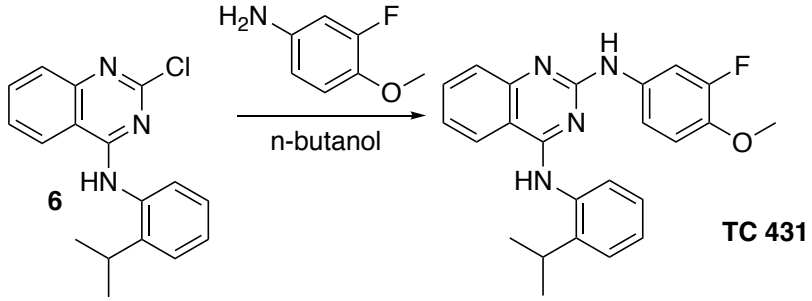

N^2-(3-fluoro-4-methoxyphenyl)-N^4-(2-isopropylphenyl)quinazoline-2,4-diamine, TC 431. A mixture of **6** (30mg, 0.1mmol) and 3-fluoro-4methoxyaniline (34mg, 0.25mmol) was refluxed in n-butanol (1ml) overnight. After cooling and addition of hexane, a precipitate formed. The precipitate was collected by filtration and washed with water and then dried under vacuum. 24mg of **TC 431** were obtained (60% yield). LC/MS: 403.72 $[M+H]^+$.

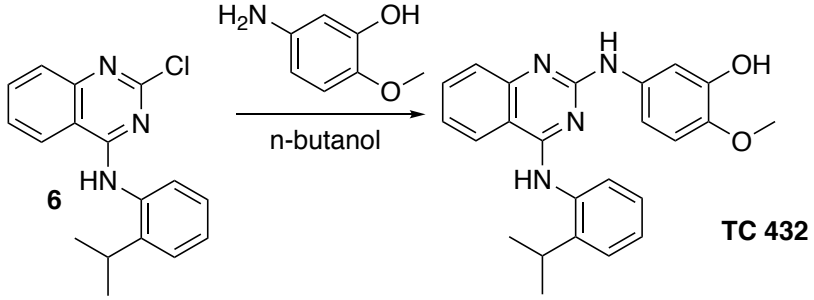

5-((4-((2-isopropylphenyl)amino)quinazolin-2-yl)amino)-2-methoxyphenol, TC 432. A mixture of **6** (30mg, 0.1mmol) and 5-amino-2-methoxyphenol (43mg, 0.31mmol) was refluxed in n-butanol (1ml) overnight. After cooling and addition of hexane, a precipitate formed. The precipitate was collected by filtration and washed with water and methanol and then dried under vacuum. 4.5mg of **TC 432** were obtained (11% yield). LC/MS: 401.63 $[M+H]^+$.

References

1. Vale RD. The molecular motor toolbox for intracellular transport. Cell. 2003;112(4):467-80.

2. Allan VJ. Cytoplasmic dynein. Biochemical Society transactions. 2011;39(5):1169-78.

3. Kural C, Kim H, Syed S, Goshima G, Gelfand VI, Selvin PR. Kinesin and dynein move a peroxisome in vivo: a tug-of-war or coordinated movement? Science (New York, NY). 2005;308(5727):1469-72.

4. Wickstead B, Gull K. Dyneins across eukaryotes: a comparative genomic analysis. Traffic. 2007;8(12):1708-21.

5. Erzberger JP, Berger JM. Evolutionary relationships and structural mechanisms of AAA+ proteins. Annual review of biophysics and biomolecular structure. 2006;35:93-114.

6. Urnavicius L, Zhang K, Diamant AG, Motz C, Schlager MA, Yu M, Patel NA, Robinson CV, Carter AP. The structure of the dynactin complex and its interaction with dynein. Science (New York, NY). 2015;347(6229):1441-6.

7. Schroer TA. Dynactin. Annual review of cell and developmental biology. 2004;20:759-79.

8. Carter AP. Crystal clear insights into how the dynein motor moves. Journal of cell science. 2013;126(Pt 3):705-13.

9. Hanson PI, Whiteheart SW. AAA+ proteins: have engine, will work. Nature reviews Molecular cell biology. 2005;6(7):519-29.

10. Simons C. Nucleoside mimetics : their chemistry and biological properties. Amsterdam, Netherlands: Gordon and Breach Science Publishers; 2001. 191 p.

11. Kobayashi T, Martensen T, Nath J, Flavin M. Inhibition of dynein ATPase by vanadate, and its possible use as a probe for the role of dynein in cytoplasmic motility. Biochemical and biophysical research communications. 1978;81(4):1313-8.

12. Gibbons IR, Cosson MP, Evans JA, Gibbons BH, Houck B, Martinson KH, Sale WS, Tang WJ. Potent inhibition of dynein adenosinetriphosphatase and of the motility of cilia and sperm flagella by vanadate. Proceedings of the National Academy of Sciences of the United States of America. 1978;75(5):2220-4.

13. Cantley LC, Jr., Josephson L, Warner R, Yanagisawa M, Lechene C, Guidotti G. Vanadate is a potent (Na,K)-ATPase inhibitor found in ATP derived from muscle. The Journal of biological chemistry. 1977;252(21):7421-3.

14. VanEtten RL, Waymack PP, Rehkop DM. Letter: Transition metal ion inhibition of enzyme-catalyzed phosphate ester displacement reactions. Journal of the American Chemical Society. 1974;96(21):6782-5.

15. Ray WJ, Jr., Puvathingal JM. Characterization of a vanadate-based transition-state-analogue complex of phosphoglucomutase by kinetic and equilibrium binding studies. Mechanistic implications. Biochemistry. 1990;29(11):2790-801.

16. Davies DR, Hol WG. The power of vanadate in crystallographic investigations of phosphoryl transfer enzymes. FEBS letters. 2004;577(3):315-21.

17. Schmidt H, Zalyte R, Urnavicius L, Carter AP. Structure of human cytoplasmic dynein-2 primed for its power stroke. Nature. 2015;518(7539):435-8.

18. Shimizu T, Toyoshima YY, Edamatsu M, Vale RD. Comparison of the motile and enzymatic properties of two microtubule minus-end-directed motors, ncd and cytoplasmic dynein. Biochemistry. 1995;34(5):1575-82.

19. Lee-Eiford A, Ow RA, Gibbons IR. Specific cleavage of dynein heavy chains by ultraviolet irradiation in the presence of ATP and vanadate. The Journal of biological chemistry. 1986;261(5):2337-42.

20. Kon T, Nishiura M, Ohkura R, Toyoshima YY, Sutoh K. Distinct functions of nucleotide-binding/hydrolysis sites in the four AAA modules of cytoplasmic dynein. Biochemistry. 2004;43(35):11266-74.

21. Bouchard P, Penningroth SM, Cheung A, Gagnon C, Bardin CW. erythro-9-[3-(2-Hydroxynonyl)]adenine is an inhibitor of sperm motility that blocks dynein ATPase and protein carboxylmethylase activities. Proceedings of the National Academy of Sciences of the United States of America. 1981;78(2):1033-6.

22. Penningroth SM, Cheung A, Bouchard P, Gagnon C, Bardin CW. Dynein ATPase is inhibited selectively in vitro by erythro-9-[3-2-(hydroxynonyl)]adenine. Biochemical and biophysical research communications. 1982;104(1):234-40.

23. Kinoshita T, Tada T, Nakanishi I. Conformational change of adenosine deaminase during ligand-exchange in a crystal. Biochemical and biophysical research communications. 2008;373(1):53-7.

24. Paschal BM, Vallee RB. Retrograde transport by the microtubule-associated protein MAP 1C. Nature. 1987;330(6144):181-3.

25. Schaeffer HJ, Schwender CF. Enzyme inhibitors. 26. Bridging hydrophobic and hydrophilic regions on adenosine deaminase with some 9-(2-hydroxy-3-alkyl)adenines. Journal of medicinal chemistry. 1974;17(1):6-8.

26. Podzuweit T, Nennstiel P, Muller A. Isozyme selective inhibition of cGMP-stimulated cyclic nucleotide phosphodiesterases by erythro-9-(2-hydroxy-3-nonyl) adenine. Cellular signalling. 1995;7(7):733-8.

27. Mitchison TJ. Towards a pharmacological genetics. Chemistry & biology. 1994;1(1):3-6.

28. Nusslein-Volhard C, Wieschaus E. Mutations affecting segment number and polarity in Drosophila. Nature. 1980;287(5785):795-801.

29. Huangfu D, Anderson KV. Signaling from Smo to Ci/Gli: conservation and divergence of Hedgehog pathways from Drosophila to vertebrates. Development (Cambridge, England). 2006;133(1):3-14.

30. Huangfu D, Anderson KV. Cilia and Hedgehog responsiveness in the mouse. Proceedings of the National Academy of Sciences of the United States of America. 2005;102(32):11325-30.

31. Huangfu D, Liu A, Rakeman AS, Murcia NS, Niswander L, Anderson KV. Hedgehog signalling in the mouse requires intraflagellar transport proteins. Nature. 2003;426(6962):83-7.

32. Goetz SC, Anderson KV. The primary cilium: a signalling centre during vertebrate development. Nature reviews Genetics. 2010;11(5):331-44.

33. Tukachinsky H, Lopez LV, Salic A. A mechanism for vertebrate Hedgehog signaling: recruitment to cilia and dissociation of SuFu-Gli protein complexes. The Journal of cell biology. 2010;191(2):415-28.

34. Hou Y, Witman GB. Dynein and intraflagellar transport. Experimental cell research. 2015;334(1):26-34.

35. Ocbina PJ, Eggenschwiler JT, Moskowitz I, Anderson KV. Complex interactions between genes controlling trafficking in primary cilia. Nature genetics. 2011;43(6):547-53.

36. Kim J, Kato M, Beachy PA. Gli2 trafficking links Hedgehog-dependent activation of Smoothened in the primary cilium to transcriptional activation in the nucleus. Proceedings of the National Academy of Sciences of the United States of America. 2009;106(51):21666-71.

37. Rubin LL, de Sauvage FJ. Targeting the Hedgehog pathway in cancer. Nature reviews Drug discovery. 2006;5(12):1026-33.

38. Xie J, Murone M, Luoh SM, Ryan A, Gu Q, Zhang C, Bonifas JM, Lam CW, Hynes M, Goddard A, Rosenthal A, Epstein EH, Jr., de Sauvage FJ. Activating Smoothened mutations in sporadic basal-cell carcinoma. Nature. 1998;391(6662):90-2.

39. Sharpe HJ, Wang W, Hannoush RN, de Sauvage FJ. Regulation of the oncoprotein Smoothened by small molecules. Nature chemical biology. 2015;11(4):246-55.

40. Basset-Seguin N, Sharpe HJ, de Sauvage FJ. Efficacy of Hedgehog pathway inhibitors in Basal cell carcinoma. Molecular cancer therapeutics. 2015;14(3):633-41.

41. Gould SE, Low JA, Marsters JC, Jr., Robarge K, Rubin LL, de Sauvage FJ, Sutherlin DP, Wong H, Yauch RL. Discovery and preclinical development of vismodegib. Expert opinion on drug discovery. 2014;9(8):969-84.

42. Yauch RL, Dijkgraaf GJ, Alicke B, Januario T, Ahn CP, Holcomb T, Pujara K, Stinson J, Callahan CA, Tang T, Bazan JF, Kan Z, Seshagiri S, Hann CL, Gould SE, Low JA, Rudin CM, de Sauvage FJ. Smoothened mutation confers resistance to a Hedgehog pathway inhibitor in medulloblastoma. Science (New York, NY). 2009;326(5952):572-4.

43. Doan HQ, Silapunt S, Migden MR. Sonidegib, a novel smoothened inhibitor for the treatment of advanced basal cell carcinoma. OncoTargets and therapy. 2016;9:5671-8.

44. Hyman JM, Firestone AJ, Heine VM, Zhao Y, Ocasio CA, Han K, Sun M, Rack PG, Sinha S, Wu JJ, Solow-Cordero DE, Jiang J, Rowitch DH, Chen JK. Small-molecule inhibitors reveal multiple strategies for Hedgehog pathway blockade. Proceedings of the National Academy of Sciences of the United States of America. 2009;106(33):14132-7.

45. Chen JK, Taipale J, Young KE, Maiti T, Beachy PA. Small molecule modulation of Smoothened activity. Proceedings of the National Academy of Sciences of the United States of America. 2002;99(22):14071-6.

46. Firestone AJ, Weinger JS, Maldonado M, Barlan K, Langston LD, O'Donnell M, Gelfand VI, Kapoor TM, Chen JK. Small-molecule inhibitors of the AAA+ ATPase motor cytoplasmic dynein. Nature. 2012;484(7392):125-9.

47. See SK, Hoogendoorn S, Chung AH, Ye F, Steinman JB, Sakata-Kato T, Miller RM, Cupido T, Zalyte R, Carter AP, Nachury MV, Kapoor TM, Chen JK. Cytoplasmic Dynein Antagonists with Improved Potency and Isoform Selectivity. ACS chemical biology. 2016;11(1):53-60.

48. Lu JM, Nurko J, Weakley SM, Jiang J, Kougias P, Lin PH, Yao Q, Chen C. Molecular mechanisms and clinical applications of nordihydroguaiaretic acid (NDGA) and its derivatives: an update. Medical science monitor : international medical journal of experimental and clinical research. 2010;16(5):Ra93-100.

49. Arasaki K, Tani K, Yoshimori T, Stephens DJ, Tagaya M. Nordihydroguaiaretic acid affects multiple dynein-dynactin functions in interphase and mitotic cells. Molecular pharmacology. 2007;71(2):454-60.

50. Famulski JK, Vos LJ, Rattner JB, Chan GK. Dynein/Dynactin-mediated transport of kinetochore components off kinetochores and onto spindle poles induced by nordihydroguaiaretic acid. PloS one. 2011;6(1):e16494.

51. Fang YI, Yokota E, Mabuchi I, Nakamura H, Ohizumi Y. Purealin blocks the sliding movement of sea urchin flagellar axonemes by selective inhibition of half the ATPase activity of axonemal dyneins. Biochemistry. 1997;36(50):15561-7.

52. Zhu G, Yang F, Balachandran R, Hook P, Vallee RB, Curran DP, Day BW. Synthesis and biological evaluation of purealin and analogues as cytoplasmic dynein heavy chain inhibitors. Journal of medicinal chemistry. 2006;49(6):2063-76.

53. Roossien DH, Miller KE, Gallo G. Ciliobrevins as tools for studying dynein motor function. Frontiers in cellular neuroscience. 2015;9:252.

54. Ye F, Breslow DK, Koslover EF, Spakowitz AJ, Nelson WJ, Nachury MV. Single molecule imaging reveals a major role for diffusion in the exploration of ciliary space by signaling receptors. eLife. 2013;2:e00654.

55. Milenkovic L, Weiss LE, Yoon J, Roth TL, Su YS, Sahl SJ, Scott MP, Moerner WE. Single-molecule imaging of Hedgehog pathway protein Smoothened in primary cilia

reveals binding events regulated by Patched1. Proceedings of the National Academy of Sciences of the United States of America. 2015;112(27):8320-5.

56. Liu X, Kapoor TM, Chen JK, Huse M. Diacylglycerol promotes centrosome polarization in T cells via reciprocal localization of dynein and myosin II. Proceedings of the National Academy of Sciences of the United States of America. 2013;110(29):11976-81.

57. Yi J, Wu X, Chung AH, Chen JK, Kapoor TM, Hammer JA. Centrosome repositioning in T cells is biphasic and driven by microtubule end-on capture-shrinkage. The Journal of cell biology. 2013;202(5):779-92.

58. Elting MW, Hueschen CL, Udy DB, Dumont S. Force on spindle microtubule minus ends moves chromosomes. The Journal of cell biology. 2014;206(2):245-56.

59. Sikirzhytski V, Magidson V, Steinman JB, He J, Le Berre M, Tikhonenko I, Ault JG, McEwen BF, Chen JK, Sui H, Piel M, Kapoor TM, Khodjakov A. Direct kinetochore-spindle pole connections are not required for chromosome segregation. The Journal of cell biology. 2014;206(2):231-43.

60. Lee CY, Horn HF, Stewart CL, Burke B, Bolcun-Filas E, Schimenti JC, Dresser ME, Pezza RJ. Mechanism and regulation of rapid telomere prophase movements in mouse meiotic chromosomes. Cell reports. 2015;11(4):551-63.

61. Sainath R, Gallo G. The dynein inhibitor Ciliobrevin D inhibits the bidirectional transport of organelles along sensory axons and impairs NGF-mediated regulation of growth cones and axon branches. Developmental neurobiology. 2015;75(7):757-77.

62. Kapitein LC, Schlager MA, van der Zwan WA, Wulf PS, Keijzer N, Hoogenraad CC. Probing intracellular motor protein activity using an inducible cargo trafficking assay. Biophysical journal. 2010;99(7):2143-52.

63. Hoogenraad CC, Wulf P, Schiefermeier N, Stepanova T, Galjart N, Small JV, Grosveld F, de Zeeuw CI, Akhmanova A. Bicaudal D induces selective dynein-mediated microtubule minus end-directed transport. The EMBO journal. 2003;22(22):6004-15.

64. Schreiber SL. Chemistry and biology of the immunophilins and their immunosuppressive ligands. Science (New York, NY). 1991;251(4991):283-7.

65. Pollock R, Clackson T. Dimerizer-regulated gene expression. Current opinion in biotechnology. 2002;13(5):459-67.

66. Putyrski M, Schultz C. Protein translocation as a tool: The current rapamycin story. FEBS letters. 2012;586(15):2097-105.

67. del Castillo U, Winding M, Lu W, Gelfand VI. Interplay between kinesin-1 and cortical dynein during axonal outgrowth and microtubule organization in Drosophila neurons. eLife. 2015;4:e10140.

68. van Bergeijk P, Adrian M, Hoogenraad CC, Kapitein LC. Optogenetic control of organelle transport and positioning. Nature. 2015;518(7537):111-4.

69. Strickland D, Lin Y, Wagner E, Hope CM, Zayner J, Antoniou C, Sosnick TR, Weiss EL, Glotzer M. TULIPs: tunable, light-controlled interacting protein tags for cell biology. Nature methods. 2012;9(4):379-84.

70. Leeson PD, Springthorpe B. The influence of drug-like concepts on decision-making in medicinal chemistry. Nature reviews Drug discovery. 2007;6(11):881-90.

71. Anderson DJ, Le Moigne R, Djakovic S, Kumar B, Rice J, Wong S, Wang J, Yao B, Valle E, Kiss von Soly S, Madriaga A, Soriano F, Menon MK, Wu ZY, Kampmann M, Chen Y, Weissman JS, Aftab BT, Yakes FM, Shawver L, Zhou HJ, Wustrow D, Rolfe M. Targeting the AAA ATPase p97 as an Approach to Treat Cancer through Disruption of Protein Homeostasis. Cancer cell. 2015;28(5):653-65.

72. https://clinicaltrials.gov/ct2/show/NCT02223598

73. Chou TF, Li K, Frankowski KJ, Schoenen FJ, Deshaies RJ. Structure-activity relationship study reveals ML240 and ML241 as potent and selective inhibitors of p97 ATPase. ChemMedChem. 2013;8(2):297-312.

74. Chou TF, Bulfer SL, Weihl CC, Li K, Lis LG, Walters MA, Schoenen FJ, Lin HJ, Deshaies RJ, Arkin MR. Specific inhibition of p97/VCP ATPase and kinetic analysis demonstrate interaction between D1 and D2 ATPase domains. Journal of molecular biology. 2014;426(15):2886-99.

75. Chou TF, Brown SJ, Minond D, Nordin BE, Li K, Jones AC, Chase P, Porubsky PR, Stoltz BM, Schoenen FJ, Patricelli MP, Hodder P, Rosen H, Deshaies RJ. Reversible inhibitor of p97, DBeQ, impairs both ubiquitin-dependent and autophagic protein clearance pathways. Proceedings of the National Academy of Sciences of the United States of America. 2011;108(12):4834-9.

76. Magnaghi P, D'Alessio R, Valsasina B, Avanzi N, Rizzi S, Asa D, Gasparri F, Cozzi L, Cucchi U, Orrenius C, Polucci P, Ballinari D, Perrera C, Leone A, Cervi G, Casale E, Xiao Y, Wong C, Anderson DJ, Galvani A, Donati D, O'Brien T, Jackson PK, Isacchi A. Covalent and allosteric inhibitors of the ATPase VCP/p97 induce cancer cell death. Nature chemical biology. 2013;9(9):548-56.

77. Wojcik C, Rowicka M, Kudlicki A, Nowis D, McConnell E, Kujawa M, DeMartino GN. Valosin-containing protein (p97) is a regulator of endoplasmic reticulum stress and of the degradation of N-end rule and ubiquitin-fusion degradation pathway substrates in mammalian cells. Molecular biology of the cell. 2006;17(11):4606-18.

78. Chou TF, Deshaies RJ. Quantitative cell-based protein degradation assays to identify and classify drugs that target the ubiquitin-proteasome system. The Journal of biological chemistry. 2011;286(19):16546-54.

79. Kawashima SA, Chen Z, Aoi Y, Patgiri A, Kobayashi Y, Nurse P, Kapoor TM. Potent, Reversible, and Specific Chemical Inhibitors of Eukaryotic Ribosome Biogenesis. Cell. 2016;167(2):512-24.e14.

80. Human AAA+ protein count was obtained as follows: in supfam.org (reference 3), search was performed for "Extended AAA-ATPase domain" and refined for proteins within the human genome.

81. Baker TA, Sauer RT. ClpXP, an ATP-powered unfolding and protein-degradation machine. Biochimica et biophysica acta. 2012;1823(1):15-28.

82. Lampson MA, Kapoor TM. Unraveling cell division mechanisms with small-molecule inhibitors. Nature chemical biology. 2006;2(1):19-27.

83. Deshaies RJ. Proteotoxic crisis, the ubiquitin-proteasome system, and cancer therapy. BMC biology. 2014;12:94.

84. Vallee RB, Williams JC, Varma D, Barnhart LE. Dynein: An ancient motor protein involved in multiple modes of transport. Journal of neurobiology. 2004;58(2):189-200.

85. Ishikawa H, Marshall WF. Ciliogenesis: building the cell's antenna. Nature reviews Molecular cell biology. 2011;12(4):222-34.

86. Schmidt H. Dynein motors: How AAA+ ring opening and closing coordinates microtubule binding and linker movement. BioEssays : news and reviews in molecular, cellular and developmental biology. 2015;37(5):532-43.

87. Iyer LM, Leipe DD, Koonin EV, Aravind L. Evolutionary history and higher order classification of AAA+ ATPases. Journal of structural biology. 2004;146(1-2):11-31.

88. Bhabha G, Cheng HC, Zhang N, Moeller A, Liao M, Speir JA, Cheng Y, Vale RD. Allosteric communication in the dynein motor domain. Cell. 2014;159(4):857-68.

89. DeWitt MA, Cypranowska CA, Cleary FB, Belyy V, Yildiz A. The AAA3 domain of cytoplasmic dynein acts as a switch to facilitate microtubule release. Nature structural & molecular biology. 2015;22(1):73-80.

90. Nicholas MP, Berger F, Rao L, Brenner S, Cho C, Gennerich A. Cytoplasmic dynein regulates its attachment to microtubules via nucleotide state-switched mechanosensing at multiple AAA domains. Proceedings of the National Academy of Sciences of the United States of America. 2015;112(20):6371-6.

91. Milokhov DS, Khilya OV, Turov AV, Zubatyuk RI, Palamarchuk GV, Shishkin OV, Chekotilo AA, Volovenko YM. Reactions of 2-(2-hetaryl)-2-(tetrahydrofuran-2-ylidene)acetonitriles with tertiary amines. Chemistry of Heterocyclic Compounds. 2013;48(12):1761-9.

92. Süsse M, Johne S. Synthese von Pyrrolo[1,2-a]chinazolinonen, Indolo[1,2-a]chinazolinonen, Pyrrolo[1,2-a]thieno[3,2-e]pyrimidinonen, Benzothieno[3,2-e]-

pyrrolo[1,2-a]pyrimidinonen und 6H-Cyclohepta[4,5]thieno-[3,2-e]pyrrolo[1,2-a]pyrimidinonen. Journal fuer Praktische Chemie. 1981;323(4):647-53.

93. Orvieto F, Branca D, Giomini C, Jones P, Koch U, Ontoria JM, Palumbi MC, Rowley M, Toniatti C, Muraglia E. Identification of substituted pyrazolo[1,5-a]quinazolin-5(4H)-one as potent poly(ADP-ribose)polymerase-1 (PARP-1) inhibitors. Bioorganic & medicinal chemistry letters. 2009;19(15):4196-200.

94. Taipale J, Chen JK, Cooper MK, Wang B, Mann RK, Milenkovic L, Scott MP, Beachy PA. Effects of oncogenic mutations in Smoothened and Patched can be reversed by cyclopamine. Nature. 2000;406(6799):1005-9.

95. He M, Agbu S, Anderson KV. Microtubule Motors Drive Hedgehog Signaling in Primary Cilia. Trends in cell biology. 2017;27(2):110-25.

96. Yang TT, Su J, Wang WJ, Craige B, Witman GB, Tsou MF, Liao JC. Superresolution Pattern Recognition Reveals the Architectural Map of the Ciliary Transition Zone. Scientific reports. 2015;5:14096.

97. Mangeol P, Prevo B, Peterman EJ. KymographClear and KymographDirect: two tools for the automated quantitative analysis of molecular and cellular dynamics using kymographs. Molecular biology of the cell. 2016;27(12):1948-57.

98. Engel BD, Ishikawa H, Wemmer KA, Geimer S, Wakabayashi K, Hirono M, Craige B, Pazour GJ, Witman GB, Kamiya R, Marshall WF. The role of retrograde intraflagellar transport in flagellar assembly, maintenance, and function. The Journal of cell biology. 2012;199(1):151-67.

99. Yamada M, Toba S, Yoshida Y, Haratani K, Mori D, Yano Y, Mimori-Kiyosue Y, Nakamura T, Itoh K, Fushiki S, Setou M, Wynshaw-Boris A, Torisawa T, Toyoshima

YY, Hirotsune S. LIS1 and NDEL1 coordinate the plus-end-directed transport of cytoplasmic dynein. The EMBO journal. 2008;27(19):2471-83.

100. Qi Y, Wang JK, McMillian M, Chikaraishi DM. Characterization of a CNS cell line, CAD, in which morphological differentiation is initiated by serum deprivation. The Journal of neuroscience : the official journal of the Society for Neuroscience. 1997;17(4):1217-25.

101. Pu J, Guardia CM, Keren-Kaplan T, Bonifacino JS. Mechanisms and functions of lysosome positioning. 2016;129(23):4329-39.

102. Barlan K, Rossow MJ, Gelfand VI. The journey of the organelle: teamwork and regulation in intracellular transport. Current opinion in cell biology. 2013;25(4):483-8.

103. Shpetner HS, Paschal BM, Vallee RB. Characterization of the microtubule-activated ATPase of brain cytoplasmic dynein (MAP 1C). The Journal of cell biology. 1988;107(3):1001-9.

104. Ori-McKenney KM, Xu J, Gross SP, Vallee RB. A cytoplasmic dynein tail mutation impairs motor processivity. Nature cell biology. 2010;12(12):1228-34.

105. Nicholas MP, Hook P, Brenner S, Wynne CL, Vallee RB, Gennerich A. Control of cytoplasmic dynein force production and processivity by its C-terminal domain. Nature communications. 2015;6:6206.

106. Gibbons BH, Gibbons IR. Vanadate-sensitized cleavage of dynein heavy chains by 365-nm irradiation of demembranated sperm flagella and its effect on the flagellar motility. The Journal of biological chemistry. 1987;262(17):8354-9.

107. Silvanovich A, Li MG, Serr M, Mische S, Hays TS. The third P-loop domain in cytoplasmic dynein heavy chain is essential for dynein motor function and ATP-sensitive microtubule binding. Molecular biology of the cell. 2003;14(4):1355-65.

108. Serafimova IM, Pufall MA, Krishnan S, Duda K, Cohen MS, Maglathlin RL, McFarland JM, Miller RM, Frodin M, Taunton J. Reversible targeting of noncatalytic cysteines with chemically tuned electrophiles. Nature chemical biology. 2012;8(5):471-6.

109. Pillai AD, Pain M, Solomon T, Bokhari AA, Desai SA. A cell-based high-throughput screen validates the plasmodial surface anion channel as an antimalarial target. Molecular pharmacology. 2010;77(5):724-33.

110. Waterman-Storer CM, Karki SB, Kuznetsov SA, Tabb JS, Weiss DG, Langford GM, Holzbaur EL. The interaction between cytoplasmic dynein and dynactin is required for fast axonal transport. Proceedings of the National Academy of Sciences of the United States of America. 1997;94(22):12180-5.

111. Gross SP, Welte MA, Block SM, Wieschaus EF. Coordination of opposite-polarity microtubule motors. The Journal of cell biology. 2002;156(4):715-24.

112. Martin M, Iyadurai SJ, Gassman A, Gindhart JG, Jr., Hays TS, Saxton WM. Cytoplasmic dynein, the dynactin complex, and kinesin are interdependent and essential for fast axonal transport. Molecular biology of the cell. 1999;10(11):3717-28.

113. Ally S, Larson AG, Barlan K, Rice SE, Gelfand VI. Opposite-polarity motors activate one another to trigger cargo transport in live cells. The Journal of cell biology. 2009;187(7):1071-82.

114. Prevo B, Scholey JM, Peterman EJ. Intraflagellar Transport: Mechanisms of Motor Action, Cooperation and Cargo Delivery. The FEBS journal. 2017.

115. Ross JL, Wallace K, Shuman H, Goldman YE, Holzbaur EL. Processive bidirectional motion of dynein-dynactin complexes in vitro. Nature cell biology. 2006;8(6):562-70.

116. Imamula K, Kon T, Ohkura R, Sutoh K. The coordination of cyclic microtubule association/dissociation and tail swing of cytoplasmic dynein. Proceedings of the National Academy of Sciences of the United States of America. 2007;104(41):16134-9.

117. Babine RE, Bender SL. Molecular Recognition of Protein-Ligand Complexes: Applications to Drug Design. Chemical reviews. 1997;97(5):1359-472.

118. Bussenius J, Anand NK, Blazey CM, Bowles OJ, Bannen LC, Chan DS, Chen B, Co EW, Costanzo S, DeFina SC, Dubenko L, Engst S, Franzini M, Huang P, Jammalamadaka V, Khoury RG, Kim MH, Klein RR, Laird D, Le DT, Mac MB, Matthews DJ, Markby D, Miller N, Nuss JM, Parks JJ, Tsang TH, Tsuhako AL, Wang Y, Xu W, Rice KD. Design and evaluation of a series of pyrazolopyrimidines as p70S6K inhibitors. Bioorganic & medicinal chemistry letters. 2012;22(6):2283-6.

119. Burla MC, Caliandro R, Camalli M, Carrozzini B, Cascarano GL, De Caro L, Giacovazzo C, Polidori G, Siliqi D, Spagna R. IL MILIONE: a suite of computer programs for crystal structure solution of proteins. Journal of Applied Crystallography. 2007;40(3):609-13.

120. Sheldrick GM. A short history of SHELX. Acta crystallographica Section A, Foundations of crystallography. 2008;64(Pt 1):112-22.

121. Spek AL. Structure validation in chemical crystallography. Acta crystallographica Section D, Biological crystallography. 2009;65(Pt 2):148-55.

122. Schindelin J, Arganda-Carreras I, Frise E, Kaynig V, Longair M, Pietzsch T, Preibisch S, Rueden C, Saalfeld S, Schmid B, Tinevez JY, White DJ, Hartenstein V, Eliceiri K, Tomancak P, Cardona A. Fiji: an open-source platform for biological-image analysis. Nature methods. 2012;9(7):676-82.

123. Roberts AJ, Kon T, Knight PJ, Sutoh K, Burgess SA. Functions and mechanics of dynein motor proteins. Nature reviews Molecular cell biology. 2013;14(11):713-26.

124. Steinman JB, Santarossa CC, Miller RM, Yu LS, Serpinskaya AS, Furukawa H, Morimoto S, Tanaka Y, Nishitani M, Asano M, Zalyte R, Ondrus AE, Johnson AG, Ye F, Nachury MV, Fukase Y, Aso K, Foley MA, Gelfand VI, Chen JK, Carter AP, Kapoor TM. Chemical structure-guided design of dynapyrazoles, potent cell-permeable dynein inhibitors with a unique mode of action. eLife. 2017;6.

125. Bingham JB, King SJ, Schroer TA. Purification of dynactin and dynein from brain tissue. Methods in enzymology. 1998;298:171-84.

126. Vale RD, Toyoshima YY. Microtubule translocation properties of intact and proteolytically digested dyneins from Tetrahymena cilia. The Journal of cell biology. 1989;108(6):2327-34.

127. Vale RD, Oosawa F. Protein motors and Maxwell's demons: does mechanochemical transduction involve a thermal ratchet? Advances in biophysics. 1990;26:97-134.

128. Roberts AJ, Numata N, Walker ML, Kato YS, Malkova B, Kon T, Ohkura R, Arisaka F, Knight PJ, Sutoh K, Burgess SA. AAA+ Ring and linker swing mechanism in the dynein motor. Cell. 2009;136(3):485-95.

129. Toropova K, Mladenov M, Roberts AJ. Intraflagellar transport dynein is autoinhibited by trapping of its mechanical and track-binding elements. Nature structural & molecular biology. 2017.

130. Tang G, Peng L, Baldwin PR, Mann DS, Jiang W, Rees I, Ludtke SJ. EMAN2: an extensible image processing suite for electron microscopy. Journal of structural biology. 2007;157(1):38-46.

131. Macarron R, Banks MN, Bojanic D, Burns DJ, Cirovic DA, Garyantes T, Green DV, Hertzberg RP, Janzen WP, Paslay JW, Schopfer U, Sittampalam GS. Impact of high-throughput screening in biomedical research. Nature reviews Drug discovery. 2011;10(3):188-95.

132. Evans BE, Rittle KE, Bock MG, DiPardo RM, Freidinger RM, Whitter WL, Lundell GF, Veber DF, Anderson PS, Chang RS, et al. Methods for drug discovery: development of potent, selective, orally effective cholecystokinin antagonists. Journal of medicinal chemistry. 1988;31(12):2235-46.

133. Bon RS, Waldmann H. Bioactivity-guided navigation of chemical space. Accounts of chemical research. 2010;43(8):1103-14.

134. Horton DA, Bourne GT, Smythe ML. The combinatorial synthesis of bicyclic privileged structures or privileged substructures. Chemical reviews. 2003;103(3):893-930.

135. Devlin J. High Throughput Screening: The Discovery of Bioactive Substances. Boca Raton, FL: CRC Press; 1997. 704 p.

136. Cheng Y, Prusoff WH. Relationship between the inhibition constant (K1) and the concentration of inhibitor which causes 50 per cent inhibition (I50) of an enzymatic reaction. Biochemical pharmacology. 1973;22(23):3099-108.

137. Bessodes M, Bastian G, Abushanab E, Panzica RP, Berman SF, Marcaccio EJ, Jr., Chen SF, Stoeckler JD, Parks RE, Jr. Effect of chirality in erythro-9-(2-hydroxy-3-nonyl) adenine (EHNA) on adenosine deaminase inhibition. Biochemical pharmacology. 1982;31(5):879-82.

138. Shiroguchi K, Toyoshima YY. Regulation of monomeric dynein activity by ATP and ADP concentrations. Cell motility and the cytoskeleton. 2001;49(4):189-99.

139. Hoang HT, Schlager MA, Carter AP, Bullock SL. DYNC1H1 mutations associated with neurological diseases compromise processivity of dynein-dynactin-cargo adaptor complexes. Proceedings of the National Academy of Sciences of the United States of America. 2017;114(9):E1597-e606.

140. Sumranjit J, Chung SJ. Recent advances in target characterization and identification by photoaffinity probes. Molecules (Basel, Switzerland). 2013;18(9):10425-51.

141. Bishop AC, Buzko O, Shokat KM. Magic bullets for protein kinases. Trends in cell biology. 2001;11(4):167-72.

142. Cohen MS, Zhang C, Shokat KM, Taunton J. Structural bioinformatics-based design of selective, irreversible kinase inhibitors. Science (New York, NY). 2005;308(5726):1318-21.

143. Kasap C, Elemento O, Kapoor TM. DrugTargetSeqR: a genomics- and CRISPR-Cas9-based method to analyze drug targets. Nature chemical biology. 2014;10(8):626-8.

144. Wacker SA, Houghtaling BR, Elemento O, Kapoor TM. Using transcriptome sequencing to identify mechanisms of drug action and resistance. Nature chemical biology. 2012;8(3):235-7.

145. Peterson AC, Russell JD, Bailey DJ, Westphall MS, Coon JJ. Parallel reaction monitoring for high resolution and high mass accuracy quantitative, targeted proteomics. Molecular & cellular proteomics : MCP. 2012;11(11):1475-88.

146. MacLean B, Tomazela DM, Shulman N, Chambers M, Finney GL, Frewen B, Kern R, Tabb DL, Liebler DC, MacCoss MJ. Skyline: an open source document editor for creating and analyzing targeted proteomics experiments. Bioinformatics (Oxford, England). 2010;26(7):966-8.